

**Mass Loss from  
Evolved Late Type Stars**

A Thesis submitted for the Degree  
of  
Doctor of Philosophy of the University of London  
by  
Kuanhatai Justtanont

Department of Physics & Astronomy  
University College London  
University of London

1992

ProQuest Number: 10608919

All rights reserved

INFORMATION TO ALL USERS

The quality of this reproduction is dependent upon the quality of the copy submitted.

In the unlikely event that the author did not send a complete manuscript and there are missing pages, these will be noted. Also, if material had to be removed, a note will indicate the deletion.



ProQuest 10608919

Published by ProQuest LLC (2017). Copyright of the Dissertation is held by the Author.

All rights reserved.

This work is protected against unauthorized copying under Title 17, United States Code  
Microform Edition © ProQuest LLC.

ProQuest LLC.  
789 East Eisenhower Parkway  
P.O. Box 1346  
Ann Arbor, MI 48106 – 1346

# Abstract

This thesis can be divided into three parts which are related together. The first part deals with the modelling of the infrared energy distributions of oxygen-rich, late type stars, mainly OH/IR stars, in order to derive the dust mass loss rates. This is done by using the radiative transfer code, assuming the spherical symmetry, but takes into account the effects of thermal re-emission and multiple scattering. Also, the grain size distribution in circumstellar shells is assumed to follow the same power law governing the size distribution of interstellar grains. The optical properties of these grains, silicates, are investigated. For stars with large mass outflows, water-ice is expected to condense onto silicate grains. These stars, seen with a deep  $3.1\mu\text{m}$  absorption feature, due to water-ice, are successfully modelled using silicates derived here, with the published amorphous water-ice optical constants.

The second part involves the study of gas kinetics of these stars, in particular the temperature distributions as results of collisional heating and radiative and adiabatic cooling. These, in turn, are used in the calculations of the CO line profiles, which also depend on mass loss rates. The dust and gas mass loss rates may represent different episodes at which mass is being lost from stars.

The final part of this thesis involves the investigation of spectroscopic observations of post-AGB stars, a phase where mass loss has stopped and the dust shells are becoming detached from the stars, and/or having the evidence of bipolarity. Both the oxygen-rich and carbon-rich sources are studied as to establish the nature of their dust.

# Acknowledgements

First of all, I would like to thank all my supervisors : Dr Xander Tielens of NASA Ames without whom I would never get this far. Three cheers for you, Xander. Also to Dr. Chris Skinner for starting me off and for all your suggestions, Dr. Bill Glencross for helping me along and proof reading this thesis. All my sincere gratitude to you all.

My years at UCL were made bearable by all my friends and colleagues, Siranee, Ian 'the Director', John 'Dekes', Mike, Robin, Mike, Roger, John, Ian, Martin, Bob and the ex-IR group and UCL members. I have to also mention friends at Ames who tried to Americanise me. You did not succeed, Paul, Bill and Carter! And to all those friends at the ROH and the ballet classes who kept me sane while I was writing up. Thanks Anabel, Christian, Belinda, Jeremy, Miho, Julia and Bruce and the RB for all those wonderful performances.

I would like to give my very deepest thank for my parents who gave me moral and financial support throughout my education. And to Doreen and Bil for your loving support.

## Declaration

The radiative transfer through dust shell code (Haisch 1979) has been obtained in the working form from Griffin (1990). The author added the ability for the code to calculate two component grains condensing at different radii. The line transfer code (Schonberg & Hempe 1986) were checked for errors by Drs. C.J. Skinner, A.G.G.M. Tielens and the author. The author rewrote the code so that it can read the temperature distribution from the heating and cooling code which was also written by the author. The  $\chi^2$  fitting program was developed by Aitken et al. (1979) and further development was done by R.J. Sylvester. The SEST data were obtained in collaboration with Drs. C.J. Skinner and I.P. Griffin. These were reduced by the author and further correction was done by C.J. Skinner. CGS3 data were reduced by the author.

# Acknowledgements

First of all, I would like to thank all my supervisors : Dr Xander Tielens of NASA Ames without whom I would never get this far. Three cheers for you, Xander. Also to Dr. Chris Skinner for starting me off and for all your suggestions, Dr. Bill Glencross for helping me along and proof reading this thesis. All my sincere gratitude to you all.

My years at UCL were made bearable by all my friends and colleagues, Siranee, Ian 'the Director', John 'Deke', Mike, Robin, Mike, Roger, John, Ian, Martin, Bob and the ex-IR group and UCL members. I have to also mention friends at Ames who tried to Americanise me. You did not succeed, Paul, Bill and Carter! And to all those friends at the ROH and the ballet classes who kept me sane while I was writing up. Thanks Anabel, Christian, Belinda, Jeremy, Miho, Julia and Bruce and the RB for all those wonderful performances.

I would like to give my very deepest thank for my parents who gave me moral and financial support throughout my education. And to Doreen and Bil for your loving support.

*To Mayura and Prajab*

# Contents

<b>Title Page</b>	<b>1</b>
<b>Abstract</b>	<b>2</b>
<b>Acknowledgements</b>	<b>3</b>
<b>List of Tables</b>	<b>8</b>
<b>List of Figures</b>	<b>11</b>
<b>1 Introduction</b>	<b>12</b>
1.1 Nucleosynthesis in AGB stars . . . . .	13
1.2 Possible mass loss mechanisms . . . . .	15
1.3 The nature of OH/IR stars . . . . .	23
1.3.1 The radio and infrared observations . . . . .	24
1.3.2 Stellar properties . . . . .	29
1.4 The final evolution . . . . .	30
1.5 Outline of the present work . . . . .	31
<b>2 Radiative Transfer in Dust Shells and Grain Parameters</b>	<b>33</b>
2.1 The radiative transfer code . . . . .	35
2.2 Efficiency factors of small grains . . . . .	38
2.3 Grain properties . . . . .	39
2.3.1 Silicate grains . . . . .	41
2.3.2 Silicate core-ice mantle grains . . . . .	43

<b>3</b>	<b>Modelling the Infrared Energy Distributions</b>	<b>50</b>
3.1	Input parameters . . . . .	50
3.1.1	Stellar parameters . . . . .	50
3.1.2	Wind terminal velocity . . . . .	52
3.1.3	Inner and outer radii of dust shells . . . . .	52
3.1.4	Density law . . . . .	52
3.1.5	Dust properties . . . . .	52
3.2	Results from modelling the infrared spectra . . . . .	54
3.2.1	Individual sources . . . . .	55
3.2.2	Uncertainties in the derived parameters . . . . .	64
3.3	Comparisons of mass loss rates . . . . .	65
3.3.1	Dust mass loss rates . . . . .	66
3.3.2	Gas mass loss rates . . . . .	71
<b>4</b>	<b>Heating and Cooling in Circumstellar Envelopes of Late-type Stars</b>	<b>79</b>
4.1	The gas dynamics . . . . .	80
4.2	Temperature structure of the gas . . . . .	82
4.2.1	Gas-grain collisional heating . . . . .	82
4.2.2	Rotational excitation of H <sub>2</sub> O molecules . . . . .	83
4.2.3	Vibrational excitation of H <sub>2</sub> O molecules . . . . .	84
4.2.4	Vibrational excitation of H <sub>2</sub> molecules . . . . .	85
4.2.5	Rotational excitation of CO molecules . . . . .	85
4.2.6	The temperature structure . . . . .	86
4.3	Variations of the input parameters . . . . .	87
4.4	Modelling O-rich stars . . . . .	99
4.4.1	GX Mon . . . . .	99
4.4.2	IRC+10011 . . . . .	102
4.4.3	OH26.5+0.6 . . . . .	104
4.5	Summary . . . . .	106
<b>5</b>	<b>CO Line Profile Calculations</b>	<b>107</b>
5.1	The ANR technique . . . . .	108
5.2	Variations in antenna temperature and line profiles . . . . .	111

5.2.1	The effects of the mass loss rates on CO line profiles . . . . .	111
5.2.2	The effect of distance on CO line profiles . . . . .	114
5.2.3	The effects of the gas kinetic temperature law on CO line profiles . .	117
5.2.4	Optical depth of each transition . . . . .	117
5.3	CO calculations for O-rich stars . . . . .	117
5.3.1	GX Mon . . . . .	119
5.3.2	IRC+10011 . . . . .	123
5.3.3	OH26.5+0.6 . . . . .	126
5.4	Summary . . . . .	128
<b>6</b>	<b>Observations of Post-AGB Objects</b>	<b>130</b>
6.1	The Cooled Grating Spectrometer 3 . . . . .	130
6.2	The nature of dust around HD 161796 and HD 179821 . . . . .	131
6.2.1	Introduction . . . . .	131
6.2.2	Observations . . . . .	132
6.2.3	Discussion . . . . .	132
6.3	Mid-infrared spectroscopy of four 21 $\mu$ m emission band sources . . . . .	142
6.3.1	Introduction . . . . .	142
6.3.2	Observations . . . . .	142
6.3.3	Discussion . . . . .	143
	<b>Concluding Remarks</b>	<b>152</b>
	<b>List of Publications</b>	<b>156</b>
	<b>References</b>	<b>157</b>

# List of Tables

3.1	Input parameters for radiative transfer calculations. . . . .	77
3.2	Estimated dust and gas mass loss rates. . . . .	78
4.1	Input parameters for the heating and cooling in the circumstellar envelopes of O-rich stars. . . . .	98
4.2	Input parameters for 3 chosen O-rich stars. . . . .	99
5.1	Parameter studies of the CO J=1-0 line fluxes and profiles. . . . .	114
5.2	Parameters for the three O-rich stars under investigation . . . . .	119
5.3	The predicted peak antenna temperatures for GX Mon. . . . .	123
5.4	The predicted peak antenna temperatures for IRC+10011. . . . .	125
5.5	The predicted peak antenna temperatures for OH26.5+0.6. . . . .	128
6.1	$\chi^2$ fitting parameters for HD 161796 and HD 179821 . . . . .	137
6.2	Wavelengths of various features seen in $10\mu\text{m}$ spectra of $21\mu\text{m}$ sources . . .	143
6.3	Ratios of the $20:18\mu\text{m}$ fluxes for the $21\mu\text{m}$ objects. . . . .	148

# List of Figures

1.1	Evolutionary tracks for stars with different masses . . . . .	13
1.2	Pulsation cycles as a function of radius for a model without dust. . . . .	17
1.3	Pulsation cycles as a function of radius for a model including dust. . . . .	18
1.4	Effects of pulsations on velocity, temperature and density without dust. . .	20
1.5	Effects of pulsations on velocity, temperature and density with dust. . . . .	21
1.6	Samples of OH maser emission line profiles . . . . .	25
1.7	The transitional diagram for an OH molecule. . . . .	26
1.8	Colour-colour diagram for <i>IRAS</i> point sources . . . . .	27
1.9	The HR diagram for a star with a core mass of $0.6M_{\odot}$ . . . . .	30
2.1	Published extinction efficiencies for silicate grains . . . . .	40
2.2	Calculated silicate extinction efficiencies . . . . .	42
2.3	The ice mantle thickness as a function of oxygen depleted . . . . .	45
2.4	Silicate core-ice mantle grain extinction efficiencies for two ice mantle thick- ness . . . . .	46
2.5	Ice extinction efficiencies as a function of the condensing temperature . . .	49
3.1	Silicate extinction efficiencies used in modelling sample stars . . . . .	53
3.2	Model fits for the infrared energy distributions for 26 OH/IR stars . . . . .	56
3.3	The relationship between dust mass loss rates and the ratios of the 25-to- $12\mu\text{m}$ fluxes . . . . .	68
3.4	Dust mass loss rate as a function of optical depths at $9.7\mu\text{m}$ . . . . .	69
3.5	Dust mass loss rate as a function of $60\mu\text{m}$ luminosity . . . . .	70
3.6	Mass loss rate as a function of OH and $35\mu\text{m}$ luminosities . . . . .	73
3.7	The comparison between dust and CO mass loss rates . . . . .	76

4.1	Heating and cooling rates in IRC+10011 (GS model) . . . . .	88
4.2	Heating, cooling rates and the resulting gas kinetic temperature for Model 1	89
4.3	Heating, cooling rates and the resulting gas kinetic temperature for Model 2	90
4.4	Heating, cooling rates and the resulting gas kinetic temperature for Model 3	91
4.5	Heating, cooling rates and the resulting gas kinetic temperature for Model 4	92
4.6	Heating, cooling rates and the resulting gas kinetic temperature for Model 5	93
4.7	Heating, cooling rates and the resulting gas kinetic temperature for Model 6	94
4.8	Heating, cooling rates and the resulting gas kinetic temperature for Model 7	95
4.9	The terminal velocity as a function of dust mass loss rate for different dust- to-gas mass ratios . . . . .	97
4.10	Heating, cooling rates and temperature structure of GX Mon . . . . .	100
4.11	Heating, cooling rates and temperature structure of IRC+10011 . . . . .	103
4.12	Heating, cooling rates and temperature structure of OH26.5+0.6 . . . . .	105
5.1	The effect of mass loss rates on the observed CO line profiles. . . . .	112
5.2	Gas kinetic temperatures and excitation temperatures for different mass loss rates. . . . .	113
5.3	The effect of distances on the observed CO line profiles. . . . .	115
5.4	The effect of excitation temperature laws on the observed CO line profiles. .	116
5.5	The radius where optical depth is unity for each transition for different mass loss rates. . . . .	118
5.6	Observed CO line profiles of GX Mon and the calculated fits. . . . .	120
5.7	Predicted CO line profiles for GX Mon. . . . .	122
5.8	Predicted CO line profiles for IRC+10011. . . . .	124
5.9	Predicted CO line profiles for OH26.5+0.6. . . . .	127
6.1	CGS3 spectra of HD 161796 and HD 179821 . . . . .	133
6.2	Infrared energy distributions of HD 161796 and HD 179821 . . . . .	135
6.3	Comparisons between HD 161796 and HD 179821 and other C-rich post- AGB stars. . . . .	136
6.4	$\chi^2$ fits of HD 161796 and HD 179821 . . . . .	138
6.5	CGS3 spectra of $21\mu\text{m}$ sources . . . . .	144
6.6	The CGS3 $10\mu\text{m}$ spectrum of IRAS 22272+5435 . . . . .	146

6.7	<i>IRAS</i> LRS spectra of IRAS 20000+3239 and IRAS 23304+6147 . . . . .	149
6.8	Spectra of GL 915 and M1-71 . . . . .	151

# Chapter 1

## Introduction

Understanding the subject of mass loss from a star is necessary in the studies of stellar evolution and the interstellar medium. The stellar mass is the most important parameter in governing how a star evolves, hence a stellar evolution model needs to have mass loss rates included in order to trace the activities throughout the life time of a star under investigation. Mass loss also depends on the chemical composition which determines the stellar opacity. For a star with mass larger than  $2M_{\odot}$ , if no mass is lost during its lifetime, it will undergo a supernova explosion since its core mass exceeds the Chandrasekhar limit. However, there is a significant number of stars with larger masses, together with the infrequent occurrence of supernovae, and a large number of white dwarfs in our galaxy, indicate that stars lose a large fraction of their initial masses before reaching the end of their evolution. Mass loss rate varies with time, with the most of the stellar mass being ejected at the end of the Asymptotic Giant phase, before the star evolves into a planetary nebula. After a star leaves the zero age main sequence, its track on the H-R diagram depends on its initial mass. For a small mass ( $1 M_{\odot}$ ) star, the hydrogen core is exhausted. Hydrogen-shell burning starts and a degenerate helium core is produced. Such a star is on the Red Giant Branch (RGB) and helium is reignited. Its luminosity increases due to hydrogen-burning in the shell. An intermediate mass star follows a track which is more horizontal, and does not climb the RGB, but moves towards central helium burning. After central helium exhaustion, stars from both groups move to the Asymptotic Giant Branch (AGB), where helium burns in a shell (see Figure 1.1). This increases the luminosities and hydrogen is still inert. Then, hydrogen shell burning starts, producing a degenerate C/O core. This double shell burning makes the system unstable, which is thought to cause

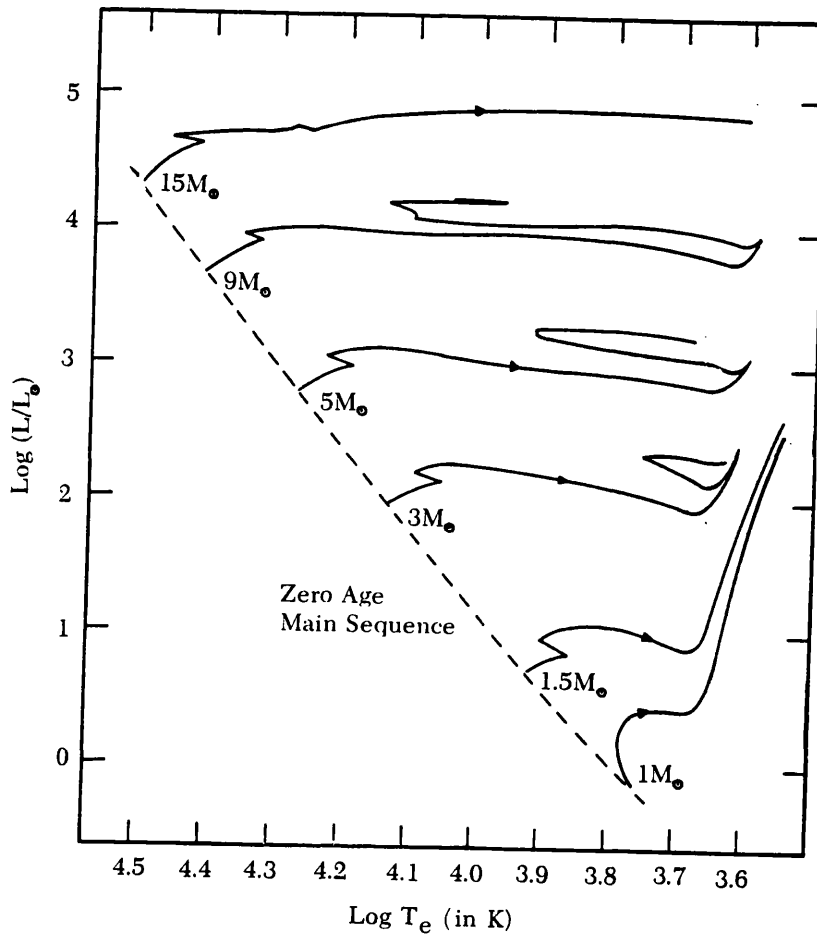


Figure 1.1: Evolutionary tracks for stars with different masses (Smith & Jacobs 1973).

significant mass loss by pulsation. By the time it leaves the AGB, the star will only have a small fraction of its initial mass left, hence it evolves into a planetary nebula and, finally, a white dwarf. The gas and dust in the envelope is returned to the interstellar medium forming molecular clouds which collapse to form new stars.

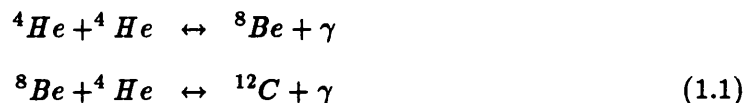
## 1.1 Nucleosynthesis in AGB stars

Intermediate mass stars are defined as those objects which develop an electron-degenerate C/O core following the helium-exhaustion at the centre. The upper limit on an initial mass is 8–9  $M_{\odot}$ . Following hydrogen-exhaustion, all stars undergo the first dredge up whereby the surface abundance of  $^{14}\text{N}$  is doubled, while  $^{12}\text{C}$  decreases by 30%. The ratio of  $^{12}\text{C}$  to  $^{13}\text{C}$  is about 20–30. The reduction of surface abundances of Li and Be by several orders of magnitude also results, but the abundance of  $^{16}\text{O}$  remains roughly unchanged. The material is mixed due to convection.

The second dredge up occurs when a star develops an electron degenerate core, to be followed by central helium-exhaustion. Hydrogen in the dredge up material is converted into helium, while  $^{12}\text{C}$  and  $^{16}\text{O}$  are converted into  $^{14}\text{N}$ . This dredge up only occurs in high

mass stars.

Before the onset of the thermal pulse, the hydrogen burning shell is extinct and helium only burns in a thin shell. The bulk of the energy produced involves the triple alpha reaction.



Since helium is in the non-degenerate region, the energy results in an increase in the local pressure and an expansion. Cooling then sets in and the helium burning slowly subsides. Once the helium luminosity is less than the surface luminosity, the expanded material falls back, and is heated up until hydrogen is reignited. An equilibrium is reached when hydrogen luminosity equals the surface luminosity. The star then enters a quiescent hydrogen shell burning phase, until the hydrogen mass in the shell becomes large, and the next helium flash occurs. The pulse interval increases as a function of the AGB lifetime. A convective shell forms as the helium burning shell becomes large. Also the maximum temperature at the base of the shell increases with each pulse (Iben & Renzini 1983).

The final relative abundance of carbon to oxygen at the end of the helium burning is expected to be 2:1 (Fowler, Caughlan & Zimmerman 1975). However, the photospheric abundance of a star is determined by the amount of material present on the surface. Since the radius where the radiative gradient exceeds the adiabatic gradient moves closer to the helium burning region, the processed materials are easily transported outwards by convection. The mixing of the  $^{12}\text{C}$  with neutron-rich isotopes is called the third dredge up. Many studies show that there is a critical core mass below which the third dredge up might not occur. This is taken to be  $\sim 0.6M_{\odot}$ . The dredge up also depends on the total mass and the metallicity of the stars (Wood 1981). The result of the third dredge up is to increase the abundance of carbon relative to oxygen.

AGB stars are divided into two main groups, C-rich and O-rich, with a few stars which have  $[\text{C}]/[\text{O}] \sim 1$ , called the S-stars. Optically, C-rich stars show the Swan bands of  $\text{C}_2$ , while the O-rich stars show the metallic oxides. Mid-infrared spectra of circumstellar shells around C-stars show a broad emission at  $11.15\mu\text{m}$ , due to SiC (Treffers & Cohen 1974), while O-rich stars have features at  $9.7$  and  $18\mu\text{m}$  (Jones & Merrill 1976). Little-Marenin (1986) discovered carbon stars (determined from their photospheric spectra) with

silicate dust shells, and discusses the possibility of an M star in a binary orbit around these C-rich stars. Willem & de Jong (1988) put forward an alternative proposal that these stars are in transition between O-rich and C-rich phase.

## 1.2 Possible mass loss mechanisms

There are several possible mechanisms which can drive mass loss in cool stars. These must be able to explain the grain formation and the low terminal velocity observed in red giants. The most efficient process involves radiation pressure on dust grains, assuming that the dust and gas are momentum coupled, then

$$\dot{M}v = \frac{\tau_d L_*}{c} \quad (1.2)$$

where  $\dot{M}$  is the mass loss rate;  $v$  is the outflow velocity;  $\tau_d$  is the integrated optical depth of dust; and  $L_*$  is the stellar luminosity. However, the mechanism which lifts the material from the stellar photosphere to the radius where dust condenses out is not known. A few proposals have been put forward to try and explain this.

Thermally driven wind proposed by Parker (1958) can explain solar-type stars, where the temperature gradient is high. However, in red giants, this is not the case. The critical temperature in this model depends on the stellar mass and the Parker radius,  $r_{crit}$ , where the flow becomes supersonic i.e.,

$$T_{crit} = 8 \times 10^6 \frac{M}{M_\odot} \frac{R_\odot}{r_{crit}} \quad (1.3)$$

where  $M$  is the stellar mass; and  $R$  is the stellar radius. The density can be expressed in term of the scale height,  $H$ , at a radius  $r$

$$\begin{aligned} \rho(r) &= \rho_0 \exp(-r/H) \\ &= \rho_0 \exp(-m_H g r / k T_{crit}) \end{aligned} \quad (1.4)$$

where  $\rho_0$  is the density at the photosphere;  $m_H$  is the hydrogen mass;  $g$  is the acceleration constant; and  $k$  is the Boltzmann constant. Since temperatures of red giants are only a few thousand degrees, the scale heights are very small. These result in very small mass loss rates ( $\dot{M} \propto \rho$ ). Castor (1981) calculated the radiative cooling time and concluded that the red giant winds are cool, since the radiative power loss is a steep function of temperature

up to  $T \geq 15000\text{K}$  (McWhirter, Thonemann & Wilson 1975). This is in agreement with the AGB stars having the spectral type M.

As mentioned previously, radiation pressure on dust is very efficient in driving mass loss. The question remains as to whether radiation pressure can initiate flows which remains sufficiently dense for dust to condense out. Elitzur, Brown & Johnson (1989) argue that mass loss can be achieved by trapping radiation in vibrational-rotational transitions of  $\text{H}_2\text{O}$  molecules. When the radiation pressure exceeds the gas pressure, i.e.,  $\frac{1}{3}aT^4 > nkT$ , mass loss occurs. This happens close to the stellar photosphere, since the gas pressure varies exponentially with radius, while the temperature and the radiation pressure vary as a power law. Their calculations suggest that the radiation pressure rises rapidly when the stellar temperature falls below 2500K, which is the case for many AGB stars. Mass loss rate from this process is calculated by

$$\dot{M} = 1.08 \times 10^{-5} \left(\frac{r}{10^{13}}\right)^2 \left(\frac{N}{10^{12}}\right) \left(\frac{T}{10^3}\right)^{1/2} \dot{M}_{\odot}/yr \quad (1.5)$$

where  $N$  is the number density in  $\text{cm}^{-3}$ ;  $T$  is the temperature at the wind initiation point at radius  $r$ .

## Pulsation driven winds

Pulsation driven wind is one of the most commonly studied mechanism, since red giants are known to be unstable due to the double shell burning (see e.g., Wood 1979). Evidences for shock waves in late type stars are

- the asymmetry of light curves;
- varying intensities in the observed emission line in phase with the luminosities;
- the discontinuities in velocity curves.

A star can be divided into zones where disturbances start and develop into shocks as they propagate outwards (e.g., Willson & Bowen 1985). The innermost zone is the static core (a degenerate C/O core for a giant), which does not participate in the pulsation. Above this, there are the inner and outer damping zones, with the pulsation driving zone in between. The pulsation driving zone is where hydrogen and helium got ionised, thereby increasing pressure in the region. Whether pulsation will occur depends on the mass of the outer

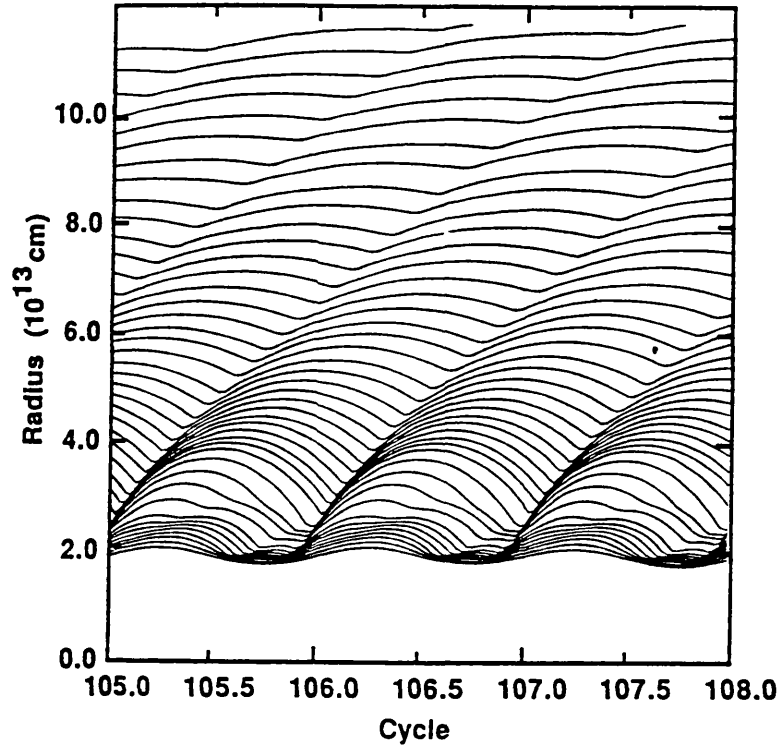


Figure 1.2: Pulsation cycles as a function of radius for a model with a fundamental period; the piston velocity amplitude is 3km/s; and dust is not included. The innermost zone is the stellar photosphere (Bowen 1988).

damping zone. If the mass in this region is too large, pulsation will be effectively damped, but if it is too small, it cannot store enough energy necessary to drive the pulsation. As the disturbances propagate outwards into a region where density is low, they develop into shock waves. At the start, the shock is isothermal because the relaxation time is short. The assumption that the material returns to its original position after encountering a shock wave still holds. As the shocks propagate farther out from the photosphere, the density decreases so much that the relaxation time becomes longer than the shock intervals. The shocks are now said to be adiabatic. The LTE assumptions break down since there is no single temperature which can describe all the processes in this region. The outermost zone is where the outflow velocity exceeds the escape velocity.

Once the gas encounters a shock, the kinetic energy is transformed into the radiation and the internal energy of the gas, which are the results of dissociation or ionisation and excitation. Generally, if the radiative cooling time is short compared to other time scales (e.g., excitation, ionisation), the gas is said to be isothermal. This condition is satisfied in

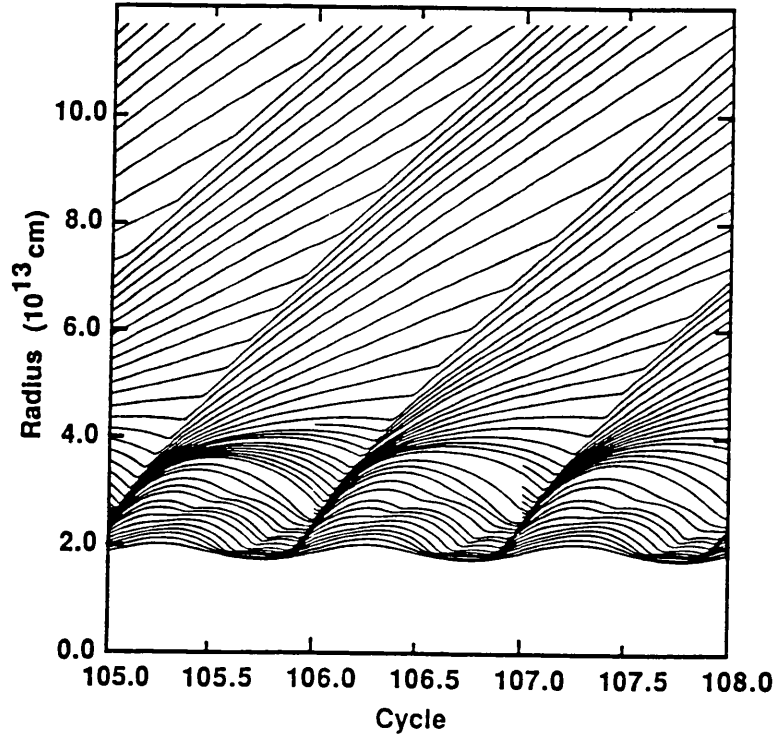


Figure 1.3: Same as Figure 1.2, except the radiation pressure on dust is included in this model (Bowen 1988).

the region where density is relatively high, e.g., the inner atmosphere of a star. However, if the radiative cooling time is long, the shock becomes adiabatic. This occurs where density is low, e.g., in the outer atmosphere of a star. If the shock is purely adiabatic, the mass loss rate will be extremely large ( $10^{-2} M_{\odot}/\text{yr}$ ) i.e., most of the shock energy is converted into the gas kinetic energy. On the other hand, if the wind is purely isothermal, most of the energy is radiated away, resulting in a mass loss rate ten orders of magnitude smaller. Clearly, the physical wind will be a combination of these.

In the periodic shock model, disturbances propagate outward through the regions where density is very low. They, then, become shock waves. If the dissipation time is longer than the the interval between each shock wave, the resulting motion of gas is outwards, i.e., gas does not have time to cool and return to its starting position before the next shock arrives.

In the isothermal model, the momentum equation is written as

$$v \frac{dv}{dr} + \frac{GM}{r^2} + \frac{c_s^2}{\rho} \frac{\partial \rho}{\partial r} = 0 \quad (1.6)$$

where  $c_s$  is the sound speed in the gas. Integrating the above equation from the post shock velocity,  $v_0$  and post shock saturation radius  $r_0$  to a general point  $v$  and  $r$ , we obtain the velocity structure

$$\beta(y^2 - 1) = \frac{H_0}{r_0} \ln\left(\frac{2r_0}{H_0} \beta^2 (1 + y)^2\right) \quad (1.7)$$

where  $y$  is the shock asymmetry parameter, i.e., the ratio of the infall velocity to the outward velocity of the gas;  $\beta$  is the ratio of the outward velocity to the escape velocity; and  $H_0$  is the post shock scale height. The density structure in this model can be described by

$$\ln\left(\frac{\rho}{\rho_0}\right) = -(1 - \gamma^2) \left(\frac{r_0}{H_0}\right) \left(1 - \frac{r_0}{r}\right) \quad (1.8)$$

where  $\rho_0$  is the post shock density; and  $\gamma^2$  is the ratio of the kinetic energy to the gravitational energy. If the effect of the temperature gradient is included, the density structure will change because the scale height changes. For the case of  $T \propto r^{-1/2}$

$$\ln\left(\frac{\rho}{\rho_0}\right) = -(1 - \gamma^2) \left(\frac{r_0}{H_0}\right) \frac{2}{3} \left(1 - \left(\frac{r_0}{r}\right)^{1/2}\right) \quad (1.9)$$

Even in the isothermal shock where mass loss is very small, the effect of the pulsation is to extend the atmosphere, i.e., mass is transported outward and the density gradient is reduced (Figures 1.2 and 1.4). In the adiabatic case, material does not return to the starting position before the next shock arrives. Hence the gas slowly progresses outward. In the case where dust condenses out in the atmosphere, the winds are further accelerated and the outflows are more efficiently driven. One major problem with the pulsation model is the uncertainty in the mechanism in transportation of energy in the convective envelope. The mixing-length theory is often used as an approximation. This results in unstable pulsation cycle if it is used during the non-linear fundamental mode pulsation. Wood (1989) developed a model for Miras, pulsating in both fundamental and the first overtone modes, which can explain the nature of the radial post-shock velocity of the Balmer emission lines. It is still not clear which mode of pulsation the stars employ. One school of thought is that stars pulsate in the fundamental mode (Bowen 1988). This is supported by the calculated velocity across the shock front, which is in reasonable agreement with the observations (Wood 1986). However, if the stars pulsate in the fundamental mode, then the luminosity of galactic Miras derived from the period-mass-radius relation using Miras in the LMC has to be  $\sim 0.6^m$  fainter than the LMC Miras, assuming the stellar effective temperature is 3000K (Wood 1989).

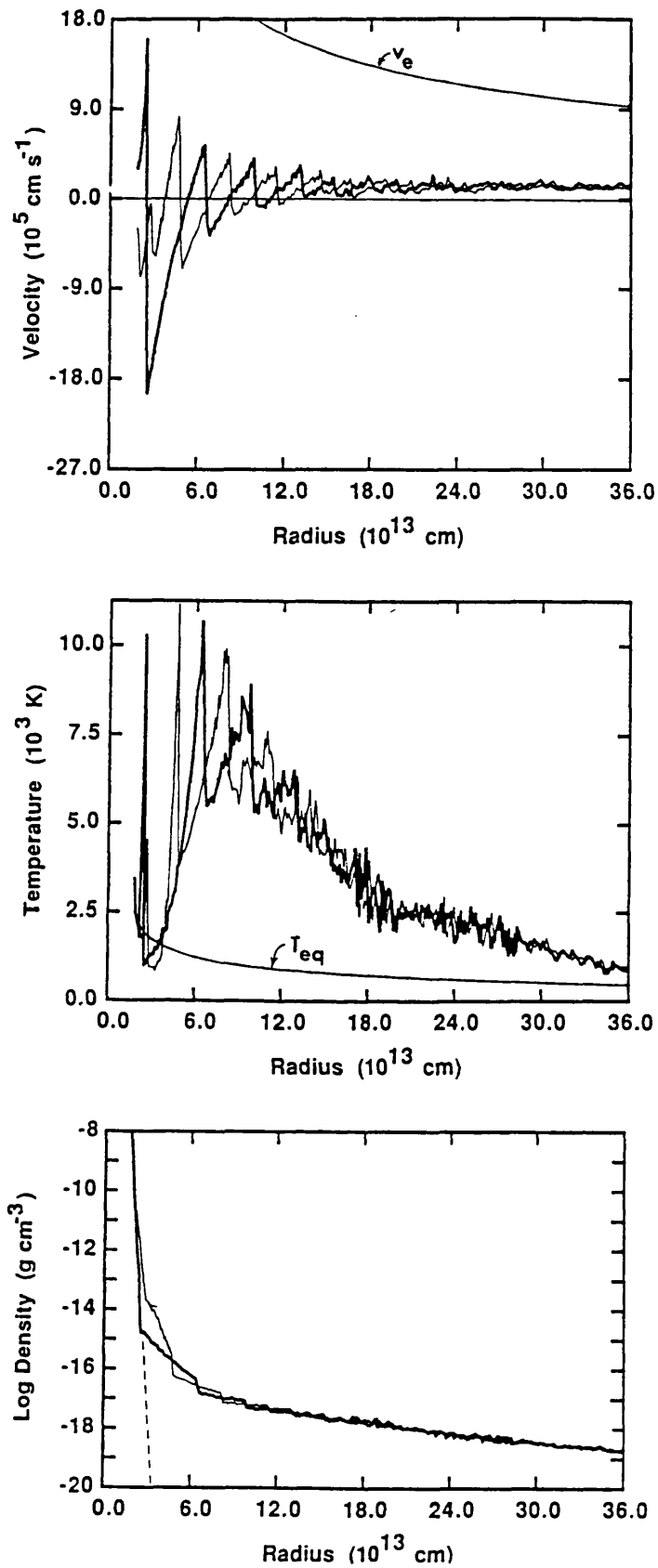


Figure 1.4: Effects of pulsations on velocity, temperature and density without dust at phase 0 (thick line) and phase 0.5 (thin line) on the model in Figure 1.2 (Bowen 1988).

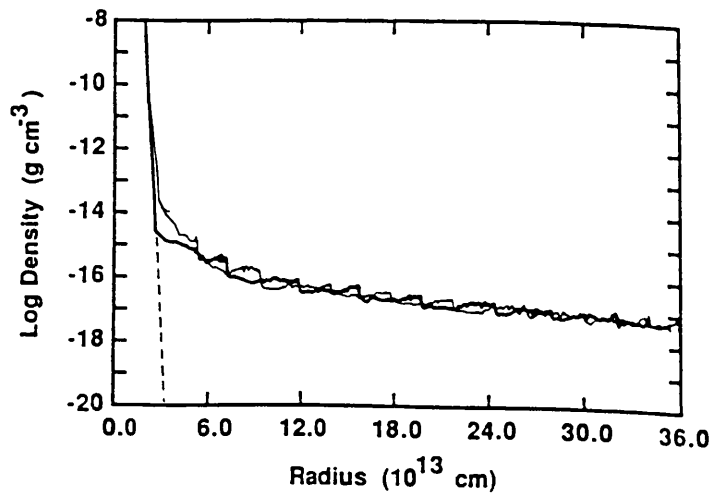
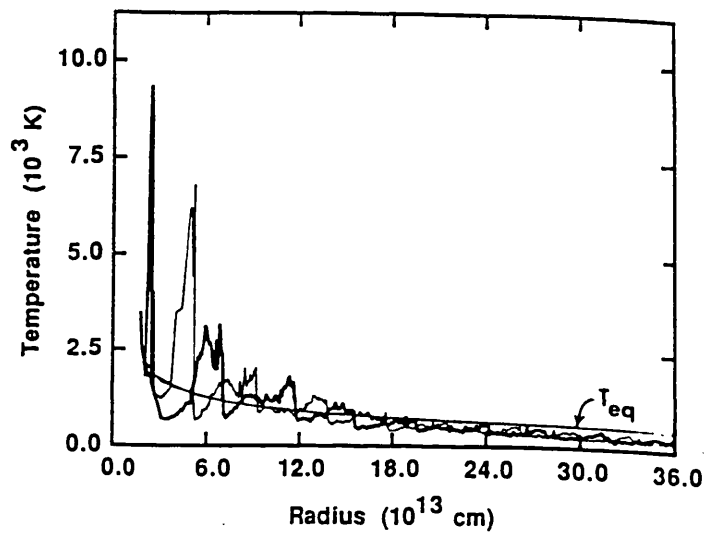
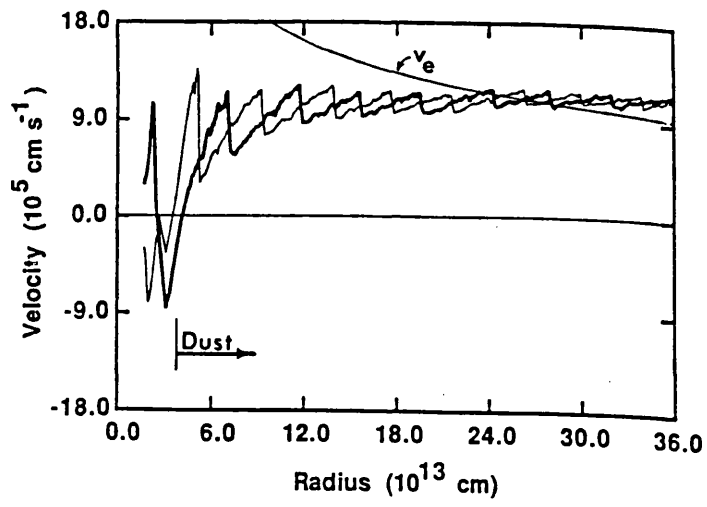


Figure 1.5: Same as Figure 1.4 but with dust included (Bowen 1988).

## Alfven wave driven wind

Other wave driven wind mechanisms include Alfven waves (Hartman & McGregor 1980), where magnetic field is invoked. Alfven waves are thought to have short wavelengths and propagate parallel to the magnetic fields. Usually, this mechanism produces very fast winds, which conflict observations of massive, cool, steady winds in red giants. This mechanism was used by Hartman & Avrett (1984) to explain the extended chromosphere in  $\alpha$  Ori. The momentum equation can be written as

$$\rho u \frac{du}{dr} = -\frac{d}{dr} \left( p + \frac{\langle \delta B^2 \rangle}{8\pi} \right) - \rho \frac{GM}{r^2} \quad (1.10)$$

where  $\rho$ ,  $u$  and  $p$  are the gas density, velocity and pressure;  $\langle \delta B^2 \rangle$  is the time-averaged square of the magnetic field fluctuation. The energy is then

$$\nabla \cdot F_w + \frac{1}{r^2} \frac{d}{dr} r^2 u \left( \frac{5}{2} p + \frac{1}{2} \rho u^2 \right) = \rho u \frac{GM}{r^2} - P_R \quad (1.11)$$

where  $P_R$  is the radiative cooling rate;  $F_w$  is the wave flux  $= (A + u) \langle \delta B^2 \rangle / 4\pi$ ; and  $A$  is the Alfven speed. Draw backs in this model are the uncertainty in the strengths of magnetic fields in cool stars, and the predicted high outflow velocities. In order for these wave mechanisms to drive enough mass to a few stellar radii for dust to form, most of the energy must be deposited inside the sonic point, since increasing energy in this region increases the mass flux. The smaller fraction of the remaining energy must then be added to the flow in the supersonic region in order to increase the velocity substantially enough for material to escape the gravitational force from the star. Here, again, the dissipation mechanism is not clearly understood. The dissipation is expressed in terms of the damping length,  $L$ , as

$$\frac{d}{dr} \ln \left( \frac{\langle \delta B^2 \rangle}{4\pi} M_A (1 + M_A)^2 \right) = -\frac{1}{L} \quad (1.12)$$

where  $M_A$  is the Alfvenic mach number ( $=u/A$ ). The assumption of constant damping length, although reasonable, does depend on the dimension chosen i.e., increasing the damping length increases the mass loss rate, but the flow speed will be small (less than the escape velocity), while decreasing the damping length will reduce mass loss rate rapidly, but the flow speed is not affected. As the damping length approaches zero, the thermally driven wind results. The special case of the damping length equals to one stellar radius seems to satisfy the condition seen in  $\alpha$  Ori. However, this strong dependence on the damping length is one failing of this model. It seems difficult for all the stars of various

properties to have the dissipation length of about one stellar radius which is required in order to explain the low velocity outflow (Holzer, Fla & Leer 1983).

## Sound wave driven wind

Another possible mechanism is the sound wave driven wind, proposed by Pijpers & Hearn (1989). The theory is the same as the Alfven wave driven wind, except that sound waves, rather than Alfven waves, are responsible for driving the wind. These may arise from acoustic wave motions at the stellar surface such as non-radial pulsation. The equation of motion is written as

$$\rho u \frac{du}{dr} = -\frac{dp}{dr} - (\nabla \cdot P_w)_r + \rho g \quad (1.13)$$

where  $P_w$  is the pressure tensor of the acoustic waves. Unlike the case for Alfven wave driven winds, this mechanism is not sensitive to the dissipation length. For similar sound wave and Alfven wave fluxes, sound waves can drive more mass loss at lower velocity, and the winds are accelerated slowly over a large distance. The slower velocity is achieved because the sound speed is much smaller than the Alfven wave speed near the star in the case of the same mass loss rate. Here, there is little difference between isothermal and adiabatic winds, unlike the situations for pulsation driven winds. Also, dust is not required in this model but its formation will assist the flow.

### 1.3 The nature of OH/IR stars

Many late type stars are found with dust shells surrounding them. These are remnants of mass lost while the stars are at the base of AGB. Since dust absorbs the visible radiation and re-emits it at longer wavelengths, the stellar energy peaks in the infrared. The first major survey of the infrared stars was undertaken by Neugebauer & Leighton (1969). Wilson & Barrett (1972) launched a survey of infrared stars by observing the OH transitions at 1612MHz, since their earlier study (Wilson & Barrett 1968) had shown that there was possible association between infrared and OH maser emission, hence the name OH/IR stars.

### 1.3.1 The radio and infrared observations

The OH masers arise from the hyperfine transitions of the OH molecules in the ground state ( $^2\Pi_{3/2}, J=3/2$ ). Some OH/IR stars are identified as Mira variables or M supergiants (Hyland et al. 1972). These OH/IR stars have oxygen-rich photospheres. All its available carbon is thought to be bound in CO molecules and excess oxygen condenses to form silicates and OH molecules. Miras with associated OH masers tend to have longer periods and cooler temperature than those without OH masers. Generally, OH masers are only found in stars with spectral type M5.5 or later (Sivagnanam, Le Squeren & Foy 1988). In order for a maser to be achieved, the level population must be inverted, i.e., the the upper state is more highly populated relative to the lower state, making the induced emission stronger than the absorption. The absorption factor,  $e^{-\tau}$ , is now the amplification factor since  $\tau$  is negative and the brightness temperature,  $T_b$ , is given by

$$T_b = T_x(1 - e^{-\tau}) \quad (1.14)$$

where  $T_x$  is the excitation temperature (negative for inverted line), resulting in an amplification of the radiation.

The characteristics of the OH emission are very striking. It has two very strong peaks (see Figure 1.6). Reid et al. (1977) proposed a model of an expanding circumstellar shell of dust and gas, where the peaks are due to the blue shifted (front), and the red shifted (back) part of the envelope. In this scheme, the separation between the two peaks represents twice the expansion velocity, with the stellar radial velocity being the central velocity between the peaks. The majority of OH/IR stars are detected at 1612MHz (satellite line), with fewer numbers detected at 1665 or 1667MHz (OH main lines). The intensity of an OH maser indicates an extremely high brightness temperature ( $\approx 10^{11}$ K). Such a high temperature is due to non-thermal process. The Rayleigh-Jeans limit dictates that for a radiatively pumped maser

$$N_p \approx \nu_p^2 T_p \quad (1.15)$$

where  $N_p$  is the number of pump photons per sec;  $\nu_p$  is the pumped frequency; and temperature  $T_p$ . The number of maser photons emitted per second is given by

$$N_m = \eta N_p \quad (1.16)$$

where  $\eta$  is the efficiency, hence the temperature of the maser is

$$T_m = \eta T_p \left( \frac{\nu_p}{\nu_m} \right)^2 \quad (1.17)$$

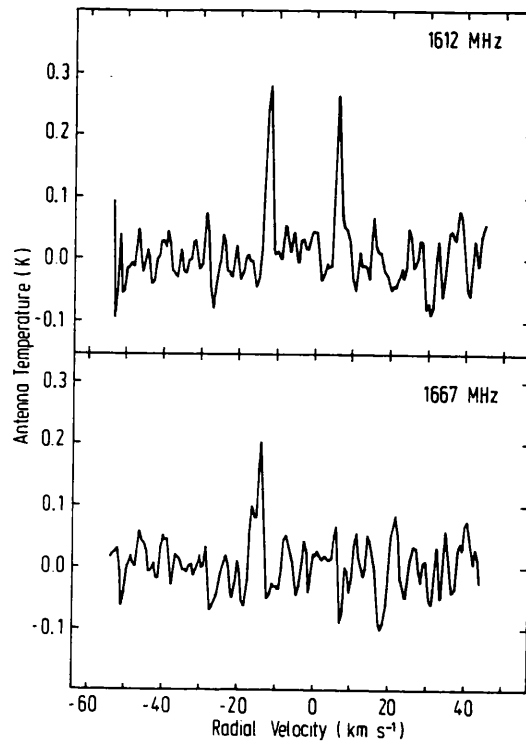


Figure 1.6: Samples of OH maser emission line profiles for FS Lib (Nguyen-Q-Rieu et al. 1979).

This results in an apparently very high temperature for maser regions, though, in fact, the temperature is very low. A more detailed discussion of radiative transfer of 1612MHz masers in red giants is given by Alcock & Ross (1986). They found that in order to explain the observed widths of the line profiles and the low surface brightness, mass is ejected discretely in blobs, rather than in continuous fashion.

For the 1612MHz line (type II maser), the inversion is achieved by absorptions of  $35\mu\text{m}$  photons by OH molecules, originally in the ground state. The molecule then cascades down to the ground state. Since the  $80\mu\text{m}$  transition ( $F=0, J=1/2$  to  $F=1, J=3/2$ ) becomes optically thick, the population only depends on the statistical weights of the excited levels ( $^2\Pi_{1/2}, J=1/2$ ) and the spontaneous decay rate. Hence, the  $F=1$  level in the ground state is over populated relative to the  $F=2$  level (Elitzur, Goldreich & Scoville 1976), leading to the 1612MHz maser (see Figure 1.7). Variations in the stellar luminosity reflect the variations in the strengths of the 1612MHz line smoothly (Harvey et al. 1974). The most important parameter governing the 1612MHz maser is the OH column density. If density is too low, there will be fewer molecules in the excited states, which reduces the

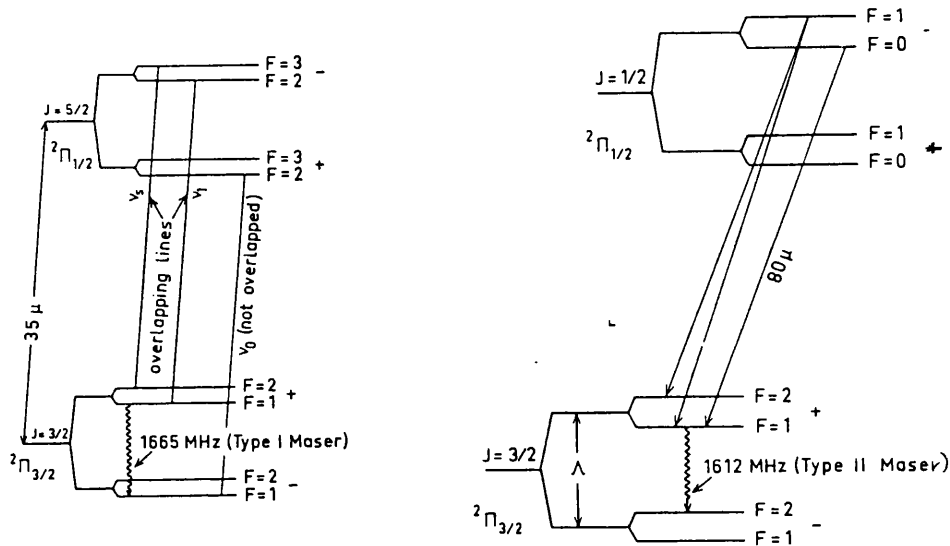


Figure 1.7: The transitional diagram for an OH molecule for type I and type II masers (Nguyen-Q-Rieu 1981).

probability of population inversion. In the case where density is too high, collision will quench the inversion. This type II maser is thought to be saturated, i.e., each absorption of the far-infrared photon produces  $\eta$  emitted maser photon.

The pumping of OH maser main line (type I) can be done by dust emission (Elitzur 1978). The inversion is achieved when dust temperature is greater than 90K, and reaches the maximum around 200K and 340K. Intensity of the 1665MHz line is affected by the variation in the stellar luminosity, but not in a smooth fashion as in the 1612MHz case. The parameter governing type I maser emission is the dust temperature. Unlike type II maser, the OH main line is not saturated. Density condition required for 1612MHz maser to operate wipes out the 1665MHz maser emission (Elitzur 1978).

There have been a number of OH maser surveys (e.g., Caswell & Haynes 1975; Baud et al. 1979). Becker, White & Proctor (1992) used the Very Large Array (VLA) telescope to survey the galactic plane at 1612MHz, and discovered 14 new sources. They found that low latitude OH masers are much redder than higher latitude sources. All the sources with  $F(60\mu\text{m})/F(25\mu\text{m}) < 0.5$  concentrated around the galactic plane. It was concluded

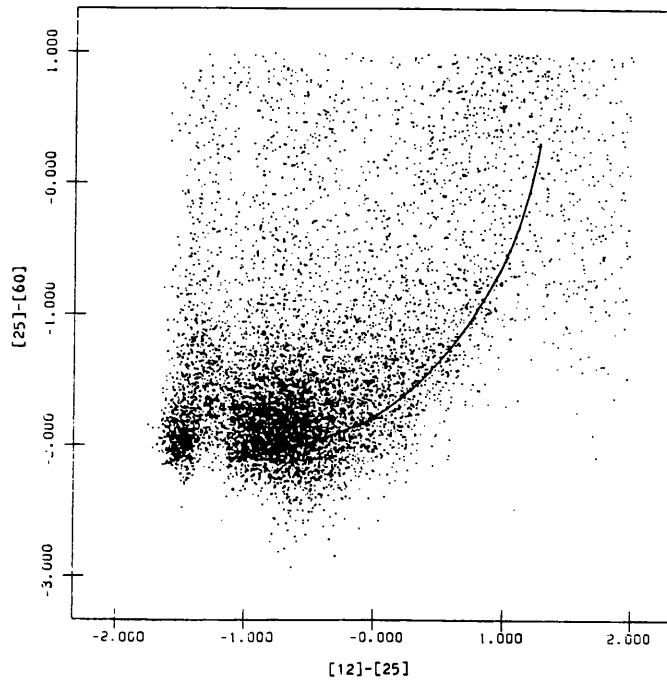


Figure 1.8: Colour-colour diagram for *IRAS* point sources taken from van der Veen & Habing 1988.

that the progenitors of OH masers are not homogeneous, which is in agreement with the conclusion by Likkel (1989) who surveyed the cold *IRAS* stars.

Near infrared photometry of late-type stars shows variations with a periods ranging between 200–2000 days. The first major infrared survey was carried out at  $2\mu\text{m}$  by Neugebauer & Leighton (1969), followed by the AFGL four colour sky survey by Price & Walker (1976). The latter survey reached the wavelength of  $27.4\mu\text{m}$ . In 1983, a further step was achieved by the launch of the Infrared Satellite (*IRAS*). Thousands of the point sources discovered were identified as late type stars (see Figure 1.8). Along with the broad band photometry which extended to  $100\mu\text{m}$ , *IRAS* also took spectra of many of these sources. The common features seen in the survey for oxygen-rich stars are emission at  $9.7$  and  $18\mu\text{m}$ , thought to be due to silicates in the circumstellar envelopes. These features correspond to the stretching of the Si–O and bending of the Si–O–Si mode of silicate, respectively. The strength of the  $10\mu\text{m}$  feature varies from star to star, depending on the number density of silicate in the envelope. Some stars have very thick dust shells, in which all the visible radiation is absorbed, and is re-emitted only in the infrared. These possess

a deep  $9.7\mu\text{m}$  absorption feature. As a result of this survey, it is possible to model the energy distributions of stars with very cool colour temperatures. Dust condensation in OH/IR stars is thought to occur at a radius where the temperature falls below the silicate condensation temperature ( $\approx 1000\text{K}$ ). Bester et al. (1991) found, using the Infrared Spatial Interferometer, that dust forms at  $3R_*$  around  $\alpha$  Ceti, at which point the temperature is in excess of  $1000\text{K}$ . The same appears to be true for the carbon star, IRC+10216 (Danchi et al. 1990).

The theory of dust formation and destruction in the circumstellar environment has been considered by many authors (e.g., Salpeter 1974; Sedlmayr 1989) It is suggested that there is a zone where dust is absent. Tielens & Allamandola (1987) proposed that dust is formed in a stationary layer, in which gas often encounters periodic shock waves. One draw back is that in order for nucleation to be efficient, the density should be  $\sim 10^{13}\text{cm}^3$  (Nuth & Donn 1982 (a)), which is higher than observed. Assuming that density is high enough in an O-rich outflow, high temperature condensates (clean silicates) will form first. The gas flow is dominated by shock waves, since scattering is unimportant. The grain temperature in the stationary layer is determined by collision. As the gas and dust move outwards into a region of lower density, they become thermally decoupled. The grain temperature is then radiatively dominated, and drops below the gas temperature. Iron can be incorporated into silicates once the temperature is below  $1000\text{K}$ , increasing the absorptivity and temperature, since "dirty" silicates have higher near infrared opacity than clean silicates (Jones & Merrill 1976). The fraction of iron in silicate is determined by the balance between the inward diffusion of iron and the increase in the temperature (Tielens 1989).

Due to the width of the features observed, silicates are thought to be amorphous. In crystalline silicate, only a small number of lattice vibrations (phonons) are optically active, resulting in a few sharp lines. However, in amorphous materials, the spread of bond angles produces a large range in bond strengths and frequencies. This results in most vibrational modes being infrared active, hence the widths of the absorption features are broader (Tielens & Allamandola 1987).

### 1.3.2 Stellar properties

It is thought that AGB stars have low to intermediate mass ( $1-8 M_{\odot}$ ). Evolutionary tracks of these stars can be deduced, using standard stellar evolution models. When a star progresses up the AGB branch, the hydrogen shell reignites, starting the double shell burning phase, which is thermally unstable. The star then begins to pulsate, and loses significant amount of mass. At this stage, the star becomes a long period variable and, if it exhibits the 1612MHz OH emission, it is said to be an OH/IR star.

The luminosity of an AGB star is a function of the core mass,  $M_{core}$ , and is given by the Paczynski relation

$$L(L_{\odot}) = 59000 \left( \frac{M_{core}}{M_{\odot}} - 0.5 \right) \quad (1.18)$$

It has an upper limit of  $53000L_{\odot}$  when the core mass approaches the Chandrasekhar limit. The mean luminosity of OH/IR stars is often taken to be about  $10^4L_{\odot}$  (e.g., Knapp & Morris 1985). The variations in the observed infrared brightness of a single star can be more than a factor of two (e.g., Lockwood 1985; Jones et al. 1990). Also due to the location of many OH/IR stars (e.g., the galactic plane), the interstellar reddening cannot be ignored in calculating their luminosities (Gehrz et al. 1985). Although the luminosities are high for OH/IR stars, their effective temperatures derived from their spectra suggest extremely cool atmosphere. Visible Miras show spectral type of late M, and OH masers are associated with stars with spectral type later than M5.5 (Sivagnanam et al. 1988). Fox & Wood (1982) derived the following relationship for AGB stars from the HR diagram.

$$M_{bol} = 38 \log T_e - 138.5 \quad (1.19)$$

where  $M_{bol}$  is the bolometric magnitude of the star; and  $T_e$  is the stellar effective temperature. Once both the luminosity and the temperature are known, the stellar radius can be calculated via

$$L = 4\pi R_*^2 T_e^4 \sigma \quad (1.20)$$

The observed periods of OH/IR stars vary from a few hundred days to  $2000^d$ , with an average value of  $1000^d$  (Herman & Habing 1985), as compared to  $350^d$  for optically visible Miras (Wood & Cahn 1977). The observed light curves at both infrared and radio wavelengths are generally asymmetric, with steep rise and slow decline. The light curves can also be used to determine distances to the stars by the technique called "phase

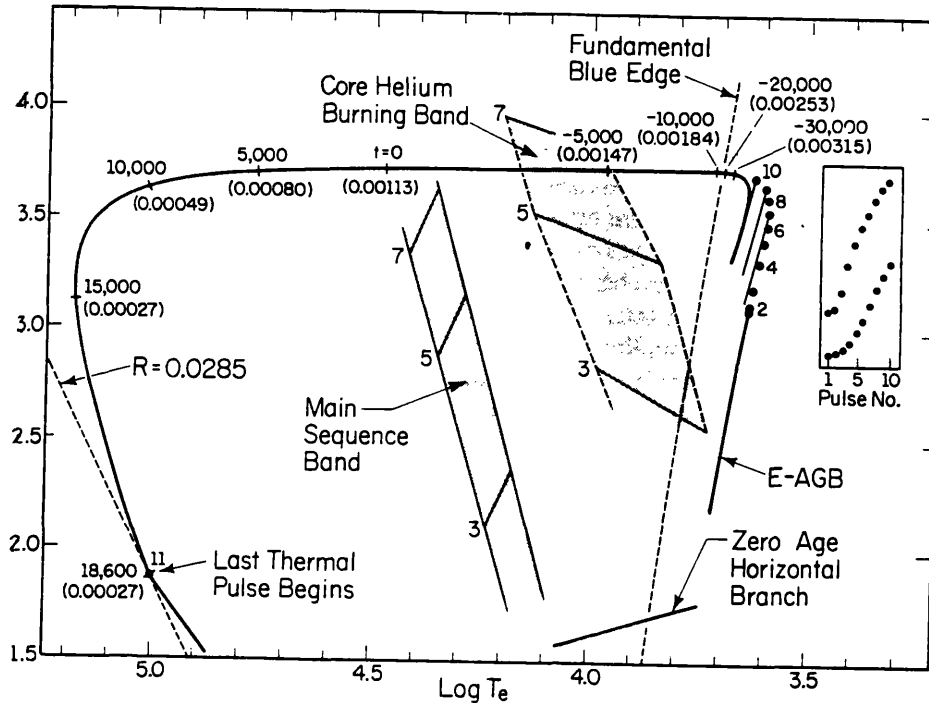


Figure 1.9: The HR diagram for a star with a core mass of  $0.6 M_{\odot}$  (Iben & Renzini 1983).

lags". If the radiation from the front and back of a circumstellar envelope is observed simultaneously, the light travel time can then be converted to the actual envelope size. Also, if the envelope is mapped, the angular size, combined with the radial size of the shell will give the distance to the source from simple geometry. This method gives distances which are accurate to about 40% (see e.g., Herman & Habing 1985; Herman, Burger & Pennix 1986; van Langevelde, van der Heiden & van Schoonevelds 1990).

## 1.4 The final evolution

After leaving the AGB, a star ceases to lose mass and evolves horizontally along the HR diagram. The circumstellar shell coasts outwards, revealing more of the central star. The convective shell around the star disappears, since the envelope mass becomes smaller. The stellar radius decreases rapidly, and consequently, the temperature rises. The combination of higher temperature and smaller radius results in an almost constant stellar luminosity (Figure 1.9). The circumstellar matter will not be affected at first. At this stage, the star is said to be post-AGB stars. As the star becomes hotter ( $T \sim 30000\text{K}$ ), matter starts to be ionised and the star becomes a planetary nebula (PN). Since the evolutionary

time for the transition phase between AGB and PN is comparatively short, the number of objects in this class is relatively small. These stars can be recognised by the doubly peaked energy distributions in the infrared (e.g., Kwok, Volk & Hrivnak 1989; van der Veen, Habing & Geballe, 1989). Some, like OH17.7-2.0, are non-variable stars (le Bertre 1987), while others, like OH231.8+4.2, show evidence of bipolarity (Bowers & Morris 1984). IRAS 09371+1212 was observed to have bipolar structure at both optical (Hodapp, Sellgren & Nagata 1988) and infrared wavelengths (Rouan et al. 1988). It is interesting to note that most AGB stars show signs of spherical symmetry from OH maser observations, but many post-AGB stars are bipolar. This may be due to an equatorial dust disk around the stars (e.g., Rouan et al. 1988; Sahai et al. 1991), or the presence of a binary companion (e.g., Reipurth 1987; Kolesnik & Pilyugin 1989). The survey of post-AGB objects have been carried out by many groups (e.g., van der Veen et al. 1989; Likkell et al. 1991; Trams et al. 1991). They all found that high galactic latitude supergiants are good candidates for post-AGB objects. These are population II, low mass stars with low surface gravity.

The calculations of evolutionary sequence of AGB stars must include mass loss in order for models to closely represent observations. This has been done by, e.g., Schonberner (1983); Wood & Faulkner (1986). The models suggest that the transition time is strongly dependent on the remnant mass. PNe are produced by interactions of fast wind ( $\sim 1,000\text{km/s}$ ) from the central star driving the outer part of the shell into the cool AGB wind (Kwok, Fitzgerald, & Purton 1978). As the star evolves further, the temperature rises high enough ( $T\sim 30000\text{K}$ ) for the gas to become ionised, when it assumes the normal properties of a PN. The nucleus evolves towards the white dwarf cooling track. The circumstellar material disperses and the interstellar medium is further enriched.

## 1.5 Outline of the present work

The work in this thesis determines the dust mass loss rates from OH/IR stars. In chapter 2, the radiative transfer code used in modelling the infrared energy distributions of selected stars is described, along with the dust parameters, namely amorphous silicates. In a star with a large outflow, ice is expected to condense out onto silicate grains. The extinction efficiencies of silicate core-ice mantle are calculated. The thickness of the ice mantle is calculated from the cosmic abundance of oxygen and is taken to be constant, regardless

of the silicate core radius. The resulting energy distributions presented in chapter 3 are compared to the near infrared photometry, *IRAS* LRS spectra and the *IRAS* photometry. This is the first time that energy distributions of stars with silicate core-ice mantle are calculated using the radiative transfer code. The dust mass loss rates obtained are relatively close to the stars. These are then compared to previous estimates of dust and gas mass loss rates which measure the outflow rates at radii larger than those obtained from the modelling of the *IRAS* spectra. The temperature structures of circumstellar envelopes of O-rich stars, using dust mass loss rates obtained from the modelling of the energy distributions, are studied in chapter 4. Here, both the adiabatic and radiative coolings are included in the calculations. The main heating mechanism involves the collision between gas and dust. The most important molecule responsible for cooling in O-rich envelopes is  $\text{H}_2\text{O}$ . The calculated gas kinetic temperature is then used in chapter 5 to calculate CO line profiles at various transitions. Also enters in the calculation is the dust temperature structure taken from chapter 3. This is the first time for O-rich stars that gas kinetic temperatures calculated from heating and cooling in the envelopes, along with the dust temperatures are used to calculate CO line profiles, which result in gas mass loss rates. The multi-frequency studies lead to mass loss rates at different radii and can be viewed as time dependent mass loss rates. Finally, in chapter 6, the morphologies of post-AGB stars are discussed, and the nature of their dust is studied in some details to see how dust evolves with time as the stars move away from the AGB.

## Chapter 2

# Radiative Transfer in Dust Shells and Grain Parameters

The work presented in this chapter involves describing the radiative transfer calculation. For O-rich stars, the stellar radiation is attenuated by silicate dust. The silicate extinction efficiencies are also investigated. Calculations of radiative transfer in circumstellar shells around late type stars have been performed by many authors in the past (e.g., Leung 1975; Jones & Merrill 1976; Rowan-Robinson 1980, 1982; Rowan-Robinson & Harris 1983; Bedijn 1987). All showed that the assumption of spherical symmetry in shells gave reasonable results for most stars modelled. Leung (1975) assumed the isotropic radiation field to be incident on the inner radius of a dust shell, which is not valid for late type stars. The model proposed by Rowan-Robinson (1980) represented a star as a black body with a certain radius and temperature, set within a spherical shell of dust, which condenses when the temperature falls below the grain condensation temperature. From this fixed inner radius, the code then iterates to find the actual temperature at this radius. Other assumptions made are that scattering by grains is isotropic and that photons are scattered once. The latter is valid as long as the shell remains optically thin. The grain absorption properties used in the code are “dirty silicates”, taken from Jones & Merrill (1976). The code then solves time independent radiative transfer equations, assuming spherical symmetry with a constant and steady atmospheric flow, i.e.,  $\rho \propto r^{-2}$ . However, in the optically thick case of OH26.5+0.6, Jones & Merrill (1976) arbitrarily assumed a layer of cold dust surrounding the circumstellar envelope in order to explain the deep

9.7 $\mu$ m absorption. Bedijn (1987) dismissed this assumption, and modified the absorption efficiencies in order to fit the observations. He used the model atmosphere flux as an input parameter instead of a central blackbody.

Although the assumption of spherical symmetry seems valid for AGB stars, as is evident from OH maser observations, it does not hold true for many post-AGB stars. Observations of these show the bipolarity clearly, e.g., in OH231.8+4.2, AFGL 618, AFGL 2688. Efstathiou & Rowan-Robinson (1990) therefore developed a radiative transfer code which can cope with axisymmetric dust distributions. The emerging flux is calculated as a function of the angle of the orientation of the disk to the line of sight. The method was applied to the M supergiant VY CMa, where the resulting optimum viewing angle of the disk is 45°.

The first part of this chapter discusses the method of solving radiative transfer through dust shells, with all the differential equations necessary to solve for the solutions of this two-dimensional (radial and angular) scheme stated. The code used in this study is based on the formalism by Haisch (1979). The calculation relies on the two-stream Eddington approximation, which assumes spherical symmetry. Unno & Kondo (1976) showed that solutions of the radiative transfer obtained from this method were as accurate as those from the equivalent approximation in plane parallel case. The code takes into account the effects of non-isotropic and multiple scattering, absorption and thermal re-emission. Unlike previously mentioned radiative transfer calculations, it can also accommodate multiple grain components and different grain sizes in the outflow. The code was modified to run on the CRAY-XMP by Hoare (1988) and on the VAX by Griffin (1990).

The second part of this chapter deals with the grain parameters used in the radiative transfer code, namely silicate grains and silicate core-ice mantle grains. Water-ice is the expected condensate in stars with large mass loss rates, and tends to condense onto already existing grains than forming pure water-ice grains. Other input parameters required for the code are stellar radius, effective temperature, distance to the object, dust mass loss rate, terminal velocity, which will be discussed in the next chapter.

## 2.1 The radiative transfer code

Following the work by Haisch (1979), the basic equations describing the radiation which will then be used in solving the radiative transfer are given below. The procedure assumes the intensity of radiation at each location to be discretised into two streams :  $I^+(r)$  applied to the outwardly directed radiation, and  $I^-(r)$  to the inward direction. These can then be written as

$$\begin{aligned} I_\nu(r, \mu) &= I^+(r) \text{ for } 1 > \mu > \mu_r \\ &= I^-(r) \text{ for } \mu_r > \mu > -1 \end{aligned} \quad (2.1)$$

where  $\mu_r$  is the cosine of angle dividing the radiation into two streams. From this, the moments equations can be written as

$$\begin{aligned} J_\nu(r) &= \frac{1}{2} \int_{-1}^{+1} I_\nu(r, \mu) d\mu \\ &= \frac{1}{2} [(I_\nu^+ + I_\nu^-) - \mu_r (I_\nu^+ - I_\nu^-)]. \end{aligned} \quad (2.2)$$

The first moment is

$$\begin{aligned} H_\nu(r) &= \frac{1}{2} \int_{-1}^{+1} \mu I_\nu(r, \mu) d\mu \\ &= \frac{1}{4} (1 - \mu_r^2) (I_\nu^+ - I_\nu^-). \end{aligned} \quad (2.3)$$

The second moment is

$$\begin{aligned} K_\nu(r) &= \frac{1}{2} \int_{-1}^{+1} \mu^2 I_\nu(r, \mu) d\mu \\ &= \frac{1}{6} [(I_\nu^+ + I_\nu^-) - \mu_r^3 (I_\nu^+ - I_\nu^-)]. \end{aligned} \quad (2.4)$$

The third moment is

$$\begin{aligned} N_\nu(r) &= \frac{1}{2} \int_{-1}^{+1} \mu^3 I_\nu(r, \mu) d\mu \\ &= \frac{1}{8} (1 - \mu_r^4) (I_\nu^+ - I_\nu^-). \end{aligned} \quad (2.5)$$

At the outer boundary condition, the flux is then given by

$$H_\nu(R_o) = \frac{1}{2} [1 + \mu_{R_o}(\nu)] J_\nu(R_o). \quad (2.6)$$

where  $R_o$  is the outer radius.

The code calculates radiative transfer in a dust shell which is divided into 150–500 radial steps, depending on the amount of dust present in the shell. For each grain size,

the grain efficiency, the albedo, and the phase function for each wavelength are read in. Dust grains are assumed to condense out where the temperature falls below the dust condensation temperature at the terminal velocity. For the future work, the code has been adapted to cope with a two-component dust, condensing at different radii.

The equation of radiative transfer in spherical coordinates is

$$\mu \frac{\partial I_\nu}{\partial r} + \frac{1 + \mu^2}{r} \frac{\partial I_\nu}{\partial \mu} = -(\kappa_\nu + \sigma_\nu) I_\nu + \kappa_\nu B_\nu + \frac{\sigma_\nu}{2} \int_{-1}^{+1} R(\mu, \mu') I_\nu(\mu') d\mu' \quad (2.7)$$

where  $\kappa_\nu$  and  $\sigma_\nu$  are the volume absorption and scattering coefficients;  $R(\mu, \mu')$  is the scattering angular redistribution function; and  $B_\nu$  is the Planck function. The grain radius,  $a$ , is allowed to vary from  $a_{max}$  to  $a_{min}$ . In this study, these are taken to be  $0.25\mu\text{m}$  to  $0.005\mu\text{m}$ , respectively (see section 2.3). The total numbers of grain radii used in the Haisch code is 20. The normalised factor of the size distribution is  $\xi(a)$  so that  $\int \xi(a) da = 1$ . The resulting absorption and scattering coefficients per unit volume are given by

$$\kappa_\nu = N(r) \int \xi(a) \kappa(\nu, a) da \quad (2.8)$$

$$\sigma_\nu = N(r) \int \xi(a) \sigma(\nu, a) da \quad (2.9)$$

where

$$\begin{aligned} N(r) &= \int n(a, r) da \\ &= \frac{3m_H n_H}{4\pi\rho} \frac{4-p}{a_{max}^{4-p} - a_{min}^{4-p}} \frac{a_{max}^{1-p} - a_{min}^{1-p}}{1-p} \end{aligned} \quad (2.10)$$

where  $n(a, r) da$  is the number density of dust grains in the range  $a \pm da$  at radius  $r$ ;  $m_H$  and  $n_H$  are the mass of hydrogen atom, and the number density of hydrogen, respectively;  $\rho$  is the specific density of the grain material;  $p$  is the index of the grain size distribution in the range of  $a_{max}$  to  $a_{min}$ ; and  $\mu$  is the mean molecular weight, which equals to 1.4 for a helium abundance of 0.1, relative to the number of hydrogen. The grain size distribution included in the radiative transfer calculation makes it a unique code, since up to date, most authors have assumed a single grain size in such calculations. The scattering angular redistribution function, in terms of Legendre polynomial,  $P_l(\mu)$ , is

$$R(a, \mu, \mu') = \sum a^{(l)}(a, \nu) P_l(\mu) P_l(\mu') \quad (2.11)$$

which can then be substituted into the transfer equation, thus fully taking into account the multiple size distribution of the grains. The moment equations can be written as

differential equations

$$\begin{aligned} \frac{1}{r^2} \frac{d}{dr} (r^2 H_\nu) &= -N(r) J_\nu \int \xi(a) \kappa(\nu, a) da \\ &+ N(r) \int \xi(a) \kappa(\nu, a) B(r, \nu, a) da \end{aligned} \quad (2.12)$$

where  $B(r, \nu, a)$  is the Planck function for a grain size  $a$  at radius  $r$  and frequency  $\nu$ .

$$\begin{aligned} \frac{dJ_\nu}{dr} + \frac{2}{r^3} \frac{d}{dr} (r^3 \mu_r(\nu) H_\nu) &= -3N(r) H_\nu \int \xi(a) [\kappa(\nu, a) + \sigma(\nu, a)] da \\ &\times \left[ 1 - \frac{1}{3} \frac{\int \xi(a) a^{(1)}(\nu, a) \sigma(\nu, a) da}{\int \xi(a) [\kappa(\nu, a) + \sigma(\nu, a)] da} \right] \end{aligned} \quad (2.13)$$

By substituting the second and the third moment for  $\mu_r(\nu)$ , then

$$\begin{aligned} \frac{d\mu_r(\nu)}{dr} &= \frac{1 - \mu_r^2(\nu)}{r\mu_r(\nu)} - \frac{2(1 + 3\mu_r^2(\nu))}{3} \frac{1}{4\mu_r(\nu)} \frac{d}{dr} (r^2 H_\nu) \\ &- \frac{2}{3} N(r) \int \xi(a) [\kappa(\nu, a) + \sigma(\nu, a)] da \\ &\times \left[ 1 - \frac{\int \xi(a) a^{(2)}(\nu, a) \sigma(\nu, a) da}{5 \int \xi(a) [\kappa(\nu, a) + \sigma(\nu, a)] da} \right] \end{aligned} \quad (2.14)$$

Equations 2.12, 2.13, 2.14 are solved numerically by the Eddington approximation scheme for the radiative transfer. The boundary conditions for solving these equations are

$$J_\nu(R_o) = \frac{2H_\nu(R_o)}{1 + \mu_{R_o}(\nu)} \quad (2.15)$$

$$I_\nu^+(R_i) = J_\nu(R_i) + 2H_\nu(R_i) \frac{1 + \mu_{R_i}(\nu)}{1 - \mu_{R_i}^2(\nu)} \quad (2.16)$$

$$\mu_{R_i}(\nu) = [1 - (R_*/R_i)^2]^{1/2} \quad (2.17)$$

where  $R_i$  is the inner radius;  $R_*$  is the stellar radius.

The calculation assumes that thermal emission is due to heating of dust grains by the local radiation field, which is taken to be a black body at a temperature approximate to that radius, i.e., there is no interchange of energy of each grain by collision.

$$N(r) \xi(a) da \int J_\nu(r) \kappa(\nu, a) d\nu = N(r) \xi(a) da \int B(r, \nu, a) \kappa(\nu, a) d\nu \quad (2.18)$$

Thus for a given  $J_\nu(r)$ ,  $B(r, \nu, a)$  can be determined at a temperature  $T(r, a)$ . It follows directly that the frequency integrated flux (equation 2.12) is zero, i.e., conservation of integrated spherical flux. We now solve for the three differential equations by assuming a temperature distribution. The resulting moments of the radiation, after the first iteration, are then checked to see if the conservation of the spherical flux is achieved. If it deviates from the expected, a new Planck function must be computed by

$$B^T(r, a) = B(r, a) + \Delta B(r, a) = \frac{\kappa_J(r, a)}{\kappa_B(r, a)} [J(r) + \Delta J(r)] \quad (2.19)$$

where  $\kappa_J(r, a)$  and  $\kappa_B(r, a)$  are the mean opacities; and  $\Delta J(r)$  is the correction of the radiation field. Therefore, a new temperature can be calculated by

$$T_{new}(r, a) = \left[ \frac{\pi}{\sigma_{SB}} B^T(r) \right]^{1/4} \quad (2.20)$$

where  $\sigma_{SB}$  is the Stefan–Boltzmann constant. This new set of temperatures is then used to solve the differential equations in order to obtain the new improved values of  $J_\nu(r)$ ,  $H_\nu(r)$  and  $\mu_r(\nu)$ . For each loop of the calculation, the cosines of the angles and radiation field are calculated one frequency at a time for all depths. The three main differential equations ( 2.12, 2.13, 2.14) are solved by using modified Runge–Kutter method.

## 2.2 Efficiency factors of small grains

For a sphere of radius  $a$ , which is small compared to the wavelength of radiation,  $\lambda$ , the Rayleigh limits can be used to estimate the absorption coefficient, ignoring scattering effects,

$$\frac{3}{4} \frac{Q_{abs}}{a} = \frac{6\pi}{\lambda} \text{Im} \left( \frac{\epsilon(\omega) - 1}{\epsilon(\omega) + 2} \right) \quad (2.21)$$

where  $\text{Im}(\epsilon(\omega))$  is the imaginary part of the dielectric function of the material at frequency  $\omega$ . In this study, the maximum grain size are comparable to the shortest wavelength considered. Here, in order to calculate the extinction, absorption and the scattering from either the dielectric function or the refractive index, the Mie (1908) theory, an electromagnetic scattering theory for a sphere, is used. However, it should be noted that not all particles are spherical, in which case, the calculated values probably deviate from the actual physical situation. The full discussion of the theory can be found in van de Hulst (1981) and Bohren & Huffmann (1983). Here, only the resulting efficiencies will be quoted

$$Q_{ext} = \frac{2}{x^2} \sum_{n=1}^{\infty} (2n + 1) \text{Re}(a_n + b_n) \quad (2.22)$$

$$Q_{sca} = \frac{2}{x^2} \sum_{n=1}^{\infty} (2n + 1) (|a_n|^2 + |b_n|^2) \quad (2.23)$$

where  $a_n$  and  $b_n$  are the scattering coefficients calculated from the Riccati–Bessel functions; and  $\text{Re}$  is the <sup>real</sup> part of the complex values. From these, the albedo of the grains,  $w$ , can be calculated by

$$w = \frac{Q_{sca}}{Q_{ext}} \quad (2.24)$$

Finally, the phase function,  $g$ , which is the average of the cosine of the scattering angle ( $= \overline{\cos\theta}$ ) is given by

$$\overline{\cos\theta}Q_{sca} = \frac{4}{x^2} \sum_{n=1}^{\infty} \frac{n(n+2)}{n+1} \text{Re}(a_n a_{n+1}^* + b_n b_{n+1}^*) + \frac{4}{x^2} \sum_{n=1}^{\infty} \frac{2n+1}{n(n+1)} \text{Re}(a_n b_n^*) \quad (2.25)$$

where \* denotes the values of the complex conjugate.

The opacity is then given by

$$\kappa(\nu, r) = \int \pi a^2 Q(a, \nu) n(a, r) da \quad (2.26)$$

By substituting the grain size distribution from equation 2.10, we get

$$\kappa_d(\nu, r) = \frac{3m_H}{4\pi} \frac{4-p}{a_{max}^{4-p} - a_{min}^{4-p}} \frac{(M_d/M_H)n_H}{\mu\rho} \int Q(a, \nu) a^{2-p} da \quad (2.27)$$

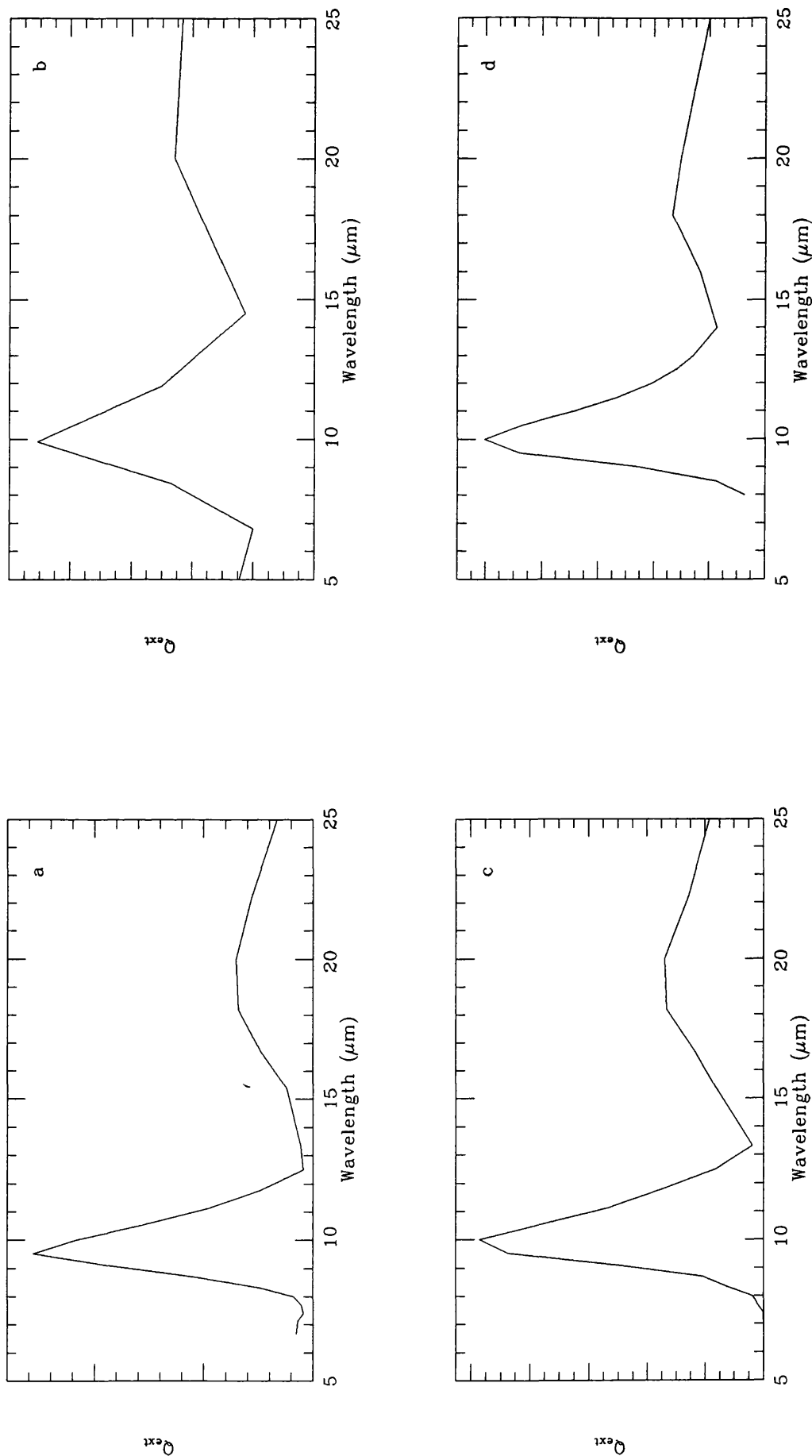
and the dust radial optical depth is given by

$$\tau_d(\nu, r) = \int_0^r \kappa_d(\nu, r') dr' \quad (2.28)$$

## 2.3 Grain properties

As a star loses mass, the ejected gas cools and condenses out to form grains, which after many years, accumulates into a shell of dust, preventing the direct observations of the star itself. For stars with oxygen-rich atmospheres, the main constituent of dust observed has spectral peaks at 9.7 and 18 $\mu\text{m}$ , which are identified with the Si-O stretching and Si-O-Si bending modes of silicates, respectively. Jones & Merrill (1976) showed that “clean” silicates cannot explain the near-infrared fluxes observed, and proposed a model for “dirty” silicate, which has higher absorption efficiencies in the region of 1–5  $\mu\text{m}$ . There is also a number of laboratory studies of various types of silicates (e.g., Kratschmer & Huffmann 1979; Day 1976, 1979; Stephens & Russell 1979; Nuth & Donn 1982) in the mid-infrared region. These show that highly disordered olivine grains,  $(\text{Mg,Fe})\text{SiO}_4$ , produced by either irradiation of heavy ions or vaporization by a laser beam, cause extinction consistent with the observations of dust in late type stars. Crystalline silicate, however, shows peaks at 10.5 and 11.5 $\mu\text{m}$  (Stephens & Russell 1979). After comparing the optical properties of silicate grains obtained from the laboratory measurements and observations, Draine & Lee (1984) proposed a model of the “astronomical silicates” which peaks at 10.5 $\mu\text{m}$ . The grain extinction efficiencies can also be obtained from the polarisation observations (Martin 1975). Unfortunately, such observations for OH/IR stars are not available for a large enough sample of stars to derive the optical properties of silicate grains.

Figure 2.1: Silicate extinction efficiencies of (a)  $\text{MgSiO}_3$  from Day (1979); (b) dirty silicate from Jones & Merrill; (c)  $\text{MgSiO}_4$  from Day (1979); (d) silicate from Pegourie & Papoular (1985).



### 2.3.1 Silicate grains

The extinction efficiencies of silicates depend on the structure of the grains, e.g.,  $\text{FeSiO}_3$  has slightly different optical properties from  $\text{Fe}_2\text{SiO}_4$ , which again differs from magnesium silicates (Day 1981).  $\text{FeSiO}_3$  shows a peak at  $9.5\mu\text{m}$  and  $\text{Fe}_2\text{SiO}_4$  has a peak at  $9.8\mu\text{m}$ , where both show peak absorption at  $20\mu\text{m}$ .

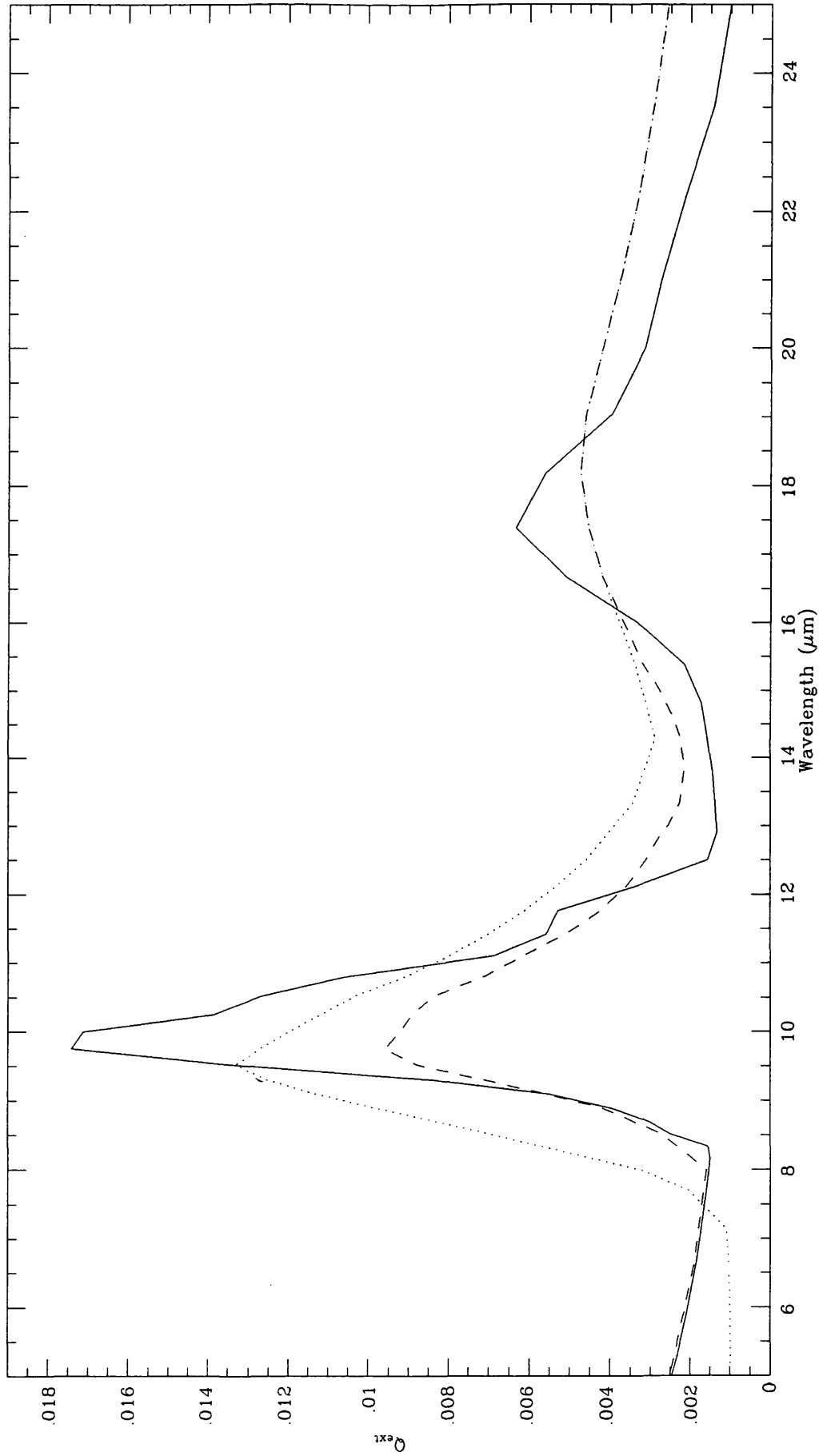
The optical constants of silicates, used here to model the stellar energy distribution in the infrared, are modified from Kratschmer & Huffmann (1978) and Draine & Lee (1984). The former are the laboratory measurements of amorphous silicates and the latter are from observations. However, when fitting the latter to the star WX Ser, the peak of the  $10\mu\text{m}$  feature is longward of  $9.7\mu\text{m}$ , hence the combination of the two optical constants were used as a starting point i.e., Draine & Lee's optical constants used between  $0.5\text{--}8\mu$  and  $13.5\text{--}25\mu\text{m}$ , with Kratschmer & Huffmann's between  $8\text{--}13.5\mu\text{m}$ . Since the stellar parameters of WX Ser are known, the optical constants are modified to fit its *IRAS* LRS spectrum. The ratio of the two peaks at  $10$  and  $20\mu\text{m}$  is scaled to be 2:1, as has been found to be the case by Bedijn (1987). From these values, the extinction efficiencies ( $Q_{ext}$ ), albedo ( $w$ ) and the phase function ( $\overline{\cos\theta}$ ) can be calculated using the Mie theory already discussed in the previous section (Figure 2.2). In the interstellar environment, the condensation and collision of grains lead to a size distribution proposed by Mathis, Rumpl & Norsieck (1977, hereafter MRN), which fits the observed the extinction curve with the following power law

$$dn = An_H a^{-3.5} da \quad (2.29)$$

where  $A = 10^{-25.11} \text{ cm}^{2.5}/\text{H}$  (Draine & Lee 1984). The above expression is found to replicate the observations of the extinction curve for grains with the size  $0.005\mu\text{m} \leq a \leq 0.25\mu\text{m}$ . Biermann & Harwitt (1980) argue that such a distribution also applies to circumstellar grains, since grain collision is found to be important in the inner part of the envelope, because of the low outflow and drift velocities of grains. Their calculation shows a remarkable agreement between the lower limit of the grain size with that estimated by MRN. However, the calculations of grain collision only estimates the lower limit of the size distribution, due to fractionation. The upper limit is set by observations of extinction and polarisation properties of the grains. The above size distribution was found to be applicable to both graphite and silicates.

In crystalline materials, vibrational excitations are associated with the plane waves.

Figure 2.2: Silicate extinction efficiencies from Kratschmer & Huffmann (solid) and Draine & Lee (dotted) as compared to our extinction (dashed).



Such vibrations are called phonons. The far-infrared absorption is mainly due to multiphonon processes which are temperature sensitive. Also materials can absorb in the damping wing which shows a quadratic dependence on the frequency. In amorphous materials, the absorption is insensitive to the temperature. Since the strength of the far-infrared absorption depends on the disorder in the charge distribution in the lattice, and the oscillator strength is independent of the vibrational mode, the frequency dependence traces the phonon spectrum. Hence amorphous materials will have the same absorptivity as crystalline forms, i.e.,

$$Q_{ext} \propto \lambda^{-p} \quad (2.30)$$

where  $p=2$ . For amorphous layer-lattice materials, the absorption does not follow the quadratic law, since their structure limits the phonon to two dimensions. Therefore, the phonon spectrum depends on frequency rather than the frequency squared, resulting in  $p=1$  (Tielens & Allamandola 1987). Day (1976) observed the far-infrared extinction of amorphous silicates and obtained the value of  $p$  between 1.25 to 1.5, which may be due to some crossed linkage between the lattice layers (Tielens & Allamandola 1987).

### 2.3.2 Silicate core-ice mantle grains

Gillet & Forrest (1973) found that several molecular clouds displayed strong absorption at  $3.08\mu\text{m}$ , which has been attributed to the OH stretching mode in water ice. In a very dense circumstellar environment, it is conceivable that water ice condense out of the flow. In fact, the  $3.08\mu\text{m}$  absorption feature has been observed in late type stars, which have very high mass loss rates, such as OH231.8+4.2 (Allen et al. 1982) and OH32.8-0.3 (Roche & Aitken 1984). Also seen is the blend between the silicate absorption at  $9.7\mu\text{m}$  and the feature due to the  $\text{H}_2\text{O}$  libration mode (de Muizon, d'Hendecourt & Perrier 1986) at  $12\mu\text{m}$ . Ice is presumably more likely to condense onto the surface of an existing grain, rather than form separate grains. Since most abundant grains are silicates, these are most likely to produce the substrates on which water-ice forms. The rate at which the volume is increased via accretion is

$$\frac{dV}{dt} = \frac{d(4\pi a^3/3)}{dt} = 4\pi a^2 n_0 v_0 \quad (2.31)$$

Hence

$$\frac{da}{dt} = n_0 v_0 \quad (2.32)$$

where  $n_0$  is the number density of the accreting gas phase species; and  $v_0$  is the average gas velocity. From this, it can be seen that the rate of accretion is independent of the core size, leading to the conclusion that all silicate grains have the same ice mantle thickness. From the abundance of carbon, oxygen and silicon, the estimated maximum thickness of the ice mantle can be calculated.

$$a_m = a_c + \Delta a \quad (2.33)$$

where  $a_c$  is the core radius; and  $a_m$  is the radius of the grain with mantle thickness  $\Delta a$  coated on the core. The volumes of a silicate grain and the ice coating per H atom are given by (see Pendleton 1987)

$$V_{Si} = \frac{f_{Si} A_{Si} m_{Si}}{\rho_{Si}} \quad (2.34)$$

$$V_{ice} = \frac{f_O A_O m_{ice}}{\rho_{ice}} \quad (2.35)$$

where  $f_x$  is the fraction of the species  $x$  condensing to form grains. In this case,  $f_{Si}$  is taken to be 1, i.e., all the silicon is in the form of silicates. Assuming that all the oxygen goes into forming silicates ( $SiO_4$ ) and carbon monoxide (CO), then the fraction of the remaining oxygen is

$$f_O = 1 - \frac{A_C}{A_O} - 4 \frac{A_{Si}}{A_O} \quad (2.36)$$

where  $A_x$  is the abundance of species  $x$ . For the MRN grain size distribution, the ratio of the volume of the core and mantle+core is reduced to

$$\frac{V_{Si}}{V_{ice}} = 1 + (3\Delta a a_{min}^{-0.5} + \Delta a^2 a_{min}^{-1.5} + \Delta a^3 a_{min}^{-2.5}) / a_{max}^{0.5} \quad (2.37)$$

where  $a_{min}$  and  $a_{max}$  are 0.005 and 0.25  $\mu m$ , respectively. For the values of cosmic silicon, carbon and oxygen abundances, it is found that the maximum thickness of the mantle cannot exceed 0.008  $\mu m$ , so not to violate the abundance of the cosmic oxygen. In the calculation of the silicate core-ice mantle grains, the thickness of the ice mantle is taken to be 0.007  $\mu m$ . From Figure 2.4, it can be seen that smaller grains show strong ice features, since their volume ratios of mantle to core are much larger than the large grains, as a result of the same mantle thickness.

The optical constants used for ice are taken from Leger et al. (1983), who cooled water vapour to 77K to form amorphous ice. The rate of deposition must be kept very low to prevent the formation of crystalline water ice (Olander & Rice 1972). The water ice observed in the interstellar and molecular clouds are thought to be amorphous because

Figure 2.3: The ice mantle thickness as a function of the fraction of oxygen (in form of water-ice) depleted

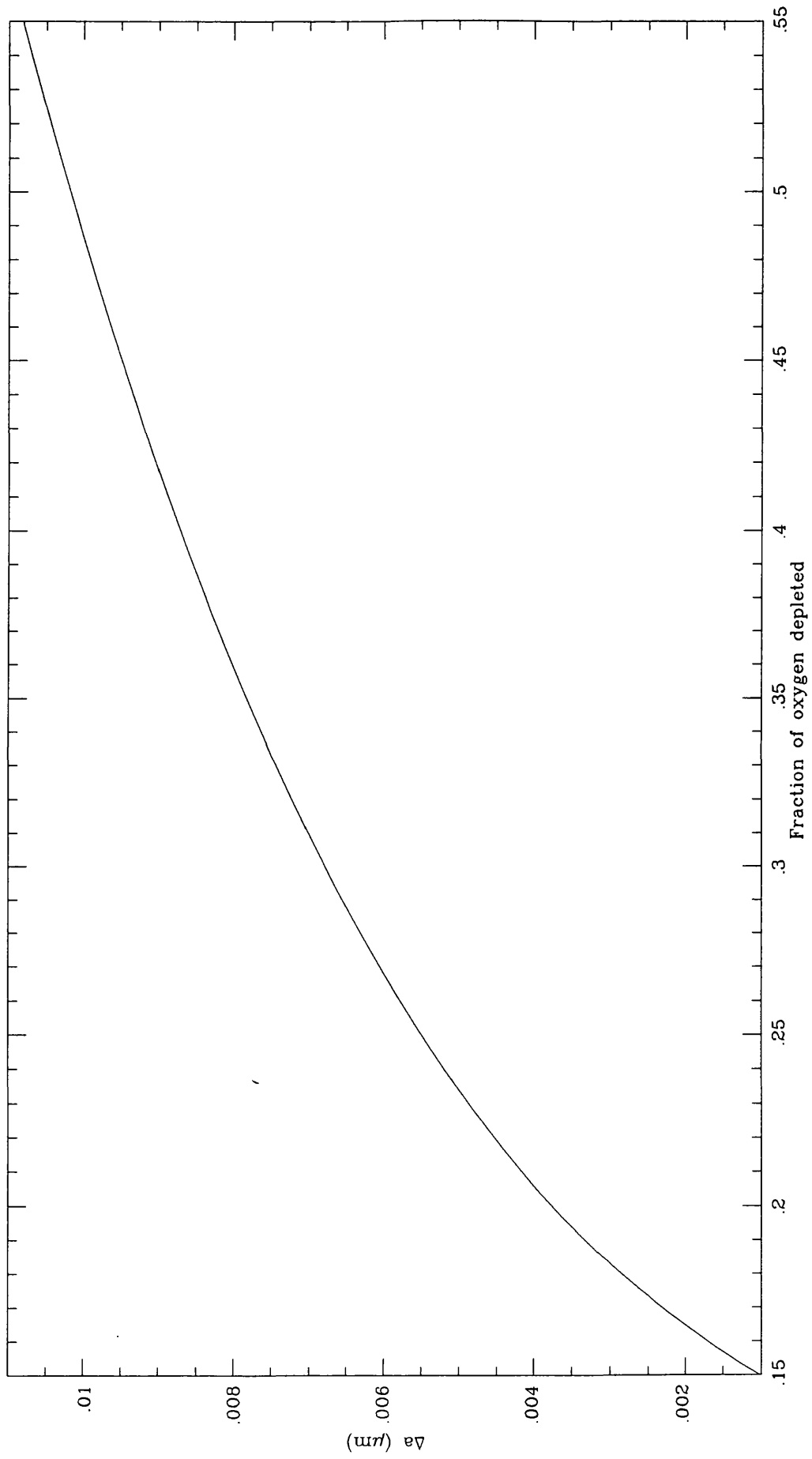
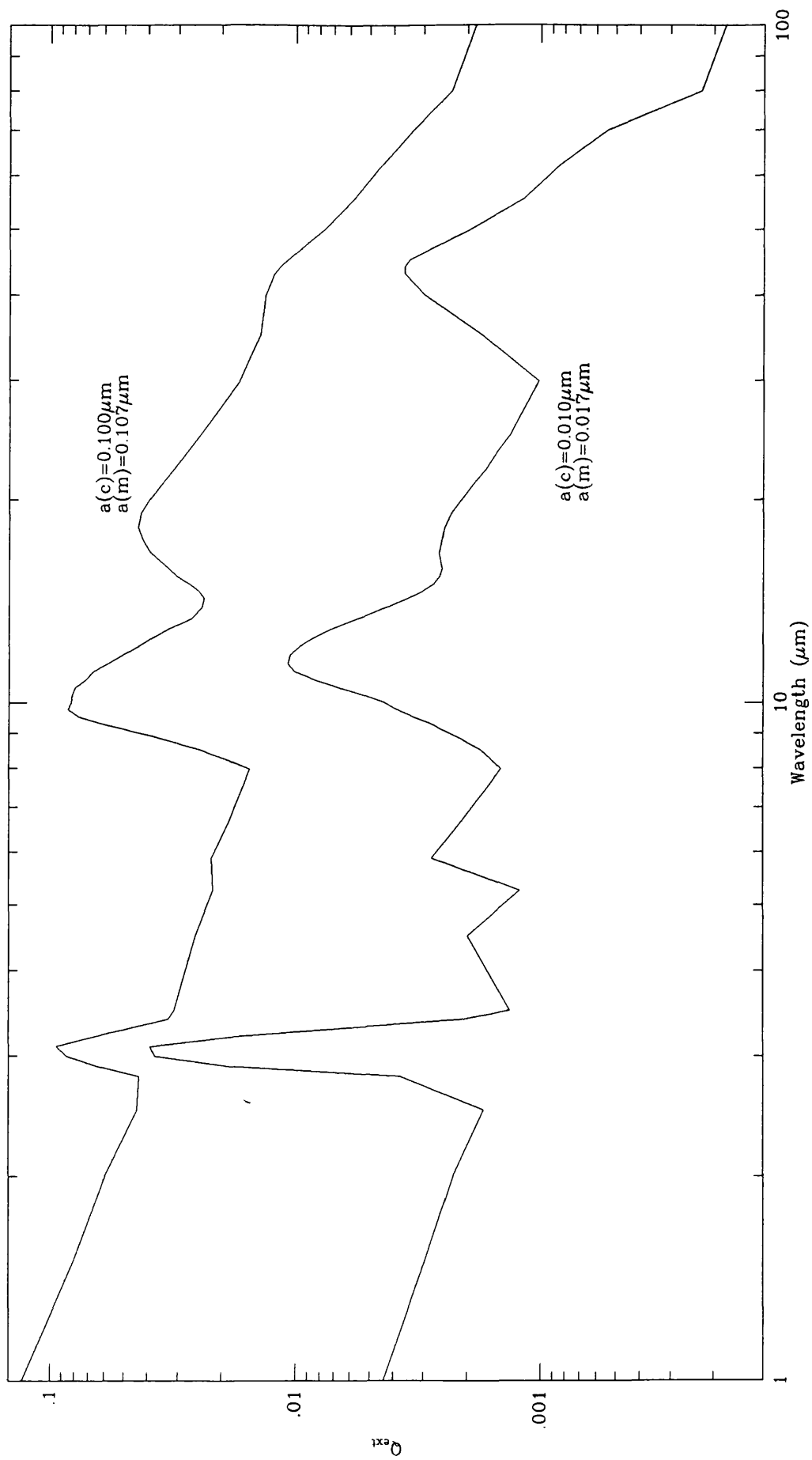


Figure 2.4: The extinction of the composite grains. The core radii of silicate are the same in both cases but the mantle thicknesses differ. The effect of extinction due to water-ice is larger for larger volume of ice which condensed onto the silicate core.



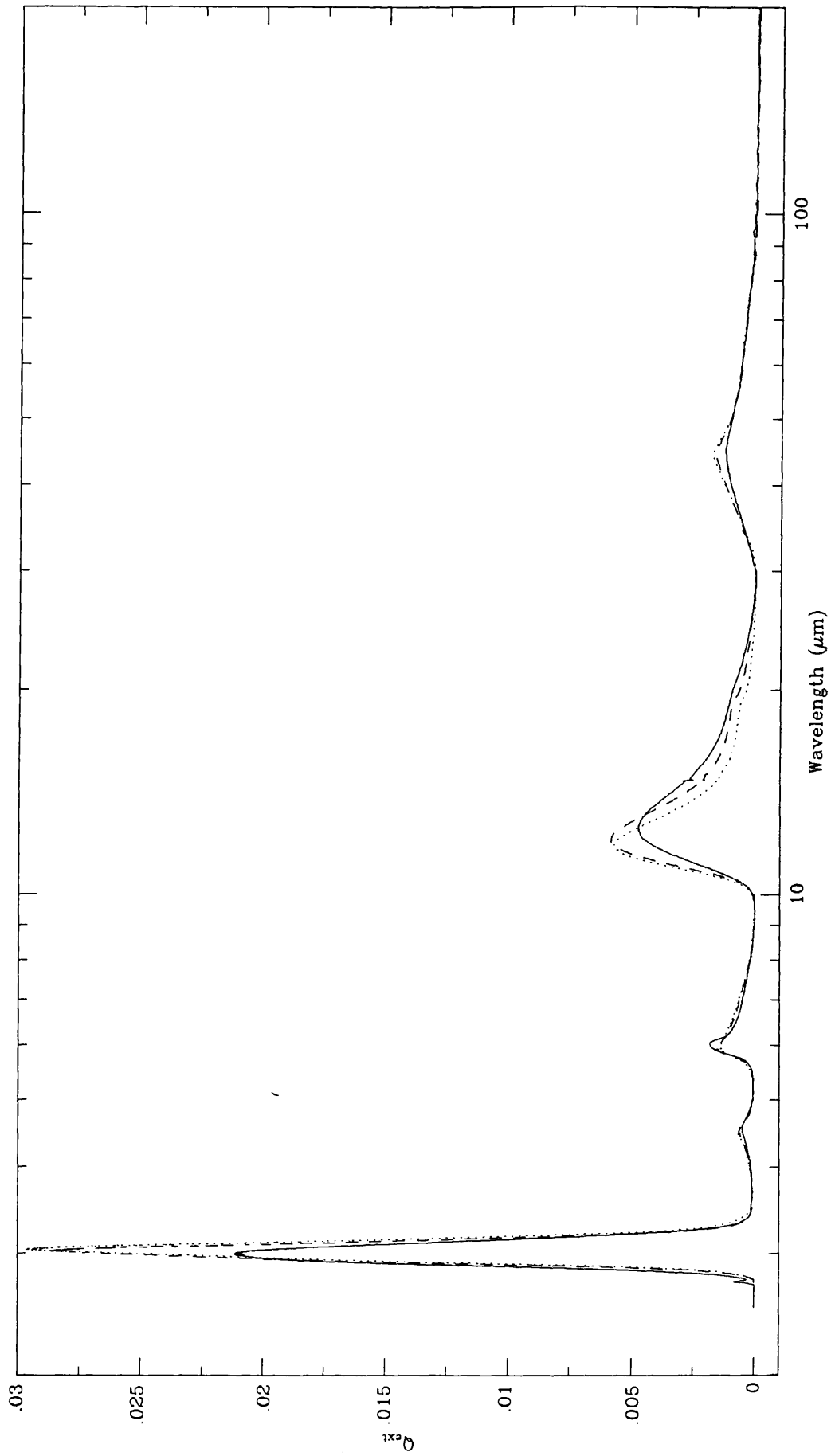
of the low temperature (Leger et al. 1979). The extinction efficiencies of amorphous ice are much smoother than those of crystalline ice reported by Bertie, Labbe & Whalley (1969). However, they show the expected features at  $3.1\mu\text{m}$ , a broad feature at  $10\mu\text{m}$  and another peak in the far-infrared region at around  $50\mu\text{m}$ . The calculation of the extinction of composite grains was done by Aannestad (1975). The materials used were crystalline olivine and crystalline ice, which resulted in very sharp features. Here, the modified optical constants of silicates and amorphous ice are used. The Mie theory applied in this case must be adapted to take into account the extinction of both core and mantle materials (Bohren & Huffmann 1983). The far-infrared fall off of the efficiency is taken to be  $\lambda^{-1}$  for  $\lambda > 80\mu\text{m}$ . It is quite unfortunate that stars with suspected ice absorption bands have high uncertainties in *IRAS* 60 and  $100\mu\text{m}$  fluxes (due to cirrus). This makes it difficult to determine whether  $\lambda^{-1}$  or  $\lambda^{-3}$  (Aannestad 1975) fall off is correct.

Forveille et al. (1987) reported a discovery of *IRAS* 09371+1212, which has an extremely large 60:25 $\mu\text{m}$  flux ratio. They propose that such a source has ice condensed either onto silicate grains or pure water-ice grains, hence the name "Frosty Leo". This was confirmed by the  $3\mu\text{m}$  observation by Rouan et al. (1988) and by Omont et al. (1990), who obtained a far-infrared spectrum of this source with the Kuiper Airborne Observatory (KAO), which showed emission peaks around 46 and  $60\mu\text{m}$ . The feature appeared to match the crystalline ice absorption efficiency rather than the amorphous ice. There is no evidence for an OH maser, and it was concluded that most of the OH condensed out to form  $\text{H}_2\text{O}$  ice. They also found the emission feature in two OH/IR stars, OH231.8+4.2 and OH127.8+0.0.

The shape of the ice optical constants depends on the temperature at which this material condenses. For grains condensed at higher temperature, the peak of the  $10\mu\text{m}$  feature shifts shortwards, and the strength of the feature is increased (Hudgins et al. 1992). Also, the feature becomes broader for lower condensation temperature. For a material condensing at high temperature (140K), the structure resembles the crystalline arrangement, while material condensing at low temperature (10K) is more likely to become amorphous. For a star with a large outflow, it may then be more realistic to consider ice coating of different condensation temperatures as we progress outwards from the star. However, this approach is not adopted in this thesis, only one condensation temperature is considered. Since the Haisch code can accommodate multiple grain components, it

would not be difficult to deal with another silicate core-ice mantle grains condensing at different temperatures.

Figure 2.5: Extinction efficiencies of water-ice condensed at different temperatures. Solid line  $T_c=100\text{K}$ ; dashed line  $T_c=10\text{K}$ ; dotted line  $T_c=140\text{K}$ .



## Chapter 3

# Modelling the Infrared Energy Distributions

This chapter discusses parameters used in the radiative transfer code and the way changes affect the resulting energy distributions, as compared to the infrared photometry and *IRAS* LRS spectra, with particular attention to dust mass loss rates. These results from the infrared modelling are compared to those derived from infrared photometry observations, and finally the comparison to the gas mass loss rates is discussed.

### 3.1 Input parameters

The Haisch (1979) code requires various input data as a basis for radiative transfer calculations. These are physical parameters which can be determined from observations.

#### 3.1.1 Stellar parameters

These include the stellar radius, effective temperature and distance to the source. These quantities are obviously related to the stellar luminosity. Since most of the stars examined are unresolved, their actual sizes are not known. However, for stars with optically thin circumstellar shells (i.e.,  $10\mu\text{m}$  feature is in emission), it is assumed that the observed *IRAS* LRS flux at  $8\mu\text{m}$  is the stellar continuum. Therefore, fitting the energy distribution to observations in this region yields the stellar radius. This also applies to stars with a self-reversed  $10\mu\text{m}$  feature. For optically thick shells, the  $8\mu\text{m}$  flux is dominated by dust emission, in which case we have to assume the effective temperature of the star, and use

the published distance or revert to the normal assumption of a constant luminosity of  $10^4 L_{\odot}$  (see below).

The effective temperature can be determined from optical spectra for optically visible stars. Since most stars have spectra peaking in the near-infrared, photometry in this region gives a reasonable estimate of the temperature (e.g., Hyland et al. 1972). For optically thick stars, however, the effective temperature is somewhat arbitrarily assumed to be 2000K, characteristic of the tip of the AGB. However, the emergent spectrum is then dominated by cool dust, which is heated by the re-radiated emission of warm dust closer in. As a result, the emergent spectrum is not very sensitive to the stellar temperature (Schutte & Tielens 1989).

The value adopted for the stellar luminosity (or equivalently, the distance) has no influence on the emergent spectrum, as long as the total dust column density is kept constant (Jones & Merrill 1976; Bedijn 1977). However, it does set the size scale of the envelope. Uncertainty in the distance actually forms the main source of error in determination the envelope parameters (i.e.,  $\dot{M}_d$ ,  $R_*$ ). This will be discussed further in the later section.

Distances to many stars have been obtained from the published literature. Each author used different methods, the most reliable one to date involves “phase lag” (e.g., Herman & Habing 1985; Herman et al. 1986; van Langevelde et al. 1990) for sources which exhibit OH masers. This method requires observations of the light curves in order to determine the light travel time between the front and back side of the envelope, which gives the diameter of the masing region. Also the sources need to be mapped in order to find their angular sizes. From these, distances can be calculated with a high degree of certainty. Another way of determining distance is to use OH maser luminosities. Baud & Habing (1983) found a tight correlation between  $L_{OH}$  and the shell radius. These are often referred to as “geometric” distances. Other methods involve using the period–OH luminosity relation (e.g. Nguyen-Q-Rieu et al. 1979), or the use of kinematic distance calculations. Since this information is usually unavailable, it is often necessary to revert to calculating distances by assuming the luminosity is  $10^4 L_{\odot}$  (e.g., Knapp & Morris 1985).

### 3.1.2 Wind terminal velocity

Terminal velocities are obtained from OH maser observations of OH/IR stars (e.g., Baud & Habing 1983; Bowers, Johnson & Spencer 1983; Gehrz et al. 1985) and from the CO outflow velocity (Knapp & Morris 1985). There is a slight difference between the velocity obtained from OH and CO observations on the order of 2 km/s (Heske et al. 1990). Note that the CO observations measure velocity of the shell at  $\sim 10^{18}$  cm while OH maser arises from a few  $10^{16}$  cm. Here, we assume that outflow velocity is the same as the terminal velocity of the gas and is constant throughout the shell. This is a reasonable assumption since the terminal velocity of the gas is reached after a few stellar radii (Tielens 1983).

### 3.1.3 Inner and outer radii of dust shells

The inner radius of a dust shell,  $r_i$ , is taken to be where dust grains first condense out. For silicates, the condensation temperature,  $T_c$ , is 1000K, and the inner radius is given by  $r_i \propto T^{-4}$ .

In the presence of dust, temperature is assumed to follow  $r^2 \propto T^{-5}$ . Here, we arbitrarily set the outer radius of the shell by

$$\log(r_o) = -2.5 \log\left(\frac{T_o r_i^{-0.4}}{T_c}\right) \quad (3.1)$$

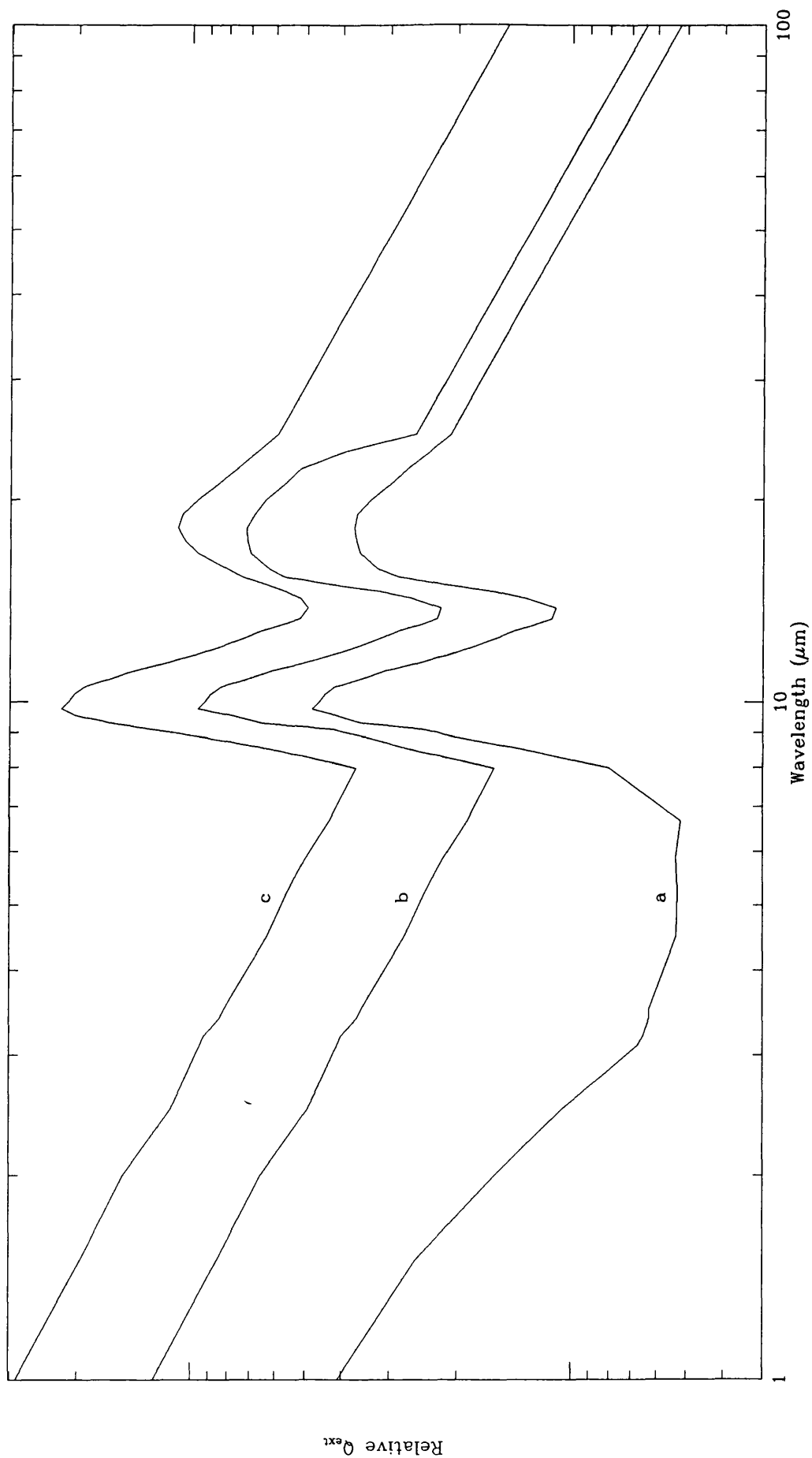
For this calculation, the temperature at the outer boundary,  $T_{out}$ , is taken to be 30K. From the radiative transfer calculation, however, it is found that the temperature at this radius falls below 10K for an optically thin envelope, which is close to values for the interstellar medium. The exact location of the outer boundary has no influence on the emergent flux between 2–100 $\mu$ m.

### 3.1.4 Density law

We assumed a constant mass loss rate and a constant outflow velocity. This results in a  $r^{-2}$  dust density dependence. Other dust density distributions, i.e., taking the acceleration near the inner radius into account, have been investigated by Schutte & Tielens (1989). However, this has little influence on the emergent spectrum, as long as the dust column density is kept constant.

### 3.1.5 Dust properties

Figure 3.1: Adopted extinction efficiencies for silicate grains for three sets of models with index for the far-infrared efficiency,  $p=1$ . (a) For OH26.5+0.6; (b) for AFGL 230; (c) for the rest of the stars. Peak strengths of 20:10 $\mu$ m is 0.8 for (a) and (b) and 0.5 for (c).



From modelling 26 sources, the index of the far-infrared emissivity,  $p$ , which is dependent on the type of material, is found to be between 1 and 1.5 (equation 2.30). This implies that grains formed in the circumstellar environment are amorphous rather than crystalline and have a layer-lattice structure (Tielens & Allamandola 1987). Sources with  $p=1.0$  have dust opacity at  $60\mu\text{m}$  of  $240\text{cm}^2/\text{g}$ , as assumed by Herman et al. (1986), and sources with  $p=1.5$  have dust opacity of  $160\text{cm}^2/\text{g}$ , as assumed by Jura (1987).

For most sources with silicate emission, the 20:10 $\mu\text{m}$  ratio is fairly constant, i.e.,  $\sim 0.5$ . This ratio also holds for sources with self-reversed 10 $\mu\text{m}$  features. However, for very optically thick stars where 10 $\mu\text{m}$  is now in total absorption, this ratio increases to about 0.8 (see Figures 3.1 and 3.2). Possibly, this is a consequence of the temperature dependence of the optical properties of circumstellar silicate grains (Bedijn 1987). Some laboratory studies have shown that the 20:10 $\mu\text{m}$  ratio increases with decreasing temperature (e.g., Day 1976). Thus, the cool dust prominent in heavily obscured sources may have, on average, an intrinsically higher 20:10 $\mu\text{m}$  ratio than the warmer dust observed in optically thin sources.

### 3.2 Results from modelling the infrared spectra

Detailed models for the infrared emission, from circumstellar shells as a function of various free parameters, have been produced by Jones & Merrill (1976), Bedijn (1977; 1987) and Schutte & Tielens (1989). Here, we concentrate on observed flux distributions of the sample of AGB stars, and on deriving interesting physical parameters of the flow (i.e., the dust mass loss rate). The radiative transfer code and the dust parameters used are described in chapter 2. However, the parameters for silicate dust need further modification in order to obtain a good fit for a few sources (see Figure 3.1).

The majority of stars in our sample were chosen from a list of OH/IR stars with known distances, OH outflow velocities and near-infrared photometry fluxes. Many of the stars have been observed in CO and therefore have their gas mass loss rates estimated. However, the near-infrared fluxes were not obtained at the same epoch as the *IRAS* data hence these will introduce uncertainties in mass loss rates determined from detailed model fits. The variations in the near-infrared fluxes can be up to a factor of two (see e.g., Evans & Beckwith 1977; Werner et al. 1980).

All the model fits are shown in Figure 3.2 and the derived parameters are listed in Table 3.1. Essentially, these fits yield the total  $10\mu\text{m}$  optical depth,  $\tau(10)$ , which can be translated into the dust mass loss rate using the derived inner radius of the dust shell,  $r_i$ , the outflow velocity,  $v_e$ , and the intrinsic strength of the  $10\mu\text{m}$  feature (Schutte & Tielens 1989)

$$\dot{M}_d \propto r_i v_e \frac{\tau(10\mu)}{S(10\mu)} \quad (3.2)$$

The derived dust mass loss rates are listed in Table 3.1.

### 3.2.1 Individual sources

Data on individual sources in Table 3.1 will be compared to previous work in order to see whether the dust mass loss rates obtained from modelling of the infrared energy distributions differ from other estimates. Before this, it is of interest to comment on a few sources which require modifications of dust parameters, mainly very optically thick sources.

#### AFGL2199

This source was classified as a carbon star by Knapp et al. (1982). However, we found this source to exhibit a self-reversed silicate feature at  $10\mu\text{m}$  and silicate emission at  $18\mu\text{m}$ .

#### OH26.5+0.6

A further study has been made of OH26.5+0.6 because of its optically thick nature. Evans & Beckwith (1977) observed the flux of this source which varied by almost 40% over a period of 1 year. The observed 10 and  $20\mu\text{m}$  features cannot be fitted by assuming the intrinsic 20:10 $\mu\text{m}$  ratio of 0.5 as in other cases. Also, the near-infrared opacity is much lower than in other stars. Clearly, a new set of optical constants is needed. This was done by scaling the 20:10 $\mu\text{m}$  ratio to 0.8 and reducing the near-infrared extinction (Figure 3.1). This can be justified by the fact that in a star with a large mass loss rate, the effective temperature of dust is relatively low, hence the peak of the dust emission shifts towards longer wavelengths, thereby increasing the ratio of the 20:10 $\mu\text{m}$  emission (Bedijn 1987). The overall fit to the infrared spectrum of this source is in Figure 3.2(f). It also shows a comparison with the LRS spectra of OH26.5+0.6 on a larger scale. The set of silicate dust properties used here produces a good fit to the detailed spectrum. This star was reported

Figure 3.2: (a) Detailed model fits (solid lines) of observed (crosses) infrared energy distributions of 26 stars. Parameters for each model are summarized in Table 3.1. The solid line for WX Ser in fig 3a is the best fit with  $Q(\text{ext}) \propto \lambda^{-1.5}$  and the dashed line corresponds to  $Q(\text{ext}) \propto \lambda^{-1.0}$ . The NIR data have been taken from Lockwood 1970; Simon, Morrison & Cruikshank 1972; Wilson et al., 1972; Dyck & Lockwood 1974; Strecker & Ney 1974; Lebofsky et al. 1976; Merrill & Stein 1976; Thomas, Robinson & Hyland 1976; Evans & Beckwith 1977; Werner et al. 1980; Jones et al. 1983; Fix & Mutel 1984; Baud et al. 1985.

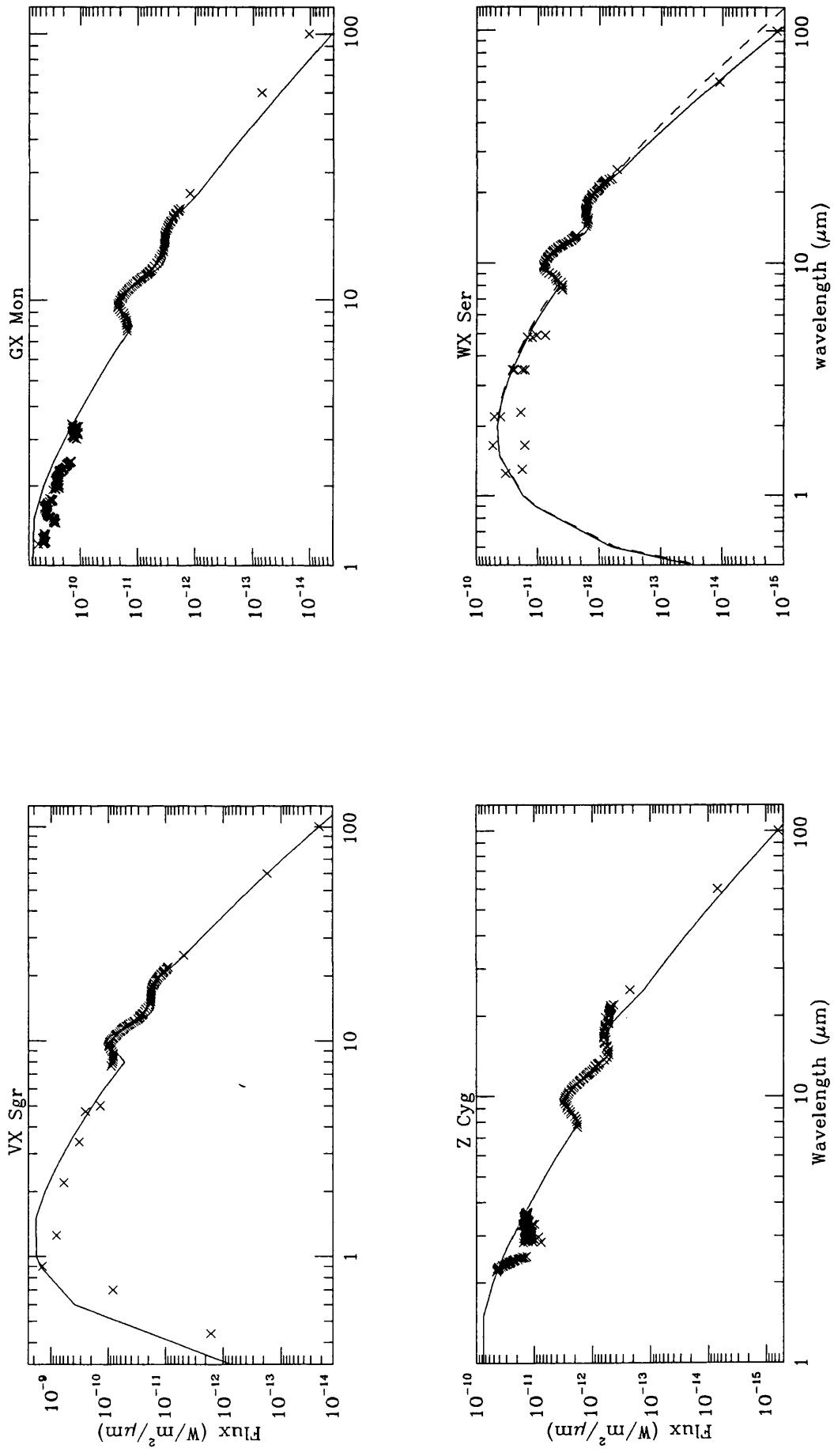


Figure 3.2: (b)

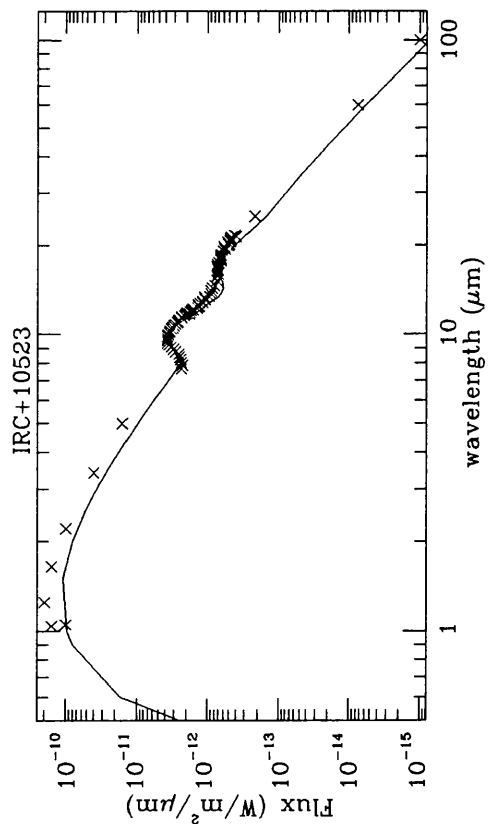
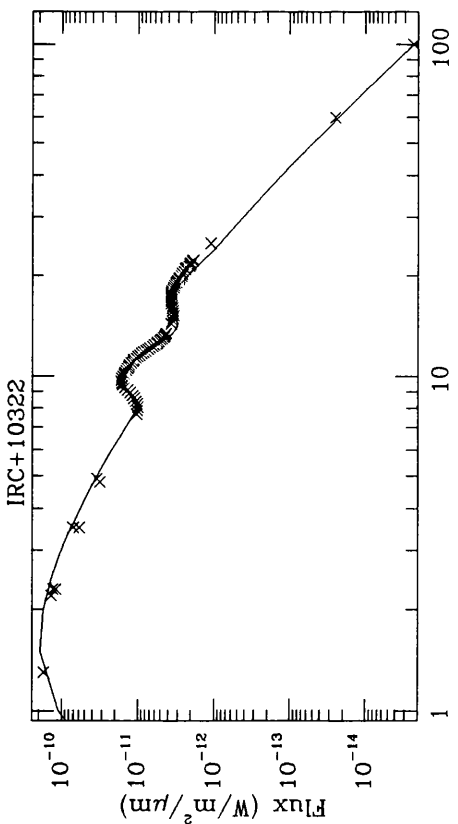
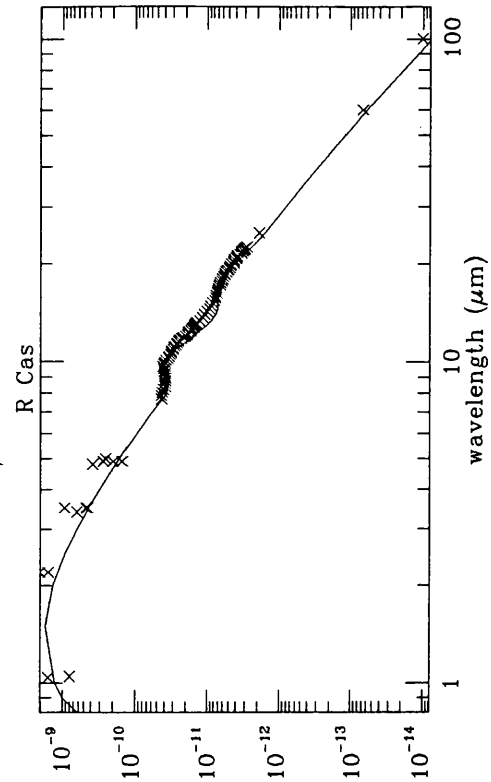
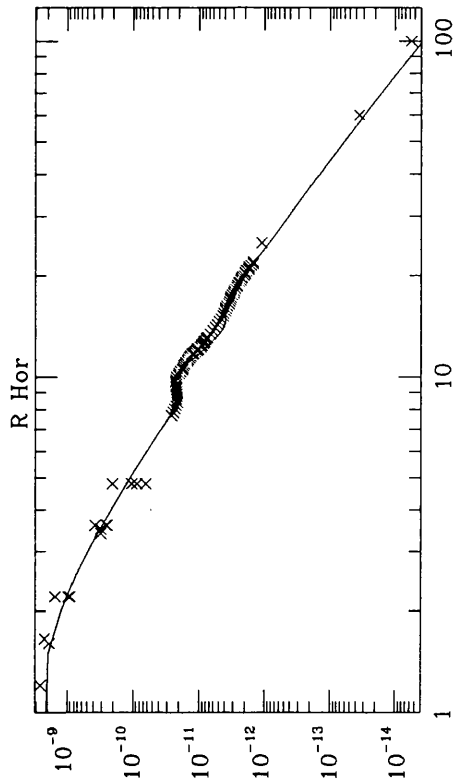


Figure 3.2: (c)

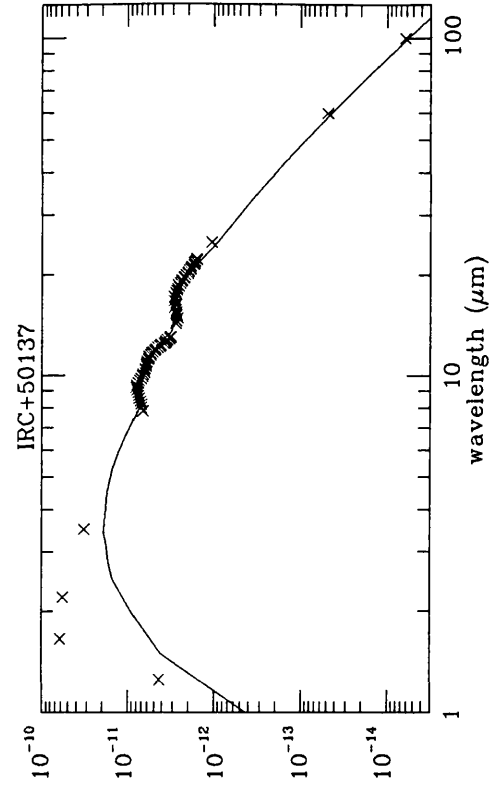
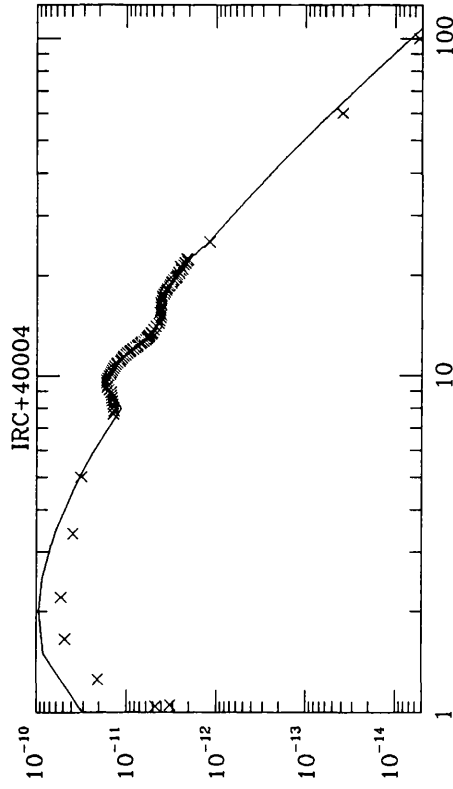
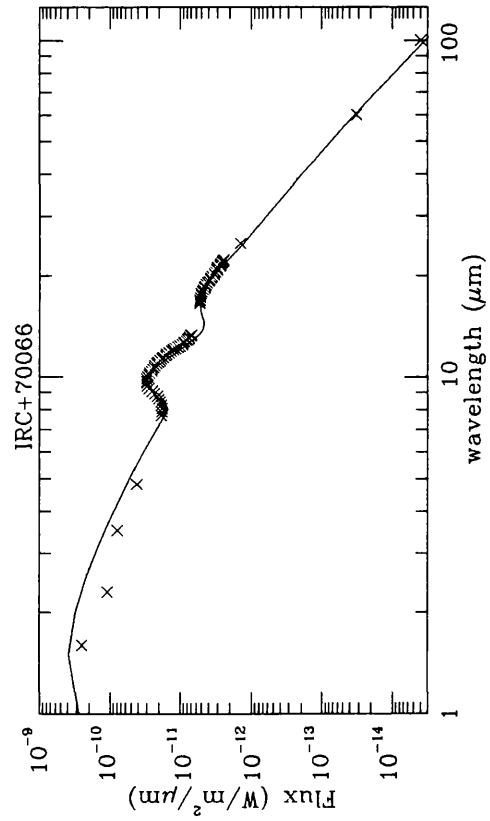
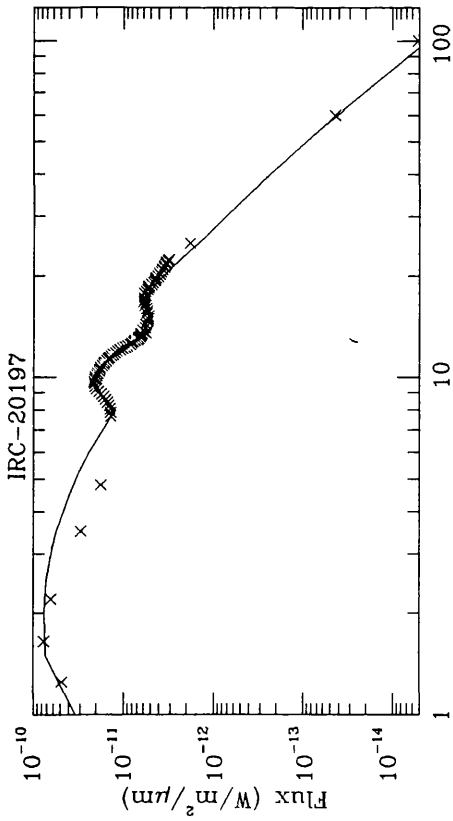


Figure 3.2: (d)

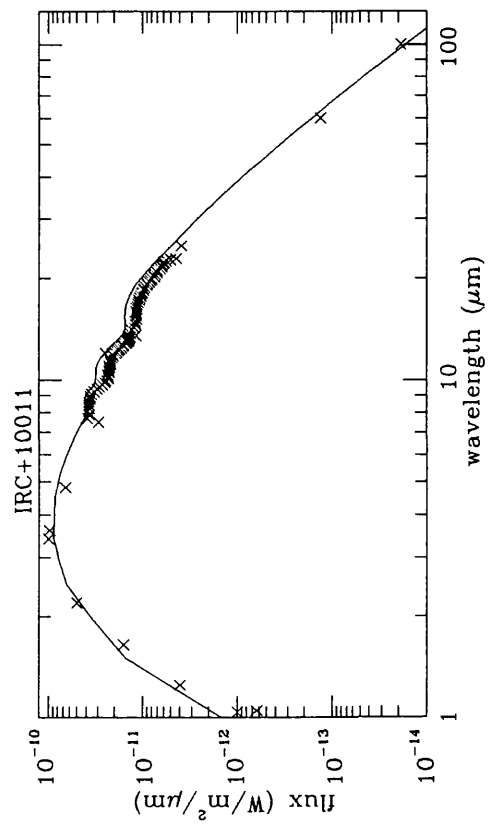
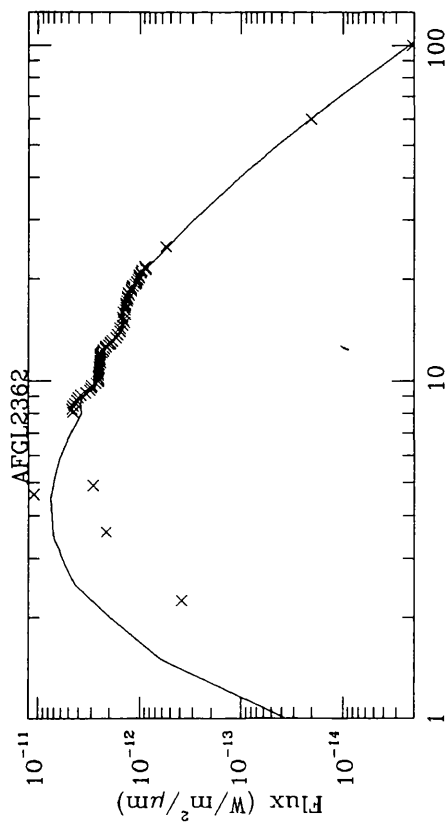
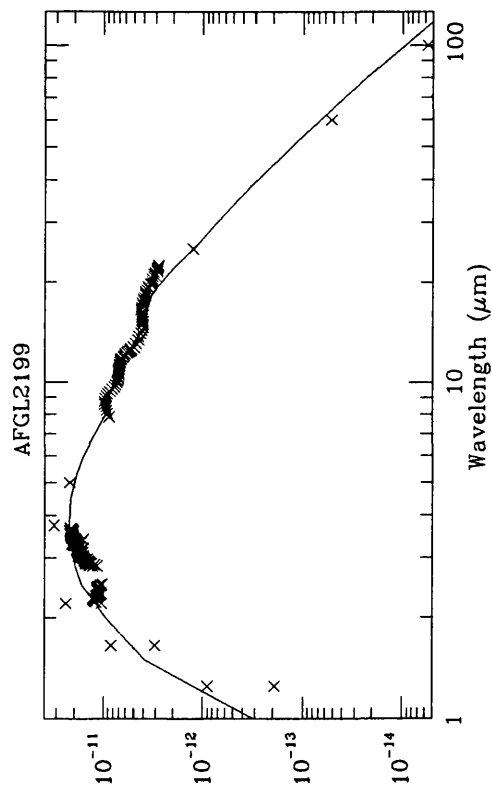
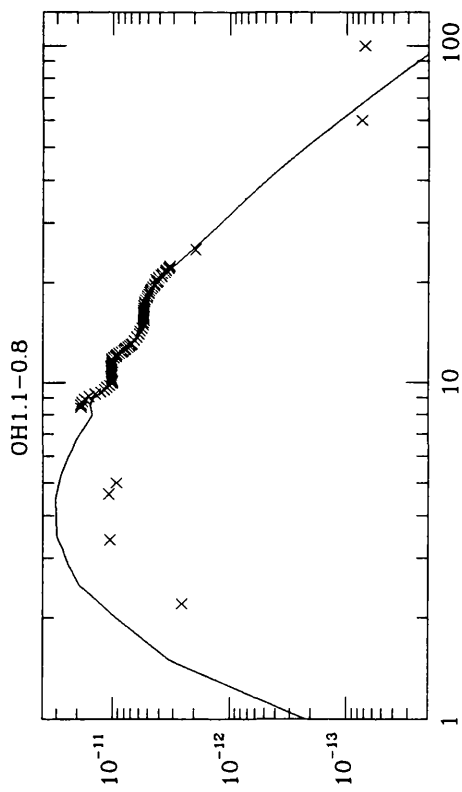


Figure 3.2: (e)

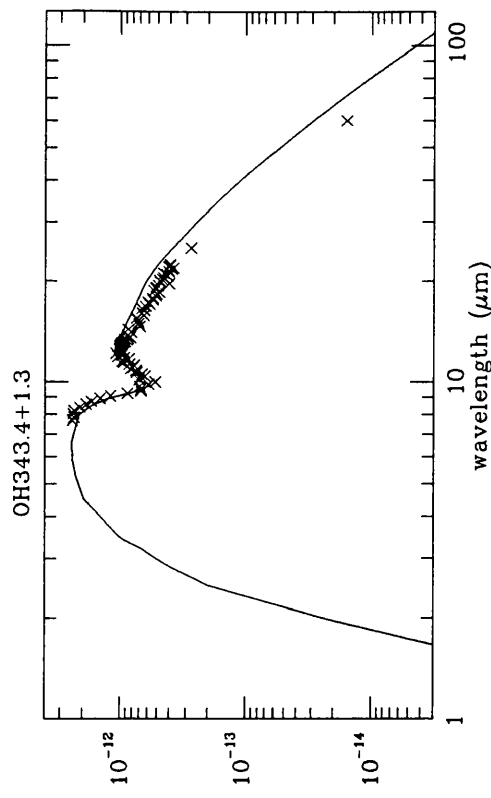
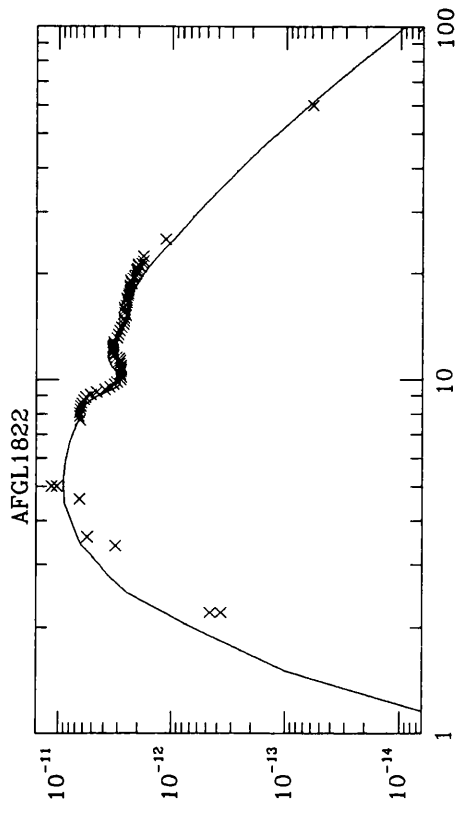
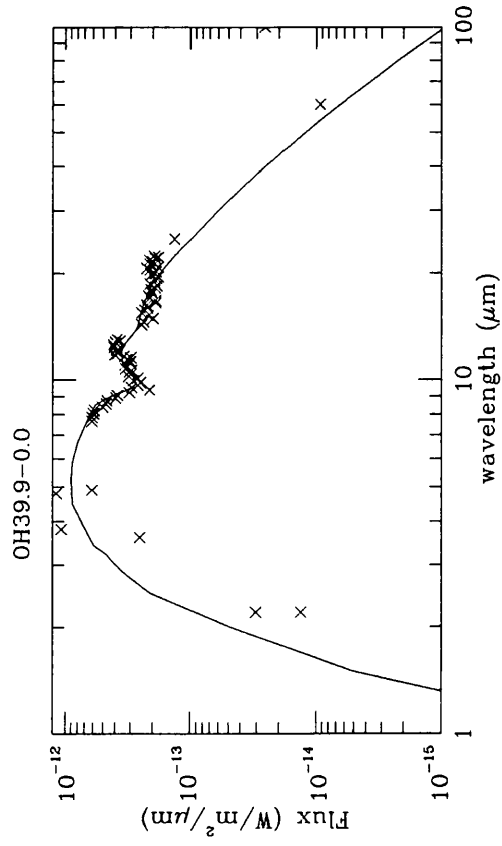
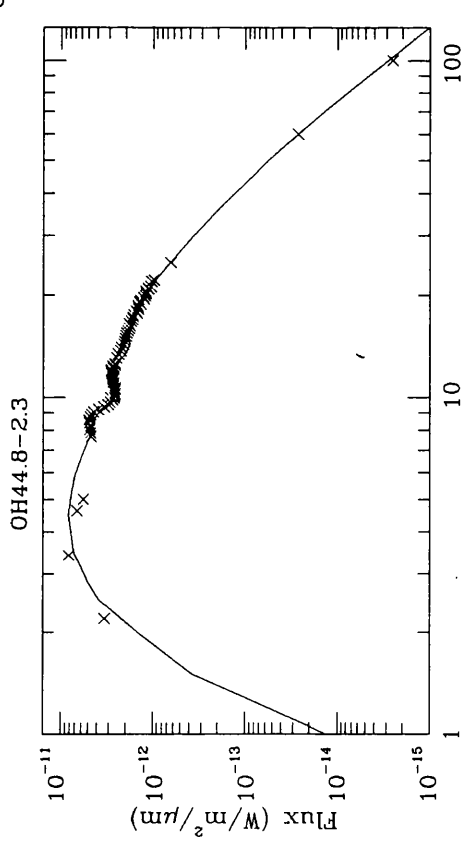


Figure 3.2: (f)

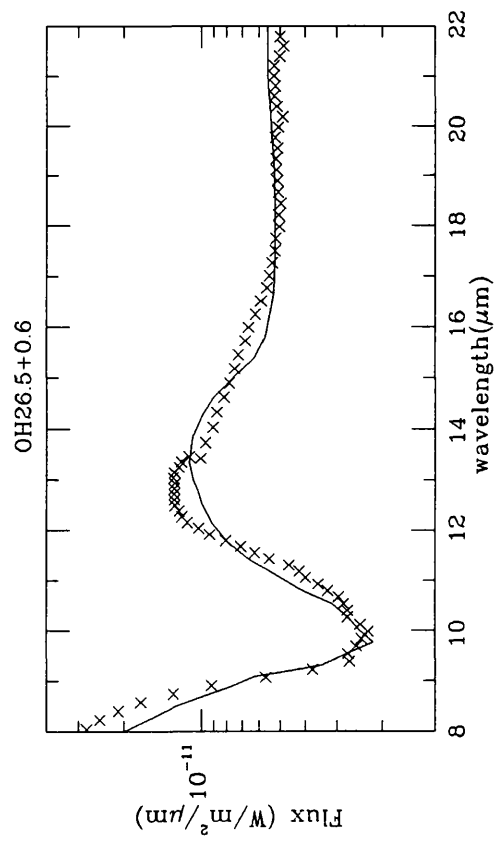
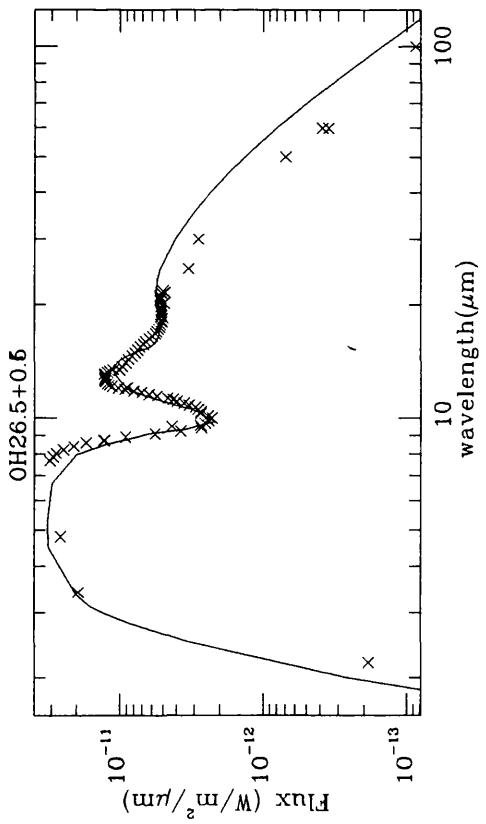
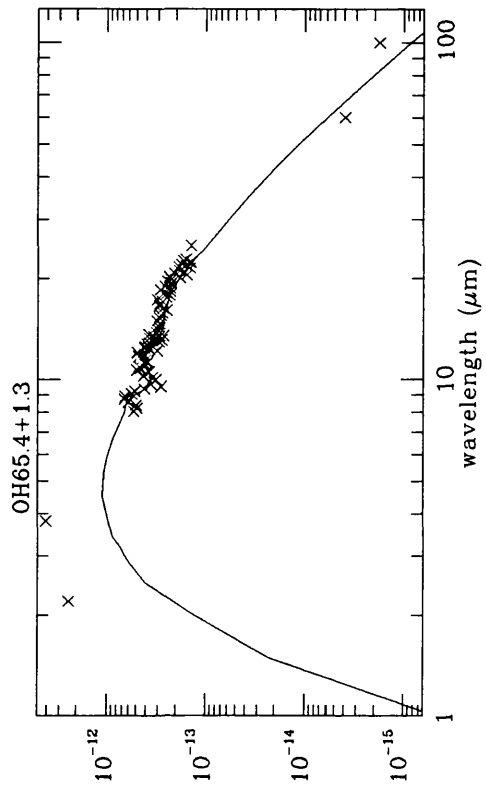


Figure 3.2: (g)

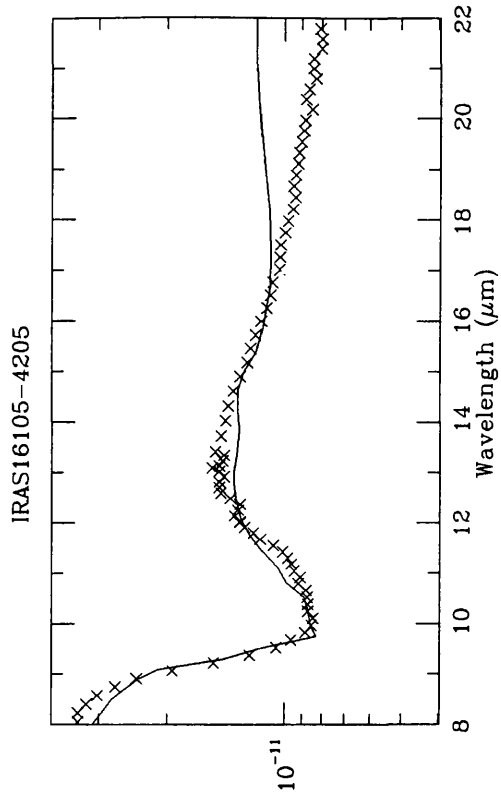
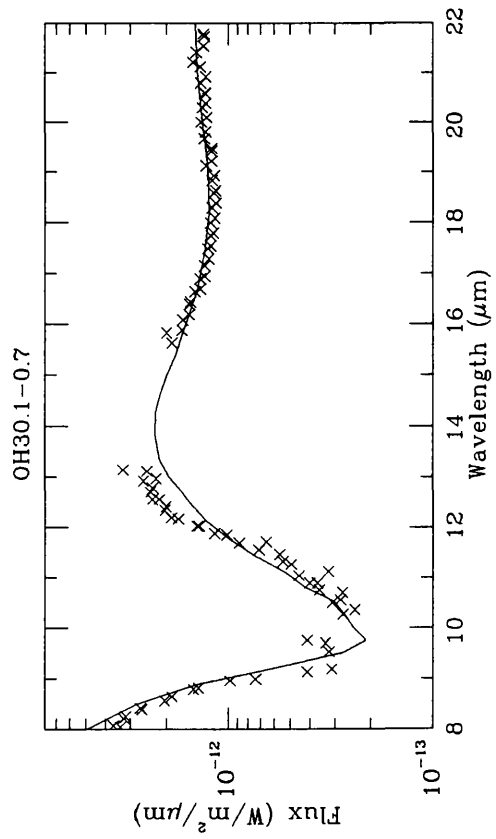
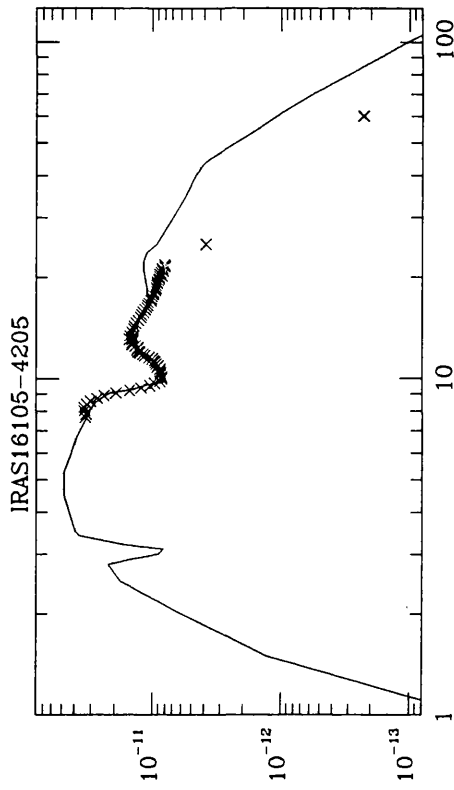
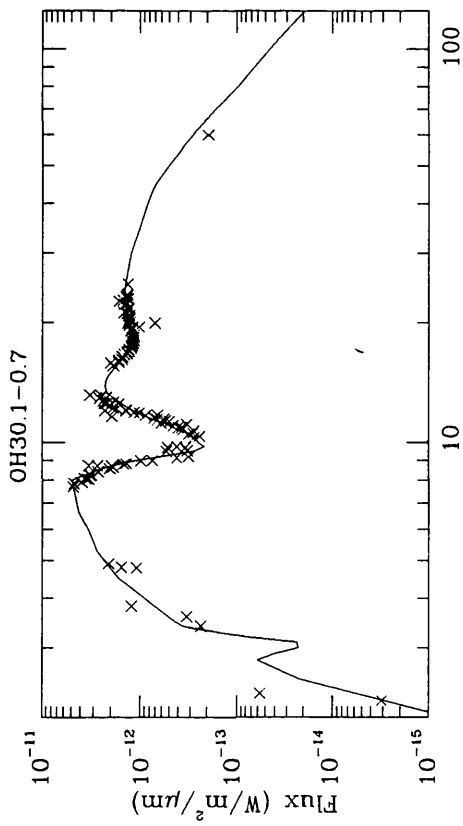
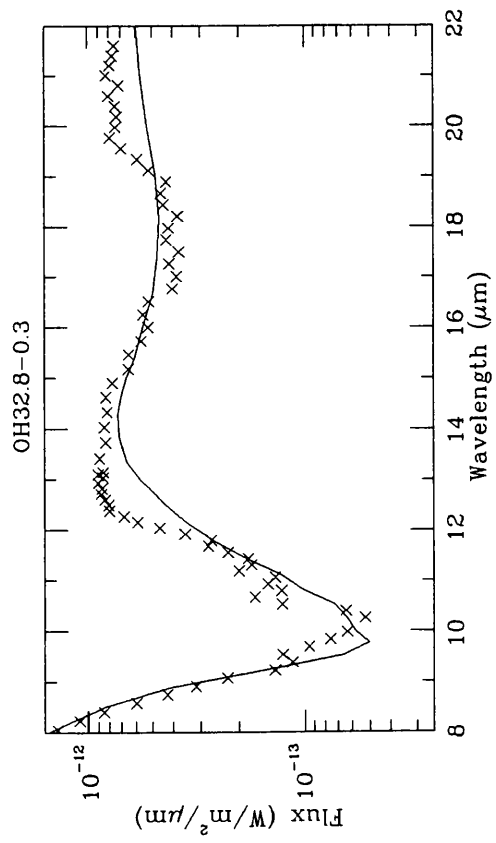
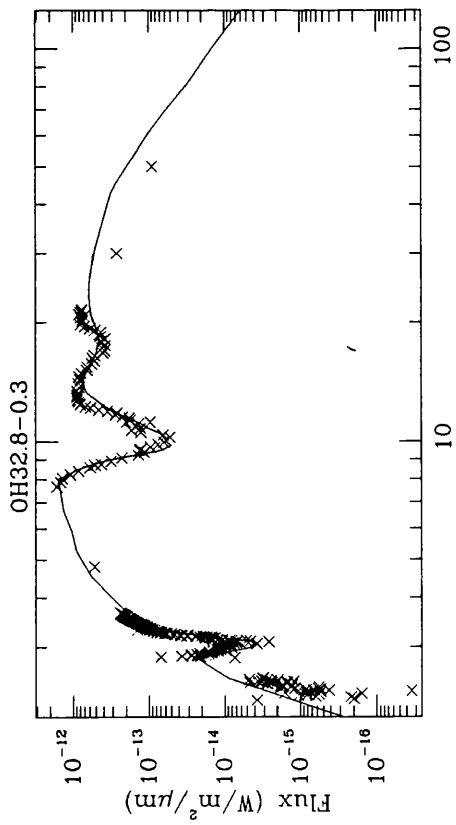
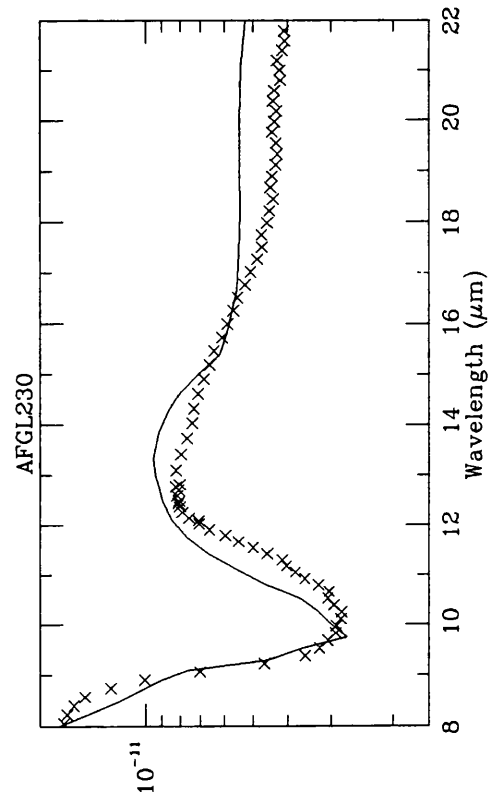
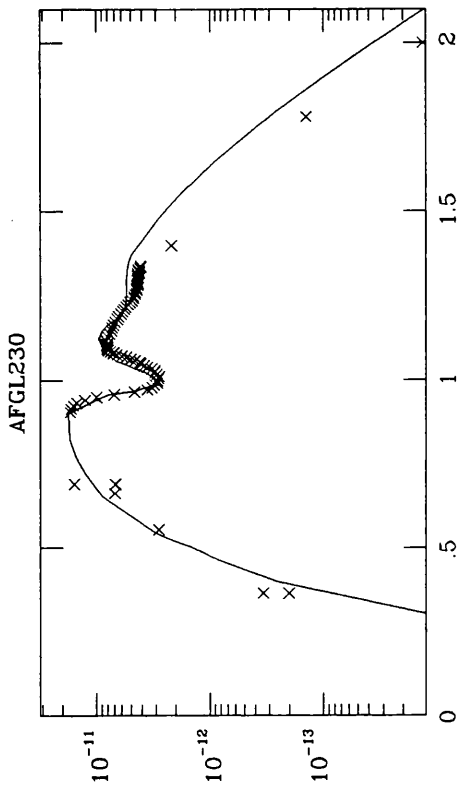


Figure 3.2: (h)



by Hesse et al. (1990) to have ice band emission in the far-infrared. However, this has not been confirmed and from our model, ice is not needed.

### **AFGL230 = OH127.8-0.0**

This source has an extremely thick circumstellar shell. Hesse et al., (1990) reported a distance of 2.8 kpc, which makes it a very luminous source ( $L_* \sim 5 \times 10^4 L_\odot$ ). Again, the intrinsic 20:10 $\mu$ m ratio for this source is taken to be 0.8. A close inspection of Figure 3.2(h) reveals that AFGL230 may have ice present, since the 10 $\mu$ m feature appears too broad to be explained by silicate absorption alone.

### **IRAS 16105-4205, OH30.1-0.7 and OH32.8-0.3**

These three sources show evidence for ice grains (de Muizon et al. 1986; Roche & Aitken 1984). All were modelled with silicate core-ice mantle grains as described in chapter 2. The result is a much broader 10 $\mu$ m feature (Figures 3.2(g,h)). Also seen are features at 3 and around 50 $\mu$ m. The former is always seen in absorption, while the latter is in emission. The model for OH32.8-0.3 slightly underestimated the depth of the 3 $\mu$ m feature. However, its LRS spectra and 3 $\mu$ m spectra (Geballe, private communication) were not obtained at the same epoch, so slight variation in strengths of the two features might be expected. Unfortunately, there is no photometric information on IRAS 16105-4205 which can be used to scale the published 3 $\mu$ m data by de Muizon et al. (1986) to the LRS spectra. The long wavelength lattice vibrations of water-ice ( $\sim 46\mu$ m) are not very apparent in the calculated spectra of these sources. Much larger mass loss rates are required to get appreciable optical depth in these modes. For OH30.1-0.7, no ice data is available, but the 10 $\mu$ m feature is too broad to be of silicate alone. With addition of the silicate core-ice mantle grains, the feature can be fitted better. The observed near and far-infrared agree to the predicted fluxes to better than a factor of two. The index of far-infrared extinction for all three sources is assumed to be 1.0, since both the silicate and water-ice are thought to be amorphous.

## **3.2.2 Uncertainties in the derived parameters**

As can be seen from equation 3.2, the uncertainty in the dust mass loss rate is most affected by uncertainty in the size scale of the envelope (i.e., the inner radius,  $r_i$ ), since

the outflow velocities for these sources are known from the CO or OH observations, and the optical depths can be deduced from the *IRAS* LRS spectra. The inner radius is calculated by assuming that the grains form where the local temperature equals the condensation temperature of silicates. Apart from the actual condensation temperature selected, the inner radius will be affected by the radiation field of the star which, in turn, depends on the assumed stellar luminosity,  $L$ , and the chosen value of the condensation temperature,  $T_c$ .

However, as noted by Schutte & Tielens (1989), variations in the adopted value for  $T_c$  are partially compensated for by variations in  $r_i$  required to fit the observed spectrum. The uncertainty in the derived mass loss rate from  $T_c$  alone is therefore small (15%). For optically thin shells, the stellar radiation field is directly determined from the observed near-infrared and  $8\mu\text{m}$  fluxes, using the estimated distance,  $D$ . That is,  $r_i$  scales as  $L^{0.5}$  and  $L$  depends only on  $D$ . The main uncertainty in the derived mass loss rate, inner radius, and stellar radius results from the adopted distance. For optically thick shells, the dust at the inner radius is heated by re-radiated infrared emission from the dust shell itself, and the stellar parameters are of little importance. Consequently, they are not well constrained. The dust radiation field at the inner boundary is well determined from the fitting procedure. Thus, again, the main uncertainty in the derived mass loss rate results from the uncertainty in the adopted distance. The most accurate distance determinations come from OH maser measurements (the phase lag method; Herman et al. 1986). This method is good to within a factor of two, implying a similar uncertainty in  $r_i$  and hence  $\dot{M}_d$ .

### 3.3 Comparisons of mass loss rates

There are various methods for the determination of mass loss rates which have been widely accepted. However, each has a certain degree of uncertainty. Once dust is formed, it is believed that the mechanism which drives mass loss is the radiation pressure on dust grains. Using the conservation of momentum, we obtain (see Salpeter 1974; Elitzur 1981)

$$\dot{M} = 2.0 \times 10^{-8} \tau_d L / v_e \quad (3.3)$$

where  $\tau_d$  is the optical depth corresponding to dust response to radiation pressure;  $L$  is stellar luminosity in solar unit; and  $v_e$  is the outflow velocity in km/s.

Mass loss rates for red giants can simply be determined using Reimers' formula (Kudritzki & Reimers 1978; Herman & Habing 1985)

$$\dot{M} = 2 \times 10^{-6} \eta \frac{L}{10^4 L_{\odot}} \frac{R}{500 R_{\odot}} \frac{M_{\odot}}{M} \quad (3.4)$$

where L,R and M are stellar luminosity, radius and mass, respectively, and  $\eta$  is a constant ( $\frac{1}{3} < \eta < 1$ ). Herman & Habing (1985) derived a modified Reimers formula based on a sample of 25 OH/IR stars

$$\dot{M} = (5.00 \pm 0.60) \times 10^{-5} \frac{L}{10^4 L_{\odot}} \frac{R}{500 R_{\odot}} \frac{M_{\odot}}{M} \quad (3.5)$$

Note that the constants in both equations differ by a large factor. It is clear that Reimers formula cannot account for the total mass loss on the AGB. Renzini (1981) proposed a phase of a rapid mass loss rate at the tip of the AGB, before stars evolve into the planetary nebula phase, called a superwind.

Another interesting method of deriving mass loss rates from the *IRAS* LRS spectra was carried out by Skinner & Whitmore (1988). However, these are only applicable for stars with silicate emission. They deduced the following relation

$$\dot{M} = 4 \times 10^{-15} B(\text{sil}) F(12\mu\text{m}) D^2 \quad (3.6)$$

where B(sil) is the relative band strength; F(12 $\mu$ m) is the *IRAS* photometry flux and D is the distance to the star in pc.

In the following sections, the dust mass loss rates, derived from infrared observations, will be compared to those from calculations performed in the previous section. They will then be compared to the gas mass loss rates, derived from the CO and OH observations.

### 3.3.1 Dust mass loss rates

Van der Veen & Habing (1988) derived the following relationship between the ratio of 25 and 12 $\mu$ m *IRAS* photometry fluxes and the observed mass loss rates, from CO and OH observations.

$$\dot{M}_{25/12} = \frac{AL(F_{25}/F_{12})^{\alpha}}{v_{15}} \quad (3.7)$$

where  $\dot{M}_{25/12}$  is in  $M_{\odot}/\text{yr}$ ; L is in  $10^4 L_{\odot}$  and  $v_{15}$  is in unit of 15 km/s;  $A=7 \times 10^{-6}$  and  $\alpha=3$ . Essentially, this relation equates the momentum in the outflow with the momentum of the absorbed photons (eqn 3.3), and replaces the dust optical depth in the above equation

with the  $F_{25}/F_{12}$  ratio. This relationship is compared in Figure 3.3, with mass loss rates derived from our detailed model fits, assuming a dust-to-gas ratio of  $4 \times 10^{-3}$ .

In order to theoretically underpin this relationship, a set of models has been constructed here using the same set of input parameters, but with various mass loss rates. The results are shown in Figure 3.3 as the solid curve. The calculated relation shows a concave curvature reflecting the shift of the peak of the Planck function through the *IRAS* 12 and  $25\mu\text{m}$  filters with increasing mass loss rate, i.e., cooler dust temperatures. Nevertheless, except for an offset in the dust-to-gas ratio, equation 3.7 gives a reasonable estimate of the mass loss rate. The best fit to our results for dust mass loss rates is given by  $A=1.8 \times 10^{-7}$ ;  $\alpha=4.96$  for  $F_{25}/F_{12} < 0.85$  and  $A=1.2 \times 10^{-7}$ ;  $\alpha=2.37$  for  $F_{25}/F_{12} > 0.85$ . The corresponding relation for the gas mass loss rate will depend on the assumed dust-to-gas ratio.

The source Z Cyg and, to a lesser extent, R Hor form an exception to the general relationship displayed in Figure 3.3, reflecting their extremely low outflow velocity (Table 3.1). Apparently, this results from a breakdown in equation 3.3 for these objects, as illustrated in Figure 3.4. Possibly, the dust and gas do not couple well with each other in objects with such low outflow velocities as Z Cyg and R Hor (i.e., large dust drift velocity). In view of the general low outflow velocity ( $\leq 4\text{km/s}$ ) of "short" period Miras (P  $\leq 400^d$ ; Sivagnanam et al. 1989), this may form a common problem for such objects, and the use of equation 3.7 in deriving their mass loss rate should be discouraged.

Using the expression for AGB stars, the absolute bolometric magnitude can be written as (Fox & Wood 1982)

$$\begin{aligned} M_{bol} &= 38 \log T_{eff} - 138.5 \\ &= 4.75 - 2.5 \log \frac{L}{L_{odot}} \end{aligned} \quad (3.8)$$

Together with the dust mass loss rates, and the observed photometric  $60\mu\text{m}$  flux, we obtain

$$4\pi D^2 S_\nu = \int Q_\nu B_\nu(T_d) 4\pi a^2 n_d(r) 4\pi r_d^2 dr_d \quad (3.9)$$

where  $r_d$  is the radius where dust forms. With the assumption that the circumstellar shell is optically thin at long wavelengths, Herman et al. (1986) derived the relationship between the  $60\mu\text{m}$  flux and the dust mass loss rate, as

$$\dot{M}_{60\mu\text{m}} = \eta_{60} F_{60} D^2 L^{-0.467} v_e \frac{240.0}{\kappa} \quad (3.10)$$

Figure 3.3: Dust mass loss rates obtained from modelling, corrected for velocity and luminosity, as a function of ratio of fluxes at 25 and 12 $\mu$ m. Solid line is from the same size stars with increasing mass loss rates. Dashed line is calculated from equation 3.7.

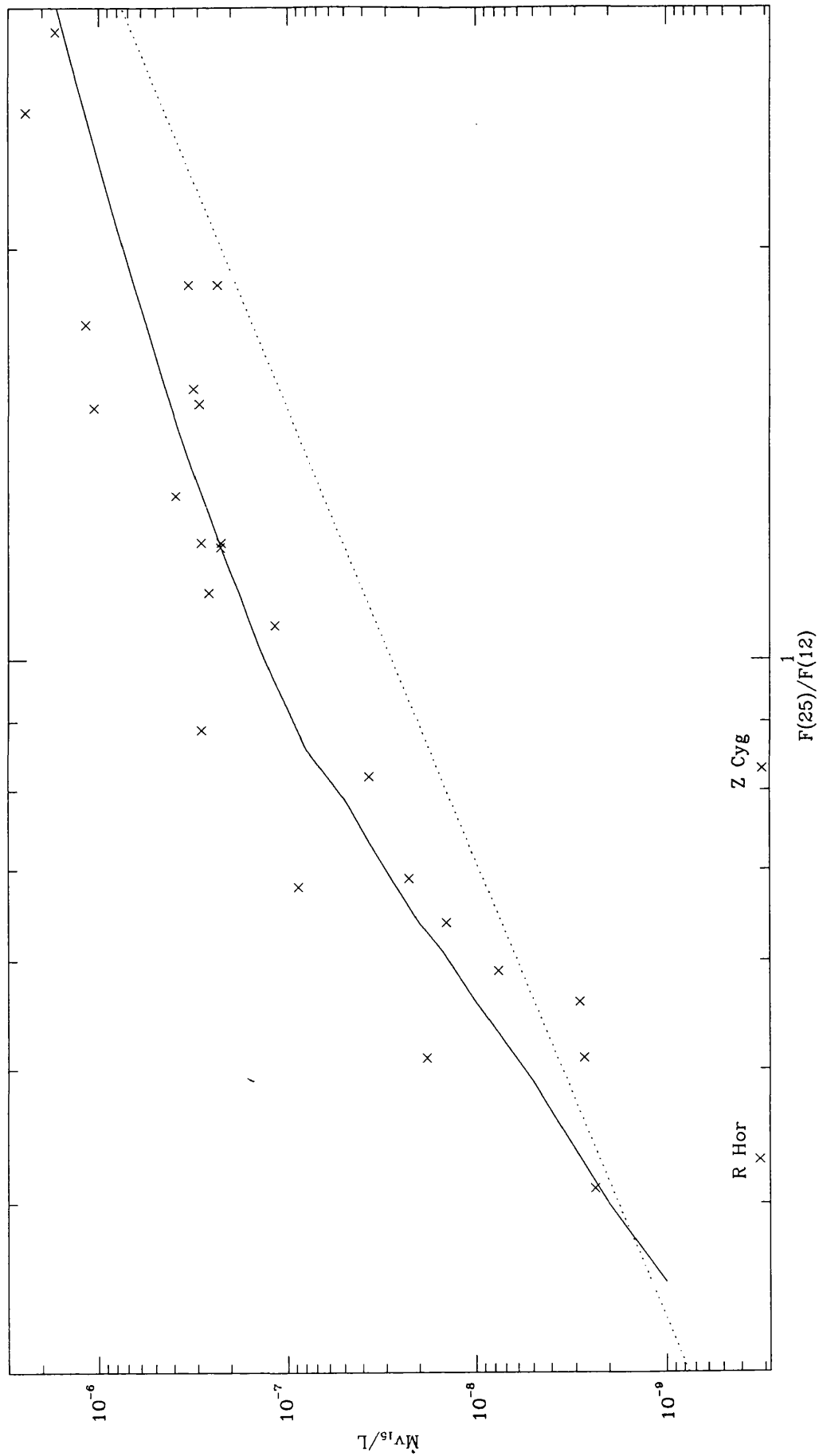


Figure 3.4: A plot of mass loss rate, corrected for velocity and luminosity, as a function of  $9.7\mu\text{m}$  optical depth. The solid line is from the running models with increasing mass loss rates. The relationship is expected to follow a straight line with a slope of  $1/c$  for radiatively driven wind.

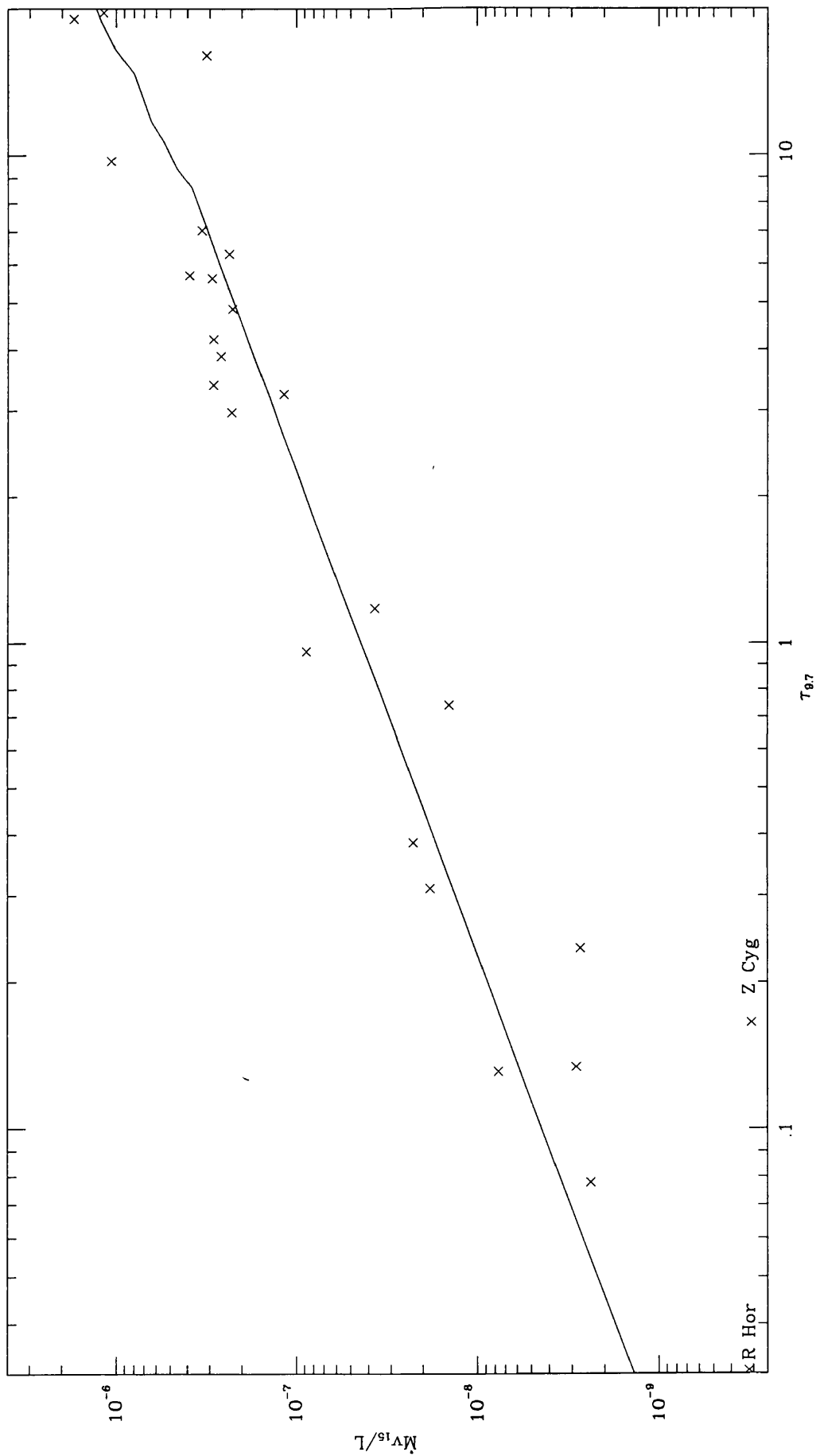
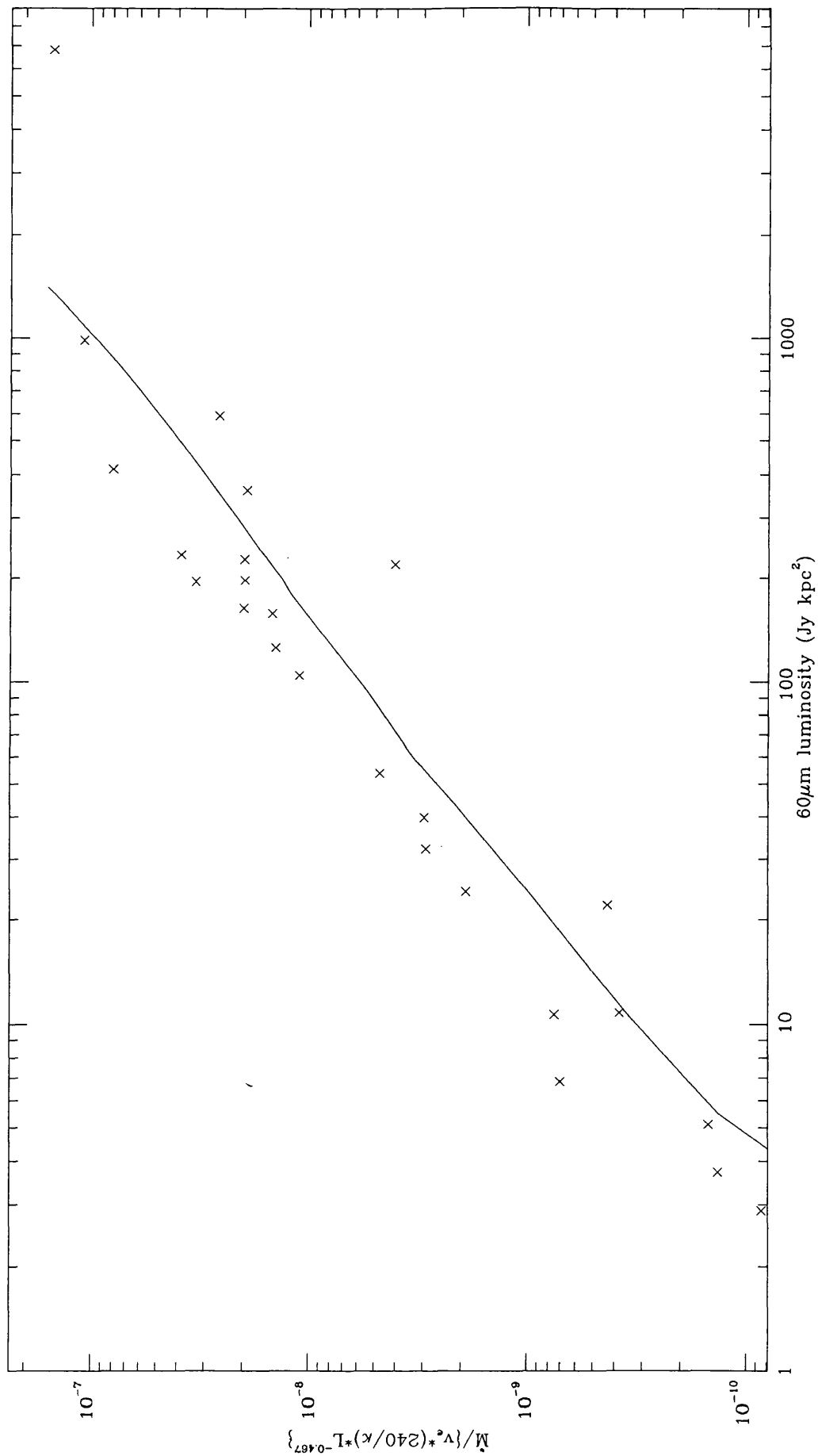


Figure 3.5: Comparison of dust mass loss rates obtained from infrared modelling, corrected for expansion velocity, dust opacity and luminosity, as a function of  $60\mu\text{m}$  luminosity. The solid line is for models of the same stars but with increasing mass loss rates.



where  $\dot{M}_{60\mu\text{m}}$  is in  $M_{\odot}/\text{yr}$ ;  $\eta_{60}=4.397\times 10^{-11}$ ;  $F_{60}$  is the *IRAS*  $60\mu\text{m}$  flux in Jy, using a power law colour correction (*IRAS* Explanatory Supplement);  $D$  is the distance in kpc;  $L$  is the luminosity in  $10^4 L_{\odot}$ ;  $v_e$  is the expansion velocity in km/s; and  $\kappa$  is the dust opacity at  $60\mu\text{m}$ .

Figure 3.5 compares the mass loss rates determined from our detailed model fits with the  $60\mu\text{m}$  luminosity. These mass loss rates have been scaled by the appropriate outflow velocity, stellar luminosity and  $60\mu\text{m}$  dust opacity. For the latter, recall that all stars with far-infrared index,  $p$  (equation 2.30), of 1.0 and 1.5 have the  $60\mu\text{m}$  opacities of  $240\text{ cm}^2/\text{g}$  and  $160\text{ cm}^2/\text{g}$ , respectively. In general, there is a tight relationship between dust mass loss rate and  $60\mu\text{m}$  luminosity. However, this relationship is somewhat steeper than indicated by equation 3.10. Essentially, this reflects the breakdown of the optically thin approximation, which forms the basis of the above equation. The solid line in Figure 3.5 represents the results of a series of models in which the total dust column density was varied. It follows that the mass loss rate determined by our detailed model fits very well. The scatter represents the accuracy of those model fits to the observed  $60\mu\text{m}$  fluxes. A better representation of the relation is

$$\dot{M}_{60\mu\text{m}} = \eta_{60, \text{new}} (F_{60} D^2)^{1.26} L^{-0.467} v_e \frac{240.0}{\kappa} \quad (3.11)$$

where  $\eta_{60, \text{new}}=1.63\times 10^{-11}$ . The derived dust mass loss rates from detailed model fits, and those directly derived from the *IRAS*  $60\mu\text{m}$  fluxes, using a new constant, are in good agreement when the appropriate  $60\mu\text{m}$  dust opacity is taken into account. Figure 3.5 shows a turnover point for very low dust mass loss rates. By extrapolation of the model (solid) curve, it is found that  $60\mu\text{m}$  luminosity becomes a constant, which is expected since this is the stellar contribution, unattenuated by dust. Table 3.2 shows the derived dust mass loss rates from various methods discussed above. In most cases,  $\dot{M}_{F_{25}/F_{12}}$  and  $\dot{M}_{60\mu\text{m}}$  agree to within a factor of two to those derived from the modelling of the infrared energy distributions.

### 3.3.2 Gas mass loss rates

In the previous section, mass loss rates estimated are those of dust grains. Here, gas mass loss rates are calculated using the work based on existing literature, but scaled to the distances listed in Table 3.1. These values can be directly compared to the dust mass loss rates, provided that the dust-to-gas mass ratio is known in these stars.

Gas mass loss rates can be determined from OH maser observations. It has been shown that OH masers are saturated and radiatively pumped (Harvey et al. 1974). Pumping is done by  $35\mu\text{m}$  photons emitted by dust in the outflow (Elitzur et al. 1976). The OH maser luminosity is proportional to the pump rate, i.e., the  $35\mu\text{m}$  luminosity. Since the latter depends mainly on the dust mass loss rate, the OH luminosity should be well correlated with the dust mass loss rate. Such correlation is well supported by airborne and space based observations (Werner et al. 1980; Herman & Habing 1985; Herman et al. 1986; Sivagnaman et al. 1989). The absolute relation to the mass loss rate is less well established, however.

The main disadvantage for this method is that only O-rich stars have OH masers, because all the available carbon is bounded up into CO molecules. There is a simple relationship between the size of the emitting region,  $R_{OH}$ , and the mass loss rate, as derived by Bowers et. al. (1983)

$$\dot{M} = 7.88 \times 10^{-7} \left( \frac{R_{OH}}{10^{16} \text{ cm}} \right)^{1.4} v^{0.6} \quad (3.12)$$

With the relationship between the luminosity and the size of the emitting region,  $S_{OH} D^2 \sim R_{OH}^2$ , Baud & Habing (1983) derived the following expression for the gas mass loss rate

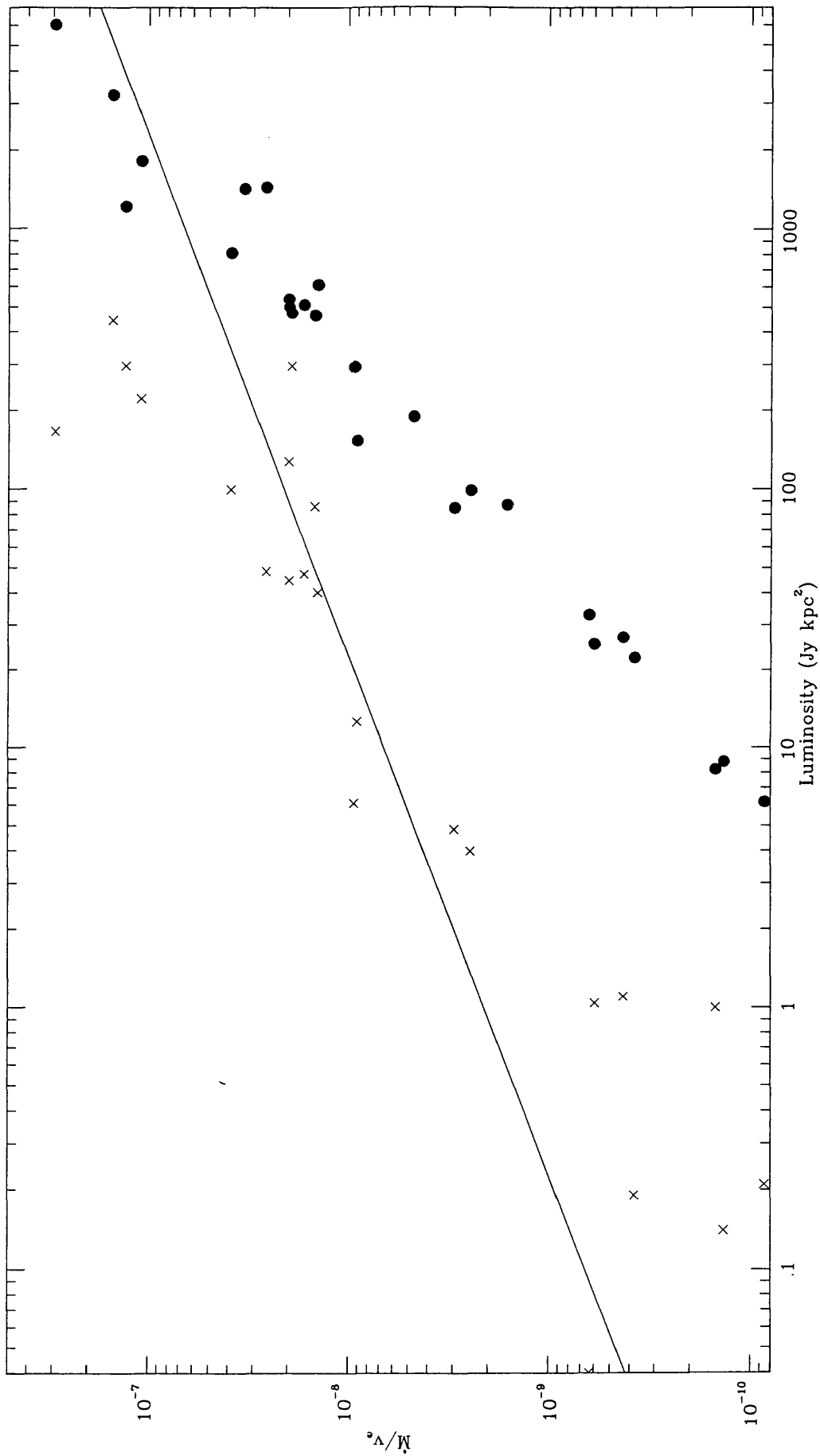
$$\dot{M}_{OH} = 2 \times 10^{-7} v_e S_{OH}^{0.5} D \frac{1.6 \times 10^{-4}}{f_{OH}} \quad (3.13)$$

where  $S_{OH}$  is the geometric mean flux of the two OH peaks in Jy; and D is the distance in kpc.

The observed OH luminosity (e.g., te Lintel Hekkert et al. 1989) and the  $35\mu\text{m}$  luminosity ( $F_{35} D^2$ ), derived from our model fits, to the *IRAS* observations are compared to the dust mass loss rate in Figure 3.6. There is clearly a good correlation over 3 orders of magnitude. The scatter in the  $35\mu\text{m}$  luminosity merely reflects the quality of our model fits to the far-infrared data. The much larger scattering in the OH luminosity correlation may represent temporal variations, which can be as large as a factor of two. The derived efficiency of the OH maser pump is about 0.3 for the higher mass loss rate, and seems to decrease with the mass loss rate (see also Herman et al. 1986). From our models, we derive the following relation between the dust mass loss rate and the OH luminosity, assuming dust-to-gas ratio of  $5 \times 10^{-3}$

$$\dot{M}_{OH} = 1.86 \times 10^{-7} v_e L_{OH}^{0.78} \frac{1.6 \times 10^{-4}}{f_{OH}} \quad (3.14)$$

Figure 3.6: A plot of mass loss rate corrected for velocity as a function of OH (crosses) and  $35\mu\text{m}$  (solid) luminosity. The solid line is mass loss rate given by Baud & Habing relation, assuming dust-to-gas ratio of  $5 \times 10^{-3}$ . For the OH mass loss rate, OH abundance is assumed to be  $1.6 \times 10^{-4}$  (equation 3.13). The mass loss rates derived from  $35\mu\text{m}$  luminosity,  $L$  is assumed to be  $10^4$  and  $\kappa_{35}$  is assumed to be 418 (cf. equation 3.9). Values of OH fluxes were taken from Epchtein et al. (1980); Baud & Habing (1983); te Lintel Heckert et al. (1989); van der Veen & Ruger (1989).



where  $L_{OH}$  is the OH luminosity in Jy kpc<sup>2</sup>;  $v_e$  is the outflow velocity in km/s; and  $f_{OH}$  is the OH abundance, in this case, assumed to be  $1.6 \times 10^{-4}$ . There is a considerable difference between our derived relation and those calculated by Baud & Habing (1983). They noted empirically that OH masers have approximately constant surface brightness, and assumed that the OH column density is constant and equals to the minimum value required for saturation (i.e.,  $N(OH) = 10^{17} \text{ cm}^{-2}$ , corresponding to  $N(H_2) = 6 \times 10^{20} \text{ cm}^{-2}$ ). Theoretically, the OH column density is set by the penetration depth of ambient UV photons, and is approximately constant over the relevant parameter space (Huggins & Glassgold 1982; Netzer & Knapp 1987).

The OH mass loss rates calculated using equation 3.14 are shown in Figure 3.6, assuming a dust-to-gas ratio of  $5 \times 10^{-3}$ . The discrepancy between these two mass loss determinations was noted earlier and (indirectly) was ascribed to the variations in the dust-to-gas ratio (Herman et al. 1986). From our results, this would imply that the ratio varies from 0.001 for optically visible Miras to 0.07 for heavily obscured OH/IR stars. The latter value is actually much larger than expected for silicate condensation in gas with the solar elemental composition ( $\sim 0.006$  for  $MgFeSiO_4$ ). Possibly, this is related to the onset of the superwind at the tip of the AGB. The dust mass loss rates determined from the infrared refer to the inner ( $\sim 3 \times 10^{14} \text{ cm}$ ) part of the envelope, where most of the opacity occurs. In contrast, the OH maser is located around a few  $10^{16} \text{ cm}$ . Thus, while the OH emission relates to material ejected about  $2 \times 10^3 \text{ yrs}$  ago, the infrared flux pertains to more recent ( $< 10^2 \text{ yr}$ ) ejecta.

Carbon monoxide is a common gaseous component of the circumstellar shells for both C- and O-rich stars, which makes it a powerful probe for mass loss rates. The structure of the molecule is simple enough for detailed studies of the rotational and vibrational transitions to be carried out. However, modelling CO profiles using different observational transitions can give results which differ by a factor of two to ten (see results from Knapp et al 1982; Knapp & Morris 1985; Heske et al. 1990). Clearly, a better model is required in order to get more accurate gas mass loss rates.

Mass loss rates from CO observations are taken from Knapp & Morris (1985) who observed stars in CO(J=1-0) transition. The mass loss rate for a star with optically thick CO line profile (parabolic shape, Morris 1975) is given by

$$\dot{M}_{CO} = 5 \times 10^{-14} T_A v_{CO}^2 f_{CO}^{-0.85} D^2 \theta^2 \quad (3.15)$$

where  $\dot{M}_{CO}$  is in  $M_{\odot}/\text{yr}$ ;  $T_A$  is the antenna temperature in K;  $v_{CO}$  is the CO outflow velocity in km/s;  $f_{CO}$  is the CO abundance;  $D$  is the distance in kpc and  $\theta$  is half-power beamwidth of the telescope in arcsec. For oxygen-rich stars, a CO abundance of  $3 \times 10^{-4}$  is appropriate.

CO mass loss rates, scaled to the appropriate distance and velocities, are compared to the dust mass loss rates in Figure 3.7. While for stars with low mass loss rates (i.e., Miras), the two are in agreement with dust a dust-to-gas ratio of 0.003, a much larger ratio (0.08–0.2) is obtained for optically thick OH/IR stars. This is not physically realistic, and instead, we attribute this discrepancy to the extremely low CO excitation temperature expected in such envelopes (Heske et al. 1990) and the consequent breakdown of equation 3.15. As for OH, the CO emission originates from far out in the envelope. Thus some of the difference between the derived dust and CO mass loss rates may indicate evolution of the mass loss rate (Baud & Habing 1983).

Other observable maser lines do not yield accurate mass loss rates. In the case of SiO masers, their luminosities are independent of mass loss rates (Jewell et al. 1984). There is, however, a weak correlation between  $\text{H}_2\text{O}$  maser luminosities and mass loss rates (Engels & Lewis 1989). This is unfortunate, since mass loss rates derived from these lines represent more recent ejection of mass from the central stars than do those derived from CO and OH maser.

Figure 3.7: Comparison of CO and dust mass loss rates. Solid line is for constant dust-to-gas ratio of  $5 \times 10^{-3}$ .

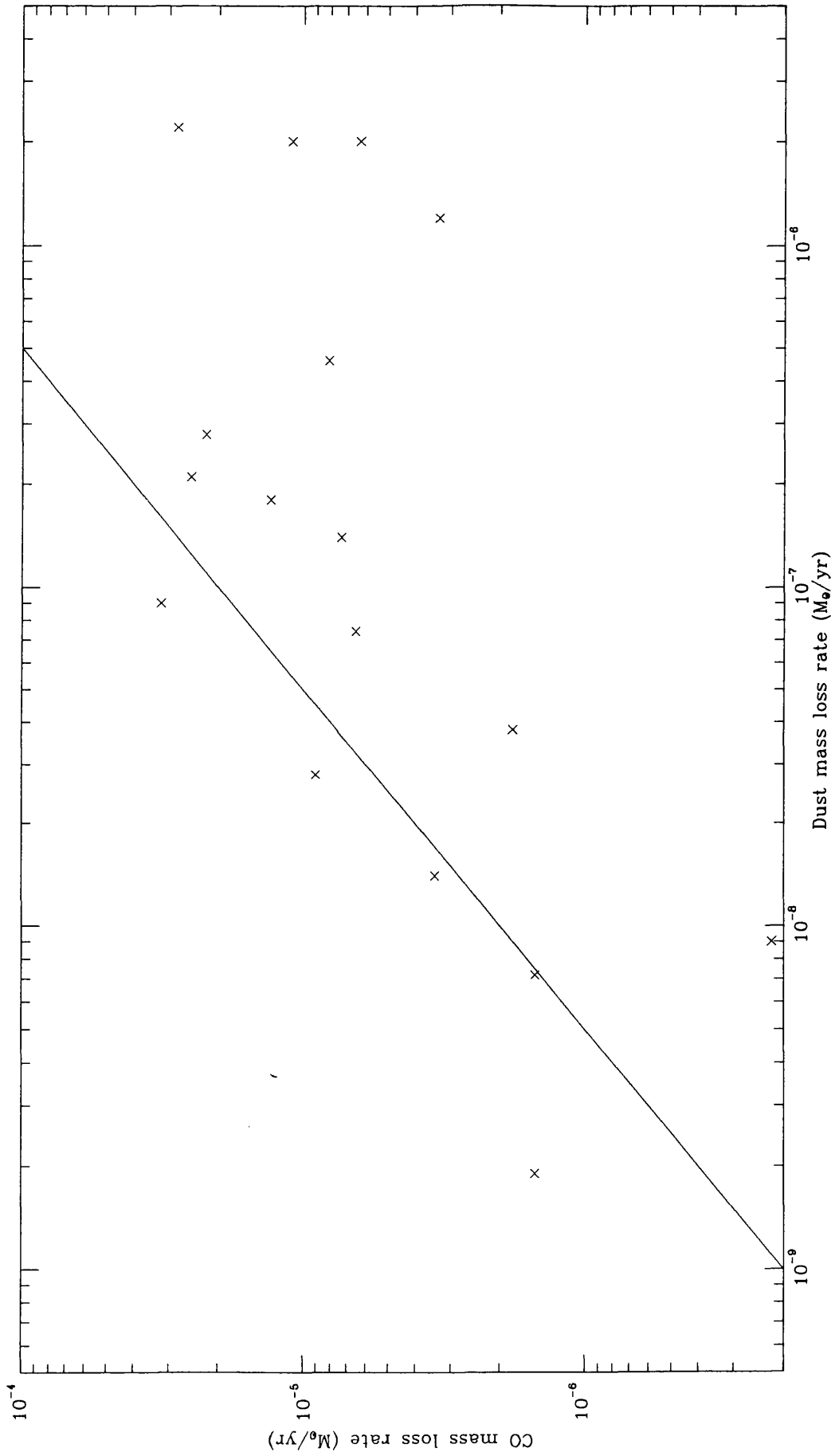


Table 3.1: Input parameters for radiative transfer calculations.

Sources	D (kpc)	T <sub>*</sub> (K)	R <sub>*</sub> (cm)	$\dot{M}_d$ (M <sub>⊙</sub> /yr)	v <sub>e</sub> (km/s)	r <sub>o</sub> (cm)	τ <sub>9.7</sub>	p <sup>(a)</sup>
AFGL 1822	1.80	2000	5.7E+13	2.6E-07	12.9	2.5E+14	6.29	1.0
AFGL 2199	1.60	1800	9.0E+13	1.8E-07	15.0	2.9E+14	3.24	1.0
AFGL 230	2.80	2000	1.4E+14	2.0E-06	12.7	7.8E+14	16.0	1.5
AFGL 2362	2.05	2000	5.5E+13	2.1E-07	17.9	2.2E+14	4.20	1.5
GX Mon	0.50	2500	4.0E+13	7.2E-09	17.5	2.5E+14	0.13	1.0
IRAS 16105	0.80	2000	6.6E+13	4.6E-07	15.0	2.9E+14	5.68	1.0
IRC+10011	0.5	2000	4.5E+13	1.4e-07	18.15	1.8E+14	3.38	1.5
IRC+10322	0.60	2000	4.8E+13	1.4E-08	15.0	1.9E+14	0.39	1.5
IRC+10523	1.10	2300	4.3E+13	4.0E-09	10.4	2.3E+14	0.13	1.0
IRC-20197	0.78	2250	4.2E+13	3.8E-08	12.0	2.1E+14	1.18	1.5
IRC+40004	1.10	2000	8.6E+13	9.0E-08	24.2	3.1E+14	0.96	1.0
IRC+50137	0.82	1850	3.9E+13	7.4E-08	14.7	1.3E+14	2.97	1.0
IRC+70066	0.80	2200	7.0E+13	2.8E-08	21.1	3.4E+14	0.31	1.5
OH1.1-0.8	1.20	2000	6.5E+13	2.5E-07	19.5	2.6E+14	3.88	1.0
OH26.5+0.6	0.98	2200	5.0E+13	1.2E-06	15.4	3.1E+14	19.6	1.0
OH30.1-0.7	2.1	2000	6.3E+13	2.0E-06	18.1	3.5E+14	20.7	1.0
OH32.8-0.3	4.30	2000	7.6E+13	2.2E-06	17.7	4.2E+14	19.0	1.0
OH343.4+1.3	3.50	2000	6.1E+13	8.0E-07	21.5	3.0E+14	9.71	1.0
OH39.9-0.0	5.50	2000	5.5E+13	3.0E-07	14.6	2.3E+14	7.02	1.0
OH44.8-2.3	2.41	2000	6.9E+13	2.8E-07	16.5	2.8E+14	4.85	1.5
OH65.4+1.3	6.00	2000	6.4E+13	3.1E-07	17.0	2.6E+14	5.61	1.0
R Cas	0.216	2100	4.0E+13	1.9E-09	11.0	1.8E+14	0.08	1.0
R Hor	0.265	2500	3.5E+13	6.2E-10	7.0	2.2E+14	0.03	1.0
VX Sgr	1.70	2500	2.5E+14	8.8E-08	19.7	1.5E+15	0.24	1.0
WX Ser	0.72	1900	3.6E+13	9.0E-09	7.4	1.3E+14	0.74	1.5
Z Cyg	0.718	2500	2.0E+13	6.0E-10	2.3	1.3E+14	0.17	1.0

(a) The far-infrared extinction efficiency is assumed to be given by

$$Q(\text{ext}) \propto \lambda^{-p}$$

Table 3.2: Mass loss estimates from various methods

Sources	$\dot{M}_{gas}$		$\dot{M}_{dust}$		
	$\dot{M}_{CO}$	$\dot{M}_{OH}$	$\dot{M}_{F25/F12}$	$\dot{M}_{60\mu m}$	$\dot{M}_d$
AFGL1822		1.5E-05	5.9E-07	2.0E-07	2.6E-07
AFGL2199	1.3E-05		2.1E-07	1.2E-07	1.8E-07
AFGL230	1.1E-05	2.9E-05	2.2E-06	1.3E-06	2.0E-06
AFGL2362	2.5E-05	8.0E-06	1.4E-07	1.7E-07	2.1E-07
GX Mon	1.5E-06	3.3E-06	1.3E-08	1.4E-08	7.2E-09
IRAS16105	8.1E-06		2.7E-07	1.8E-07 <sup>(a)</sup>	4.6E-07
IRC+10011	7.3E-06	9.1E-06	4.4E-08	6.5E-07	1.4E-07
IRC+10322	3.4E-06	5.1E-07	1.8E-08	9.2E-09	1.4E-08
IRC+10523		8.2E-07	1.4E-08	3.5E-09	4.0E-09
IRC-20197	1.8E-06	4.3E-06	7.1E-08	2.6E-08	3.8E-08
IRC+40004	3.2E-05		2.8E-08	4.8E-08	9.0E-08
IRC+50137	6.5E-06	5.8E-06	6.1E-08	4.3E-08	7.4E-08
IRC+70066	9.0E-06		9.9E-09	2.0E-08	2.8E-08
OH1.1-0.8		2.2E-05	1.5E-07	1.3E-07	2.5E-07
OH26.5+0.6	4.6E-05	4.8E-05	4.7E-07	3.0E-07	1.2E-06
OH30.1-07	6.3E-06	3.1E-05	8.7E-08	1.2E-05 <sup>(a)</sup>	2.0E-06
OH32.8-0.3	2.8E-05	6.7E-05	1.9E-06	1.7E-05 <sup>(a)</sup>	2.2E-06
OH343.4+1.3		3.9E-05	2.5E-07	3.3E-07	8.0E-07
OH39.9-0.0		4.5E-05	4.8E-07	4.3E-07	3.0E-07
OH44.8-2.3	2.2E-05	2.0E-05	2.4E-07	1.8E-07	2.8E-07
OH65.4+1.3		3.5E-05	3.5E-07	1.6E-07	3.1E-07
R Cas	7.0E-07	7.5E-07	1.8E-09	1.2E-09 <sup>(c)</sup>	1.9E-09
R Hor		7.2E-07	5.4E-09 <sup>(b)</sup>	4.6E-10 <sup>(c)</sup>	6.2E-10
VX Sgr		3.8E-05	2.1E-07	1.8E-07	8.8E-08
WX Ser	2.2E-07	1.4E-06	1.3E-08	3.6E-09	9.0E-09
Z Cyg		4.2E-07	1.4E-07 <sup>(b)</sup>	5.2E-10	6.0E-10

(a) – 60 $\mu$ m flux is dominated by ice emission. Dust mass loss rate determined from 60 $\mu$ m flux is unreliable.

(b) – dust and gas are not well coupled in these objects. Dust mass loss rate determined from this method is unreliable.

(c) – the 60 $\mu$ m flux is dominated by the star. Dust mass loss rate determined from the 60 $\mu$ m flux is unreliable.

## Chapter 4

# Heating and Cooling in Circumstellar Envelopes of Late-type Stars

The work presented in this chapter involves the study of the gas kinetic temperatures in circumstellar shells of O-rich stars. In order to obtain the temperature structure of the envelope, the main heating and cooling processes operating in it must be taken into account. Various authors have considered the temperature structure of late type stars but have mainly concentrated on C-rich objects. In these stars, CO is the molecule mainly responsible for the radiative cooling. Since CO is a linear molecule with a rather simple rotational spectrum, the calculation of the cooling rate is quite well determined (see e.g., Kwan & Hill 1976; Hollenbach & McKee 1979; Kwan & Linke 1982). However, for O-rich stars, H<sub>2</sub>O, which has extremely complicated vibrational and rotational transitions, is abundant, and is much more efficient in cooling than CO. In view of this, it is expected that temperature structures for O-rich stars differ from those for C-rich stars. Goldreich & Scoville (1976, hereafter, GS) have made a theoretical study of heating and cooling in the circumstellar envelope of the OH/IR star, IRC+10011, which is the basis of our study. Following their formulation, we obtain the temperature structure of O-rich stars as a function of the physical parameters of the flow. Basically, in order to obtain the temperature distribution, we need to solve the equations of motion of the gas and the energy balance simultaneously, since velocity is coupled to the temperature (Tielens 1983).

## 4.1 The gas dynamics

In this section, the equations of motion of gas and momentum transfer between gas and dust are derived, based on work by GS and Tielens (1983). Main assumptions in the calculation are that mass loss is spherically symmetric and the outflow is constant. These lead to the continuity equation

$$\dot{M} = 4\pi r^2 \rho(r) v(r) \quad (4.1)$$

where  $r$  is the distance from the central star;  $\rho(r)$  and  $v(r)$  are the gas density and outflow velocity at that radius. It is also assumed that the outflow is driven by radiation pressure on the dust formed at the radius where the dust temperature falls below the condensation temperature (1000K for silicates). It is known that AGB stars undergo long period radial pulsation. As discussed in chapter 1, this will cause materials to be lifted up and cool as it moves away from the central star, until the temperature is low enough for dust grains to condense out. Since cross sections of dust are much larger than those for gas, dust gains more momentum and is driven outwards, with the gas being dragged along with it. Due to frequent collisions between the gas molecules, the momentum gained from collisions between dust and gas is redistributed. Dust and gas are said to be momentum coupled (Gilman 1972). The equation of motion of the gaseous ejecta in this scheme, ignoring the thermal pressure gradient, can be written as

$$v \frac{dv}{dr} = \frac{\kappa(r)L}{4\pi r^2 c} - \frac{GM_*}{r^2} \quad (4.2)$$

where  $L$  is the stellar luminosity;  $G$  is the gravitational constant;  $M_*$  is the stellar mass; and  $\kappa(r)$  is the opacity per unit mass of gas.

$$\kappa(r) = \frac{Q n_d \sigma_d}{m_{H_2} n_{H_2} (1 + f/2)} \quad (4.3)$$

where  $n_d$  is the dust number density;  $\sigma_d$  is the geometric cross section of dust;  $Q$  is the flux weighted momentum transfer efficiency factor; and  $f$  is the ratio of the number of atomic to molecular hydrogen. From an observation of IRC+10011 during a lunar occultation by Zappala et al. (1974), GS assumed  $\kappa(r)$  to be

$$\kappa(r) = \gamma \left( 1 + \frac{\Delta r^2}{(10R)^2 + r^2} \right) \quad (4.4)$$

where  $R$  is the stellar radius. Here, all the grain size parameters are hidden in the  $\kappa$  term. Essentially, this assumption leads to an extended region with a size of  $\sim \Delta R$  in which the

gas is accelerated to its terminal velocity. However, recent infrared observations (Danchi et al. 1990; Bester 1991) have shown that dust forms reasonably close to the stellar photosphere. Moreover, theoretical studies show that once radiation pressure becomes important, acceleration of the flow is instantaneous and  $\Delta$  is much smaller than assumed by GS (c.f., Kwok 1976; Tielens 1983). In order to get a more general picture, we need to consider the more general formalism for the velocity structure. We therefore write the equation of motion of the gas as

$$v \frac{dv}{dr} = (\Gamma - 1) \frac{GM_*}{r^2} \quad (4.5)$$

where  $\Gamma$  is now defined as the ratio of the radiation pressure on the dust to the gravitational force. With the MRN grain size distribution and silicate efficiencies for each grain radius (see chapter 2), the expression for  $\Gamma$ , given by Tielens (1983), can now be written as

$$\Gamma = \int \int \frac{\sigma_d Q(a, \lambda) L(\lambda) n_d(a)}{4\pi c GM_* \rho} d\lambda da \quad (4.6)$$

where  $Q(a, \lambda)$  is the radiation pressure efficiency for grains of radius  $a$  at wavelength  $\lambda$ ;  $n_d(a)$  is the dust number density; and  $\rho$  is the gas density. Here, for O-rich stars, silicate optical constants, used to model the energy distributions in chapter 3, are used to calculate the radiation pressure efficiencies. The dust mass loss rates obtained from chapter 3 also enter the velocity calculation via the dust number density. The total dust mass loss rate can be written as the sum of the dust mass loss rate for each grain size,  $\dot{M}(a)$

$$\begin{aligned} \dot{M}_d &= \int \dot{M}(a) da \\ &= \int n_d(a) \frac{4}{3} \pi a^3 \rho_s 4\pi r^2 (v + v_{drift}) da \end{aligned} \quad (4.7)$$

where  $n_d(a)$  is assumed to be given by the MRN grain size distribution ( $= Aa^{-3.5} n_H$  with  $A$  being a constant and  $n_H$  is the hydrogen density);  $\rho_s$  is the specific density of dust; and  $v_{drift}$  is the drift velocity for the dust grains through the gas. Hence

$$\dot{M}_d = \int Aa^{-3.5} n_H \frac{4}{3} \pi a^3 \rho_s 4\pi r^2 (v + v_{drift}) da \quad (4.8)$$

The drift velocity of a grain of size  $a$  can be calculated by equating the radiation pressure force with the gas drag force. This leads to

$$v_{drift}^2(a) = \int \frac{Q(a, \lambda) L(\lambda) v}{\dot{M} c} d\lambda \quad (4.9)$$

Hence the factor  $\Gamma$  can be written as

$$\begin{aligned}\Gamma &= \int \int \frac{\pi a^2 Q(a, \lambda) L(\lambda)}{4\pi c G M_*} \frac{\dot{M}(a)}{\frac{4}{3} a^3 \rho_s 4\pi r^2 (v + v_{drift})} \frac{4\pi r^2 v}{\dot{M}} d\lambda da \\ &= \frac{3v}{16\pi \rho_s c G M_* \dot{M}} \int \int \frac{Q(\lambda, a) L(\lambda) \dot{M}(a)}{a(v + v_{drift})} d\lambda da\end{aligned}\quad (4.10)$$

where  $\dot{M}$  refers to the gas mass loss rate. The numerical procedure used here is as follows. At the inner radius, where dust condenses out ( $r_i$ ), the gas is assumed to flow with the local sound velocity at the gas temperature,  $T$ . Hence

$$\begin{aligned}v &= c_s(T) \\ &= \left(\frac{5kT}{3\mu m_H}\right)^{0.5}\end{aligned}\quad (4.11)$$

where  $\mu$  is the mean molecular weight. Then, adopting the dust mass loss rates obtained from chapter 3 and assuming the dust-to-gas ratio,  $\delta = \dot{M}_d/\dot{M}$ , the drift velocity and  $\Gamma$  can be calculated from equation 4.9 and 4.10. The momentum equation (4.5) can then be integrated numerically to calculate the gas velocity as a function of radius. The only free parameter in our scheme is the dust-to-gas mass ratio, since the inner radius follows from the infrared modelling in chapter 3, and the gas temperature at that radius has little influence on the velocity structure. The parameter  $\delta$  is varied until the calculated terminal velocity of the gas agrees with the observed value.

## 4.2 Temperature structure of the gas

In order to calculate the gas kinetic temperature as a function of radius, all the major heat sources and sinks must be considered. Here, we include heating by collision between dust and gas, radiative cooling by molecules present in the outflow and the adiabatic expansion.

### 4.2.1 Gas-grain collisional heating

The main heating in the circumstellar envelope is due to collisions between gas and dust grains. The viscous heat input per unit volume due to a grain size  $a$  is

$$H = \frac{1}{2} m_{H_2} n_{H_2} v_{drift}^3(a) n_d(a) \pi a^2 \quad (4.12)$$

Each grain size contributes differently to the heating rate. Although bigger grains have larger radiation pressure efficiencies, there are fewer of them in the outflow following the

$a^{-3.5}$  law. The heating rate can be seen to depend on the mass loss rate and velocity of the outflow. The higher mass loss rate and larger outflow velocity result in the higher heating rate i.e.,  $H \propto \dot{M}^2 v_{drift}^3 = \dot{M}^{0.5} v^{1.5}$ . The final expression of the heating rate can be written as

$$\begin{aligned} H &= \frac{1}{2} m_{H_2} n_{H_2} (1 + f/2) \pi \int a^2 n_d(a) v_{drift}^3(a) da \\ &= \frac{1}{2} m_{H_2} n_{H_2} (1 + f/2) \pi A n_H \int a^{-1.5} v_{drift}^3(a) da \end{aligned} \quad (4.13)$$

where the constant A follows from equation 4.8. Thermal heating by gas-surface collision can be calculated from

$$H_{g-s} = n_d n_H \sigma_d \left( \frac{8kT}{\pi m_H} \right)^{0.5} \alpha_T (2kT - 2kT_d) \quad (4.14)$$

where  $T$  and  $T_d$  refer to the gas and dust temperatures, respectively; and  $\alpha_T$ , is the thermal accommodation coefficient (=0.2, Burke & Hollenbach 1983). This heating arises in energy exchange between gas and dust, but in our case, this is many orders of magnitude smaller than the viscous heating, and is thence ignored.

#### 4.2.2 Rotational excitation of H<sub>2</sub>O molecules

For an O-rich outflow, this mechanism contributes significantly to the cooling of the envelope. On returning to the rotational ground state, rotationally excited H<sub>2</sub>O molecules emit photons, which may escape from the circumstellar shell. This effectively cools the gas. The structure of an H<sub>2</sub>O molecule is complicated, and, following GS, can be approximated to a three-level system, with two effective rotational levels in the vibrational ground state and one rotational level in the first vibrationally excited state. The cooling rate per unit volume between the excited level and the ground level is given by

$$C_1 = n_{H_2O} (1 + f) h\nu n_{H_2O} \langle \sigma^* v_{th} \rangle [exp(-h\nu/kT) - exp(-h\nu/kT_x)] \quad (4.15)$$

where  $T_x$  is the rotational excitation temperature; and  $\langle \sigma^* v_{th} \rangle$  is the collisional rate constant. The excitation temperature can be calculated from the rate equation, using an escape probability formalism to describe the radiative transfer in the line. The rate equation for a three-level system can then be written as (see GS)

$$\begin{aligned} C(H_2O) \frac{h\nu_{21}}{k} \left( \frac{1}{T_x} - \frac{1}{T} \right) &= \beta_{21} A_{21} + \epsilon W A_{31} \left( \frac{h\nu_{21}}{k} \right) exp\left( \frac{-h\nu_{31}}{kT_*} \right) \left( \frac{1}{T_*} - \frac{1}{T_x} \right) \\ XT_x^{1/2} \left( \frac{1}{T_x} - \frac{1}{T} \right) &= \beta_{21} A_{21} + Z T_x^{1/2} \left( \frac{1}{T_*} - \frac{1}{T_x} \right) \end{aligned} \quad (4.16)$$

where  $\nu_{21}$  ( $=1.3 \times 10^{11} T_x^{0.5}$  Hz) and  $\nu_{31}$  ( $=1.13 \times 10^{14}$  Hz) are the transitional frequencies; and  $\epsilon = (d \ln v / d \ln r)$  is the velocity gradient. The collisional rate per second,  $C(\text{H}_2\text{O})$ , is given by

$$C(\text{H}_2\text{O}) = 2 \times 10^{-11} T_x^{0.5} n_{\text{H}_2} (1 + f) \quad (4.17)$$

where  $\beta_{21}$  is the escape probability;  $A_{21}$  is Einstein's A coefficient; and  $W$  is the dilution factor for the stellar radiation. The escape probability is given by

$$\begin{aligned} \beta_{21}(r) A_{21} &= \frac{16\pi v}{3r\lambda_{21}^3(n_1 - n_2)} \left(1 + \frac{\epsilon}{2}\right) \\ &= \frac{16\pi v (1.3 \times 10^{11})^3}{400rc^3 n_{\text{H}_2} h\nu/k} T_x^3 \left(1 + \frac{\epsilon}{2}\right) \\ &= Y T_x^3 \end{aligned} \quad (4.18)$$

By substituting the escape probability into equation 4.16, we get

$$X T_x^{1/2} \left(\frac{1}{T_x} - \frac{1}{T}\right) - Y T_x^3 - Z T_x^{1/2} \left(\frac{1}{T_*} - \frac{1}{T_x}\right) = 0 \quad (4.19)$$

which can easily be solved by the Newton iteration method. It is quite simple to see how all the processes in equation 4.16 affect the rotational excitation temperature of  $\text{H}_2\text{O}$ . The spontaneous emission tends to reduce  $T_x$  to zero while collision tends to thermalise the system so that  $T_x = T$ . At the same time, the absorption of the near-infrared photons will make  $T_x = T_*$ . Note that in the inner part of the envelope, where  $T < T_x$ ,  $C_1$  becomes negative, i.e., absorption of the near-infrared photons followed by collisional de-excitation results in the heating of the gas.

### 4.2.3 Vibrational excitation of $\text{H}_2\text{O}$ molecules

In view of the high critical density, collisional excitation followed by radiative decay of vibrational levels of  $\text{H}_2\text{O}$  is unimportant, for the cooling of the gas and can safely be ignored. GS incorrectly identify the reaction  $\text{OH} + \text{H}_2 \rightarrow \text{H}_2\text{O} + \text{H} + 0.67\text{eV}$  as a cooling term for the gas. This reaction is actually exothermic in the forward direction. It leaves  $\text{H}_2\text{O}$  in a vibrational excited state (Schatz & Elgersma 1980). While this vibrational fraction ( $\sim 56\%$ ) of the excess chemical energy is lost through radiative cooling, about 35% of the total energy is converted to translational energy which heats the gas. The remainder goes into rotational excitation. After taking the activation barrier ( $\sim 0.27\text{eV}$ ) into account, the net heating of the gas is about 0.1eV per reaction. Comparison with other heating sources, this is small and is neglected in the future calculations.

The reverse reaction is endothermic and thus leads to cooling of the gas. However, its rate is dependent on the vibrational excitation of H<sub>2</sub>O. Since the forward reaction leads to vibrational excitation, the reverse reaction requires vibrationally excited H<sub>2</sub>O from detailed balance. This is borne out by detailed calculations, which show that the reverse rate is reduced by a factor of 100 for H<sub>2</sub>O in v=0 level (Herbst & Knudson 1981). As a result, in the envelope where the density is below the critical density for H<sub>2</sub>O, the reverse reaction is frozen out and consequently plays no role in the energy balance. Finally, we note that near the photosphere where H<sub>2</sub>O is in LTE, the forward and backward reactions do not lead to significant net heating or cooling of the envelope.

#### 4.2.4 Vibrational excitation of H<sub>2</sub> molecules

The cooling by H<sub>2</sub> molecules must be treated differently from H<sub>2</sub>O molecules, because they lack a dipole moment and the energy levels are widely spaced. Due to their low Einstein A values, the lines are optically thin. Moreover, H<sub>2</sub> is in LTE through a larger part of the envelope. The large energy spacing allows us to consider only the ground and the first vibrationally excited level. The molecules are excited by collision with themselves and with H atoms. The heat loss per unit volume is

$$C_2 = A_{1,0} h\nu_{1,0} n_1 \quad (4.20)$$

where  $A_{1,0}$  is the spontaneous emission rate from the first vibrationally excited state;  $h\nu_{1,0}$  is the energy of the emitted photon; and  $n_1$  is the number density of vibrationally excited H<sub>2</sub> molecules. The latter follows from the rate equation, so

$$n_1 = n_{H_2} \frac{(n_H \langle \sigma^* v_{th} \rangle_H + n_{H_2} \langle \sigma^* v_{th} \rangle_{H_2}) \exp(-h\nu_{1,0}/kT)}{(n_H \langle \sigma^* v_{th} \rangle_H + n_{H_2} \langle \sigma^* v_{th} \rangle_{H_2}) [1 + \exp(-h\nu_{1,0}/kT)] + A_{1,0}} \quad (4.21)$$

where  $\langle \sigma^* v_{th} \rangle_H$  and  $\langle \sigma^* v_{th} \rangle_{H_2}$  are the de-excitation rate constants for collision of vibrationally excited H<sub>2</sub> molecules with H atoms, and H<sub>2</sub> molecules, respectively. In a high density regime, this reduces to the Boltzmann distribution.

#### 4.2.5 Rotational excitation of CO molecules

Another molecule which is always present in the circumstellar envelope is CO. GS ignored its cooling effect, but we include it here to see how it affects the temperature of O-rich stars. Similar to the calculation for H<sub>2</sub>O rotational cooling, the formulation for CO

rotational cooling is given by

$$C_3 = n_{H_2}(1+f)n_{CO} \langle \sigma^* v_{th} \rangle h\nu \left[ \exp\left(-\frac{h\nu_{21}}{kT}\right) - \exp\left(-\frac{h\nu_{21}}{kT_x}\right) \right] \quad (4.22)$$

where  $T_x$  is excitation temperature for CO molecules, which can be defined in a similar manner to equation 4.16. However, since CO is a diatomic molecule, the values for each parameters entering in the calculation of the excitation temperature will differ from those for H<sub>2</sub>O, due to the differing  $Z_{rot}$ , the rotational partition function. The frequency  $\nu_{21} = 4.89 \times 10^{10} T_x^{0.5}$  Hz. The collisional rate is given by

$$C(CO) = 10^{-11} T_x^{0.5} n_{H_2} (1+f) \quad (4.23)$$

The escape probability for CO molecules is then

$$\begin{aligned} \beta_{21} A_{21} &= \frac{16\pi v (4.89 \times 10^{10})^3}{33.08 r c^3 n_{CO}} T_x^{5/2} (1 + \epsilon/2) \\ &= Y' T_x^{5/2} \end{aligned} \quad (4.24)$$

Hence the equation for the excitation temperature can be written as

$$\begin{aligned} C(CO) \frac{h\nu_{21}}{k} \left( \frac{1}{T_x} - \frac{1}{T} \right) &= \beta_{21} A_{21} + \epsilon W A_{31} \left( \frac{h\nu_{21}}{k} \right) \exp\left(-\frac{h\nu_{31}}{kT_*}\right) \left( \frac{1}{T_*} - \frac{1}{T_x} \right) \\ X' T_x^{1/2} \left( \frac{1}{T_x} - \frac{1}{T} \right) &= Y' T_x^{5/2} + Z' T_x^{1/2} \left( \frac{1}{T_*} - \frac{1}{T_x} \right) \end{aligned} \quad (4.25)$$

#### 4.2.6 The temperature structure

In order to calculate the temperature as a function of radius, all the described processes must be taken into account. The total cooling rate is

$$C_{tot} = C_1 + C_2 + C_3 \quad (4.26)$$

Hence, the temperature structure of the envelope, i.e., the gas kinetic temperature, is governed by

$$\frac{1}{T} \frac{dT}{dr} = \frac{-4}{3r} \left( 1 + \frac{\epsilon}{2} \right) + \frac{2(H - C_{tot})}{3v n_{H_2} kT (1+f)} \quad (4.27)$$

where the first term on the right-hand side is the adiabatic cooling. It can be seen that if other cooling processes are ignored, the gas will simply cool with the slope of  $T \propto r^{-4/3}$ ;  $H$  and  $C_{tot}$  are the total heating and cooling rates per unit volume of all the processes described in the previous section. Typically, it will be seen that in the inner and mid-part of the envelope, the slope of the temperature departs from the  $-4/3$  due to gas-grain

heating and other cooling processes, which dominate in these regions. However, in the outer part, the adiabatic expansion dominates, hence the slope tends towards the value of  $-4/3$ .

The inner boundary condition for solving the above differential equation is the specification of the grain condensation radius, i.e., where the dust temperature falls below 1000K for silicates. Dust grains are assumed to form at the local sound velocity. We also need to input the stellar mass, the effective temperature, the dust mass loss rate, and the dust-to-gas mass ratio. The reason why we choose to enter dust mass loss rate, rather than the gas mass loss rate, is because we have already determined the dust component in the previous chapter. Once we specify all these values, the code proceeds to calculate the radiation pressure efficiencies, averaged over the stellar luminosity for each grain size, in order to calculate  $\Gamma$  from equation 4.10, which is then used to solve for the velocity at point  $r$  (equation 4.5). Hence, the density structure can be determined, along with the heating and cooling rates, which enable us to solve for the gas kinetic temperature of the envelope.

### 4.3 Variations of the input parameters

In this section, we will investigate how various input parameters affect the final temperature structure in models of circumstellar envelopes. We define a standard model, which closely resembles that of IRC+10011 used by GS (see Table 4.1 and Figures 4.1, 4.2). The main differences are the radiation pressure efficiencies calculated in our model, and the actual solution of the momentum equation. We take the silicate dust properties used to model the infrared energy distributions, whereas GS assumed a constant value of 0.5 for the dust extinction efficiencies throughout. Once we obtain the temperature structure for our standard model, we vary the input parameters, and see how the heating and cooling by various mechanisms, and the resulting gas kinetic temperature change. The results show that gas kinetic temperature is insensitive to small changes (a factor of two) in the input parameters. Any changes in the heating rates are compensated by similar changes in the cooling rates, which retain the gas temperature to within the same range of values.

From the earlier discussion, we know that the heating and cooling mechanisms are dependent on the flow of the gas. We now look at how the velocity is affected by changes

Figure 4.1: The resulting gas kinetic temperature from the calculation of heating and cooling in the circumstellar envelope of IRC+10011 (GS model) In the cooling panel, solid is adiabatic cooling; dash is  $H_2O$  rotational cooling; dot-dash is  $H_2O$  vibrational cooling and dot is  $H_2$  vibrational cooling.

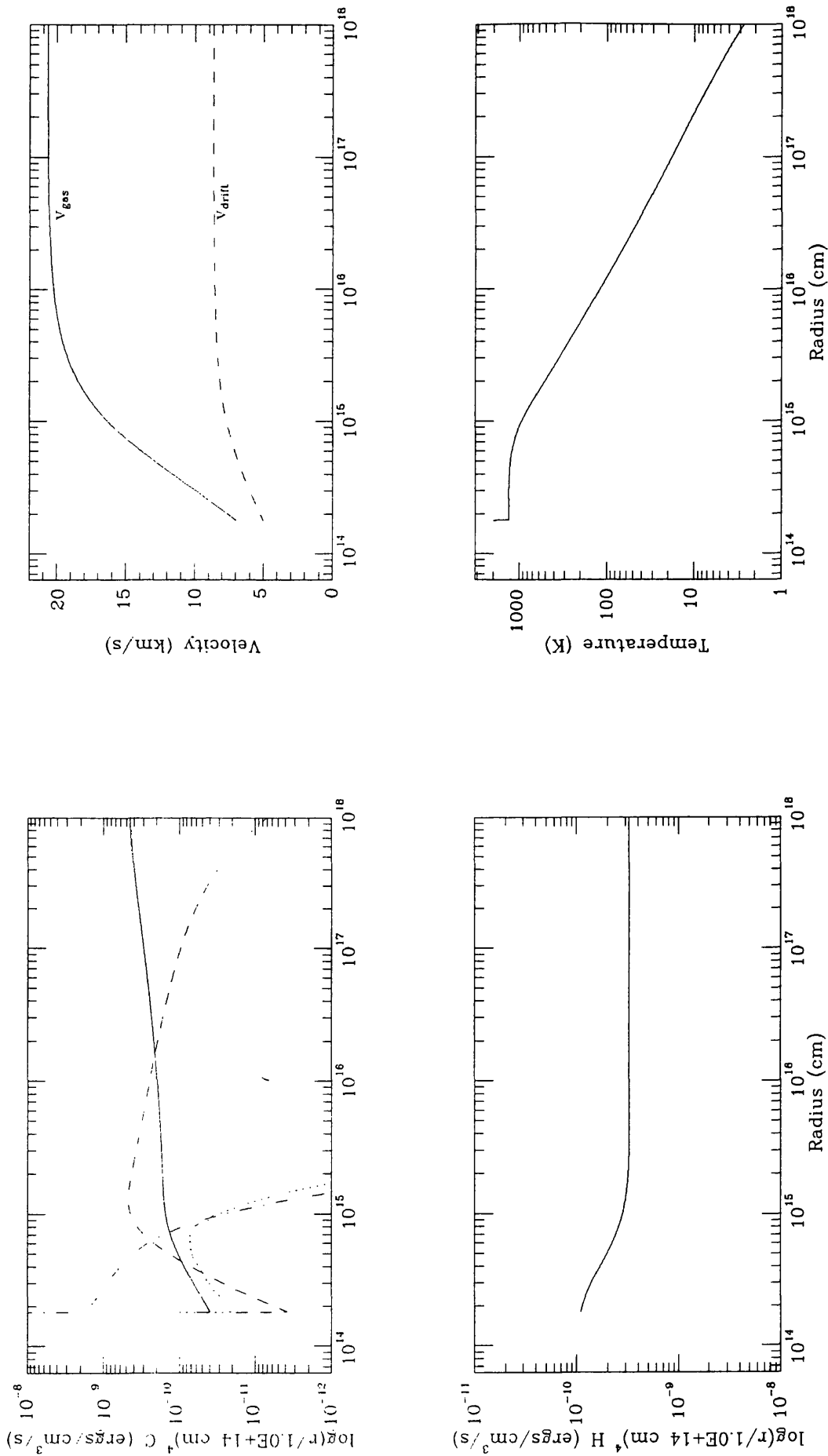


Figure 4.2: The resulting gas kinetic temperature from the calculation of heating and cooling in the circumstellar envelope of model 1. In the cooling panel, solid is adiabatic cooling; dash is  $\text{H}_2\text{O}$  rotational cooling; dot-dash is CO rotational cooling and dot is  $\text{H}_2$  vibrational cooling.

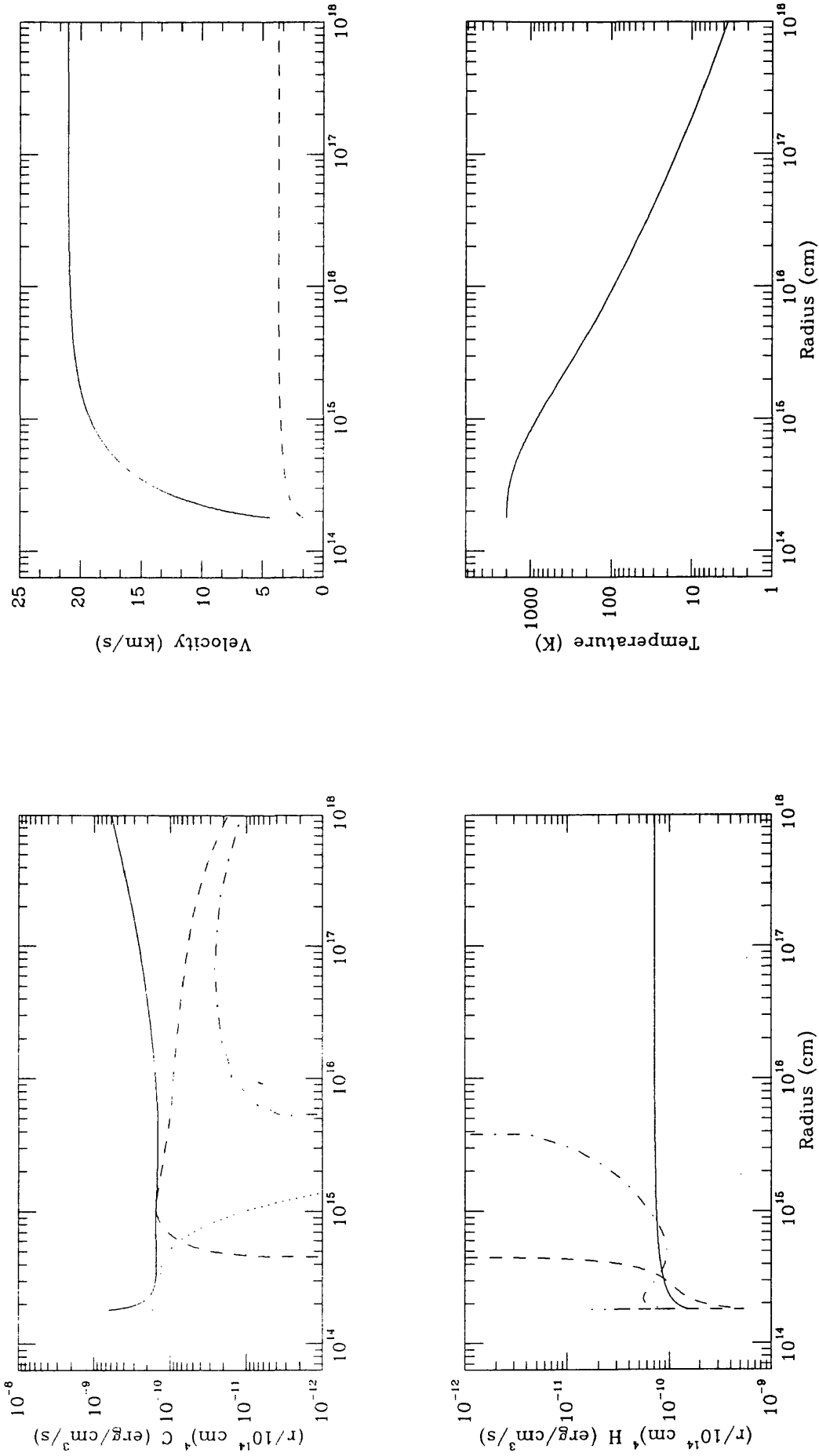


Figure 4.3: The resulting gas kinetic temperature from the calculation of heating and cooling in the circumstellar envelope of model 2.

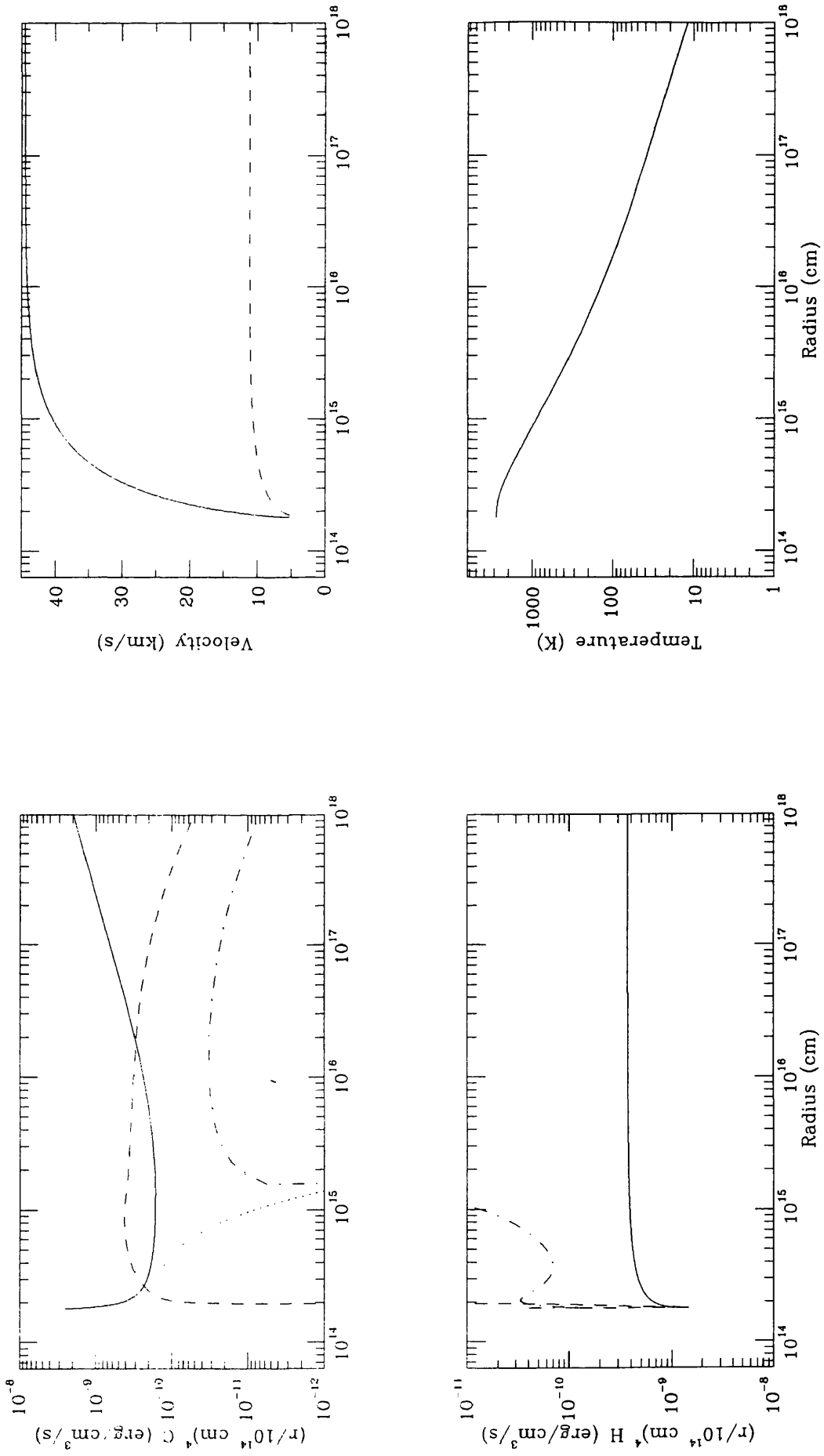


Figure 4.4: The resulting gas kinetic temperature from the calculation of heating and cooling in the circumstellar envelope of model 3.

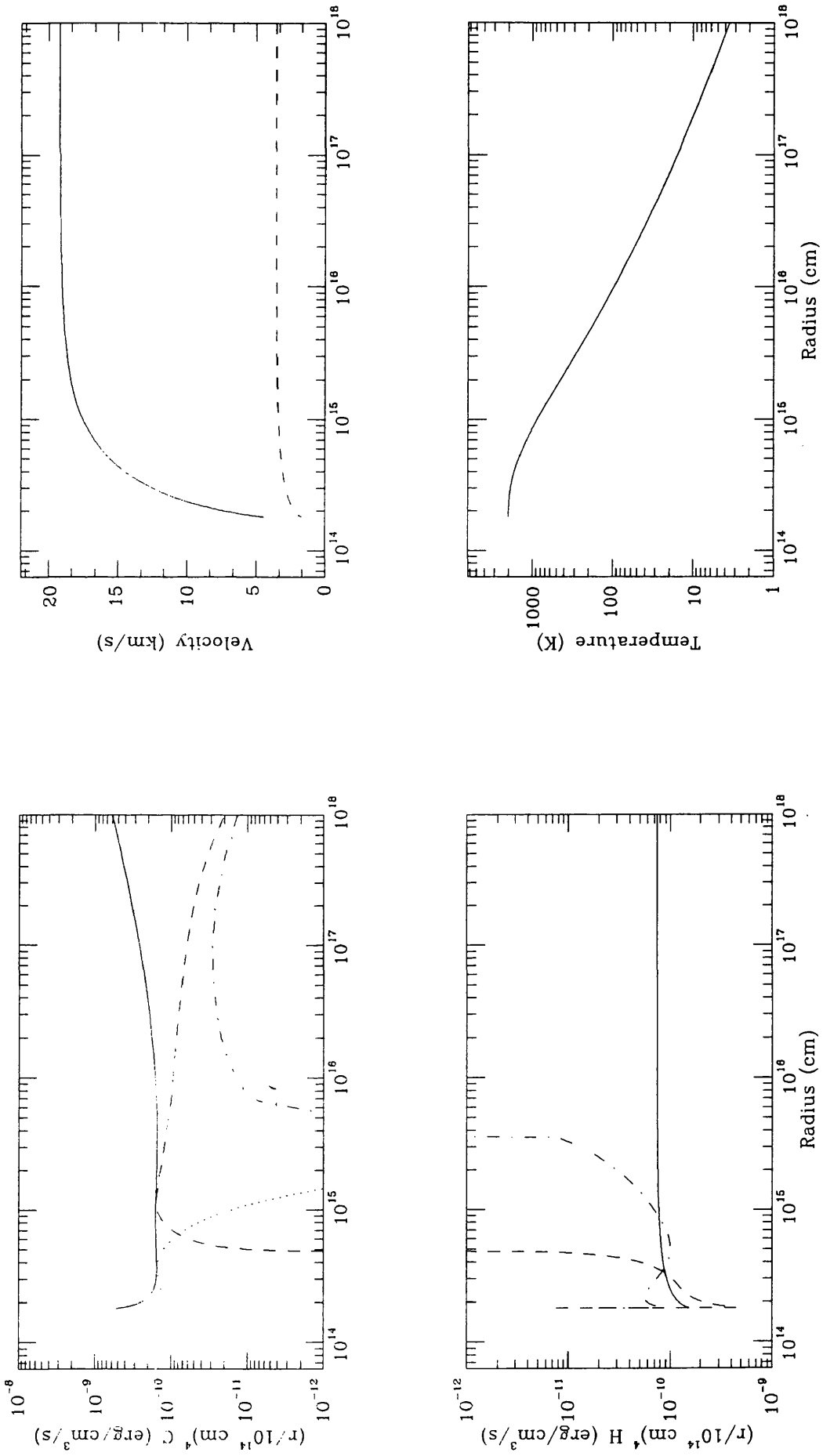


Figure 4.5: The resulting gas kinetic temperature from the calculation of heating and cooling in the circumstellar envelope of model 4.

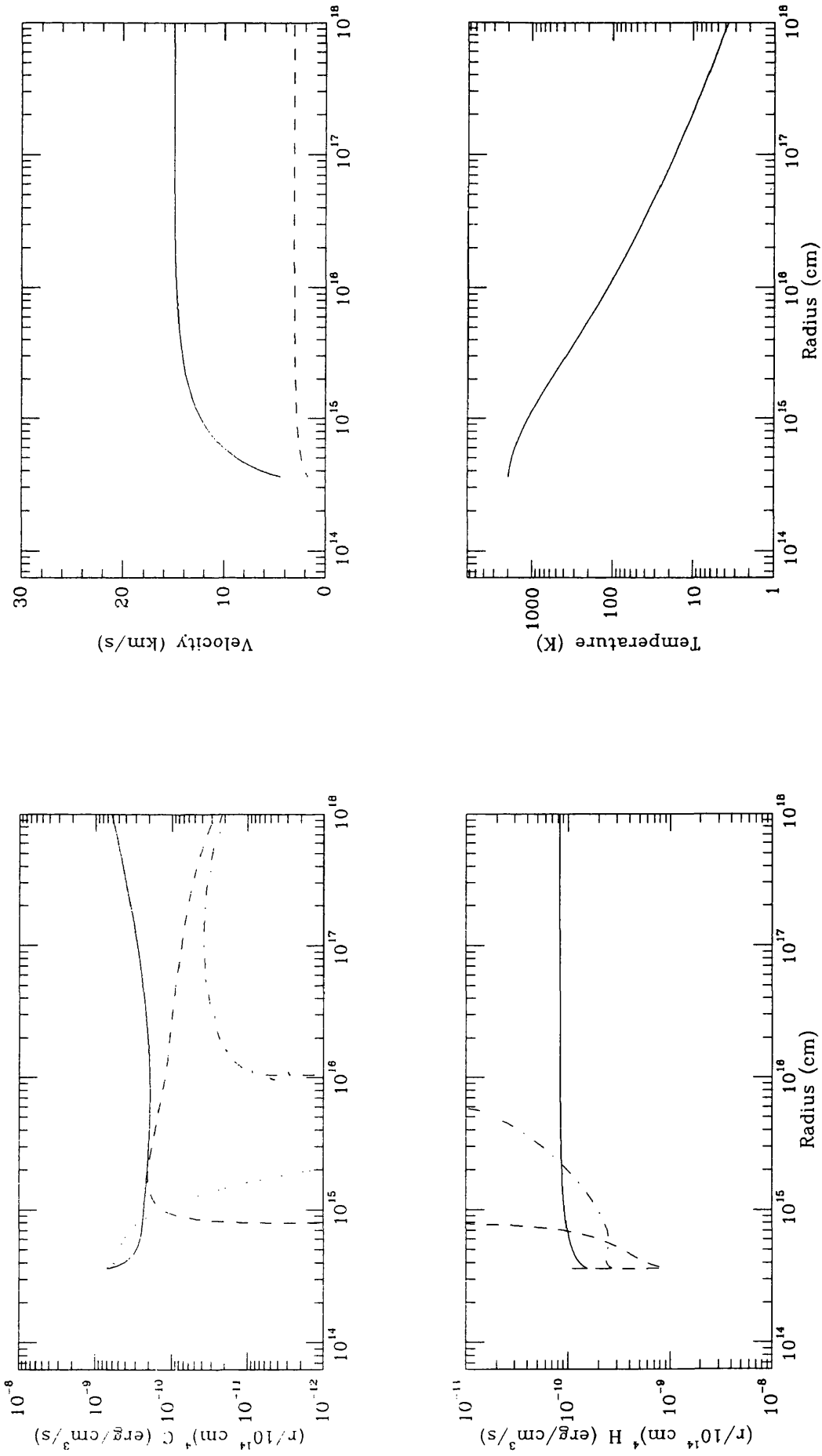


Figure 4.6: The resulting gas kinetic temperature from the calculation of heating and cooling in the circumstellar envelope of model 5.

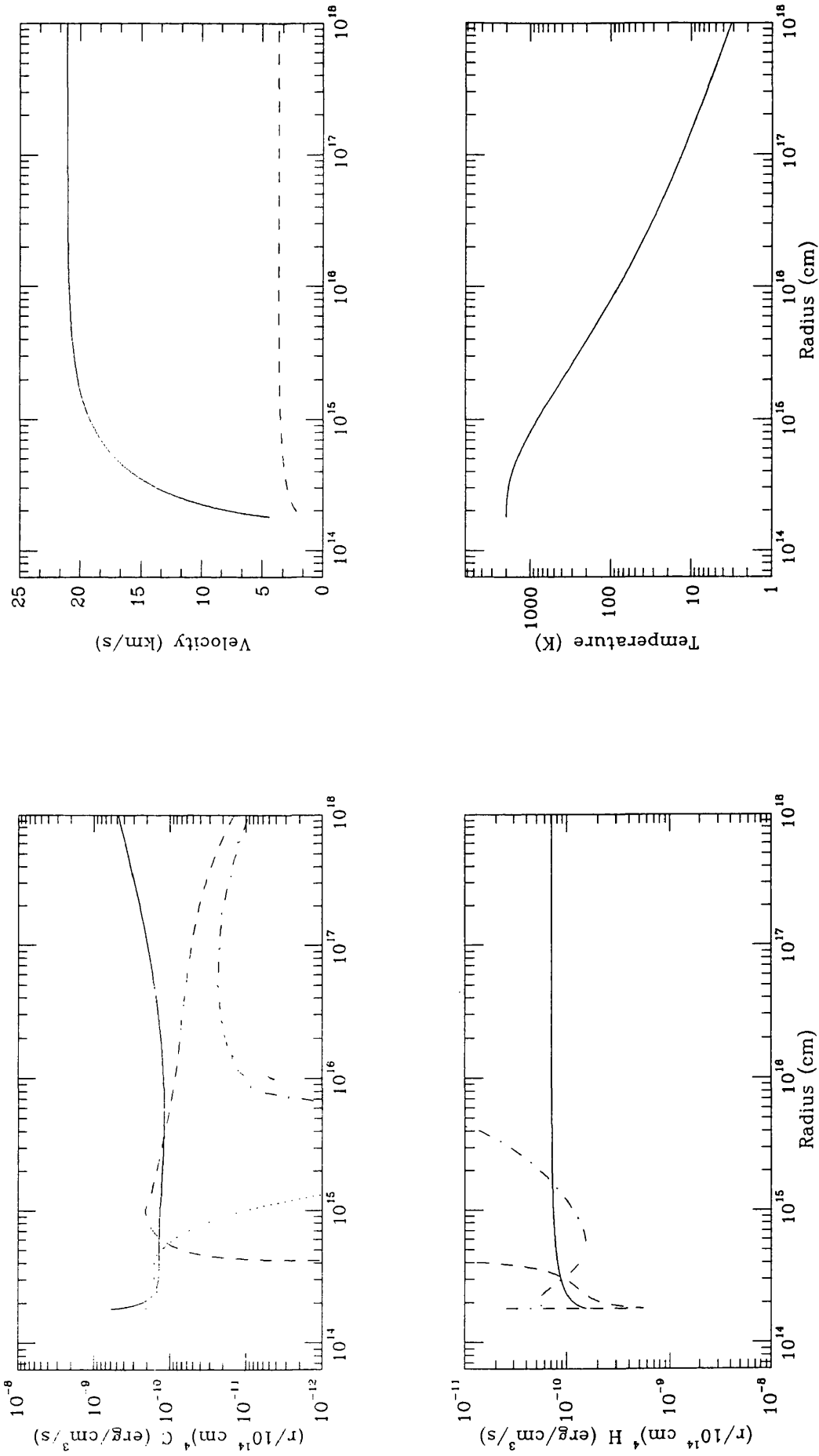


Figure 4.7: The resulting gas kinetic temperature from the calculation of heating and cooling in the circumstellar envelope of model 6.

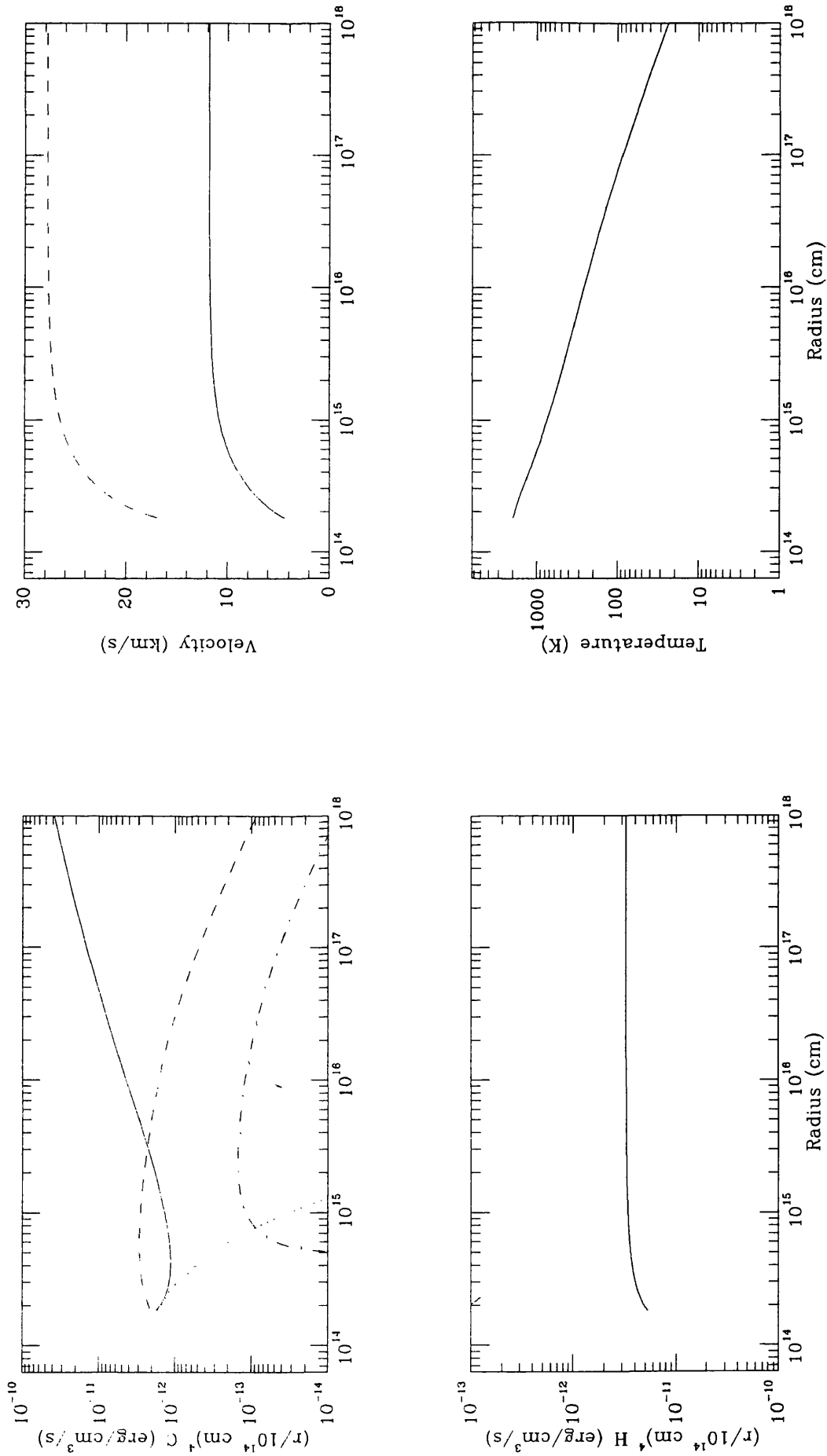
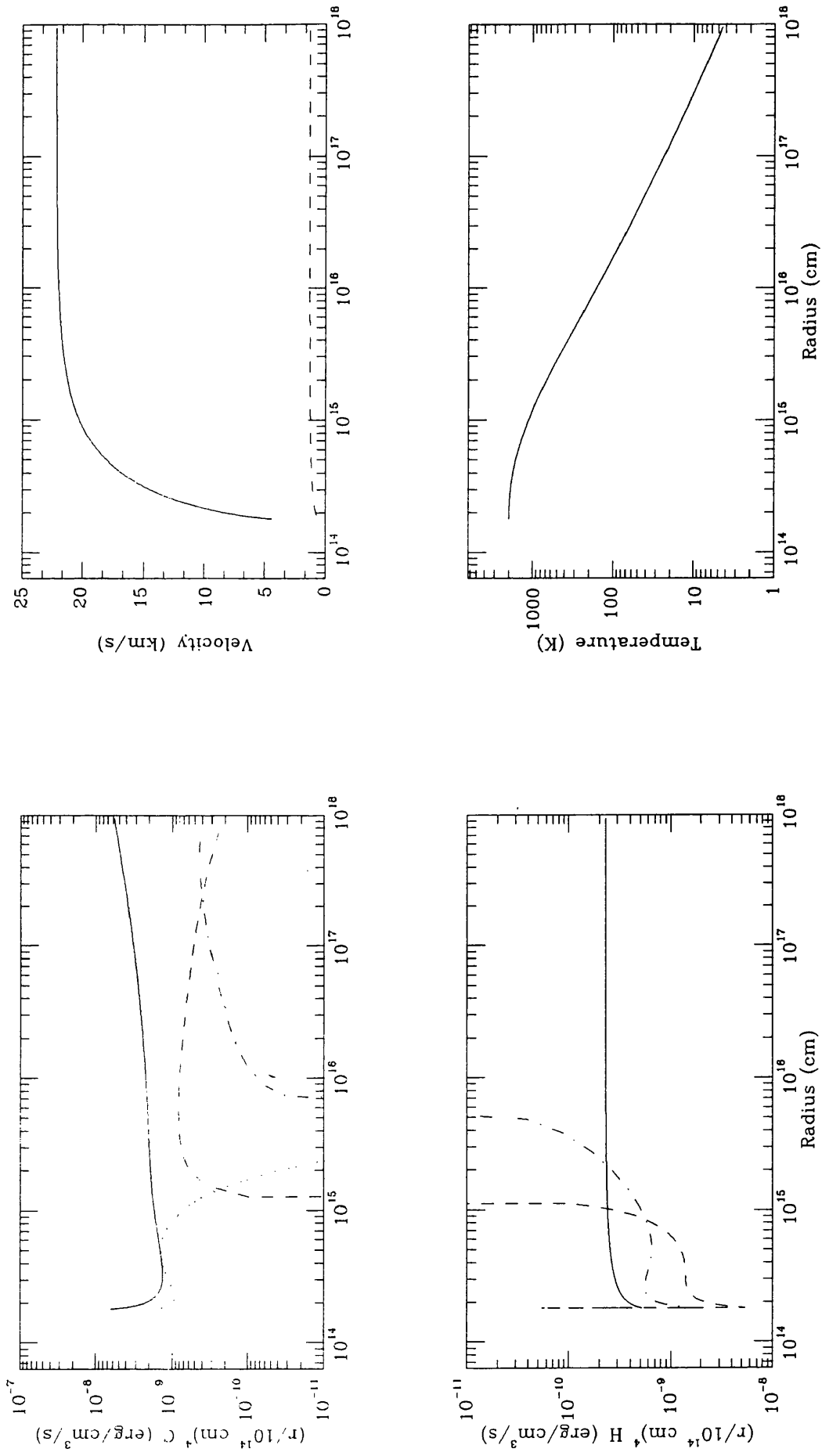


Figure 4.8: The resulting gas kinetic temperature from the calculation of heating and cooling in the circumstellar envelope of model 7.

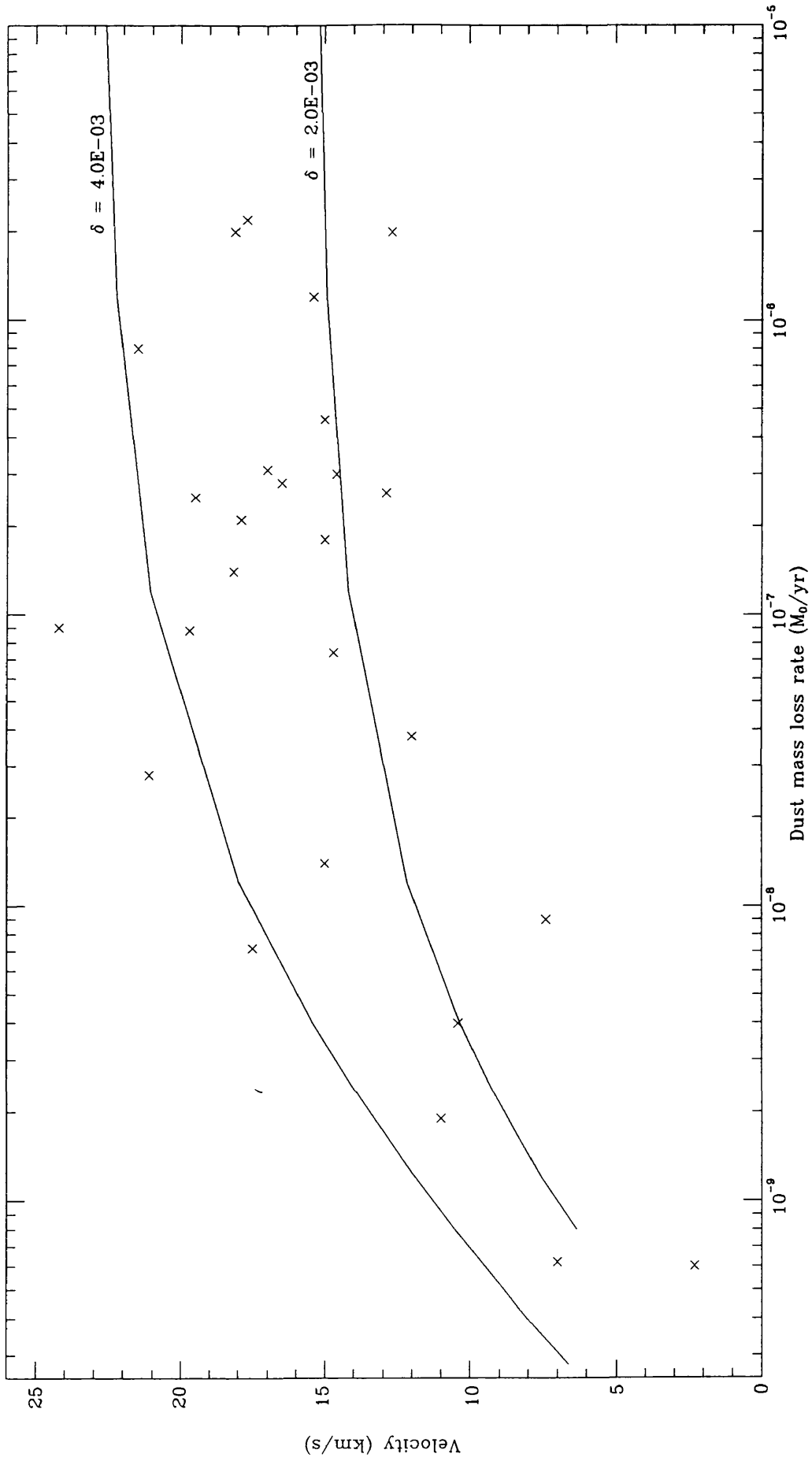


in the stellar parameters. Increasing the stellar effective temperature, or the stellar radius (Figure 4.3), results in the increase in the stellar luminosity, and since  $v \propto L$ , the velocity increases, as well. Since this also means an increase in the drift velocity, the heating rate increases by a large factor ( $H \propto v_{drift}^3$ ). The increased velocity also affects the cooling, since photons escape more easily, i.e.,  $T_x$  depends on  $v$  (see equation 4.18). However, the cooling rate does not increase by the same factor, which results in a higher gas kinetic temperature throughout the envelope.

The assumed stellar mass also affects the terminal velocity, since the gas will require more energy to overcome the stronger gravitational force of the star (equation 4.5). Increasing the stellar mass from 1 to 2  $M_{\odot}$  (Figure 4.4), the terminal velocity decreases by a small factor, roughly as  $M^{0.5}$ . Since this has a very small effect on the velocity flow, the temperature is hardly altered by an increase in the stellar mass. The escape velocity is also influenced by the inner radius of the shell (Figure 4.5). So, increasing the radius where dust condenses out will decrease the terminal velocity of the gas ( $v \propto v_{esc} \propto r_i^{1/2}$ ). Both the heating and cooling rates are only slightly affected, so the overall result is a small increase in the temperature for a factor of two increase in the dust condensation radius. Changing the ratio of the atomic-to-molecular hydrogen (Figure 4.6) does not affect the velocity or the heating rate but changes the cooling rates slightly. The overall effect is a very small change on the temperature structure.

The main parameter that influences the structure of circumstellar shells is the mass loss rate. The observed mass loss rates for AGB stars range from  $10^{-7}$  (Figure 4.7) to  $10^{-4} M_{\odot}/\text{yr}$  (Figure 4.8). So, we will now look at how the mass loss rates influence the heating and cooling in the envelope. In this case, we have 3 models with the dust mass loss rates of  $1.2 \times 10^{-9}$ ,  $1.2 \times 10^{-7}$  and  $10^{-6} M_{\odot}/\text{yr}$ . The gas mass loss rate is calculated by simply specifying the dust-to-gas mass ratio. As can be seen from the Figures 4.2, 4.7 and 4.8, a higher mass loss rate yields a higher terminal velocity of the flow, since there is more dust to intercept the radiation and hence accelerates the gas by the transfer of its momentum. However, there comes a point where increasing the mass loss rate has little effect on the terminal velocity. This occurs when the drift velocity is low compared to the gas velocity (see Figure 4.9). One further issue illustrated in Figure 4.9 is that dust-to-gas mass ratios ( $\delta$ ) may not be constant for all stars. The two lines give the terminal velocity as a function of dust mass loss rates for two values of  $\delta$ . It can be seen

Figure 4.9: The terminal velocity as a function of dust mass loss rates for different dust-to-gas mass ratio.



	$T_*$	$M_*$	$R_*$	$R_i$	$\dot{M}_d$	$\dot{M}_d/\dot{M}$	$n_H/n_{H_2}$	$v$
	(K)	( $M_\odot$ )	(cm)	(cm)	( $M_\odot/\text{yr}$ )	( $\%$ )	(km/s)	
GS	2000	1	6.0E+13	1.8E+14	1.2E-07	4.0E-03	1	20.00
model 1	2000	1	6.0E+13	1.8E+14	1.2E-07	4.0E-03	1	21.06
model 2	2830	1	6.0E+13	1.8E+14	1.2E-07	4.0E-03	1	44.46
model 3	2000	2	6.0E+13	1.8E+14	1.2E-07	4.0E-03	1	19.20
model 4	2000	1	6.0E+13	3.6E+14	1.2E-07	4.0E-03	1	15.01
model 5	2000	1	6.0E+13	1.8E+14	1.2E-07	4.0E-03	0.5	21.07
model 6	2000	1	6.0E+13	1.8E+14	1.2E-09	4.0E-03	1	11.87
model 7	2000	1	6.0E+13	1.8E+14	1.0E-06	4.0E-03	1	22.18

Table 4.1: Input parameters for the heating and cooling in the circumstellar envelopes of O-rich stars.  $\delta$  is the dust-to-gas mass ratio and  $f$  is the ratio of the atomic to molecular hydrogen.

that not all the data points lie on either curve, but scatter about. Some of the scatter in  $\delta$  may also reflect variations in the stellar luminosity among the stars and in stellar effective temperature (i.e., the average radiation pressure efficiency). This relationship between mass loss rate and terminal velocity is very similar to the relation between period and mass loss rate (Sivagnanam et al. 1989), since extreme OH/IR stars have the longest periods and lose mass at higher rates than ordinary Miras. The influence of mass loss rates on the temperature structure of the envelope is quite complex. The increase in the mass loss rate has a direct consequence on the drift velocity (equation 4.9), and thus on the viscous heating rate, which scales as  $H \propto \dot{M}^{0.5}v^{1.5}$ . The high mass loss rate influences “cooling” rates in two ways. First, the increase in the dust emission leads to a higher infrared pumping rate. Coupled with the increase density in the envelope, H<sub>2</sub>O and CO heatings are important over a larger part of the envelope. Second, the increase in the density leads to a higher H<sub>2</sub>O cooling rate per unit volume in the outer part of the envelope (cf. Figure 4.8). It should be noted that since the rotational transitions are highly optically thick, the rotational levels are close to LTE, and hence the cooling rate per H<sub>2</sub>O molecule is highly independent of the density (i.e., mass loss rate). Now, for low mass loss rates ( $\dot{M}_d \leq 10^{-7} M_\odot/\text{yr}$ ), the second effect dominates and an increase in the mass loss rate results in a slightly cooler outer envelope (compare figs 4.6 and 4.7). For

	$T_*$	$M_*$	$R_*$	$R_i$	$\dot{M}_d$	$\dot{M}_d/\dot{M}$	$\dot{M}$
	(K)	( $M_\odot$ )	(cm)	(cm)	( $M_\odot/\text{yr}$ )	( $\zeta$ )	( $M_\odot/\text{yr}$ )
GX Mon	2500	1	4.0E+13	2.5E+14	7.2E-09	5.20E-03	1.44E-06
IRC+10011	2000	1	4.5E+13	1.8E+14	1.4E-07	5.35E-03	2.62E-06
OH26.5+0.6	2200	3.5	5.0E+13	3.1E+14	1.2E-06	4.45E-03	2.70E-04

Table 4.2: Input parameters for 3 chosen O-rich stars.

high mass loss rates ( $\dot{M}_d \geq 10^{-7} M_\odot/\text{yr}$ ), the first effect dominates, and the enhanced heating over the inner envelope results in an increase in the temperature over the entire outflow.

## 4.4 Modelling O-rich stars

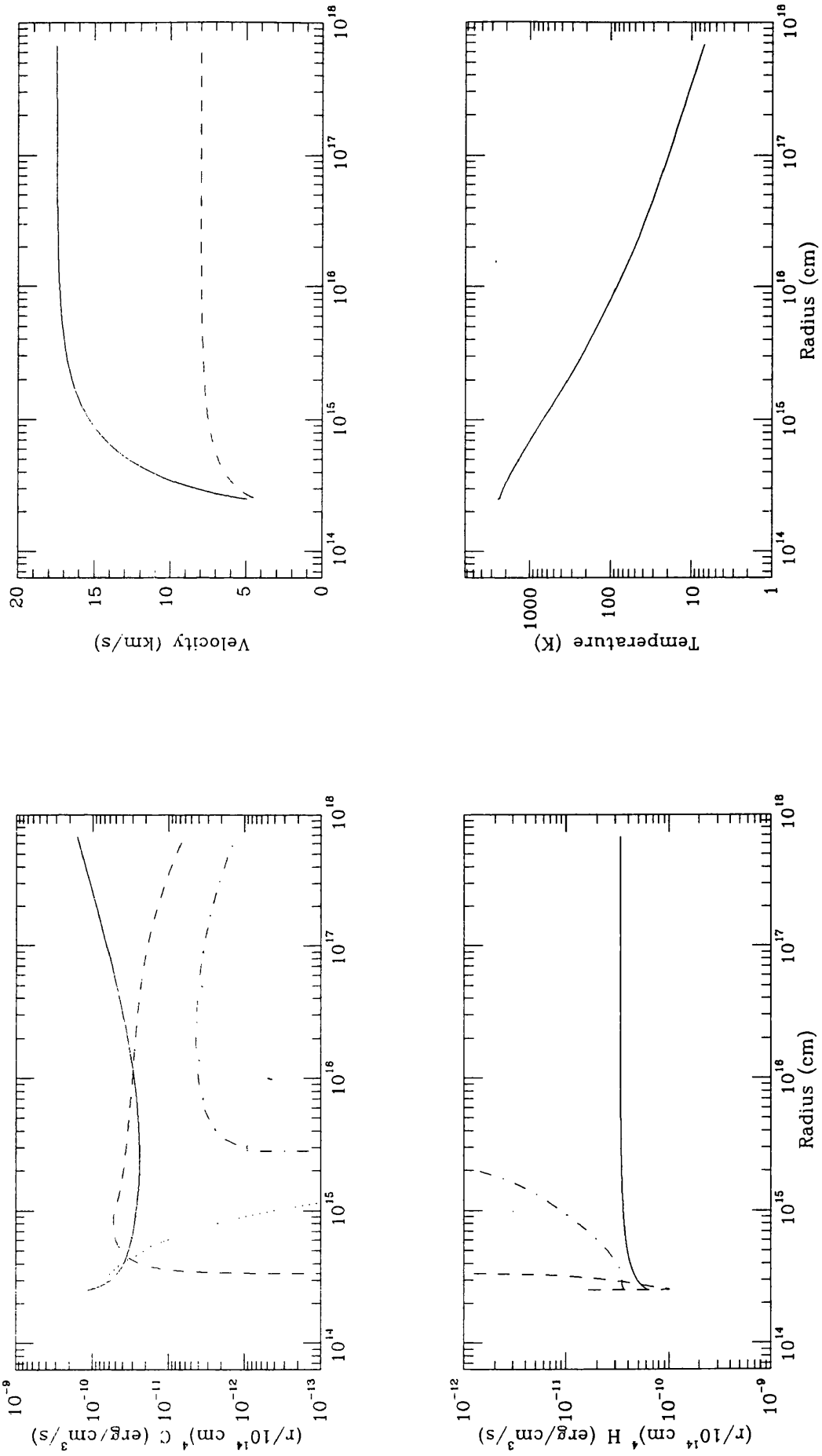
The stars chosen for the calculation are taken from those in chapter 3. These are selected on the ground that they have dust mass loss rates which cover a wide range, from  $7.2 \times 10^{-9}$  to  $1.2 \times 10^{-6} M_\odot/\text{yr}$ . Results will be discussed source by source. The input parameters required for each star are listed in Table 4.2, most of which are taken from the infrared modelling in chapter 3, namely, the stellar effective temperature, the stellar radius, the dust condensation radius and the dust mass loss rate. The gas mass loss rate is calculated by specifying the dust-to-gas mass ratio,  $\delta$ . The parameter  $\delta$  is adjusted so that the value of the observed terminal velocity is obtained. The code then calculates the velocity, density and gas kinetic temperature as a function of radius. The final temperature structure will be used in the calculations of the CO line profiles in the next chapter.

### 4.4.1 GX Mon

This star has the  $10\mu\text{m}$  silicate feature in emission, which implies that its envelope is optically thin. Its spectrum peaks around  $1.2\mu\text{m}$ , hence the effective temperature is about 2500K. Its terminal velocity, measured from the OH masers, is 17.5 km/s (te Lintel Hekkert et al. 1989). The stellar radius and the condensation radius are taken from infrared modelling. Cosmic carbon and oxygen abundances have been assumed (Andrses & Grevesse 1989).

From the result, we obtain the terminal velocity of 17.5 km/s for GX Mon for  $\delta =$

Figure 4.10: The resulting gas kinetic temperature for GX Mon.



$5 \times 10^{-3}$ , which translates to a gas mass loss rate of  $1.4 \times 10^{-6} M_{\odot}/\text{yr}$ . The velocity acceleration zone extends out to  $10^{16}$  cm. The dust drift velocity for a star with such a low mass loss rate is large, compared to the gas velocity, since dust grains do not collide with the gas often enough to transfer much of their momentum to the gas, hence they drift rapidly outwards (Figure 4.10)

At the innermost radius where dust condenses, CO rotational excitation contributes to the heating, rather than cooling, of the gas. This is due to the fact that in this region, the excitation temperature of CO molecules is higher than the gas kinetic temperature. As a result of the large drift velocity throughout the envelope, heating by gas-grain collision dominates over other heating processes.

For the cooling rates, adiabatic expansion is the dominant cooling mechanism over most of the envelope, especially at large distances from the star. It can be clearly seen that the H<sub>2</sub>O rotational cooling is much more efficient by an order of magnitude throughout compared to the CO rotational cooling. These cooling rates decrease with increasing radius due to decreasing number densities of the molecules. Cooling by H<sub>2</sub> vibrational excitation is only significant in the inner part of the envelope, and drops off sharply once the density drops below the critical density. The increase in the adiabatic cooling in the outer part of the envelope (Figure 4.10) is due to the factor of  $(r/10^{14})^4$ , which is multiplied so all the heating and cooling curves can be plotted on the same scale.

The resulting temperature structure clearly does not follow a simple power law expected by various authors (see Kwan & Hill 1976; Wattenbach et al. 1988). The temperature drops off more rapidly in the inner part ( $r < 3 \times 10^{15}$ ), which reflects the efficient cooling by molecules. In the outer parts, the temperature law can be approximated by  $T \propto r^{-0.5}$ .

One last note on this source and, in general, for sources with relatively low mass loss rates, is that the CO abundance drops off rapidly with radius. The CO abundance is mainly governed by the penetration of UV radiation from the interstellar medium. Essentially this process leads to an outer radius beyond which CO is dissociated. Mamon, Glassgold & Huggins (1988), using the new photodissociation rate from Letzelter et al. (1987), obtained the following expression for the CO abundance

$$x = x_0 \exp\left[-\ln 2 \left(\frac{r}{r_{1/2}}\right)^\alpha\right] \quad (4.28)$$

where  $x$  and  $x_0$  are the CO abundance at radius  $r$  and the initial abundance, respectively;

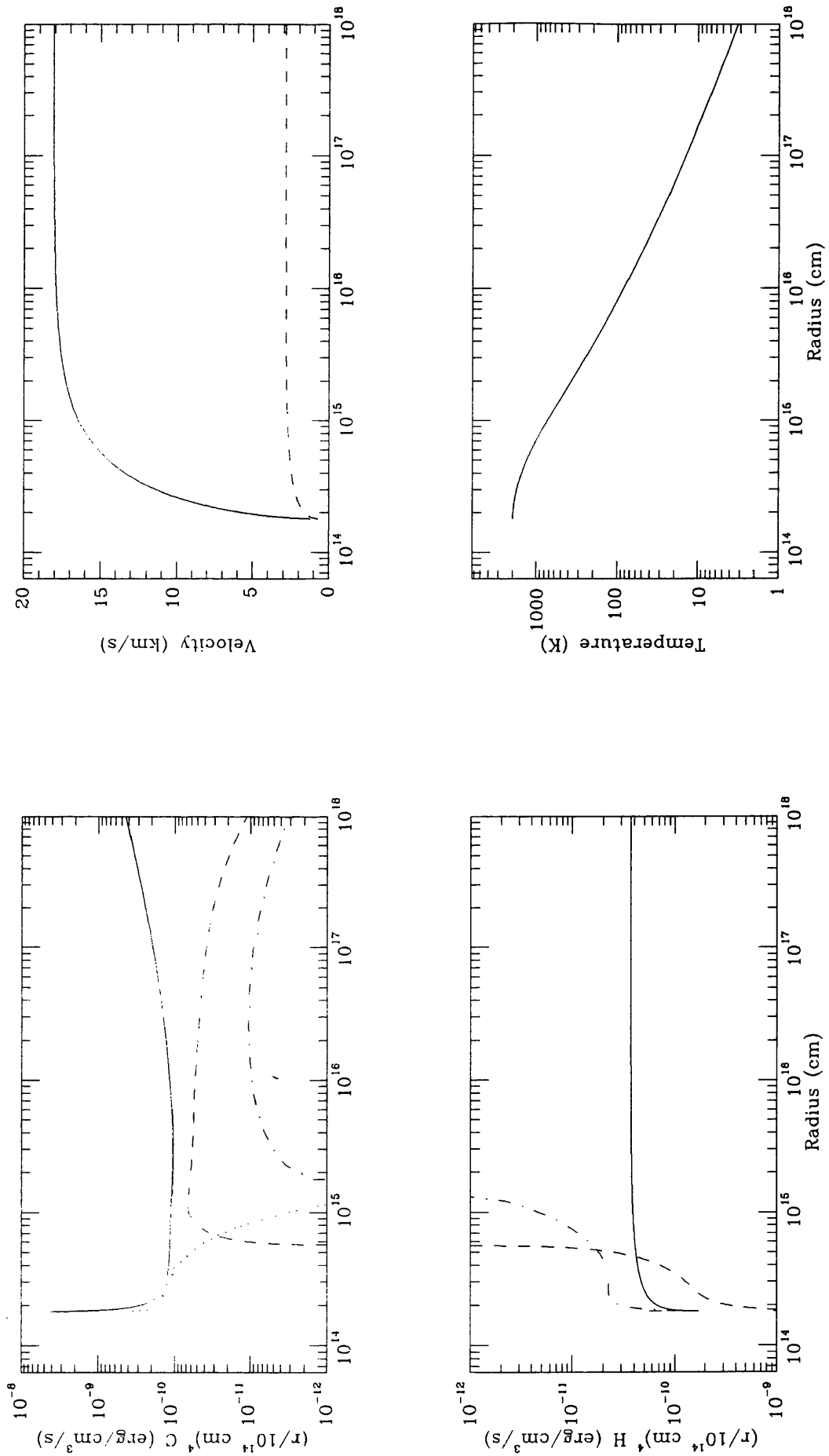
$r_{1/2}$  is the radius where the abundance drops to half the initial value; and  $\alpha$  is a parameter determining the run of the density. The above equation is a good estimate as long as  $x/x_0$  is greater than 0.05. For the mass loss rate of GX Mon, the photodissociation radius is approximately  $1.2 \times 10^{17}$  cm. In principle, this effect reduces the cooling rate for GX Mon beyond the photodissociation radius. However, at this radius, CO cooling is negligible compared to either H<sub>2</sub>O or the adiabatic cooling, hence this does not affect the final gas kinetic temperature. At this radius the temperature is about 40K, which is higher than the ambient interstellar medium. This radius will be used in the next chapter as a cut off point for CO.

#### 4.4.2 IRC+10011

Here, we can make a comparison between our model (Figure 4.11) and that calculated by GS (Figure 4.1). There are major differences which must be borne in mind when comparing the two results. We include a grain size distribution, using the silicate optical constants, which fitted the observed infrared spectrum, excluded H<sub>2</sub>O vibrational cooling, and included CO rotational cooling. From the constraint of the observed terminal velocity, the gas mass loss rate is determined to be  $2.6 \times 10^{-5} \dot{M}_{\odot}/\text{yr}$ , which is similar to GS value of  $3 \times 10^{-5} \dot{M}_{\odot}/\text{yr}$ . The stellar radius, derived from the infrared continuum model is  $4.7 \times 10^{13}$  cm, as opposed to  $6 \times 10^{13}$  cm.

Whereas GS arbitrarily adopted the average radiation pressure efficiency of 0.5, our calculated value turns out to be much smaller, 0.03. In our model, the rise in velocity is much steeper. This has a profound effect on all other calculated values, since the flow determines the density structure in the envelope. As expected from the smaller radiation pressure efficiency and differing grain sizes, we obtain a lower drift velocity of 3 km/s, as oppose to 9 km/s by GS. The density of molecular hydrogen in the inner envelope is different. We see a sharp drop in density before it follows the  $r^{-2}$  law. From this, the heating rate is expected to be less than that obtained by GS, which is evident when comparing Figure 4.1 to Figure 4.11. In the GS case, the heating rate increases from the dust condensation radius, while it decreases in our model, because of the difference in the MRN grain size distribution assumed, i.e., there are more smaller grains with small absorption cross section, whereas GS assumed the constant dust grain cross section. The heating radius for both H<sub>2</sub>O and CO rotations shift outward compare to GX Mon, since

Figure 4.11: The resulting gas kinetic temperature for IRC+10011.



the infrared pumping is more important (cf. section 4.3). Also higher density resulting in increasing number of vibrationally excited  $H_2$  state, leading to a higher cooling rate.

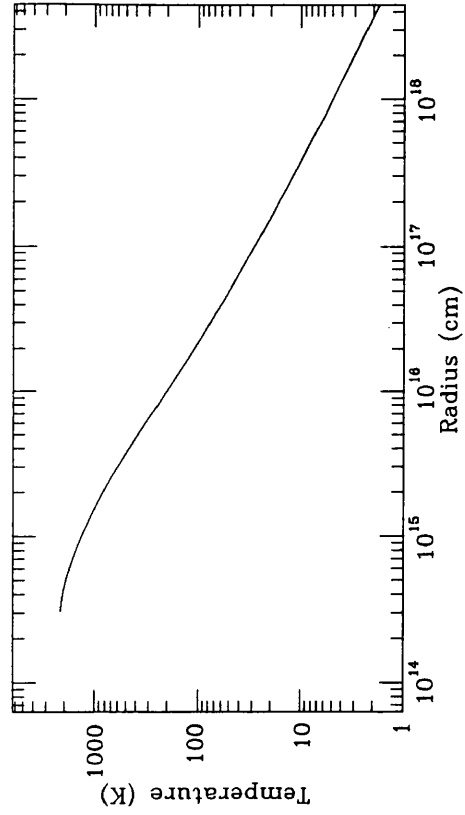
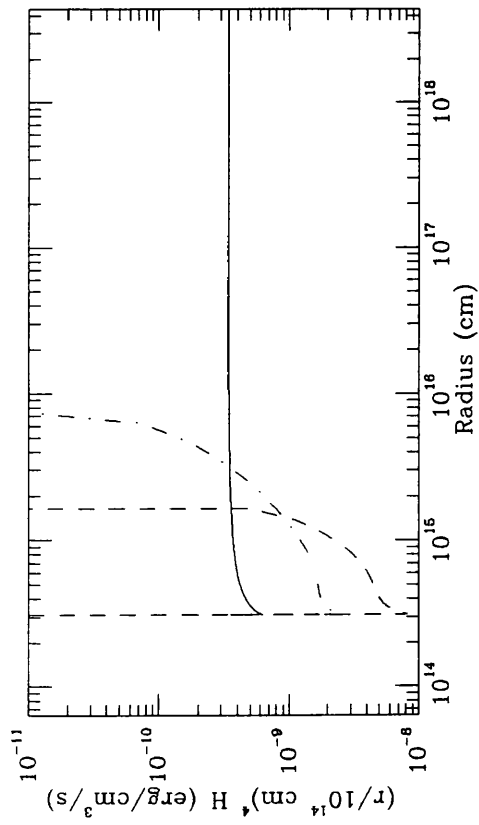
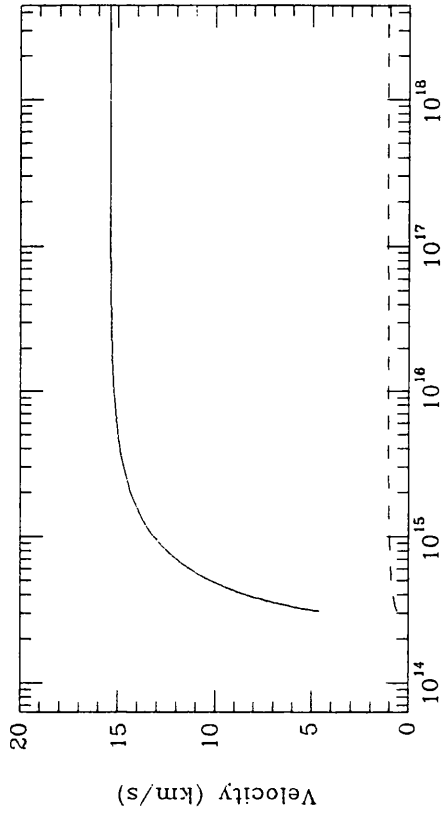
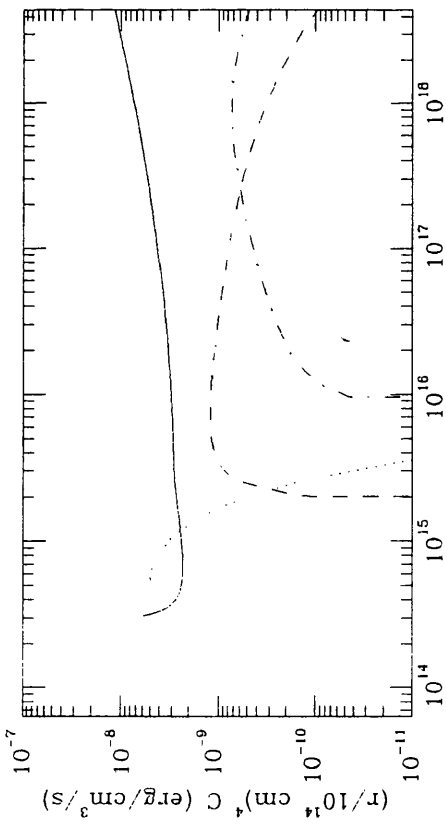
The final temperature is therefore very different between the two models. The combination of the slow rise in the gas velocity, and the resulting density structure in GS model gives a plateau of the temperature in the inner radius. In our model, the plateau is not as prominent. In the inner part ( $r < 10^{15}$ cm), the temperature decreases slowly then varies approximately as  $1/r$ , and the slope becomes less steep beyond  $10^{16}$  cm. It is evident that the slopes of IRC+10011 and GX Mon are different for both inner and outer parts of the envelopes. The CO dissociation radius for this source is  $5.4 \times 10^{17}$  cm, and the corresponding temperature at this radius is 4K.

#### 4.4.3 OH26.5+0.6

In modelling the infrared energy distribution of this source, we have to modify the optical constants in order to get a ratio of  $20:10\mu\text{m}$  of 0.8 (chapter 3). We have used these values to calculate the radiation pressure efficiencies as input values for our gas outflow model. The high dust mass loss rate and the constraint of the terminal velocity implies that the gas mass loss rate is  $2.7 \times 10^{-4} M_{\odot}/\text{yr}$  which is very high. From the high dust and gas mass loss rate, this source seems to be in the superwind phase.

Due to the high gas density in the envelope, the transfer of momentum from dust grains to gas is very efficient, resulting in very small drift velocity of the grains (1km/s). Although the drift velocity is low, the density is very high, hence the viscous heating rate of this source is higher than for the previous sources discussed. The optical constants used for this source give higher radiation pressure efficiencies. Also, due to the high density, the heating by  $H_2O$  and CO rotational excitation is maintained out to a few times  $10^{15}$ cm. Likewise, the cooling rate per unit volume due to adiabatic expansion is also higher due to the higher density. From Figure 4.12, it is seen that  $H_2$  cooling plays an important role, partly due to the high density and partly due to the higher stellar effective temperature as compared to IRC+10011. Although the cooling rates are higher than in the other two cases, the viscous heating maintains the high gas kinetic temperature. Because of the very high mass loss rate, the CO self shielding is very effective. This means that the photodissociation radius for this source is very large. This radius extends out to  $4 \times 10^{18}$  cm, where the temperature is just below 2K. In reality, the temperature can, of course,

Figure 4.12: The resulting gas kinetic temperature for OH26.5+0.6.



never fall below the 2.73K background. While we have neglected this heating source, this has little influence on the temperature structure of the outflow.

## 4.5 Summary

In this chapter, we have shown that the gas kinetic temperature of a stellar outflow depends, in a complicated way, on the stellar and outflow parameters. Although varying the stellar parameters does not change the temperature significantly, the temperature versus radius relationship cannot be approximated by just one single power law. Since the gas temperature determines which molecular lines are observed, which are then used to estimate the gas mass loss rates, any uncertainties in the temperature structure will surely result in large uncertainties in the calculated mass loss rates. We have not attempted to calculate the temperature structure for C-rich stars, but we predict that the kinetic temperature will be generally higher. Essentially, in our models for O-rich stars, the most efficient molecule in cooling is H<sub>2</sub>O. This molecule is not present in C-rich outflows. As a result, the temperature of these latter objects will be higher, particularly around 10<sup>15</sup>–10<sup>16</sup> cm radius, where H<sub>2</sub>O cooling dominates in our model. In the outer envelope, the adiabatic cooling dominates so the absence of H<sub>2</sub>O molecules will not make much difference here. We have neglected a number of other heating sources associated with the penetration of the UV photons from the incident interstellar radiation field (e.g., photoelectric heating, CO and H<sub>2</sub> photodissociation, C-ionisation). However, on further investigation, these are smaller than the viscous heating by an order of magnitude or more in the case where the envelope is extremely optically thick.

## Chapter 5

# CO Line Profile Calculations

In this chapter, the molecular line transfer calculation for CO is presented, with an emphasis on the ANR technique, which facilitates the faster convergence of the results than the conventional  $\Lambda$  iteration. Variations of the input parameters are investigated in order to study their effects on the line profiles. Finally, line profiles for three stars studied in the previous chapter are calculated and compared with observations, and higher rotational transitions of CO lines are predicted for these stars.

Observations of the millimeter lines of CO have commonly been used to determine the gas mass loss rate of red giants. The structure of the molecule is well studied, hence the line transfer process can be accurately calculated. The abundance of CO in the outflow is appreciable, thereby making it an extremely useful tool to probe into the subject of mass loss in late type stars. Fortunately, CO is present in both O-rich and C-rich stars, unlike OH masers, which are only present in the former. CO has been detected in a number of late type stars (e.g., Knapp et al. 1982; Knapp & Morris 1985; Heske et al. 1990) in the  $v=0$ ,  $J=1-0$ ;  $2-1$  and  $3-2$  rotational transitions.

Morris (1975) calculated the dependence of the line profiles on various physical parameters. His approach was simple, but yielded reasonable results. Bujarrabal & Nguyen-Q-Rieu (1981) presented a radiative transfer calculation in molecular lines, which applied the Sobolev approximation, i.e., the turbulent velocity is small enough to be neglected. However, for a typical outflow velocity of a late type star (20 km/s), this is no longer true, since the turbulent velocity is of an order of 1 km/s. The use of the Sobolev approximation must be avoided if the correct line profile is to be obtained, as shown by Hamann (1981). The method of the comoving frame for a two-level atom was developed by Mihalas, Kunz &

Hummer (1975, hereafter MKH), based upon the elimination scheme, which greatly facilitated the computation of the line transfer in spherically expanding atmospheres. However, this fails for a multilevel system, since the occupation numbers become non-linear. Instead, here, the calculation of the line profiles is based on a series of studies by Hempe & Schonberg (1986) Schonberg & Hempe (1986) and Schonberg (1988), which calculates the line transfer in the comoving frame, using an approximate Newton-Ralphson (ANR) operator. The advantage of this method over those which use the  $\Lambda$  operator (e.g., Scharmer 1981; Hamann 1985) is that faster convergence can be achieved.

## 5.1 The ANR technique

Below is the formalism of the radiative transfer code used to model CO rotational and vibrational-rotational lines. The code is based on work by Schonberg & Hempe (1986) which solves for the population in various levels. For a molecule with  $N$  levels, the rate equation is

$$F_l = n_i \sum_{j \neq i} (A_{ij} + C_{ij} + B_{ij} \Lambda_{ij} S_{ij}) - \sum_{j \neq i} n_j (A_{ji} + C_{ji} + B_{ji} \Lambda_{ij} S_{ij}) = 0 \quad (5.1)$$

where  $A_{ij}$ ,  $B_{ij}$  and  $B_{ji}$  are the Einstein A and B coefficients;  $C_{ij}$  is the collisional rates;  $\Lambda$  is the  $\Lambda$ -operator; and  $S_{ij}$  is the source function. The particle conservation law, after normalisation, dictates

$$\sum_j n_j - 1 = 0 \quad (5.2)$$

Replacing one of the  $F_i$ 's in equation 5.1 by equation 5.2, we arrive at a set of equations  $F_l$ , which we can solve with a Newton-Ralphson method. The solution of  $(m+1)^{th}$  iteration of the vector of occupation numbers,  $\mathbf{n}_l^{m+1}$ , at depth  $l$  is

$$\mathbf{n}_l^{m+1} = \mathbf{n}_l^m - [F_l'(\mathbf{n}_l^m, J_l^m)]^{-1} F_l(\mathbf{n}_l^m, J_l^m) \quad (5.3)$$

where  $J$  is the scattering integral in the line;  $F_l$  is a vector containing the set of equations at depth  $l$ ; and  $F_l'$  is the differential of matrix  $F_l$  with respect to  $\mathbf{n}$ . The diagonal elements of the matrix are

$$\frac{\partial F_i}{\partial n_i} = \sum_{j \neq i} (A_{ij} + C_{ij} + B_{ij} J_{ij}) + \sum_{j \neq i} (n_i B_{ij} - n_j B_{ji}) \frac{\partial J_{ij}}{\partial n_i} \quad (5.4)$$

and the non-diagonal elements are

$$\frac{\partial F_i}{\partial n_j} = (n_i B_{ij} - n_j B_{ji}) \frac{\partial J_{ij}}{\partial n_j} - (A_{ji} + C_{ji} + B_{ji} J_{ij}) \quad (5.5)$$

The derivative of the scattering integral is given by

$$\frac{\partial J_{ij}}{\partial n_i} = \frac{\partial J_{ij}}{\partial \kappa_{ij}} \frac{\partial \kappa_{ij}}{\partial n_i} + \frac{\partial J_{ij}}{\partial S_{ij}} \frac{\partial S_{ij}}{\partial n_i} \quad (5.6)$$

where  $\kappa_{ij}$  is the opacity. Hence

$$\frac{\partial J}{\partial S} = \int_0^1 \int_{-\infty}^{+\infty} \frac{\partial u}{\partial S} \phi(x) dx d\mu \quad (5.7)$$

$$\frac{\partial J}{\partial \kappa} = \int_0^1 \int_{-\infty}^{+\infty} \frac{\partial u}{\partial \kappa} \phi(x) dx d\mu \quad (5.8)$$

and for  $i < j$

$$\frac{\partial \kappa_{ij}}{\partial n_i} = \frac{g_j \kappa_{ij}}{n_i g_j - n_j g_i} \quad (5.9)$$

$$\frac{\partial S_{ij}}{\partial n_i} = \frac{g_j S_{ij}}{n_i g_j - n_j g_i} \quad (5.10)$$

For  $i > j$  then

$$\frac{\partial \kappa_{ij}}{\partial n_i} = \frac{g_j \kappa_{ij}}{n_j g_i - n_i g_j} \quad (5.11)$$

$$\frac{\partial S_{ij}}{\partial n_i} = \frac{g_j n_j S_{ij}}{n_i (n_j g_i - n_i g_j)} \quad (5.12)$$

The radiative transfer equation in the comoving frame can be written in terms of the Feautrier variables  $u$  and  $v$ , following MKH and Hamann (1981). The equations of energy are now linear and can be discretised as

$$T_k u_{k+1} + U_k u_k + V_k v_k = -S \quad (5.13)$$

$$G_k u_{k+1} + H_k v_k = v_{k+1} \quad (5.14)$$

where the subscript  $k$  is the frequency index.  $T_k, U_k, V_k, G_k$  and  $H_k$  are the matrices, while  $u_k, v_k$  and  $S$  are depth vectors. The ANR operator can now be used to obtain the derivative of the scattering integrals with respect to the source function.

$$\frac{\partial u_{k+1,l}}{\partial S_l} = -T_{k,l}^{-1} [U_{k,l} \frac{\partial u_{k,l}}{\partial S_l} + V_{k,l-1/2} \frac{\partial v_{k,l+1/2}}{\partial S_l} + V_{k,l+1/2} \frac{\partial v_{k,l+1/2}}{\partial S_l} + \frac{\partial S_l}{\partial S_L}] \quad (5.15)$$

where  $S_L$  is the line source function.

$$\frac{\partial v_{k+1,l+1/2}}{\partial S_l} = G_{k,l} \frac{\partial u_{k+1,l}}{\partial S_l} + H_{k,l} \frac{\partial v_{k,l+1/2}}{\partial S_l} \quad (5.16)$$

$$\frac{\partial v_{k+1,l-1/2}}{\partial S_l} = -G_{k,l-1} \frac{\partial u_{k+1,l}}{\partial S_l} + H_{k,l-1} \frac{\partial v_{k,l-1/2}}{\partial S_l} \quad (5.17)$$

Similarly, the derivatives of the scattering integrals with respect to the opacity are

$$\begin{aligned} \frac{\partial u_{k+1,l}}{\partial \kappa_l} = & -T_{k,l}^{-1} \left[ \frac{\partial T_{k,l-1}}{\partial \kappa_l} u_{k+1,l-1} + \frac{\partial T_{k,l}}{\partial \kappa_l} u_{k+1,l} + \frac{\partial T_{k,l+1}}{\partial \kappa_l} u_{k+1,l+1} \right. \\ & + \frac{\partial U_{k,l}}{\partial \kappa_l} u_{k,l} + U_{k,l} \frac{\partial u_{k,l}}{\partial \kappa_l} + \frac{\partial V_{k,l-1/2}}{\partial \kappa_l} v_{k,l-1/2} + V_{k,l-1/2} \frac{\partial v_{k,l-1/2}}{\partial \kappa_l} \\ & \left. + \frac{\partial V_{k,l+1/2}}{\partial \kappa_l} v_{k,l+1/2} + V_{k,l+1/2} \frac{\partial v_{k,l+1/2}}{\partial \kappa_l} + \frac{\partial S_l}{\partial \chi_L} \right] \end{aligned} \quad (5.18)$$

where  $\chi_L$  is the line opacity.

$$\frac{\partial v_{k+1,l+1/2}}{\partial \kappa_l} = G_{k,l} \frac{\partial u_{k+1,l}}{\partial \kappa_l} + H_{k,l} \frac{\partial v_{k,l+1/2}}{\partial \kappa_l} \quad (5.19)$$

$$\frac{\partial v_{k+1,l-1/2}}{\partial \kappa_l} = -G_{k,l} \frac{\partial u_{k+1,l}}{\partial \kappa_l} + H_{k,l-1} \frac{\partial v_{k,l-1/2}}{\partial \kappa_l} \quad (5.20)$$

At the frequency  $k=1$  (the blue wing boundary condition), all the derivatives vanish.

There are three spatial boundary conditions

- the outer boundary condition where there is no incident radiation, except for the 2.73K background;
- the inner boundary condition for rays that intersect the stellar core where the incident radiation is the photospheric intensity; and
- the inner boundary for the rays which do not intersect the core.

These yield the following equations

$$T_{k,l} u_{k+1,l} + T_{k,l+1} u_{k+1,l+1} + U_{k,l} u_{k,l} = 0 \quad (5.21)$$

$$T_{k,l-1} u_{k+1,l-1} + T_{k,l} u_{k+1,l} + U_{k,l} u_{k,l} = 0 \quad (5.22)$$

$$T_{k,l-1} u_{k+1,l-1} + T_{k,l} u_{k+1,l} + U_{k,l} u_{k,l} + V_{k,l-1/2} v_{k,l-1/2} + S_l = 0 \quad (5.23)$$

The code first calculates the starting occupation numbers, then uses these to calculate the source function, and opacity at each depth for each transition. Then, the radiation field is calculated at all depths for each transition in the comoving frame, using the ANR operator. This radiation field is then used to check the level populations, to see whether the equilibrium is satisfied to a specified level of precision. If not, a new set of occupation numbers is calculated and the whole process is repeated, until the convergence is reached.

The CO collisional cross section with H<sub>2</sub> are taken from Flower & Launey (1985) and McKee et al. (1982). The data on the v=1-0 transitions are from Chackerian (1976) and Stricker (1978), with other molecular data from Huber & Herzberg (1979).

## 5.2 Variations in antenna temperature and line profiles

Since CO line profiles can be studied in all types of late-type stars, they are very useful tools for probing the molecular outflow. In this section, we investigate the effects of mass loss rates, distances and the gas kinetic temperatures on the line profile. This uses the code described in the previous section. The resulting J=1-0 antenna temperature for a telescope with a 10m diameter, and beamsize of 65.5" is listed in Table 5.1 for each model studied.

### 5.2.1 The effects of the mass loss rates on CO line profiles

In order to demonstrate how CO line profiles depends on the stellar mass loss rate, we present the results of three data sets. These have the same input parameters except for the mass loss rates (models 1, 2 and 3). As seen from the Figure 5.1, the model with the smallest mass loss rate has a doubly peaked CO profile. This is simply because the CO optical depth is less than unity, and all the molecules are "seen". The two peaks represent the front and back part of the envelope which are moving at the expansion velocity. Note that there is asymmetry in the profile, with the blue-shifted peak showing slightly higher temperature than the red-shifted one.

When the mass loss rate is increased to  $3.0 \times 10^{-5} M_{\odot}/\text{yr}$ , the profile becomes flatter, but remnants of the double peak can still be seen. In this case, the optical depth of CO line is approaching unity. The antenna temperature is higher than the previous case, simply because there are more CO molecules along the line of sight. If the mass loss rate is increased further, the line now becomes optically thick and the profile becomes parabolic (see Figure 5.1, Morris 1975).

As for the excitation temperature compared to the gas kinetic temperature, both are the same out to a very large distance from the star for the model with a large mass loss rate. In this case, the density in the envelope is high enough for the collision to populate all the levels, i.e., Boltzmann distribution. The same is true for the model with

Figure 5.1: The predicted CO line profile for different mass loss rates.

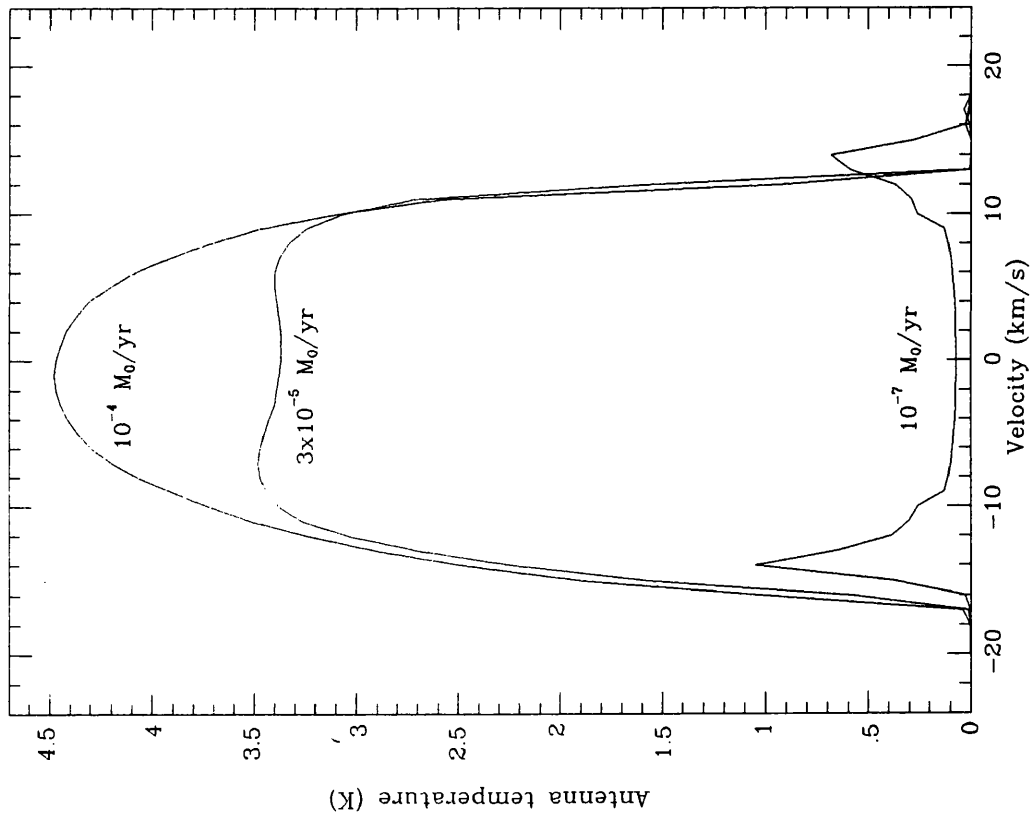
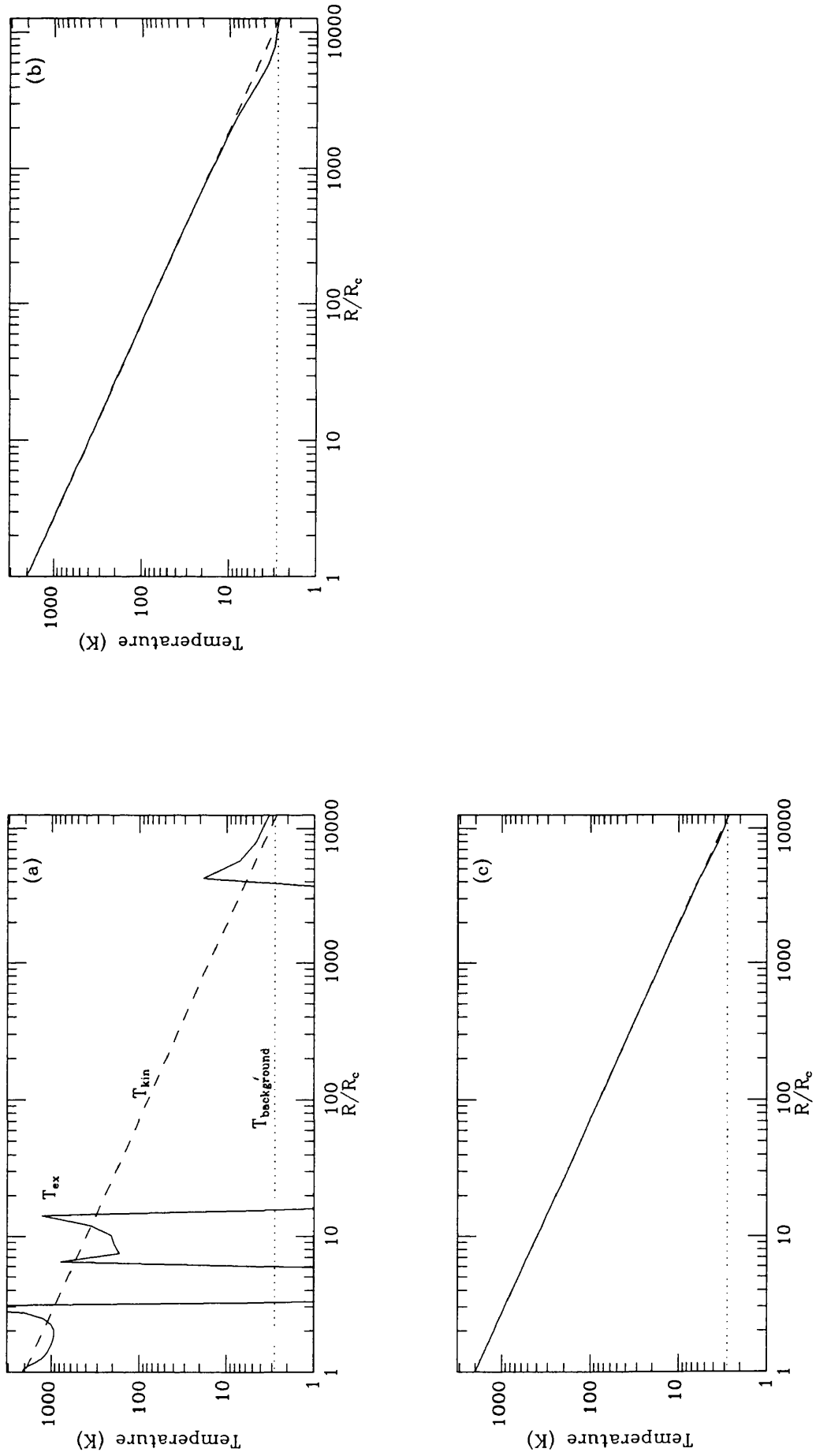


Figure 5.2: The gas kinetic temperatures, excitation and background temperatures for (a)  $\dot{M} = 5 \times 10^{-7} M_{\odot}/\text{yr}$ ; (b)  $\dot{M} = 5 \times 10^{-5} M_{\odot}/\text{yr}$ ; (c)  $\dot{M} = 10^{-4} M_{\odot}/\text{yr}$ .



Model	$\dot{M}$ ( $M_{\odot}/\text{yr}$ )	$\epsilon$	D (pc)	$T_A(\text{J}=1-0)$ (K)
1	3.0E-05	0.7	300	6.21
2	5.0E-07	0.7	300	0.90
3	1.0E-04	0.7	300	7.72
4	3.0E-05	0.7	150	12.6
5	3.0E-05	0.7	600	2.37
6	3.0E-05	0.5	300	14.7
7	3.0E-05	0.8	300	2.01

Table 5.1: Parameter studies of the CO J=1–0 line fluxes and profiles.

a moderate mass loss rate, but the radius where the excitation temperature deviates from the kinetic temperature is smaller. For the case with a small mass loss rate, the excitation temperature rises off to infinity, before becoming negative, i.e., masing regions (Figure 5.2). This affects all transitions from J=3–2 upwards. Although this has not yet been observed, it is very pronounced in many transitions and occurs at the envelope expansion velocity. The maser emerges where the density is high enough for the collision to over populate the upper level with respect to the lower level, but not too high that collision can thermalise the system.

### 5.2.2 The effect of distance on CO line profiles

For an envelope which is unresolved, increasing the distance will only reduce the received flux, leaving the shape of the profile unchanged, i.e., flux is proportional to  $D^{-2}$ . For a resolved source of a given intrinsic diameter, the line profile is often a function of distance (see Figure 5.3). The profile also depends on the position of the source within the beam. For a relatively nearby star, assuming the object to be at the centre of the beam, the profile is doubly peaked (model 4). As the distance increases, the line peak becomes flatter (model 1) and finally parabolic (model 5), reflecting the increased beam averaged optical depth. As we have already discussed in chapter 3, distances obtained from the literature can be uncertain by a factor of two or more, depending on the method used to derive them.

Figure 5.3: The predicted CO line profile for differing distances.

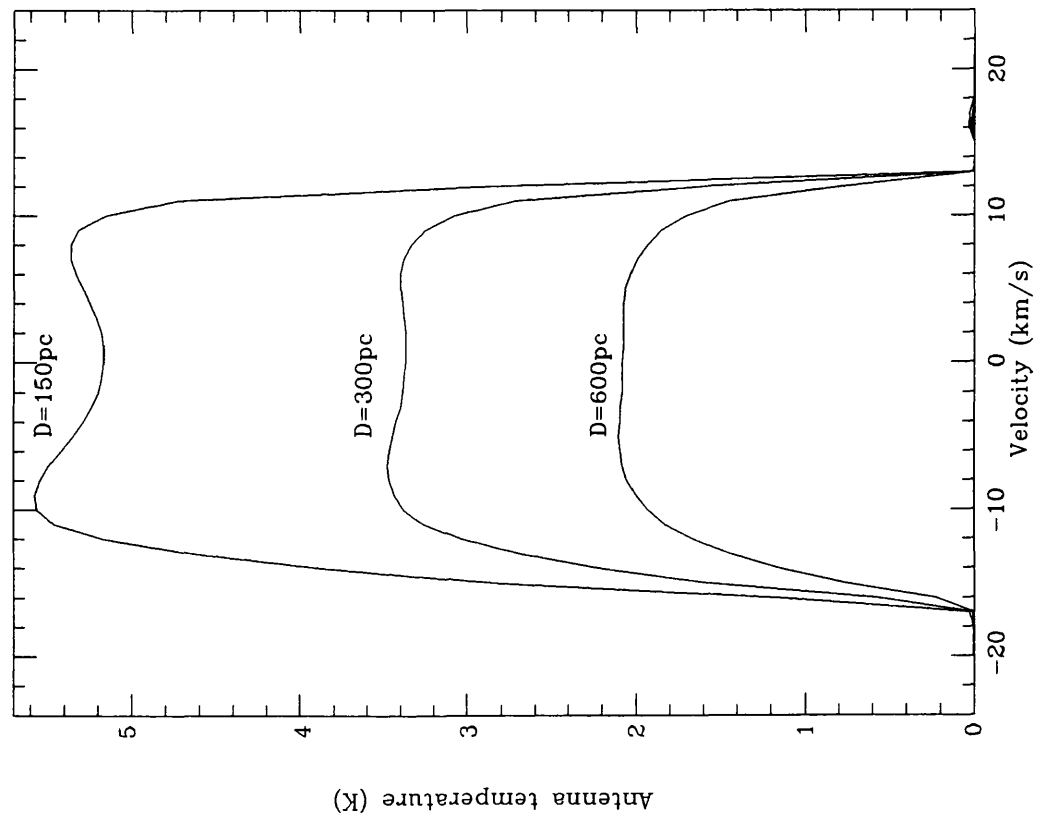
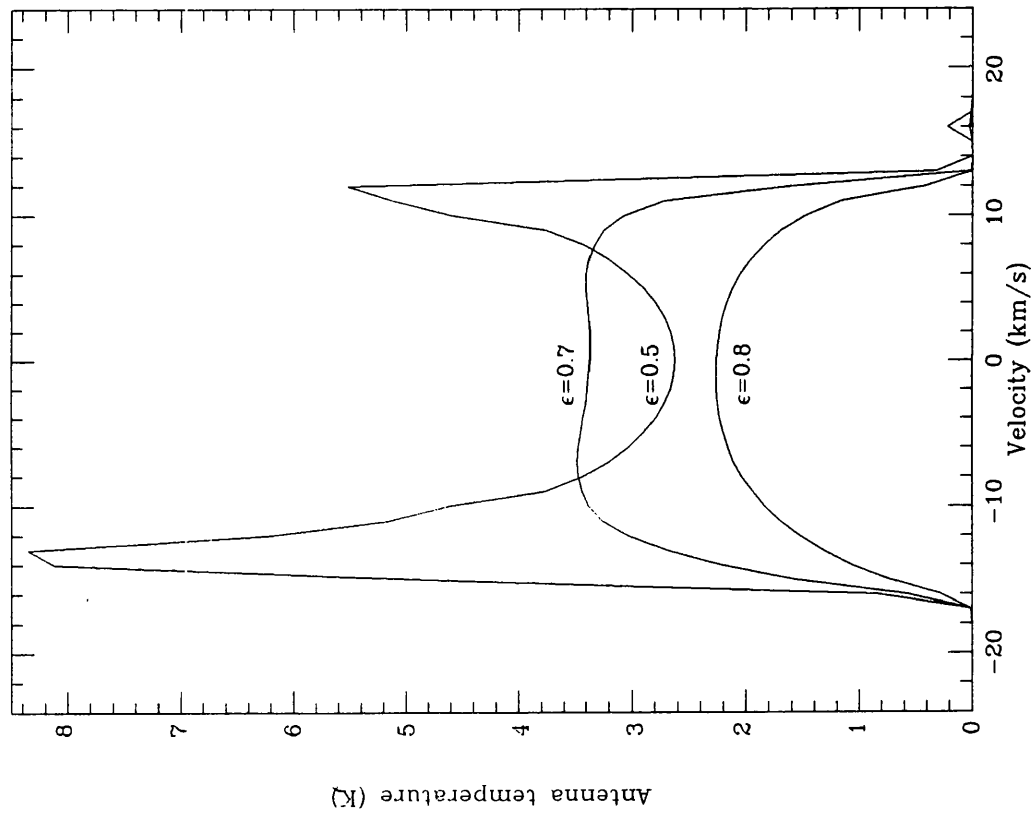


Figure 5.4: The predicted CO line profile for different temperature laws.



### 5.2.3 The effects of the gas kinetic temperature law on CO line profiles

To demonstrate the effect of the gas kinetic temperature, we present three cases with different temperature laws,  $\epsilon = 0.5, 0.7$  and  $0.8$  (model 1, 6 and 7; Figure 5.4), where

$$T(r) \propto \left(\frac{r}{R_*}\right)^{-\epsilon} \quad (5.24)$$

The smaller the index, the higher the temperature in the outer envelope, in which case more CO molecules are highly excited. Only relatively small numbers remain in the  $J=1$  levels, making the  $J=1-0$  transition optically thin. For a steeper temperature law, the line becomes more optically thick due to the lower temperature in the outer envelope and the resulting increase in the population of the  $J=1$  level.

### 5.2.4 Optical depth of each transition

We also consider here the effect of mass loss rate on the optical depth,  $\tau$ , of each line. It is expected that the surface where  $\tau = 1$  for higher transitions lies closer to the star than those for lower transitions. Increasing the mass loss rate has the effect of moving these surfaces farther from the central star. Figure 5.5 shows the radius of the shell where CO optical depth is unity as a function of upper  $J$  value of each transition for three different mass loss rates (model 1,2 and 3).

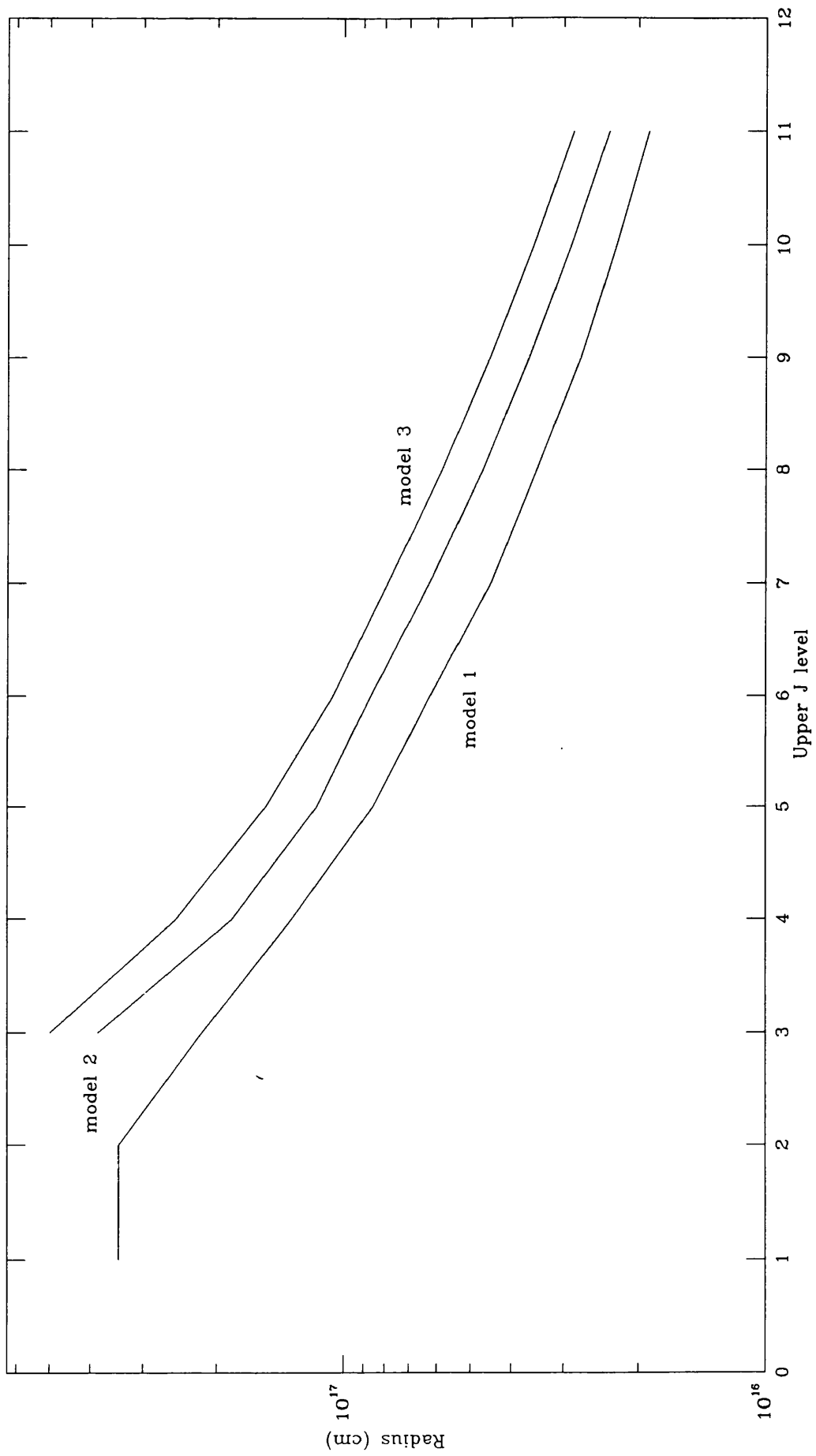
## 5.3 CO calculations for O-rich stars

In this section, we combine the results from previous chapters in order to get a comprehensive model of dust and gas mass loss rates for the same stars. The gas kinetic temperature, along with previously used parameters, are used as inputs for the CO code to get a more consistent picture of processes going on in the circumstellar envelopes. Such a self-consistent model has been calculated only for C-rich stars (Sahai 1990). The inputs are listed in Table 5.2 for the three stars, GX Mon, IRC+10011 and OH26.5+0.5. The dust mass loss rates are determined from the modelling of the observed infrared continuum. The dust temperatures are taken to follow a power law of

$$T_d(r) \propto \left(\frac{r}{R_*}\right)^{-\eta} \quad (5.25)$$

where  $\eta$  can be obtained by modelling the infrared energy distribution of each star. Although the dust temperature is not strictly a simple power law, due to back heating of

Figure 5.5: The radius at which  $\tau=1$  for different transitions for different mass loss rates.



dust in the inner part of the circumstellar shell, we can approximate  $\eta$  to a single number without seriously affecting the actual values. The dust-to-gas mass ratio, and hence the gas mass loss rate, follow from solving the momentum equation, which results in the observed terminal velocity. The gas temperature distribution is then derived from the energy equation (cf. chapter 4). As for the gas mass loss rates, we start off with the results from the previous chapter but iterate until the profiles and antenna temperatures are comparable to the observed lines. Table 5.2 lists the input parameters used in fitting the CO line profiles to all three stars.

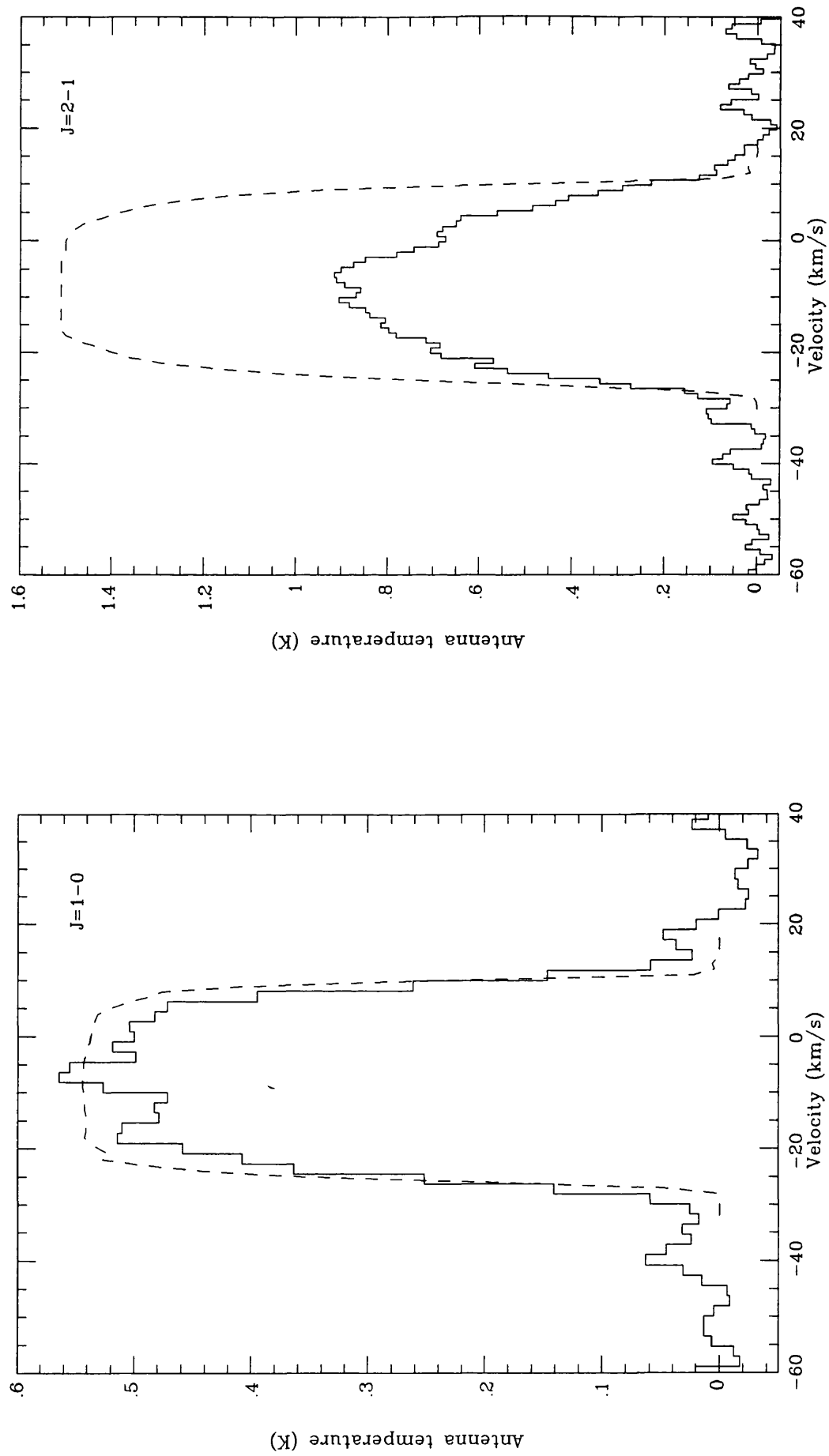
Source	$\dot{M}$ ( $M_{\odot}/\text{yr}$ )	D (pc)	$\eta$	p	$T_A(\text{J}=1-0)$	$T_A(\text{J}=2-1)$
GX Mon	8.0E-6	850	0.54	1.0	0.54	1.51
IRC+10011	1.5E-5	650	0.58	1.5	0.41	1.89
OH 26.5+0.6	2.7E-4	1000	0.58	1.0	0.50	1.43

Table 5.2: Parameters for the three O-rich stars under investigation, where  $\eta$  is the index for dust temperature as a function of distance, and p is the index for the far-infrared emissivity (equation 2.30).

### 5.3.1 GX Mon

For this source, we observed both the J=1-0 and 2-1 lines with the Swedish-European Southern Observatory Telescope (SEST), which is a 15m sub-millimeter telescope with a beam size of 44" and 22", respectively. These data were reduced by C.J.Skinner and are only for line modelling. Both lines have been corrected for beam efficiency (Figure 5.6). However, due to the lack of proper extinction calibration, the observed antenna temperatures may have been underestimated. From the observed profiles, the velocity for the outer envelope is 19 km/s, which is slightly higher than the OH maser velocity of 17.5 km/s (te Lintel Hekkert et al. 1989). Comparison with the previous demonstration models in the previous section, the J=2-1 line is optically thick, since it takes on a parabolic shape, while the J=1-0 line is flat (i.e., becoming optically thick). The combination of the mass loss rate obtained from the previous chapter, and the estimated distance, leads to optically thin lines for both transitions. With an expected CO photodissociation radius of  $1.2 \times 10^{17}$  cm (10" at 850 pc), this source is unresolved. In order to match both observed profiles, the mass loss rate must be increased. However, this results in increased

Figure 5.6: The observed CO line profiles (solid) and the best fits (dotted) for GX Mon for  $J=1-0$  and  $J=2-1$  lines.



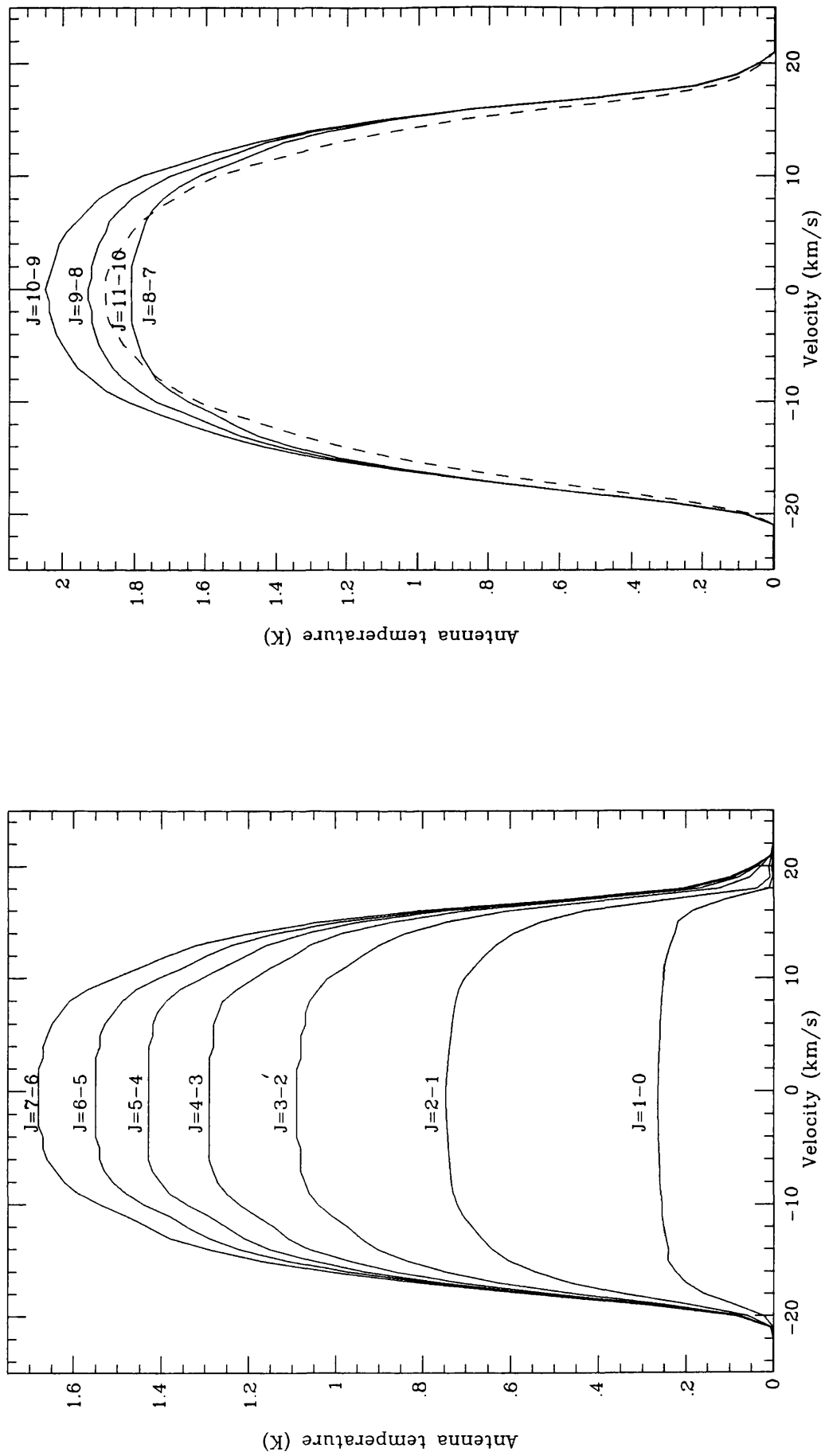
peak antenna temperatures, which have to be compensated for by moving the star farther away. As discussed in the previous chapter, the mass loss rate determines the outer radius where CO is photodissociated by the interstellar ultraviolet radiation. By increasing the mass loss rate, this radius is increased by the factor calculated by eqn 4.28 taken from Mamon et al. (1988). The calculated ratio of the two lines is 2.8, while the observed is 1.6. The best fit profile for J=1-0 line is obtained with a mass loss rate of  $8 \times 10^{-6} M_{\odot}/\text{yr}$  and a distance of 850 pc (Figure 5.6). However, this model overestimates the antenna temperature of J=2-1 line. This may be due to the calculated profile assumes a uniformly illuminated conical beam, which may not be valid for this case where the angular size of the source is comparable to the beam size.

There are also other data available on this source. For example, Margulis et al. (1990), who used the 14m telescope of the Five College Radio Astronomy Observatory (FCRAO) with a beamsize of  $45''$  to observe the J=1-0 line, report a main beam temperature of about 0.4K. From our calculation, using the input parameters which fit the SEST J=1-0 data, we arrive at an antenna temperature of 0.48K, which is close to the observed value. The observed profile is flat, which is in good agreement with the calculated profile.

The gas mass loss rate derived from CO modelling ( $8 \times 10^{-6} M_{\odot}/\text{yr}$ ) is somewhat larger than that derived from the infrared dust emission and momentum equation ( $2 \times 10^{-6} M_{\odot}/\text{yr}$  scaled to a distance of 850 pc, from chapter 4). Since the infrared emission originates close to the star, while the CO originates in the outer part of the shell, this may imply that mass loss rate has decreased over the last 4000 yrs. This is supported by the  $60\mu\text{m}$  dust mass loss rate, derived from the  $60\mu\text{m}$  *IRAS* flux, which is higher than the dust mass loss rate obtained from infrared modelling (see Table 3.2; and Jura, private communication). The  $60\mu\text{m}$  method also tends to measure the dust mass loss rate at a large distance from the star. The discrepancy between the observed and calculated 2-1 antenna temperatures may reflect a decreasing mass loss rate with time, or be due to the calibration of the lines. The latter can be uncertain by a factor of two (Sahai, private communication).

We are able to predict the higher transitions of GX Mon, currently up to J=11-10 transition (see Figure 5.7). We assume that the source is observed with a 10m telescope, using a beamsize which is diffraction limited for each transition, i.e.,  $\theta = 1.22\lambda/d$ , where  $d$  is the telescope diameter. It can be seen that most transitions are on the border of the envelope becoming optically thick. It is only for the high transitions that line shapes become parabolic, indicative of an optically thick nature. There is a slight asymmetry in the line wing for lower transitions. We see more fluxes in the front part of the envelope,

Figure 5.7: The predicted antenna temperature for each rotational transitions of GX Mon for a 10m telescope working at the diffraction limit for each transition.



Transition	beamwidth (")	$T_A$ (K)
1-0	43.7	0.26
2-1	21.8	0.75
3-2	14.6	1.09
4-3	10.9	1.29
5-4	8.7	1.43
6-5	7.3	1.55
7-6	6.2	1.68
8-7	5.5	1.81
9-8	4.9	1.93
10-9	4.4	2.05
11-10	4.0	1.88

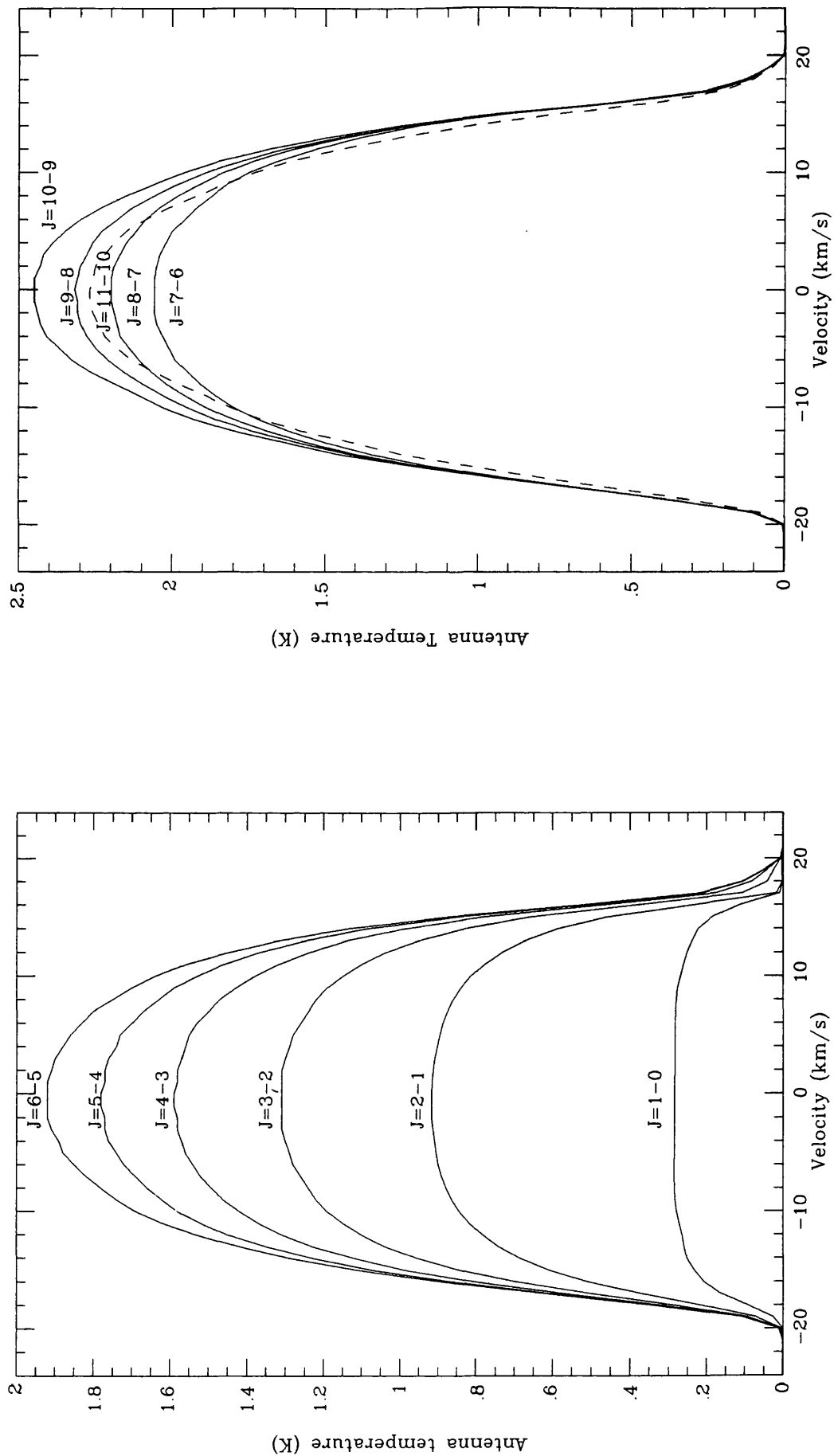
Table 5.3: The predicted peak antenna temperatures for GX Mon.

which is moving towards us, than in the back of the envelope. The observations of high transitions of CO lines are desirable if the nature of mass loss is to be probed at different distances from the central star. This, in turns, will indicate the history of mass loss from the stars. Also, the gas kinetic temperature of the envelope can be estimated and compared to the calculations.

### 5.3.2 IRC+10011

The data on IRC+10011 were obtained from Knapp et al. (1982) for the J=2-1 transition, and Knapp & Morris (1985) for the J=1-0 transition. The J=2-1 line profile is more rounded than the J=1-0 line, indicative of a higher optical depth for the former. The calculated antenna temperatures of J=1-0 and J=2-1 lines agree quite well with the observations. In order to match profiles and the peak antenna temperatures, the distance has to be increased from 500 pc to 800 pc, which is still within the uncertainty of the distance estimated. The former value is obtained by assuming that the luminosity is  $10^4 L_{\odot}$  (Hyland et al. 1972). The gas mass loss rate derived from the CO observations is  $1.0 \times 10^5 M_{\odot}/\text{yr}$ , which is about a factor of two less than that estimated from the radiation pressure driven wind. In order to drive the outflow at 18.1 km/s, the dust mass loss rate is taken to be  $5.8E-8 M_{\odot}/\text{yr}$  compared to  $1.4E-7 M_{\odot}/\text{yr}$ , calculated from the mid-infrared

Figure 5.8: The predicted antenna temperature for each rotational transitions of IRC+10011 for a 10m telescope working at the diffraction limit for each transition.



Transition	beamwidth (")	$T_A$ (K)
1-0	65.5	0.29
2-1	32.7	0.92
3-2	21.8	1.31
4-3	16.4	1.59
5-4	13.1	1.78
6-5	10.9	1.92
7-6	9.4	2.06
8-7	8.2	2.20
9-8	7.3	2.32
10-9	6.6	2.45
11-10	6.0	2.27

Table 5.4: The predicted peak antenna temperatures for IRC+10011.

modelling. The ratio of the 2-1 to 1-0 line is calculated to be 6.2, while the observation gives 10.6. However, the latter is very uncertain due to very low signal-to-noise (see line profiles from Knapp et al. (1982) and Knapp & Morris (1985)). Sopka et. al. (1989) observed the J=1-0 transition with the Onsala 20m telescope with a beamsize of 33" and obtain a temperature of 0.92K, while Margulis et al. (1990) used the 14m telescope at FCRAO with a beamsize of 45" and obtained a temperature of 0.6K. Our model yields very good agreements, the antenna temperatures being 1.02K and 0.54K, respectively. However, we do not match the observed line profile for the latter feature. We obtained a flat profile for the former case, but a slightly doubly peak profile for the latter.

Here, we also predict the higher CO transitions of this source for a telescope with a diameter of 10m, and the beamsize limited by the diffraction at each line frequency (Table 5.4). As can be seen from Table 5.4, the antenna temperature rises as a function of the J value, and reaches a maximum for J=10-9 before starting to decline. The profiles start off as being flat for lower transitions, and becomes progressively more rounded (Figure 5.8). As for GX Mon, the line profile is noticeably asymmetric in low transitions, where the blue wing is more extended than the red wing in velocity space.

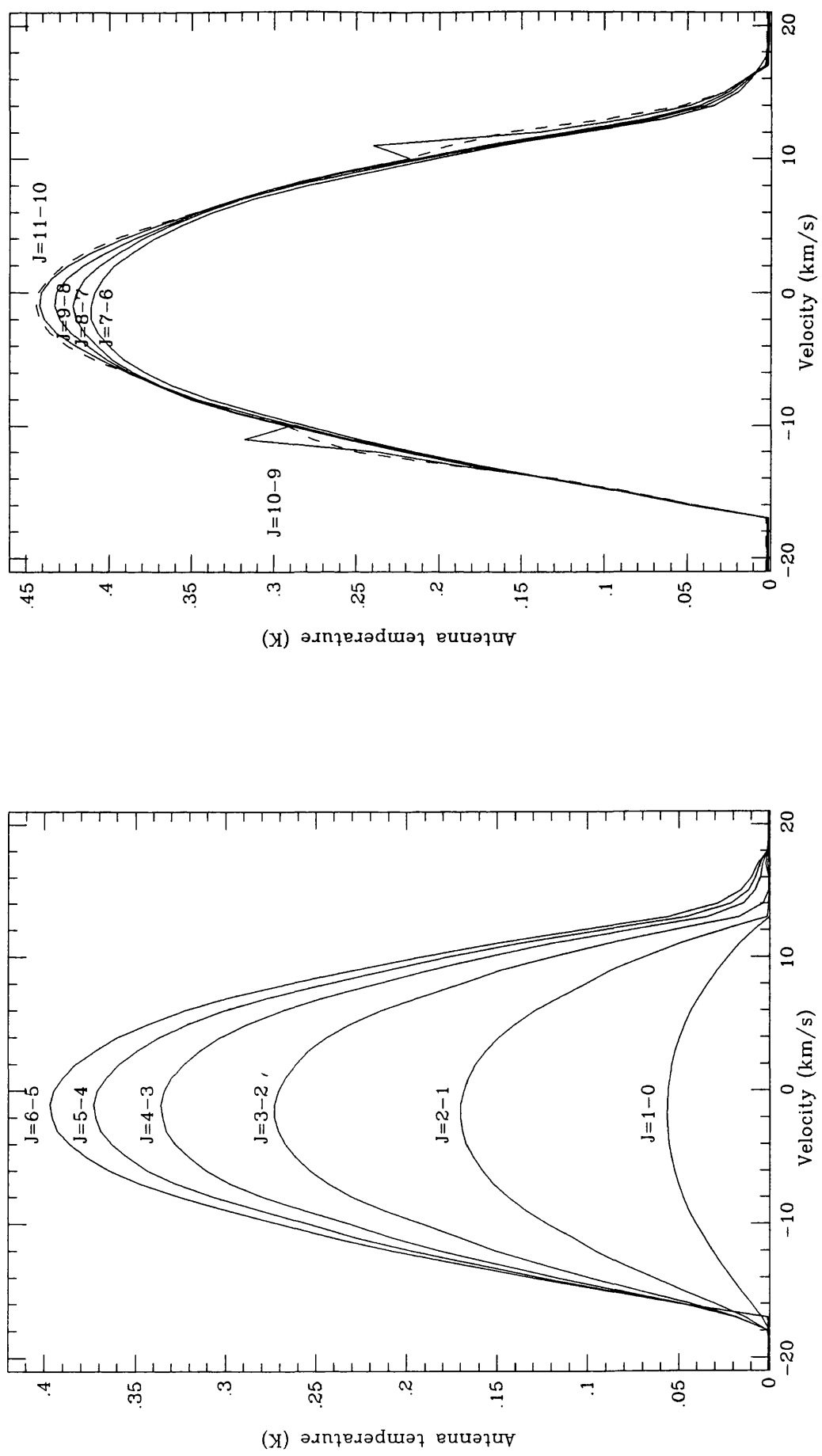
### 5.3.3 OH26.5+0.6

From the previous chapter, the calculated gas mass loss rate is extremely high,  $2.7 \times 10^{-4} M_{\odot}/\text{yr}$ . Such a high mass loss rate suggests that the star is in a superwind phase. This phase only lasts a small fraction of the total life time of the AGB phase. Thus, the assumption of the steady mass loss rate may break down here. There may have been a period in the past when the mass loss rate was much lower. With this reasoning, the CO density in the outer envelope would be much lower than estimated from the constant outflow. Coupled with the fact that very high mass loss rate leads to extremely low temperature in the outer part of the envelope ( $\sim 2.8\text{K}$ ), the resulting flux in low rotational transitions are much less than expected for the mass loss rate. This is because the temperature is too low to even excite the CO molecule to the first rotational transition.

In order to model this source correctly, we should take into account the variable mass loss rates over the past  $10^4 - 10^5$  yrs. Instead, we take a discontinuity in mass loss rate, i.e., close to the star, mass loss rate is  $2.7 \times 10^{-4} M_{\odot}/\text{yr}$ , and farther out in the envelope, the mass loss rate is  $2.7 \times 10^{-5} M_{\odot}/\text{yr}$ , which is still a reasonable value for a star at the tip of the AGB. The antenna temperature of the high rotational transitions are thought to be representative of the present high mass loss nature of the star. In the outer envelope, the density may have been less, assuming that the superwind phase only occurred in the past 1000 yrs. The density in the outer envelope then represents the density prior to the onset of this superwind phase. With a mass loss rate of  $2.7 \times 10^{-5} M_{\odot}/\text{yr}$  in the outer part, the CO photodissociation radius is  $6.3 \times 10^{17}$  cm. If the outflow velocity is constant, it will take  $8.8 \times 10^4$  yrs for the enhanced density, due to the superwind, to reach the outer part of the envelope. As the superwind approaches the outer part of the shell, the envelope size will progressively increase due to more CO self shielding to  $4 \times 10^{18}$  cm. Conversely, for an assumed superwind lifetime of  $8.8 \times 10^4$  yrs, the envelope would contain  $23 M_{\odot}$ , which is unacceptably large.

We adopt a temperature of  $r^{-0.9}$  law, instead of using the temperature structure calculated in the previous chapter. We find that the gas kinetic temperature, calculated from the heating, and cooling in the circumstellar shell lead to a too high antenna temperature compared with observations. Although the gas temperature falls to a very low value at the outer edge of the shell, CO molecules can still be excited by radiation closer in, to give a high antenna temperature, since the CO density is very high. We chose the mentioned

Figure 5.9: The predicted antenna temperature for each rotational transition of OH26.5+0.6 for a 10m telescope working at the diffraction limit for each transition.



Transition	beamwidth (")	$T_A$ (K)
1-0	65.5	0.06
2-1	32.8	0.17
3-2	21.8	0.27
4-3	16.4	0.34
5-4	13.1	0.37
6-5	10.9	0.40
7-6	9.4	0.41
8-7	8.2	0.42
9-8	7.3	0.43
10-9	6.6	0.44
11-10	6.0	0.44

Table 5.5: The predicted peak antenna temperatures for OH26.5+0.6.

power law since the temperature for J=2-1 transition matched the observations by Heske et al. 1990.

Table 5.5 shows the predicted antenna temperatures for all transitions up to J=11-10. The telescope diameter is assumed to be 10m, working at its diffraction limit for each transition (Table 5.5 and Figure 5.9). The antenna temperature keeps increasing as we go to higher transitions and the turn over may be just after J=11-10 line. Another feature to note from Figure 5.9 is the line profile of the J=10-9 transition shows a slight sign of maser emission. Up till now, the CO masers have never been observed but it has been predicted in the past (e.g., Morris 1975, 1980).

## 5.4 Summary

In this chapter, we have attempted to calculate gas mass loss rates in a self-consistent way for O-rich stars, using results from chapters 3 and 4. Only C-rich stars have been modelled in this way (Sahai 1990). Previously, the gas kinetic temperature is taken to be a power law with an exponent of 0.7 (Schonberg 1988). Also, the dust temperature is thought to follow another power law. Our models take into account the gas and dust temperatures as calculated from the heating and cooling in the envelopes, and from mid-

infrared modelling. We have chosen three stars with differing mass loss rates in order to see how these affect the calculations.

From modelling CO rotational lines, it is clear that mass loss is not a static phenomenon. The results from chapter 4 mainly depend on the dust mass loss rates, obtained from fitting the near and mid-infrared spectra, which correspond to dust lying relatively close to the star. The CO mass loss rates derived from the J=1-0 and J=2-1 transitions, however, measure the gas mass loss rate in the outer part of the envelopes. For GX Mon, there is evidence that mass loss was enhanced in the past by comparing the dust mass loss rates calculated from fitting the *IRAS* LRS spectra and that obtained from the 60 $\mu$ m. This is also reflected in the higher predicted temperature in the J=2-1 transition compared to observations, when fitting the line profile for the J=1-0 transition. This may also be partly due to the calibration uncertainty and that the assumption of the uniformly illuminated beam is not valid when the angular size of the source is comparable to the beam size.

In the case of IRC+10011, the dust mass loss rate derived from chapter 3 leads to too high CO J=1-0 and 2-1 lines. We have to reduce the mass loss rate in order to fit the line profiles obtained from various observations. The estimated mass loss is a factor of three lower than that calculated in the literature (e.g., GS, Knapp & Morris 1985).

An even more extreme case is OH26.5+0.6, which has a mass loss rate estimated by infrared continuum model and the momentum equation of  $2.7 \times 10^{-4} M_{\odot}/\text{yr}$ . The observations of this source show very low temperatures for both J=1-0 and 2-1 transitions, which has been interpreted as the envelope having too low temperature to even excite CO molecules into the first excitation state (Heske et al. 1990). Here, we propose an alternative interpretation for OH26.5+0.6. Since the dust mass loss rate is high, this leads to extremely high gas mass loss rate calculated from radiation pressure dominated system. We know that OH26.5+0.6 is an extreme case of OH/IR stars since it has a long period of 1570<sup>d</sup> (Suh, Jones & Bowen 1990). It is very likely that this source is in the superwind phase that only lasts a few thousand years. There must have been a period when the star was losing mass at a more tenuous rate. By probing the outer part of the envelope, the enhanced mass loss due to the superwind has not yet have time to reach this radius, and hence we are looking at the remnant of the red giant wind, which is much lower than estimated from the mid-infrared mass loss rate.

In order to model these stars successfully, the code should take into account the variable mass loss rates in the stellar life time. This is an ambitious project but may lead to a better understanding of mass loss, and hence stellar evolution on the AGB.

## Chapter 6

# Observations of Post-AGB Objects

In this chapter, we present the 10 and 20  $\mu\text{m}$  spectra of a few post-AGB objects. These stars are natural progression of AGB stars, after mass loss ceases. The dust shell becomes detached from the star, slowly revealing the stellar photosphere which has been obscured due to continuous mass outflow. A number of these sources were observed using the Cool Grating Spectrometer 3 (CGS3), which had been commissioned on UKIRT in July 1990. They are divided into two categories, one which are O-rich, while the other has C-rich photosphere.

### 6.1 The Cooled Grating Spectrometer 3

CGS3, a common-user 10  $\mu\text{m}$  and 20  $\mu\text{m}$  grating spectrometer was built at University College London. It was commissioned on UKIRT in July, 1990. The spectrometer contains an array of 32 discrete As:Si photoconductive detectors, and three interchangeable, permanently mounted gratings, covering the 10  $\mu\text{m}$  and 20  $\mu\text{m}$  atmospheric windows. Two grating settings give a fully sampled 64-point spectrum of the chosen waveband. The two low-resolution gratings were used for the observations described here. The 10  $\mu\text{m}$  low resolution filter covers the wavelength range between 7.4–13.3  $\mu\text{m}$ , with a resolution of 55. The 20  $\mu\text{m}$  filter covers the range between 15.4–24.1  $\mu\text{m}$  with a resolution of 74. The high resolution grating, with a resolution of 330, operates in the 10  $\mu\text{m}$  region only. The break in the 10 and 20  $\mu\text{m}$  spectra is due purely to the atmospheric absorption by  $\text{CO}_2$  and  $\text{H}_2\text{O}$ ,

which covers the region between 13.5 to 16 $\mu$ m. The sensitivity for both the low resolution filters are as follow : the signal which gives 1 $\sigma$  in 1 sec with the 10 $\mu$ m filter is 1Jy, while it is 4Jy for the 20 $\mu$ m filter.

## 6.2 The nature of dust around HD 161796 and HD 179821

Ground-based 7.4–24 $\mu$ m spectra of two post-AGB objects, HD 161796 and HD 179821, show emission features at 10–12 $\mu$ m and at 19 $\mu$ m. These features also appear to be present in the *IRAS* LRS spectrum of another post-AGB object, Roberts 22. HD 161796 and HD 179821 also exhibit a very rapid increase in flux between 13 $\mu$ m and 15.5 $\mu$ m. In view of the O-rich photosphere of HD 161796, and the presence of OH maser emission around all three objects, we ascribe these features to various oxides. However, the observed spectral features are quite different from the canonical silicate features observed in most O-rich giants. The 10–12 $\mu$ m and 19 $\mu$ m bands may be due to olivines, while the rapid rise in flux between 13 $\mu$ m and 15.5 $\mu$ m may be due to iron oxides. We argue that HD 161796 and the bipolar nebulae Roberts 22 and NGC 6302 have all undergone the third dredge-up, with most of the dredged-up carbon having been converted to nitrogen by envelope-burning. C-rich grain material, produced during the interval between the end of the third dredge-up, and the moment when envelope-burning finally reduced the [C]/[O] ratio below unity again, could be responsible for the UIR bands now being excited in Roberts 22 and NGC 6302.

### 6.2.1 Introduction

It is known that low and intermediate mass stars evolve from red giants on the asymptotic giant branch (AGB) to become planetary nebulae. Objects in transition between these two phases are difficult to find, since the time it takes a star to pass through the transition phase (post-AGB) is comparatively short. Following the AFGL and *IRAS* surveys, a class of post-AGB objects, supergiants of intermediate spectral type, has been identified (Lamers et al. 1986; Parthasarathy & Pottasch 1986). Many of these objects are associated with optically bright stars, with an infrared excess due to detached dust shells, hence the resulting energy distributions show doubly peaked profiles (see e.g., Kwok et al. 1989; van der Veen et al. 1988). They are believed to be low core mass stars ( $\sim 0.6 M_{\odot}$ ) in

the preplanetary nebula (PPN) phase, rapidly transiting from the AGB to the planetary nebula stage. Abundance analyses show some of them to be metal-poor (Bond 1991), and their low surface gravity reflects their small stellar mass and high luminosity. Here, we report ground-based 7.4–24 $\mu\text{m}$  spectra of two of these objects and compare them to those of other PPN.

### 6.2.2 Observations

We observed HD 161796 (= IRAS 17436+5003) and HD 179821 (= AFGL 2343 = IRAS 19114+0002) in May 1991 with the 3.8m UKIRT using CGS3. All observations were made through a 5.5 arcsec circular aperture, and the spectral resolution, as determined from the FWHMs of ionic forbidden lines in planetary nebula spectra, was 0.18 $\mu\text{m}$  for the 10 $\mu\text{m}$  spectra, and 0.27 $\mu\text{m}$  for the 20 $\mu\text{m}$  spectra.

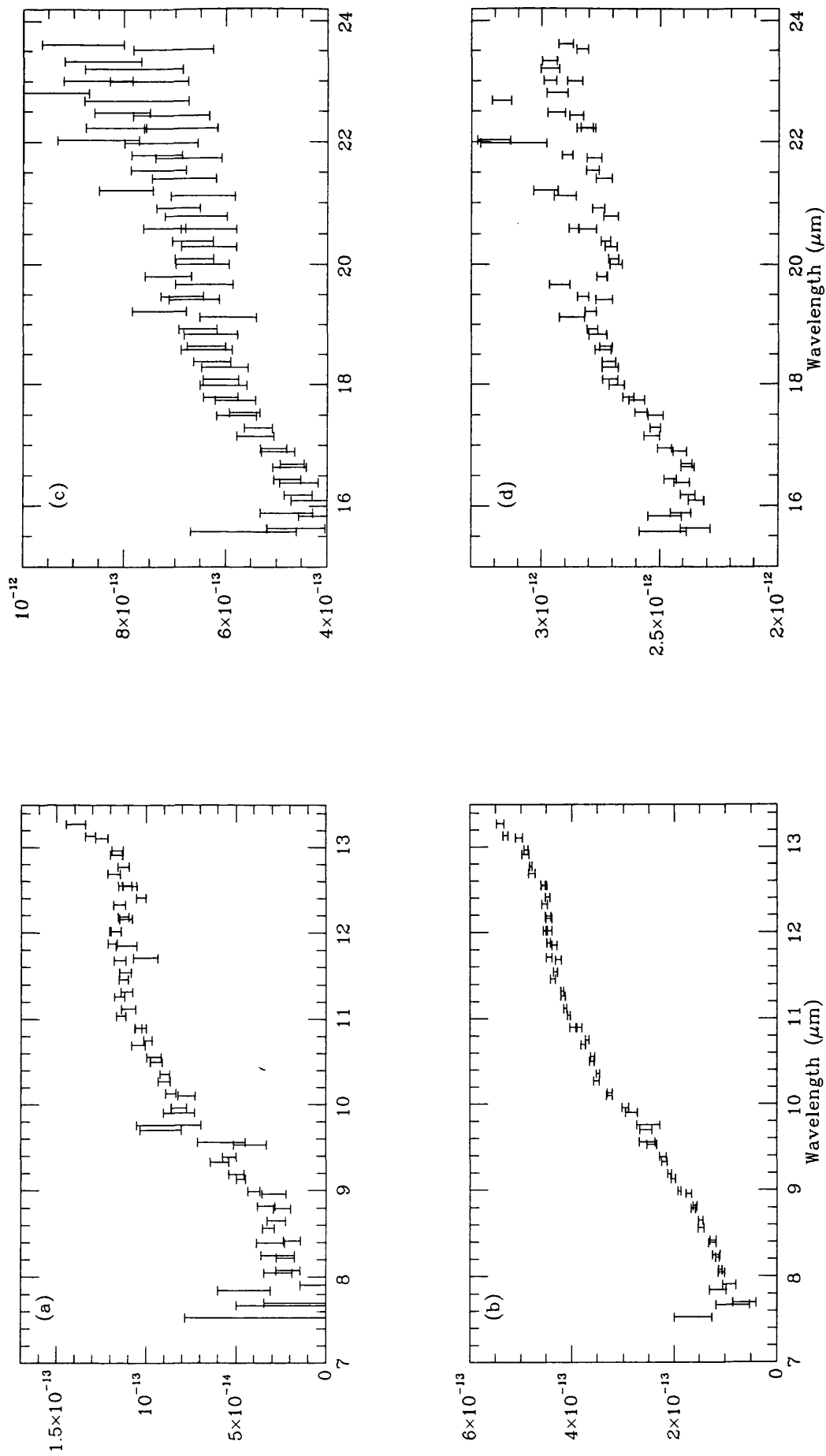
The spectra were flux calibrated using  $\alpha$  Boo as a standard. We were not able to completely cancel the telluric ozone feature at 9.7 $\mu\text{m}$ , hence the residual structure in the spectrum of HD 161796 at 9.7 $\mu\text{m}$  should be ignored. The flux levels of the 10 $\mu\text{m}$  spectra were found to be in good agreement with those of the respective *IRAS* LRS spectra, but the flux level of the 20 $\mu\text{m}$  spectrum of HD 161796 required a downwards adjustment of 20% to agree with the LRS flux level, while the 20 $\mu\text{m}$  spectrum of HD 179821 required an upwards adjustment of 30%.

The CGS3 spectra are shown in Figure 6.1, with the error bars representing the  $1\sigma$  statistical uncertainties in the fluxes. The rather large error bars associated with the 20 $\mu\text{m}$  spectra were due to poorer than average atmospheric conditions at the time the spectra were acquired.

### 6.2.3 Discussion

HD 161796 and HD 179821 have been classified as F3 Ib and G5 Ia, respectively (Ferne & Garrison 1984; Hrivnak, Kwok & Volk 1989). Their overall energy distributions (Figure 6.2; van der Veen et al. 1989; Humphreys & Ney 1974) show doubly peaked profiles, typical of post-AGB sources. The near-infrared and visible emission is due to direct stellar photospheric radiation, while the mid- and far-infrared emission probably originates in a detached dust shell ejected during the AGB phase. In contrast to many well-known PPNe, the atmosphere of HD 161796 has solar oxygen and carbon abundances, with

Figure 6.1: The CGS3 10 and 20 $\mu$ m spectra of HD 161796 (a and c) and HD 179821 (b and d). The flux unit is in  $W\ m^{-2}\ \mu m^{-1}$ . The error bars represent 1  $\sigma$  uncertainty in the observed fluxes.



nitrogen enhanced by 0.9 dex relative to solar, while metals (ie., Fe) are poor (Luck, Bond & Lambert 1990). HD 161796 and HD 179821 both show OH maser emission (Likkell et al. 1991), again indicative of an O-rich circumstellar environment.

The 7.4–24 $\mu$ m spectra of the two objects are very similar. They have very weak, broad 10–12 $\mu$ m features. Their spectra rise sharply between 13 $\mu$ m and 15.5 $\mu$ m and peak around 25 $\mu$ m (examination of the lower resolution *IRAS* LRS spectra extracted from the data base confirms that this sharp rise is real, and not an artifact of our CGS3 calibration procedures). There is a distinct feature in the long wavelength region peaking at about 19 $\mu$ m. The emission features observed in these two objects are quite different from those observed in most O-rich giants. To some extent, this reflects the low emission temperature of the dust in these sources ( $\sim 150$ K) as compared to O-rich giants ( $\sim 1000$ K). However, the sharp rise in the emission between 13 and 15.5 $\mu$ m, as well as the emission feature peaking around 19 $\mu$ m, has not been observed before in any spectrum of an O-rich star.

Figure 6.3 compares these spectra with those of other well known PPNe. One characteristic of all the comparison objects (Roberts 22, IRAS 22272+5435 and IRAS 07134+1005) is the presence of the UIR features at 3.3, 6.2 and 7.7 $\mu$ m, commonly ascribed to polycyclic aromatic hydrocarbons (PAHs, Leger & Puget 1984; Allamandola, Tielens & Barker 1985), which are absent in the spectra of HD 161796 and HD 179821. The *IRAS* LRS spectrum of Roberts 22 (= He 3-404) shows a 10–12.5 $\mu$ m feature as well as a very broad band peaking between 17 and 22 $\mu$ m. The former feature is similar to the 10–12 $\mu$ m feature present in the spectra of HD 161796 and HD 179821, while the 19 $\mu$ m feature present in their CGS3 spectra may correspond to the broad 17–22 $\mu$ m feature seen in the LRS spectrum of Roberts 22. The other two PPNe also show broad-band emission features in their LRS 8–23 $\mu$ m spectra (Figure 6.3; Kwok et al. 1989; Buss et al. 1990), including the 21 $\mu$ m band discovered by Kwok et al. (1989) However, the broad feature peaking at 12 $\mu$ m in their spectra extends out to 17 $\mu$ m, and appears to differ from the 10–12 $\mu$ m features present in the spectra of Roberts 22, HD 161796 and HD 179821. The photosphere of IRAS 22272+5435 is C-rich (Hrivnak & Kwok 1991), and the 12 $\mu$ m feature in the spectra of it and IRAS 07134+1005 is thought to be due to PAH clusters or hydrogenated amorphous carbon (HAC) grains (Buss et al. 1990), with the 11.4 $\mu$ m feature due to SiC also probably present. The fact that HD 161796 is O-rich (Luck et al. 1990) indicates that the 10–12 $\mu$ m and 19 $\mu$ m features observed in its spectrum are likely to be due to ox-

Figure 6.2: Infrared energy distributions of HD 161796 and HD 179821. The open circles are the near infrared photometric data for HD 161796 from Humphreys & Ney (1974); the stars are the near infrared photometric from van der Veen et al. (1989); the solid dots are the colour-corrected *IRAS* PSC fluxes and the crosses are the CGS3 data.

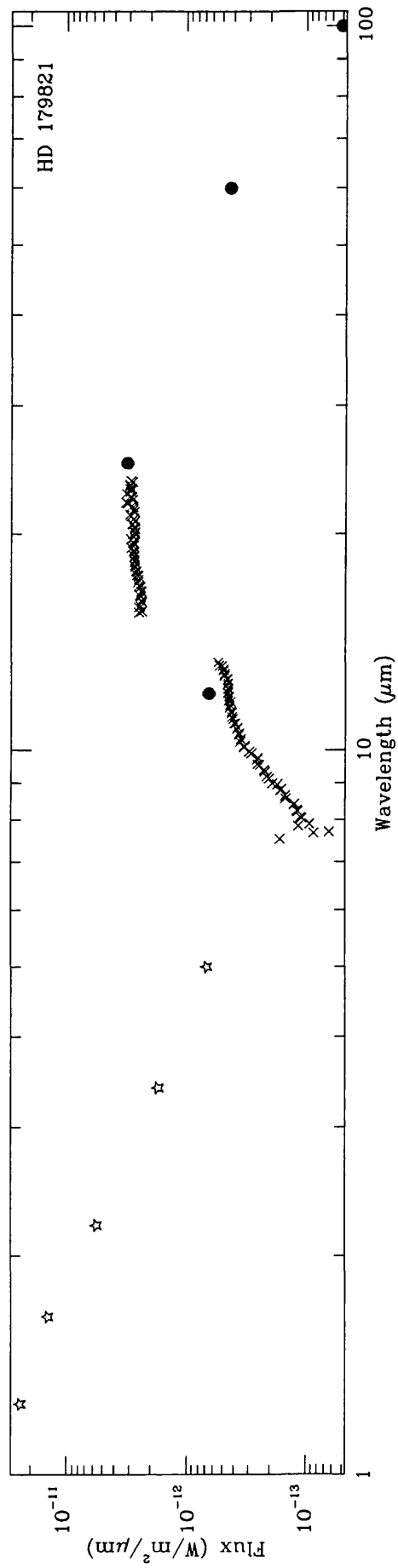
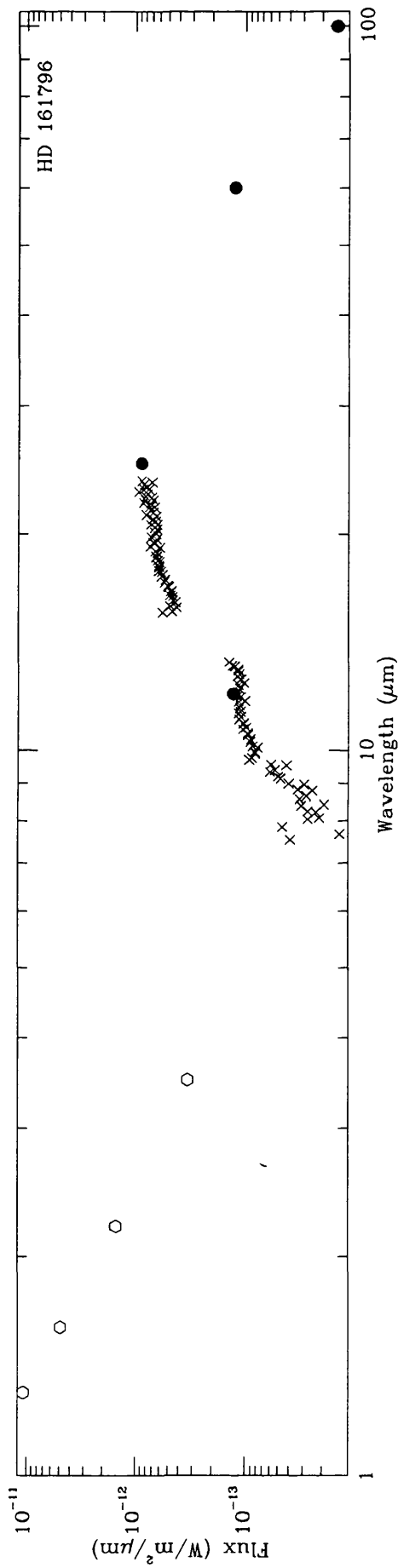
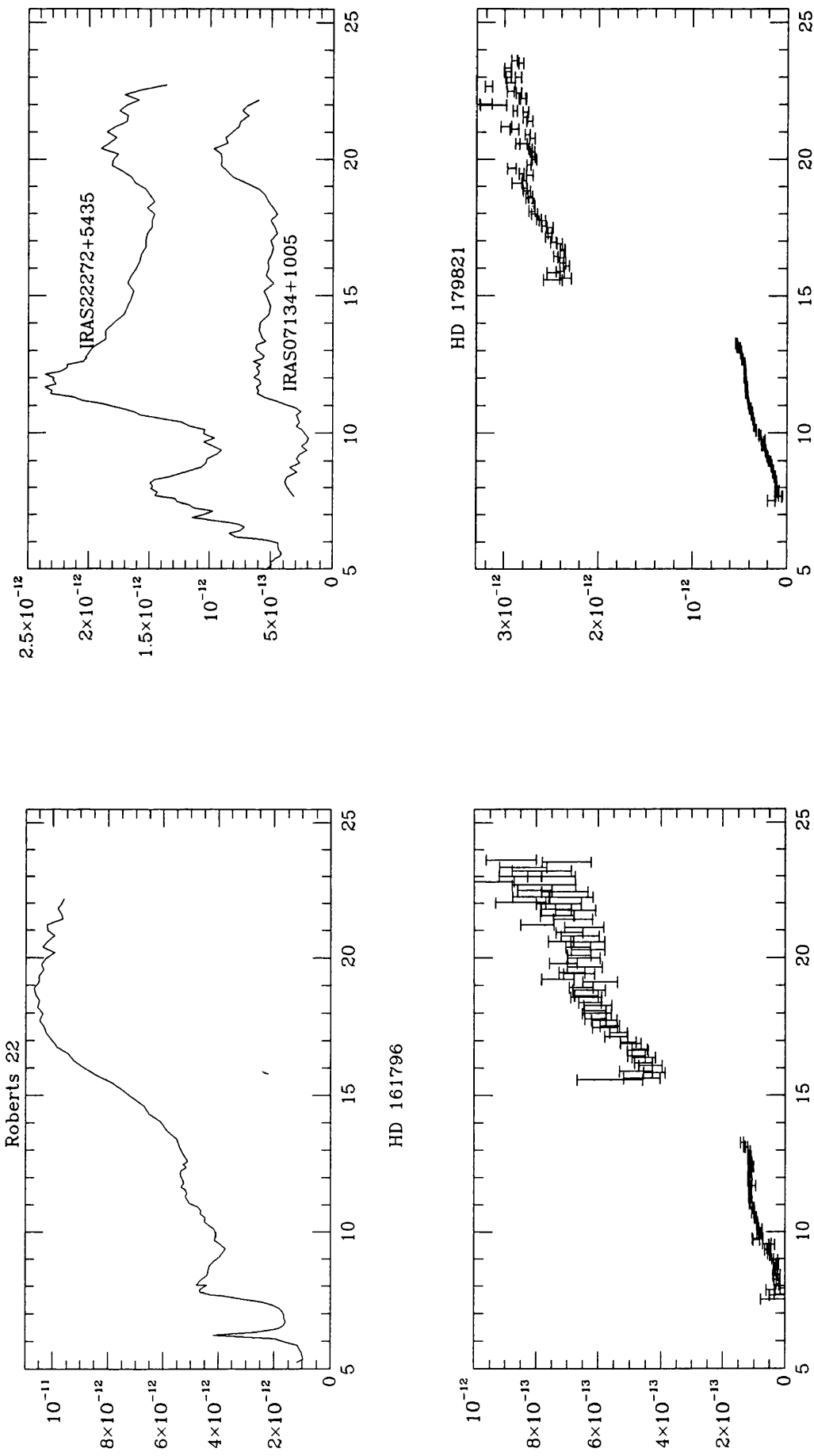


Figure 6.3: The CGS3 spectra of HD 161796 and HD 179821 are compared with the *IRAS* LRS spectra of three comparison sources. The flux unit is in  $W m^{-2} \mu m^{-1}$ . The spectrum of *IRAS* 22272+5435 between 5–8  $\mu m$  is taken from Buss et al. (1990) and the 5–8  $\mu m$  of Roberts 22 is from Cohen et al. (1989).



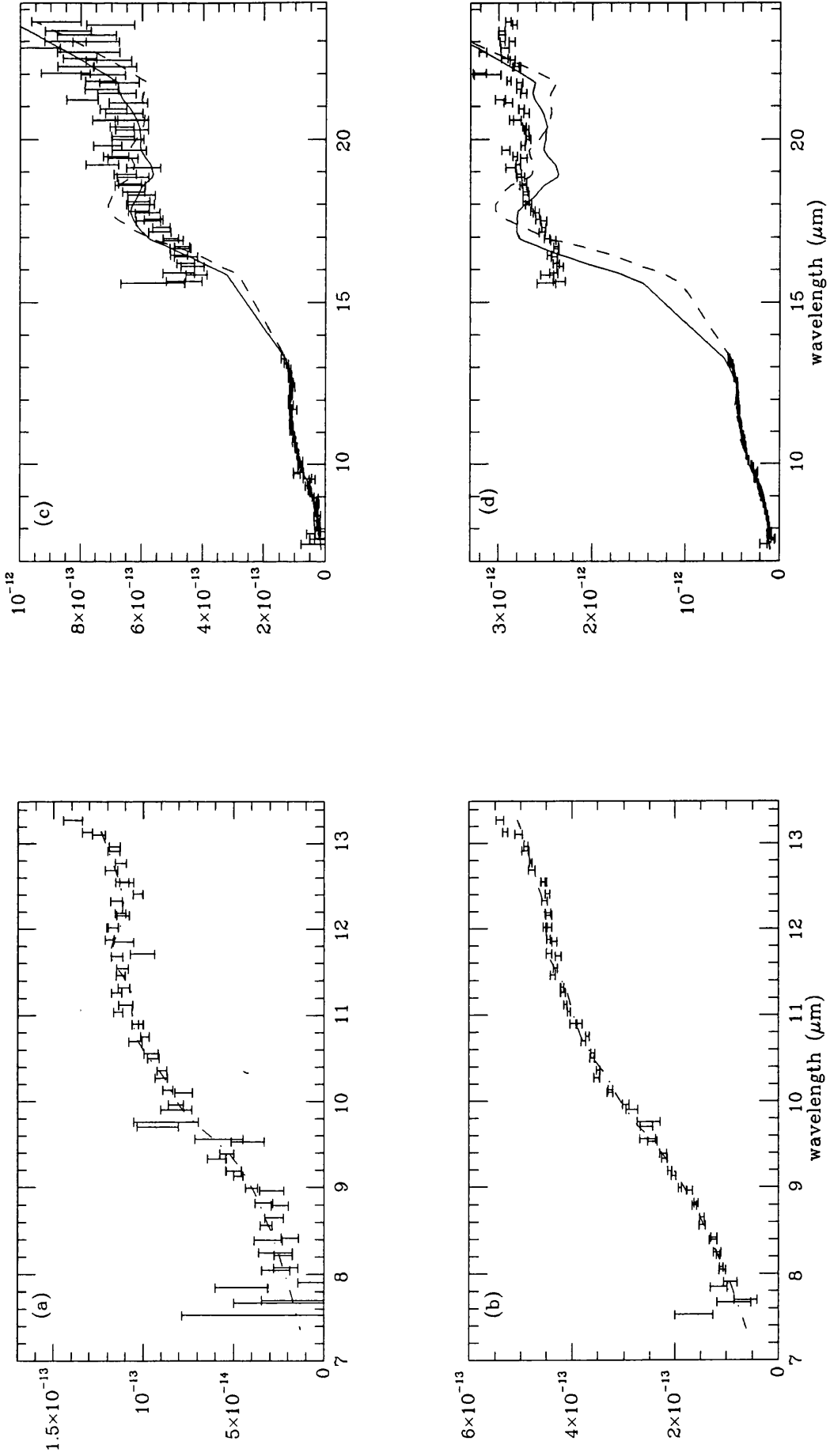
Sources	BB× emissivity		Olivine		Magnetite		$\chi^2/N_f$	
	fraction	T(K)	fraction	T(K)	fraction	T(K)		
HD 161796	0.73	157	0.27	88			1.57	a
	0.83	159	0.17	84			3.30	b
	0.72	161	0.27	93	0.01	70	2.37	b
HD 179821	0.88	157	0.12	91			0.91	a
	0.79	158	0.21	86			20.98	b
	0.48	225	0.34	95	0.18	95	12.05	b

Table 6.1:  $\chi^2$  fitting parameters for both stars : (a)  $10\mu\text{m}$  fit only, (b) 10 and  $20\mu\text{m}$  fit. The heading ‘fraction’ refers to the fraction of calculated flux produced by each component.

ide carriers. The prominent  $21\mu\text{m}$  feature in the spectra of the two IRAS-named sources peaks significantly longwards of the  $19\mu\text{m}$  features seen in the spectra of HD 161796 and HD 179821, consistent with the  $21\mu\text{m}$  band being due to a different (C-rich) carrier (see section 6.3).

Disordered olivine,  $(\text{Mg,Fe})_2\text{SiO}_4$ , shows a broad band peaking at  $10\text{--}11\mu\text{m}$ , with another peak at  $18\text{--}19\mu\text{m}$  (Kratschmer & Huffman 1979, Koike & Tsuchiyama 1992), so olivine is a possible candidate for identification with the features seen in the spectra of HD 161796 and HD 179821. We have fitted our observed spectra using a  $\chi^2$  minimization routine based on the one described for the  $10\mu\text{m}$  region by Aitken et al. (1979), Aitken & Roche (1982) and Whitmore (1986). The program has been extended (Sylvester 1992, private communication) to include extra grain materials, and to enable the fitting of  $20\mu\text{m}$  spectra simultaneously with  $10\mu\text{m}$  spectra. First of all, we fitted just the  $10\mu\text{m}$  spectra of HD 161796 and HD 179821, using a combination of two components: (a) a featureless continuum having a  $\lambda^{-1}$  emissivity; and (b) material with the grain properties measured for radiation-disordered olivine by Kratschmer & Huffman (1979). Good fits were obtained to the  $10\mu\text{m}$  spectra of both stars, as shown by the low values obtained for  $\chi^2/N_f$  (Table 6.1). The relatively low temperature of the olivine component ( $\sim 90$  K, Table 6.1) shifts the peak of the feature to longer wavelengths than normally encountered. The entries under ‘fraction’ in Table 6.1 represent the fraction of the flux at  $10.0\mu\text{m}$  contributed by each component.

Figure 6.4: The least square fit to the spectra of HD 161796 and HD 179821 using material with  $\lambda^{-1}$  emissivity (see Table 6.1) (a)  $10\mu\text{m}$  fit using olivine of HD 161796 (dash) (c) 10 and  $20\mu\text{m}$  fit using olivine (dash); olivine and magnetite (solid) for HD 161796; (b)  $10\mu\text{m}$  fit using olivine of HD 179821 (dash) (d) 10 and  $20\mu\text{m}$  fit using olivine (dash); olivine and magnetite (solid) for HD 179821.



Although excellent fits to the  $10\mu\text{m}$  spectra were obtained using just olivine and continuum components, a simultaneous fit to the  $10$  and  $20\mu\text{m}$  spectra using just these two components produced a much worse fit (dashed lines in Figures 6.4(c) and 6.4(d); see also Table 6.1). In particular, the rapid increase in flux between  $13$  and  $15.5\mu\text{m}$  could not be matched. Cox (1990) has discussed the potential importance of iron oxides for the interpretation of mid-infrared astronomical spectra. As shown in his Figure 3, the infrared absorption spectra of  $\text{Fe}_3\text{O}_4$  (magnetite) and  $\text{Fe}_2\text{O}_3$  (maghemite) both show low-level featureless absorption in the  $10\mu\text{m}$  region, along with a rapid rise in absorption between  $13$  and  $16\mu\text{m}$ . We therefore carried out a three-component fit to our observed spectra, adding a magnetite component to the olivine and blackbody (BB)  $\times$  emissivity components. The optical constants for magnetite are from Lien 1990. As shown in Figure 6.4(c) and 6.4(d) (solid line) and Table 6.1, improved fits are obtained by the addition of a magnetite component. The  $10\mu\text{m}$  region is largely unaffected by the addition of a magnetite component. However, even with the addition of magnetite, the fits to the  $20\mu\text{m}$  region could clearly do with further improvement.  $\text{Fe}_3\text{O}_4$  possesses prominent emissivity peaks at  $17$  and  $25\mu\text{m}$  and these do not appear to be present in the observed spectra of HD 161796 and HD 179821. On the other hand, compared to the  $\text{Fe}_3\text{O}_4$  spectrum, the spectrum of  $\gamma\text{-Fe}_2\text{O}_3$  reproduced by Cox (1990) shows a sharper rise between  $13$  and  $16\mu\text{m}$  and a much flatter plateau longwards of  $16\mu\text{m}$ . We would therefore expect  $\gamma\text{-Fe}_2\text{O}_3$  to provide an improved fit, but suitable optical constants are unfortunately unavailable to us. The observed peak at  $18\text{--}19\mu\text{m}$  is not properly matched by the radiation-disordered silicate of Kratschmer & Huffman (1979). Koike & Tsuchiyama (1992) have found that the  $18\mu\text{m}$  peak of amorphous olivine shifts to longer wavelengths upon heating or hydration, so it would be valuable to have optical constants for such material.

Aluminum oxide is an expected high temperature condensate in O-rich outflows (cf. Tielens 1989). Aluminum oxides show a prominent band around  $12\mu\text{m}$ , and they may contribute to the observed  $10\text{--}12\mu\text{m}$  feature in these two HD stars. Thermodynamic considerations suggest that iron can condense in the metallic form or become incorporated into silicates, depending on the physical conditions. It is conceivable that kinetic considerations favour nucleation and growth of iron oxides instead. Alternatively, metallic iron may simply 'rust' in the  $\text{H}_2\text{O}$ -rich outflow from these objects. In all probability, the  $12\mu\text{m}$  feature in the spectra of HD 161796, HD 179821, Roberts 22 have the same carrier.

Likewise, we expect the  $19\mu\text{m}$  feature to be due to the same material in all three sources.

The olivine grain component is found to have a temperature of  $\sim 90\text{K}$  around both stars (Table 6.1). We find, from a detailed spherical transfer model for silicate grains around a  $6000 L_{\odot}$  F-star, that for a standard MRN grain size distribution, such a grain temperature corresponds to a typical distance of  $2.4 \times 10^{16}$  cm from the star. The measured CO expansion velocities are  $14 \text{ km s}^{-1}$  and  $33 \text{ km s}^{-1}$  for HD 161796 and HD 179821, respectively (Likkell et al. 1991). The corresponding ages since shell ejection would therefore be 540 years for HD 161796 and 230 years for HD 179821. Such ages are broadly consistent with the transition times expected for H-shell burning nuclei with masses between  $0.60$  and  $0.64 M_{\odot}$  (see Figure 6.2 of Schoenberner 1989).

Roberts 22, whose  $10\text{--}25\mu\text{m}$  spectrum is similar to those of HD 161796 and HD 179821 (Figure 6.3), is a bipolar nebula with an A2 Ie central star and OH maser emission (Allen, Hyland & Caswell 1980). The dust around it appears to be concentrated in a circumstellar disk, but mass ejection at the tip of the AGB may have occurred preferentially in the equatorial plane. The high-excitation bipolar planetary nebula NGC 6302 resembles Roberts 22 in that its infrared spectrum simultaneously exhibits the signatures of C-rich material (the  $8.6$  and  $11.3\mu\text{m}$  UIR bands; Roche & Aitken 1986) and O-rich material (an  $18\mu\text{m}$  silicate emission feature is prominent in a CGS3 spectrum which we have acquired; in addition, Payne, Phillips & Terzian (1988) suggest that an OH maser is associated with the nebula). The nebula itself is O-rich (Aller et al. 1981). Lester & Dinerstein (1984) found the  $10\mu\text{m}$  emission from NGC 6302 to be concentrated in a disk-like configuration. Bipolar type I planetary nebulae, such as NGC 6302, are believed to originate from stars at the high mass end of the PN progenitor star mass distribution (Zuckerman & Gatley 1988). The nitrogen abundance is significantly enhanced in NGC 6302 (Aller et al. 1981), but the total C+N+O abundance significantly exceeds solar, once the highest ionization stages of C, N and O are allowed for. Since the CN and CNO cycles operating before the first and second dredge-ups cannot increase the total C+N+O abundance, this indicates that the third dredge-up of material from the helium burning regions must have occurred, followed by the conversion of much of the dredged-up carbon to nitrogen by envelope-burning (via the CN cycle at the bottom of the hydrogen envelope, cf. Renzini & Voli 1981). There would have been a phase, immediately after the third dredge-up had occurred, when the envelope was C-rich, until envelope burning by the CN cycle once

again reduced the  $[C]/[O]$  ratio below unity (Brett 1991). O-rich grains would have been produced before the third dredge-up and after the envelope-burning, with C-rich grains produced immediately after the third dredge-up. With the subsequent evolution of the central star to higher temperatures, the conditions in the ejected nebulosity became favorable for the excitation of the UIR bands, which would be seen superposed on the emission by the O-rich grains. A similar scenario seems applicable to Roberts 22.

Luck et al. (1990) found nitrogen to be enhanced by 0.9 dex relative to solar in the spectrum of HD 161796, but at the same time found carbon and oxygen to have solar abundances. This indicates that in these low mass ( $\simeq 1M_{\odot}$ ) stars the dredge-up of carbon has been followed by envelope burning, as well (Luck et al. 1990). It is somewhat surprising that these two post-AGB stars have undergone envelope burning, since their initial main sequence masses, and current core masses, are presumably smaller than those of Roberts 22 and NGC 6302. Since the C-rich UIR bands can be excited by stars as cool as 5000 K (Buss et al. 1990; 1992; Hrivnak & Kwok 1991), their absence in the spectra of HD 161796 and HD 179821 may imply the absence of a C-rich phase during the evolution of these stars, which would require the envelope burning to have operated extremely quickly. Alternatively, a transient C-rich photospheric phase may have occurred sufficiently long ago that the C-rich ejecta are now far enough from the cool central star that the UIR bands are inefficiently excited. As the stars become hotter and emit more energetic photons, extended UIR emission may then become apparent. While other post-AGB supergiants of intermediate spectral type do manage to exhibit UIR band emission now (e.g., the Cygnus egg, IRAS 22272+5435, HR 4049), their photospheres are C-rich, so that C-rich material undoubtedly exists close to the stars, making it more easy to excite significant UIR band emission. The differences in stellar evolution between various types of post-AGB stars are presently not well understood. Further IR spectroscopic studies of post-AGB supergiants may be very useful to unravel these questions, where we emphasize that circumstellar dust may provide a memory of previous stellar evolution phases.

## 6.3 Mid-infrared spectroscopy of four $21\mu\text{m}$ emission band sources

In the previous section, we studied two post-AGB stars which exhibit silicate features, indicating their O-rich nature. Here, we report  $10\mu\text{m}$  and  $20\mu\text{m}$  spectroscopic observations of four C-rich post-AGB objects, which exhibit the unidentified emission feature at  $21\mu\text{m}$ . Three are from the list of Kwok et al. (1989), while the fourth, SAO 163075, is discovered to also exhibit a (weak)  $21\mu\text{m}$  emission feature. The  $10\mu\text{m}$  spectra of these objects exhibit UIR bands whose peaks all fall longwards of the usual peak wavelengths associated with such features. This may be related to the fact that they are the lowest excitation objects so far found to exhibit UIR emission bands. We also found narrow emission features superimposed on the long wavelength wing of the  $21\mu\text{m}$  emission bands of IRAS 04296+3429 and IRAS 22272+5435.

### 6.3.1 Introduction

It is generally believed that Asymptotic Giant Branch (AGB) stars are the precursors of planetary nebulae (PNe). IRAS discovered a significant number of objects which are thought to be post-AGB, i.e., transition objects between the AGB and PN phases. These vary from bipolar outflow sources to stars with detached dust shells, where the spectra of the latter show doubly peaked profiles due to the central star and the dust shell, respectively. Kwok et al. (1989) reported a group of these evolved objects, which exhibit a very strong  $21\mu\text{m}$  emission feature. All of the  $21\mu\text{m}$  band sources so far studied in detail in the optical have been found to have C-rich photospheres (e.g., Hrivnak & Kwok 1991).

Since all the sources with  $21\mu\text{m}$  emission features known to date show evidence for C-richness, the possible carriers are thought to be carbon-based (Kwok et al. 1989; Buss et al. 1990). Two of the sources (IRAS 22272+5435 and IRAS 04296+3429) show unusually strong  $3.4\mu\text{m}$  emission bands (Geballe et al. 1992).

### 6.3.2 Observations

We observed IRAS 04296+3429 and IRAS 22272+5435 (= SAO 34504) in October 1990; IRAS 07134+1005 (= SAO 96709) in May 1991 and SAO 163075 in May 1991, and June 1992 with the 3.8m UKIRT using CGS3 (see section 6.1). The spectral type are G0 Ia,

wavelength ( $\mu\text{m}$ )				assignment
IRAS 22272	IRAS 04296	IRAS 07134	Usual UIR Bands	
	8.01		7.7	aromatic C-C stretching band
8.34	8.39			
8.72			8.6	aromatic C-H in-plane bend
10.7	10.75	10.6		
11.55	11.47	11.55	11.25	aromatic C-H out-of-plane bend
12.20	12.21	12.28		
12.70	12.72		12.7	C-H out-of-plane bend for triply adjacent H atoms

Table 6.2: Wavelengths of various features seen in  $10\mu\text{m}$  spectra of  $21\mu\text{m}$  sources

G5 Ia, F5 I and F3 I, respectively.

The spectra were flux calibrated with respect to  $\alpha$  Tau,  $\alpha$  Boo and  $\beta$  Peg. The absolute flux levels at both  $10$  and  $20\mu\text{m}$  have been adjusted by small amounts to agree with the *IRAS* LRS spectra. The resulting spectra are shown in Figure 6.5

### 6.3.3 Discussion

From Figure 6.6, we can see that the  $10\mu\text{m}$  spectrum of IRAS 22272+5435 shows many features, which are thought to be associated to PAH molecules. Other sources in our sample also show similar emission features. The central wavelengths of these emission features are listed in Table 6.2, along with the possible corresponding identification.

The infrared emission of individual type of PAH cannot match the observed infrared spectra, but the ensemble of various types of 20–50 C atoms per molecule may be the explanation (Cohen, Tielens & Allamandola 1985). In the interstellar medium, the most stable PAHs are the ones with symmetric structures. Another explanation for the UIR bands are the HAC clusters (e.g., soot), which display emission features at  $6.25$  and  $7.7\mu\text{m}$  (Rosen & Novakov 1978). Note that the wavelengths of the emission features in the  $10\mu\text{m}$  spectra of the  $21\mu\text{m}$  feature objects are all longer than the wavelengths of the UIR features

Figure 6.5: The observed CGS3 spectra of 21  $\mu\text{m}$  sources. The flux unit is  $\text{W m}^{-2} \mu\text{m}^{-1}$ . The error bars represent a  $1\sigma$  uncertainty in the observed fluxes.

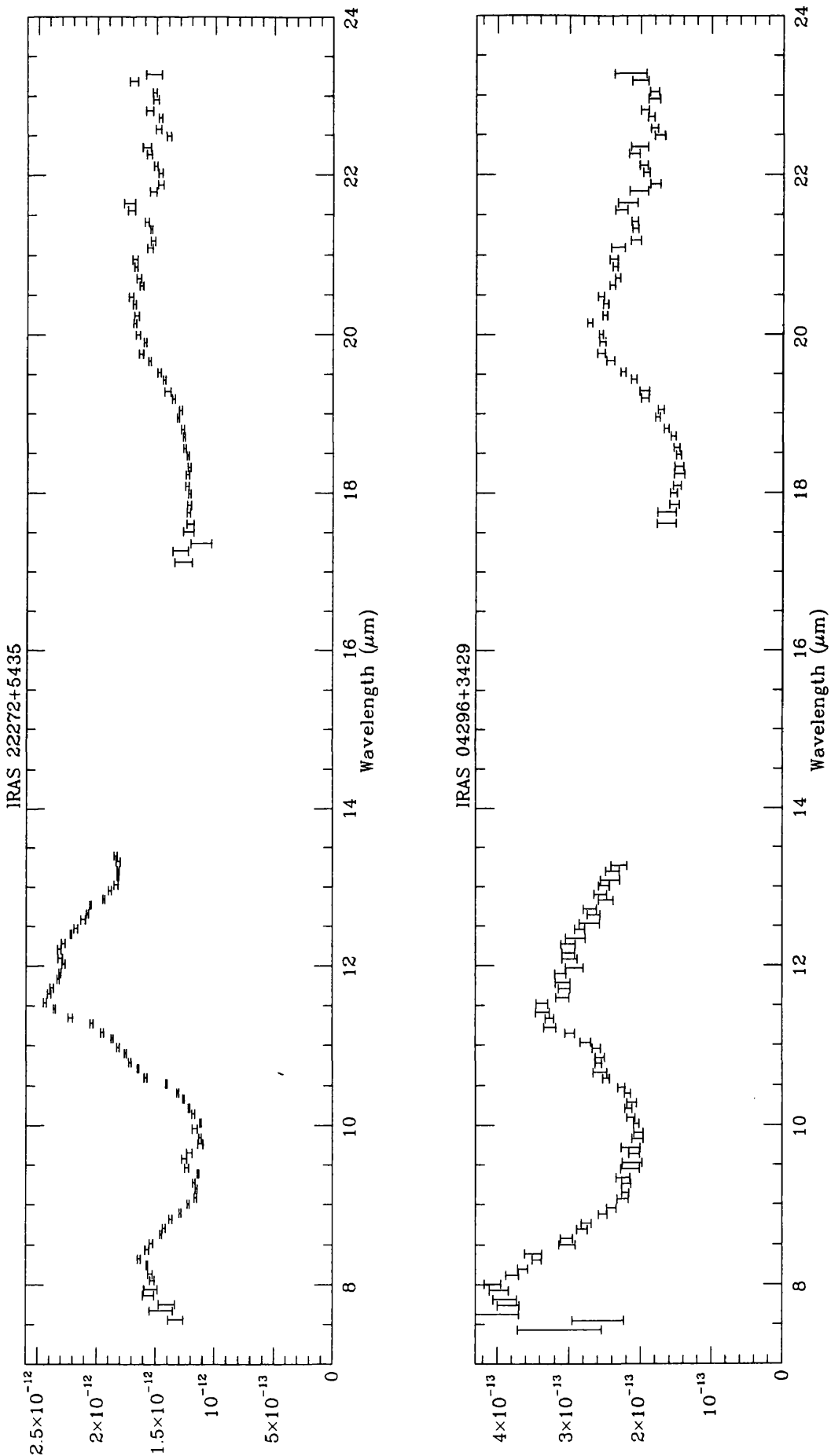
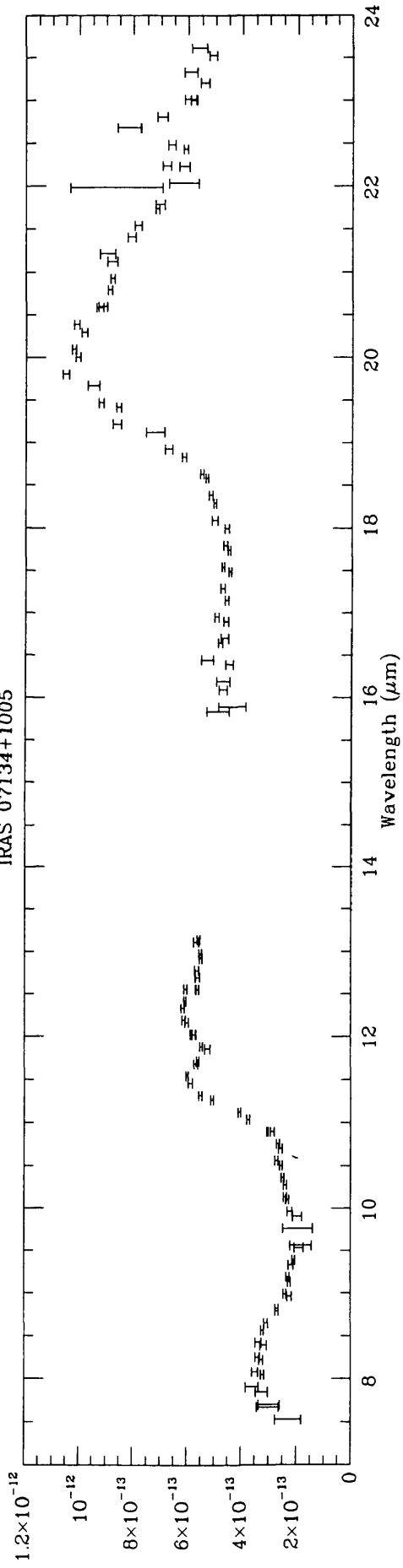


Figure 6.5: continued  
IRAS 07134+1005



SAO 163075

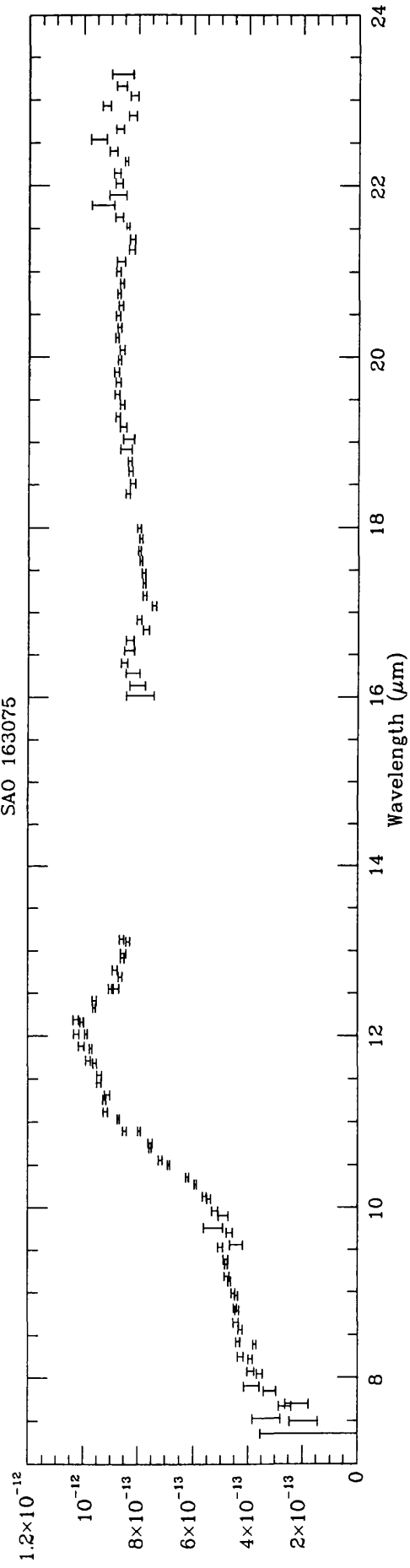
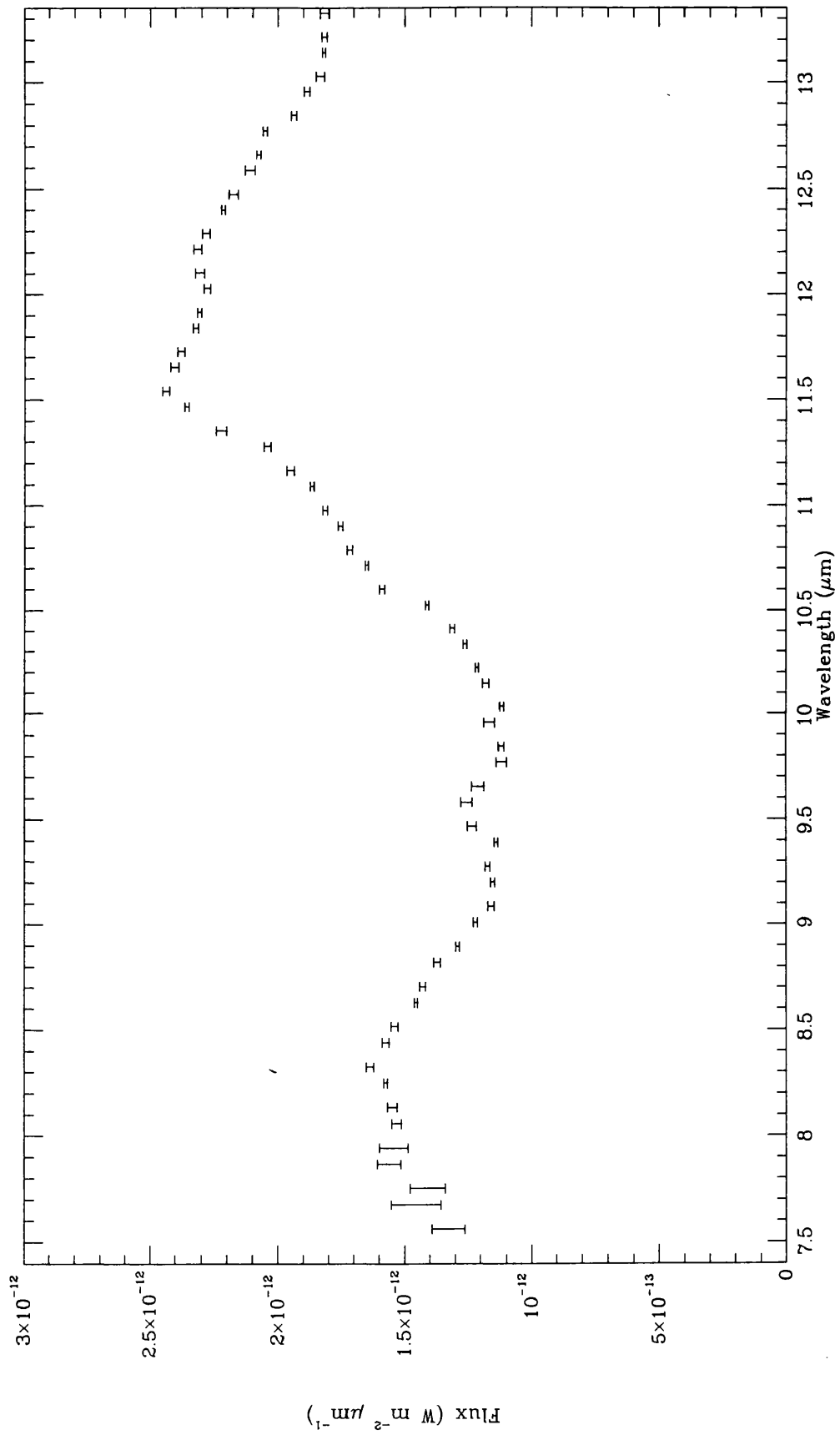


Figure 6.6: The CGS3 10 $\mu$ m spectrum of IRAS 04296+3429, showing the PAH features (see Table 6.2). The emission at 9.5 $\mu$ m is due to telluric ozone.



in PN, HII regions and reflection nebulae (see Roche, Aitken & Smith 1991). This may be due to the fact that the exciting photons from the F and G-type central stars (the latest objects so far found to exhibit the UIR bands) have lower energies than the photons from the sources more usually associated with UIR band emission, and hence can only excite lower excitation transitions of the hydrocarbon molecules involved. Variations in the strengths of these features may also be due to different compositions of PAH molecules. Each feature tends to have slightly different profile from one source to the next, which may be the results of different absorption bands in different PAH molecules. Cohen et al. (1985) discovered that more hydrogenated PAHs display features at longer wavelengths than less hydrogenated ones. It could be that temperatures in earlier spectral type stars are high enough to strip off hydrogen atoms from the PAH rings. Spectra of young PNe (e.g., M1-71) shows distinctly the  $11.3\mu\text{m}$  feature, which is produced by PAHs which have one hydrogen atom per ring (Cohen et al. 1985). The spectrum of SAO 163075 shows a very prominent  $12\mu\text{m}$  feature, with an emission at  $11.3\mu\text{m}$ . However, there is no evidence of the rise at the short wavelength end of the spectrum. The lack of the  $7.7\mu\text{m}$  feature is surprising, since it is one of the strongest feature in C-rich sources. From the infrared spectrum, it is likely that this source is C-rich, due to the  $11.3$ ,  $12.2$  and  $21\mu\text{m}$  features. Optical spectroscopy of this star will help determine its photospheric abundance in order to pin point the nature of its dust.

We also observed the  $17$ - $24\mu\text{m}$  spectral region of the four objects. In the case of IRAS 04296+3429 and IRAS 22272+5435 (see Figure 6.5), the extended long wavelength wing of the '21 $\mu\text{m}$  band' (which actually peaks at about  $20.2\mu\text{m}$ ) exhibits at least five subsidiary peaks, whose wavelengths do not correspond to any features present in the sky spectra taken at the same time, or in HITRAN theoretical atmospheric spectra for Mauna Kea. We also checked the  $20\mu\text{m}$  spectrum of the carbon-star GL 3068, which was observed on the same night as IRAS 04296+3429, but this was found to be smooth and featureless. Therefore, we believe the structure found in the  $21\mu\text{m}$  bands of IRAS 04296+3429 and IRAS 22272+5435 to be real. The peak wavelengths of the emission peaks are  $20.55$ ;  $21.05$ ;  $21.68$ ;  $22.38$  and  $23.02\mu\text{m}$ . These features may have a similar relation to the main peak at  $20.2\mu\text{m}$  as the  $3.4$  and  $3.5\mu\text{m}$  emission bands have to the well-known  $3.3\mu\text{m}$  emission feature seen in many objects (e.g., Geballe et al. 1985), i.e. they could be overtones of a fundamental transition. In this respect, it is interesting that the two sources, found to

Source	Spectral type	F(20 $\mu$ m)/F(18 $\mu$ m)	Comment
IRAS 20000+3239	G8Ia	0.17	<i>IRAS</i> LRS spectrum
IRAS 22272+5435	G5Ia	0.20	CGS3 spectrum
IRAS 23304+6147	G2Ia	0.40	<i>IRAS</i> LRS spectrum
IRAS 04296+3429	G0Ia	0.35	CGS3 spectrum
IRAS 07134+1005	F5I	0.90	CGS3 spectrum
SAO 163076	F3I	0.09	CGS3 spectrum

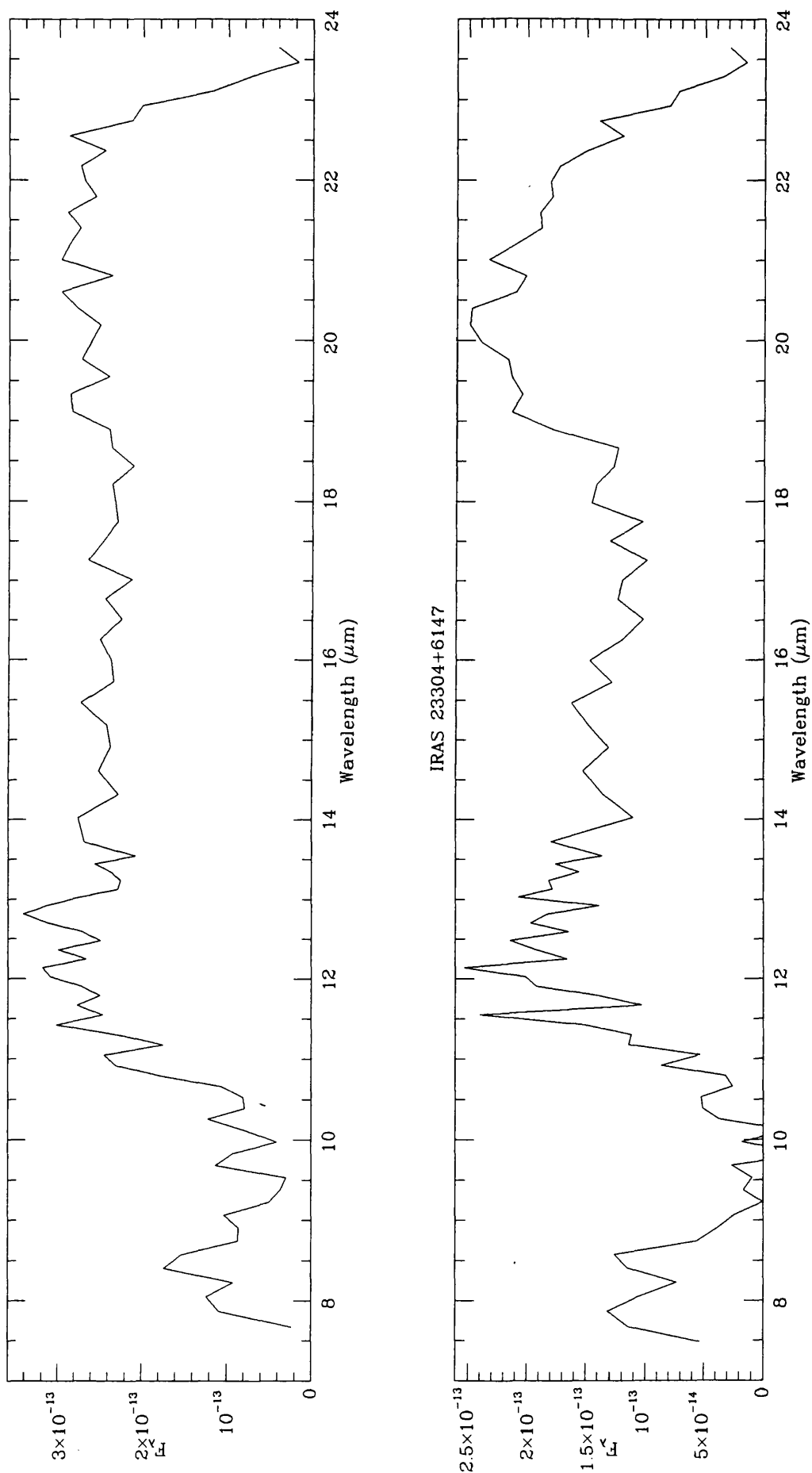
Table 6.3: Ratios of the 20:18 $\mu$ m fluxes for the 21 $\mu$ m objects.

exhibit subsidiary peaks in the red wing of their 21 $\mu$ m feature (IRAS 04296+3429 and IRAS 22272+5435), were found by Geballe et al. (1992) to have much stronger than normal 3.4 $\mu$ m and 3.5 $\mu$ m features, relative to the 3.3 $\mu$ m feature, whereas in the spectrum of IRAS 07134+1005, whose 21 $\mu$ m feature does not exhibit as obvious emission sub-peaks in its red wing (see Figure 6.5), the 3.3 $\mu$ m and 3.4 $\mu$ m features have their more usual ratio (Kwok, Hrivnak & Geballe 1990). Another possible explanation is that these peaks are the hot bands of the molecules responsible for the 21 $\mu$ m emission, e.g., the 2–1, 3–2, 4–3 transitions. The carrier of the 21 $\mu$ m feature is not conclusively established, but is believed to be carbon-based. Buss et al. (1990) suggested large PAH clusters or HAC grains (> 100 C atoms) pumped by visible photons.

The 21 $\mu$ m feature is also seen in many HII regions. Cox (1990) proposed that the feature is due to iron oxides. Also, Onaka, de Jong & Willems (1989) proposed that the weak 12 $\mu$ m features in some O-rich stars are due to aluminium oxide. However, since the sources studied in this section are C-rich, it is unlikely that oxides are carriers of these features.

There is also a relationship between the strength of the 21 $\mu$ m emission and the spectral type. The feature appears in spectral type as late as G8, as shown in the spectrum of IRAS 20000+3239 (Figure 6.7 from the *IRAS* LRS data base). If the spectra is normalised at 12 $\mu$ m, the apparent prominence of the 21 $\mu$ m feature increases in earlier spectral type, and reaches the maximum in IRAS 07134+1005 (see Table 6.3). The feature almost disappears in spectral type F3 (SAO 163075). The flux ratio of IRAS 23304+6147 in Table 6.3 is larger than expected. This may be due to the low signal-to-noise ratio in its spectrum. With this in mind, the correlation between the strength of the 21 $\mu$ m feature and

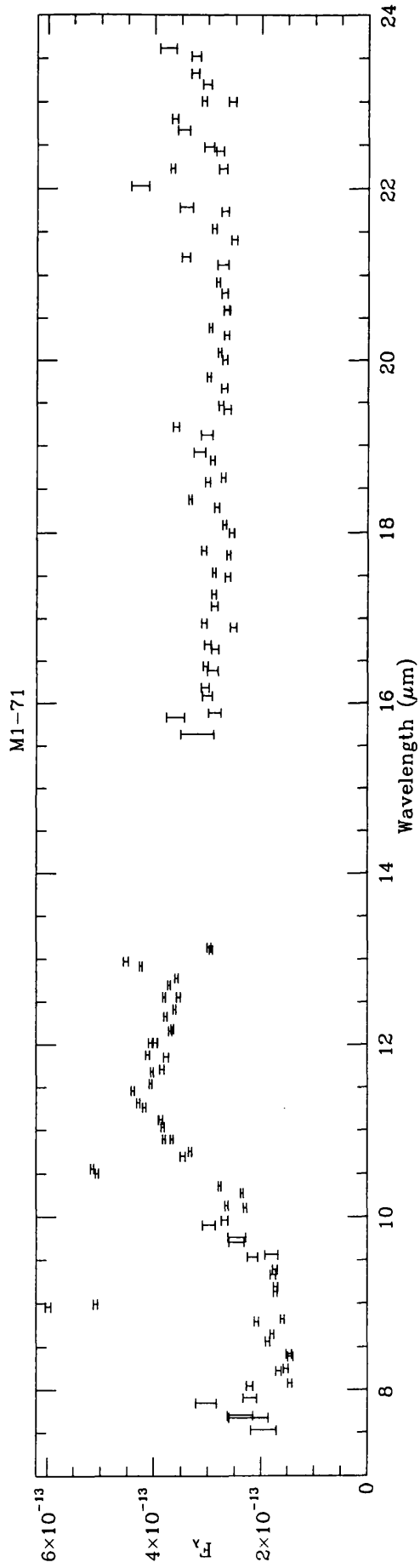
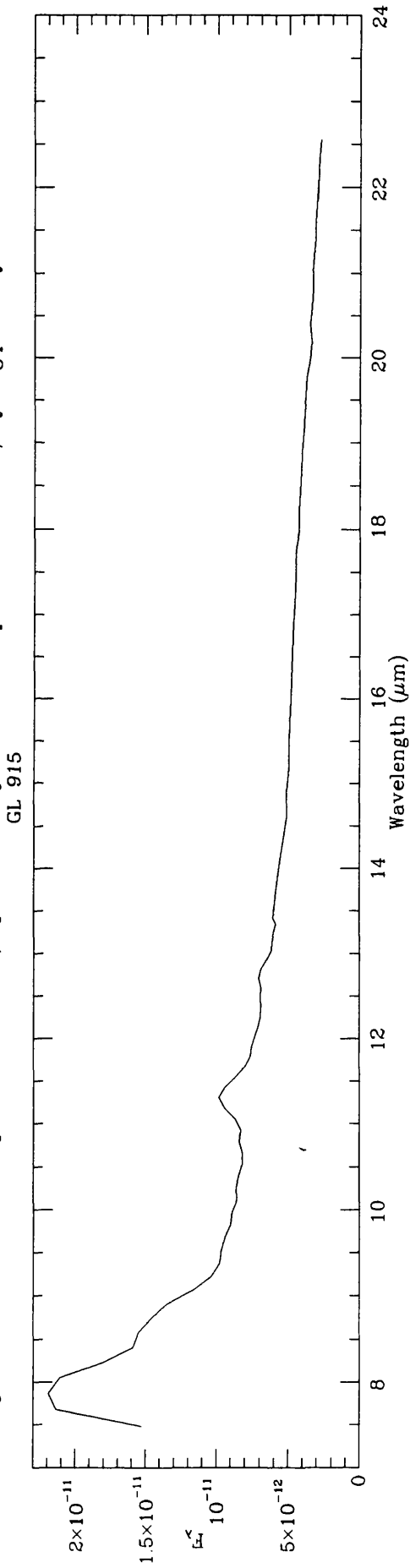
Figure 6.7: The *IRAS* LRS spectra of IRAS 20000+3239 and IRAS 23304+6147 which exhibit the 21  $\mu\text{m}$  emission feature.



the spectral type seems to holding. This ties in with the idea that carriers of the  $21\mu\text{m}$  band are large clusters of molecules, or grains, which are very fragile. They can be excited by low energy (visible) photons, but the harsh UV photons from stars with spectral type earlier than F3 can destroy them. However, there are other PAH features which exist throughout these spectral types and still survive in the PN stage. An alternative explanation is that we are witnessing an ageing sequence, since an earlier spectral type implies that the nebula is older. Both ideas are supported by the fact that the spectrum of a B9 star, GL 915 (spectral type B9, Figure 6.8) does not have any evidence of  $21\mu\text{m}$  emission. Also, there is an increase in the  $12.2$  to  $11.5\mu\text{m}$  ratio with increasing spectral type. Again, the partially hydrogenated PAHs responsible for  $11.5\mu\text{m}$  features may be dehydrogenated, giving rise the  $11.3\mu\text{m}$  feature often seen in PNe. This effect may be due not only to the temperature, since differences in temperatures in these spectral types are small, but may also be due to the molecules being exposed to these photons for a long period of time i.e., annealing process and stripping off of hydrogen atoms from the ring. Since the plateau of the  $10.5$ – $13\mu\text{m}$  feature indicate the number of hydrogen atoms attaching to the ring to be either 1, 2 or 3 (Allamandola 1988), the emergent of the  $11.3\mu\text{m}$  feature indicates the process of dehydrogenation in hotter stars (e.g., Figure 6.8 of GL 915 and M1–71). This puts a severe constraint on the PAH structures and formation theory.

As can be seen from morphological studies of dust around post-AGB stars, dust grains are further processed even after their ejection. Amorphous silicate grains form during the AGB phase are annealed by the harsh radiation from stars, which may result in crystalline silicates eventually. As for C-rich stars, studies of their spectra reveal the structure of PAHs and other carbonaceous grains. These grains become part of the interstellar medium as the stars become white dwarfs and fade away. Hence, in order to understand various components of the interstellar medium, such studies are crucial.

Figure 6.8: The *IRAS* LRS spectrum of GL 915, a post-AGB object and CGS3 spectrum of M1-71, a young planetary nebula.



# Concluding Remarks

The study of mass loss from late type stars enables us to learn more about stellar evolution and obtain an understanding of dust enrichment of the interstellar medium. The problem needs to be studied at a very wide range of wavelengths, though due to extinction by the circumstellar envelope of the star itself, infrared, sub-millimetre and radio observations yield more information than higher frequency observations. This thesis illustrates how observations at long wavelengths probe different regions in circumstellar shells.

The radiative transfer code (Haisch 1979) used in modelling infrared energy distributions of OH/IR stars takes into account physical effects that happen in radiative transfer, for examples : multiple scattering, absorption and thermal re-emission. Unlike other radiative transfer codes, multiple grain size effects are included. The grain size distribution is taken to be the same as the MRN distribution for interstellar grains. In order to improve the results for stars with large outflows, the effect of radiation pressure, presently ignored, should be added. The extinction efficiencies used for O-rich outflows are those for silicates. These are modified values from the published work by Kratschmer & Huffmann (1979) and Draine & Lee (1985), with the 20:10 $\mu$ m ratio being 0.5 for most stars, and 0.8 for stars with a very deep silicate absorption. In stars with large mass loss rates, ice is expected to form in the outflows. It tends to condense onto already existing grains so efficiencies calculated for silicate core-ice mantle depends on the volume of each material. For these stars, modelling of energy distributions can be improved by including different sets of ice optical constants, which condense at different temperatures. Dust grains condensing at differing temperature tend to have slightly different extinction properties. Unfortunately, such data are not available for silicate grains, otherwise, a similar approach could also be taken.

Models of energy distributions are compared to observations of published near-infrared

photometry and *IRAS* LRS spectra, together with *IRAS* broad band photometry at 12, 25, 60 and 100 $\mu\text{m}$ . Stars chosen are those with information on their velocities and distances. Some of them are optically thin, i.e., the 9.7 $\mu\text{m}$  silicate feature is in emission, while some are optically thick, with the silicate feature in absorption. Some stars were chosen because they have evidence of ice in their outflows. Models for combination grains are successfully obtained for the first time. Dust mass loss rates, one of the results from these models presented in chapter 3, are outflow rates relatively close to central stars. The same is true for mass loss rates derived from ratios of *IRAS* fluxes at 25 and 12 $\mu\text{m}$ , while 60 $\mu\text{m}$  photometry can be used to obtain dust mass loss rates farther out in the shells. It is shown that estimated dust mass loss rates using various methods are in reasonable agreement. Also, gas mass loss rates are calculated using expressions from the literature, and are compared to dust mass loss rates in order to estimate dust-to-gas mass ratios for these stars. Radio observations of OH masers can be used to obtain gas mass loss rates (e.g., Bowers et al. 1983) out to a few  $10^{16}\text{cm}$ , and the sub-millimetre CO J=1-0 and J=2-1 lines have also been shown to be a very useful tool in estimating gas mass loss rates in the outermost region of circumstellar shells (e.g., Knapp & Morris 1985). Dust mass loss rates estimated from chapter 3 reflect the more recent period of mass loss from stars than mass loss rates derived from radio and sub-millimetre observations, since infrared emission arises closer to the central stars ( $\sim 10^{15}\text{cm}$ ). Results show that silicate dust models used are reasonable, and that the main uncertainty in estimating dust mass loss rates comes from the estimated distances to the stars. Comparisons between dust and gas mass loss rates lead to conclusions that either the dust-to-gas mass ratio is not a constant from star to star, or that mass loss rates vary with time. If mass loss rates do vary with time, a radiative transfer code made to cope with this would be valuable.

The resulting dust mass loss rate is used to calculate heating and cooling rates in the corresponding circumstellar shell in order to obtain the gas kinetic temperature, which is a very important parameter in CO line modelling. It has been shown that most changes in physical parameters hardly affect the final temperature structure. The parameter which can change significantly from one star to the next in AGB objects is the mass loss rates, which spans the range of  $10^{-7}$  to  $10^{-4}M_{\odot}/\text{yr}$ . For O-rich stars, the most efficient molecule which cools the gas is  $\text{H}_2\text{O}$ . It has a relatively complex structure compared to CO, which is a diatomic molecule. High mass loss rate stars have higher gas kinetic temperatures at

the same radius compared to those with low mass loss rates, due to higher viscous heating rates. The stars chosen for the calculation are those with differing mass loss rates. In order to improve the final results, more precise treatments of the H<sub>2</sub>O and CO cooling are reviewed, and adding smaller heating effects, which were neglected in the calculations in chapter 4. A major improvement would be to cope with time-dependent mass loss rates, which would result in a density profile that deviates from the  $\bar{r}^2$  dependence.

The modelling of CO line profiles is based on previously published work by Schonberg & Hempe (1986) and Schonberg (1988). The code takes into account the full treatment of radiative transfer of vibration and rotation transitions in CO lines. The resulting gas kinetic temperature from heating and cooling calculation and the dust temperature distribution from infrared modelling are used as inputs for the code. This is the first time that a self-consistent model for O-rich stars is presented. The outer boundary for the CO is limited by the photodissociation radius of CO, due to ambient UV radiation (Mamon et al. 1988).

From this thesis, combinations of infrared energy distributions and CO line modelling already suggest a variation in mass loss rate which occurs as a function of time. This can be studied further by observations of higher transitions of CO molecules. At present, we can predict both peak antenna temperatures and CO line profiles up to J=11-10 rotational lines for both v=0 and v=1 vibrational transitions and all the vi-rotational lines connecting these two vibrational states. The eleven rotational lines in the v=0 ground state alone would be more than sufficient in determining the actual kinetic temperature of the gas. This will also answers the question of why a star with a very thick dust shell has very low CO J=1-0 antenna temperature (see Heske et al. 1991). KAO observations, which will be carried out next year, will pinpoint the actual trend of the kinetic temperature, which can be used to improve the heating and cooling model, and also the CO line model. Some data are available for even higher transitions (e.g., J=17-16) and molecular data on CO need to be added in order for these to be modelled.

We also studied the morphology of some O-rich and C-rich post-AGB stars, using their mid-infrared spectra. We discovered interesting features in these spectra, which can be interpreted as evolution of dust from AGB stars. We obtained a large number of mid-infrared spectra of both classes of AGB and post-AGB stars, using CGS3. Further studies of these samples are underway. These will enable us to gain more insight into

dust composition, and evolution of this stage in these stars. It is interesting to note that most of these processed materials in the circumstellar envelopes will be returned to the interstellar medium, and enrich it for the next generation of stars.

# List of Publications

- Justtanont, K., 1989, From Miras to Planetary Nebulae : Which path for stellar evolution? eds. M.O. Mennessier and A. Omont (Gif sur Yvette:Editions Frontieres), p. 214  
(Modelling the Energy Distribution of Late Type Stars)
- Justtanont, K., Tielens, A.G.G.M. (1992) ApJ, 389, 400  
(Mass Loss from OH/IR Stars : Models for infrared emission of circumstellar dust shells)
- Skinner, C.J., Barlow, M.J., Justtanont, K., 1992, MNRAS, 255, 31p  
(Silicate Dust in a Vega-Excess System)
- Justtanont, K., Barlow, M.J., Skinner, C.J., Tielens, A.G.G.M., 1992, ApJ, 392, L75  
(The nature of the dust around the post-AGB objects, HD 161796 and HD 179821)
- Skinner C.J., Tielens, A.G.G.M., Barlow, M.J., Justtanont, K., 1992, ApJ, submitted  
(Methanol Ice in the Protostar GL2136)
- Justtanont, K., Barlow, M.J., Skinner, C.J., 1992, IAU Symposium 155, in press  
(Mid-infrared spectroscopy of four  $21\mu\text{m}$  emission band sources)
- Justtanont, K., Skinner, C.J., Tielens, A.G.G.M., in preparation  
(Modelling of the CO line profiles)

# References

- Aannestad P.A., 1975, ApJ, 200, 30
- Aitken, D.K., & Roche, P.F. 1982, MNRAS, 200, 217
- Aitken, D.K., Roche, P.F., Spenser, P.M. & Jones, B. 1979, ApJ, 233, 925
- Alcock, C., Ross, R.R., 1986, ApJ, 305, 837
- Allamandola, L.J., 1988, IAU Symp 135, eds. L.J. Allamandola & A.G.G.M. Tielens  
p 129
- Allamandola, L.J., Tielens, A.G.G.M., & Barker, J.R., 1989, ApJS, 71,733
- Allen, D.A., Hyland, A.R., & Caswell, J.L. 1980, MNRAS, 192, 505
- Allen, D.A., Baines, D.W.T., Blades, J.C., & Whittet, D.C.B., 1982, MNRAS, 199, 1017
- Aller, L.H., Ross, J.E., O'Mara, B.J., & Keyes, C.D. 1981, MNRAS, 197, 95
- Andrses, E., & Gre vess, N., 1989, Geochimica et Cosmochimica Acta, 53, 197
- Baud, B., & Habing, H.J., 1983, A&A, 127, 73
- Baud, B., Habing, H.J., Matthews, H.E., & Winnberg, A., 1979, A&ASS, 35, 179
- Baud, B., Sargent, A.I., Werner, M.W., & Bentley, A.F., 1985, ApJ, 292, 628
- Becker, R.H., White, R.L., Proctor, D.D., 1992, AJ, 103, 544
- Bedijn, P.J., 1977, PhD thesis, Rijksuniversiteit Leiden
- Bedijn, P.J., 1987, A&A, 186, 136
- Bertie, J.E., Labbe, H.J., & Whalley, E., 1969, J Chem Phys, 50, 4501
- Bester, M., Danchi, W.C., Degiacomi, C.G., & Townes <sup>Geballe, T.R.,</sup> C.H., 1991, ApJ, 367, L27
- Biermann, P., & Harwit, M., 1980, ApJ, 241, L107
- Bohren, C.F., & Huffman, D.R., 1983 Absorption and Scattering of Light by Small  
Particles, (New York:John Wiley&Sons)
- Bond, H.E. 1991, in IAU Symp. 145, Evolution of Stars: The Photospheric Abundance  
Connection, ed. G. Michaud & A. Tutukov (Dordrecht:Kluwer), p341

- Bowen, G.H., 1988, ApJ, 339, 844
- Bowers, P.F., 1978, A&A, 64, 307
- Bowers, P.F., Johnston, K.J., & Spencer, J.H., 1983, ApJ, 274, 733
- Bowers, P.F., Morris, M., 1984, ApJ, 276, 646
- Brett, J.M. 1991, MNRAS, 249, 538
- Bujarrabal, V.J. & Nguyen-Q-Rieu, 1981, A&A, 102, 65
- Burke, J.R., & Hollenbach, D.J., 1983, ApJ, 265, 223
- Buss, Jr, R.H., Cohen, M, Tielens, A.G.G.M., Werner, M.W., Bregman, J.D.,  
Wittenborn, F.C., Rank, D., & Sandford, S.A., 1990, ApJ, 365, L23
- Buss, Jr, R.H., Tielens, A.G.G.M., Cohen, M., Werner, M.W., Bregman, J.D.,  
Witteborn, F.C., 1992, ApJ, submitted
- Castor, J., 1981, Physical Processes in Red Giants, eds. I. Iben, Jr & A. Renzini,  
(Dordrecht:Reidel), p285
- Caswell, J.L., Haynes, R.F., 1975, MNRAS, 173, 649
- Cohen, M., Tielens, A.G.G.M., Allamandola, L.J., 1985, ApJ, 299, L93
- Cohen, M., Tielens, A.G.G.M., Bregman, J., Witteborn, F.C., Rank, D.M.,  
Allamandola, L. J., Wooden, D.H., & de Muizon, M. 1989, ApJ, 341, 246
- Cox, P., 1990, A&A, 236, L29
- Chackrian, C., 1976, J Chem Phys, 65, 4428
- Danchi, W.C., Bester, M., Degiacomi, C.G., McCullough, P.R., & Townes, C.H., 1990,  
ApJ, 359, L59
- Day, K.L., 1976, ApJ, 203, L99
- Day, K.L., 1979, ApJ, 234, 158
- Day, K.L., 1981, ApJ, 246, 110
- de Muizon, M., d'Hendecourt, L.B., & Perrier, C., 1986, Proceedings of the first IRAS  
conference, ed. F.P. Israel, (Dordrecht:Reidel), p221
- Draine, B.T., & Lee, H.M., 1984, ApJ, 285, 89
- Dyck, H.M., & Lockwood, G.W., <sup>Capps, R.W.,</sup> 1974, ApJ, 189, 89
- Efstathiou, A., & Rowan-Robinson, M., 1990, MNRAS, 245, 275
- Elitzur, M., 1978, A&A, 62, 305
- Elitzur, M., 1981, Physical Processes in Red Giants, eds. I. Iben, Jr & A. Renzini,  
(Dordrecht:Reidel), p363

- Elitzur, M., Brown, J.A., & Johnson, H.R., 1989, ApJ, 341, L95
- Elitzur, M., Goldreich, P., & Scoville, N., 1976, ApJ, 105, 384
- Engels, D., & Lewis, B.M., 1989, From Miras to Planetary Nebulae : Which path for stellar evolution?, eds, M.O. Mennessier, A. Omont, (Gif-sur-Yvette:Editions Frontieres), p250
- Epchtein, N., Guibert, J., Nguyen-Q-Rieu, Turon, P., & Wamsteker, W., 1980, A&A, 85, L1
- Evans, N.J., & Beckwith, S. 1977, ApJ, 217, 740
- Fernie, J.D., & Garrison, R.F. 1984, ApJ, 285, 698
- Fix, J.D., & Mutel, R.L., 1984, AJ 89, 406
- Flower, D.R., & Launey, J.M., 1985, MNRAS, 214, 271
- Fowler, w.,A., Caughlan, G.R., Zimmerman, B.A., 1975, Ann Rev Astron Astrophys, 13, 69
- Fox, M.W., & Wood, P.R., 1982, ApJ, 259, 198
- Forveille, T., Morris, M., Omont, A., & Likkell, L. 1987, A&A, 176, L13
- Geballe, T.R., Tielens, A.G.G.M., Kwok, S., & Hrivnak, B.J., 1992, ApJ, submitted
- Geballe, T.R., Lacy, J.H., Persson, S.E., McGregor, P.J., & Soifer, B.T., 1985, ApJ, 292, 500
- Geballe, T.R., Tielens, A.G.G.M., Kwok, S., & Hrivnak, B.J., 1992, ApJ, 387, L89
- Gehrz, R.D., Kleinmann, S.G., Mason, S., Hackwell, J.A., & Grasdalen, G.L., 1985, ApJ, 290, 296
- Gillett, F.C., & Forrest, W.J., 1973, ApJ, 179, 483
- Gilman, R.C., 1972, ApJ, 178, 423
- Goldreich, P., & Scoville, N., 1976, ApJ, 205, 144
- Griffin, I.P. 1990, PhD thesis, University of London
- Haisch, B.M., 1979, A&A, 72, 161
- Hamann, W.R., 1981, A&A, 93, 353
- Hamann, W.R., 1985, A&A, 148, 364
- Hartman, L., & Avrett, E.H., 1984, ApJ, 284, 238
- Hartman, L., & McGregor, K.B., 1980, ApJ, 242, 260
- Harvey, P.M., Bechis, K.T., Wilson, W.J., & Ball, J.A., 1974, ApJS, 27, 311
- Herbst, E., & Knudson, S., 1981, ApJ, 245, 529

- Hempe, K., & Schonberg, K., 1986, *A&A*, 160, 141
- Herman, J., Burger, J.H., & Pennix, W.X., 1986, *A&A*, 167, 247
- Herman, J., & Habing, H.J., 1985, *Physics Reports*, 124, 255
- Heske, A. Forveille, T., Omont, A., van der Veen, W.E.C.J., & Habing, H.J., 1990,  
*A&A*, 239, 173
- Hoare, M.G., 1988, PhD thesis, University of London
- Hodapp, K.-W., Sellgren, K., Nagata, T., 1988, *ApJ*, 326, L61
- Hollenbach, D.J., & McKee, C.F., 1979, *ApJS*, 41, 555
- Holzer, T.E., Fla, T., & Leer, E., 1983, *ApJ*, 275, 808
- Hrivnak, B.J., & Kwok, S., 1991, *ApJ*, 371, 631
- Hrivnak, B.J., Kwok, S., & Volk, K.M., 1989, *ApJ*, 346, 265
- Huber, K.P., & Herzberg, G., 1979, *Molecular and Molecular Structure*, (van Nostrand:  
Reinhold)
- Hudgins, D.M., Sanford, S.A., Allamandola, L.J., & Tielens, A.G.G.M., 1992, *J Phys  
Chem Ref Data*, in press
- Huggins, P.J., & Glassgold, A.E., 1982, *ApJ*, 252, 201
- Humphreys, R.M., & Ney, E.P. 1974, *ApJ*, 190, 399
- Hyland, A.R., Beckwith, E.E., Frogel, J.A., & Neugebauer, G., 1972, *A&A*, 16, 204
- Iben Jr., I., & Renzini, A. 1983, *Ann Rev A&A* 21, 271
- Jewell, P.R., Barla, W., Walmsley, C.M., & Wilson, T.L., 1984, *A&A*, 130, L1
- Jones, T.J., Bryja, C.O., Gehrz, R.D., Harrison, T.E., Johnson, J.J., Klebe,  
D.I., Lawrence, G.F., 1990, *ApJSS*, 74, 785
- Jones, T.J., Hyland, A.R., & Gatley, I., 1983 *ApJ*, 273, 660
- Jones, T.J., & Merrill, K.M., 1976, *ApJ*, 209, 509
- Jura, M., 1987, *ApJ*, 313, 743
- Koike, C., & Tsuchiyama, A., 1992, *MNRAS*, in press
- Knapp, G.R., & Morris, M., 1985, *ApJ*, 292, 640
- Knapp, G.R., Phillips, T.G., Leighton, R.B., Lo, K.Y., Wannier P.G., Wootten, H.A.,  
& Huggins, P.J., 1982, *ApJ*, 252, 616
- Kolésnik, I.G., Pilyugin, L.S., 1989, *IAU Sym No 131, Planetary Nebulae*, ed  
S.Torres-Peimbert, (Dordrecht:Kluwer) p460
- Kratschmer, W., & Huffman, D.R., 1979, *Astrophys. Space Sci.*, 61, 195

- Kudritzki, R.P., & Reimers, D., 1978, A&A, 70, 227
- Kwan, J., & Hill, F., 1976, ApJ, 215, 781
- Kwan, J., & Linke, R.A., 1982, ApJ, 254, 587
- Kwok, S., 1976, J Roy Astron Soc Can, 70, 49
- Kwok, S., Fitzgerald, P.M., Purton, C.R., 1978, ApJ, 219, L125
- Kwok, S., Hrivnak, B.J., & Geballe, T.R., 1990, ApJ, 360, L23
- Kwok, S., Volk, K.M., & Hrivnak, B.J., 1989, ApJ, 345, L51
- Lamers, H.J.G.L.M., Waters, L.B.F.M., Garmany, C.D., Perez, M.R., & Waelkens, C.,  
1986, A&A, 154, L20
- Le Bertre, T., 1987, A&A, 180, 160
- Lebofsky, M.J., Kleinmann, S.G., Reike, G.H., & Low, F.J., 1976, ApJ, 206, L157
- Leger, A., Gauthier, S., Defourneau, D., & Rouan, D., 1983, A&A, 117, 164
- Leger, A., Klein, J., de Cheveigne, S., Guinet, C., Defourneau, D., & Belin, M., 1979,  
A&A, 79, 256
- Leger, A., Puget, J.L., 1984, A&A, 135, L5
- Lester, D.F., & Dinerstein, H.L. 1984, ApJ, 281, L67
- Letzelter, C., Eidelsberg, M., Rosatas, F., Breton, J., & Thieblemont, B., 1987, Chem  
Phys, 114, 273
- Leung, C.M., 1975, J Quant Spectrosc Radiat Transfer, 16, 559
- Lien, D.J. 1990, ApJ, 355, 680
- Likkell, L., 1989, ApJ, 344, 350
- Likkell, L., Forveille, T., Omont, A., & Morris, M. 1991, A&A, 246, 153
- Little-Marenin, I.R., 1986, ApJ, 307, L15
- Lockwood, G.W., 1970, ApJ, 160, L47
- Lockwood, G.W., 1985, ApJSS, 58, 167
- Luck, R.E., Bond, H.E., & Lambert, D.L. 1990, ApJ, 357, 188
- Margulis, M., van Blerkom, D.J., Snell, R.L., & Kleinmann, S.G., 1990, ApJ, 361, 673
- McKee C.F., Storey, J.W.V., Watson, D.M., & Green, S., 1982, ApJ, 259, 647
- McWhirter, R.W.P., Thonemann, P.C., & Wilson, R., 1975, A&A, 40, 63
- Mamon, G.A., Glassgold, A.E., & Huggins, P.J., 1988, ApJ, 328, 797
- Martin, P.G., 1975, ApJ, 202, 393
- Mathis, J.S., Rumpl, W., & Norsieck, K.H., 1977, ApJ, 217, 425

- Merrill, K.M., & Stein, W.A., 1976, PASP, 88, 294
- Mie, G., 1908, Ann Physik, 25, 377
- Mihalas, D., Kunaz, P.B., & Hummer, D.G., 1975, ApJ, 202, 465
- Morris, M., 1975, ApJ, 197, 603
- Morris, M., 1980, ApJ, 236, 823
- Netzer, N., & Knapp, G.R., 1987, ApJ, 323, 734
- Neugebauer, G., & Leighton, R.B., 1969, Two Micron Sky Survey : A preliminary catalogue (Washington:NASA)
- Nguyen-Q-Rieu, 1981, Physical Processes in Red Giants, eds. I. Iben Jr & A. Renzini, (Dordrecht:Reidel) p395
- Nguyen-Q-Rieu, Laury-Micoulaut, C., Winnberg, A., Schultz, G.V., 1979, A&A, 75, 351
- ~~Nguyen-Q-Rieu, Laury-Micholant, C., Winnberg, A., & Schultz, G.V., 1979, A&A, 75, 351~~
- Nuth, J.A., & Donn, B., 1982(a), J Chem Phys, 77, 2631
- Nuth, J.A., & Donn, B., 1982, ApJ, 257, L103
- Olander, D., & Rice, S.A., 1972, Proc Nat Acad Sci, 69, 98
- Omont, A., Moseley, S.H., Forveille, T., Glaccum, W.J., Harvey, P.M., Likkell, L., Loewenstein, R.F., & Lisse, C.M., 1990, ApJ, 355, L27
- Onaka, T., de Jong, T., & Willem, F.J., 1989, A&A, 218,169
- \* p.165 Parker, E.N., 1958, ApJ, 128, 664
- Parthasarathy, M., & Pottasch, S.R. 1986, A&A, 154, L16
- Payne, H.E., Phillips, J.A., & Terzian, Y. 1988, ApJ, 326, 368
- Pijpers, F.P., & Hearn, A.G., 1989, A&A, 209, 198
- Price, S.D., Walker, R.G., 1976, The AFGL FourSky Survey, AFGL TR-76-0208
- Reid, M.J., Muhleman, D.O., Moran, J.M., Johnston, K.L., & Schwartz, P.R., 1977, ApJ, 214, 60
- Riepurth, B., 1987, Nature, 325, 787
- Renzini, A., 1981, Physical Processes in Red Giants, eds. I. Iben, Jr & A. Renzini, (Dordrecht:Reidel), p431
- Renzini, A., & Voli, M. 1981, A&A, 94, 175
- Roche, P.F., & Aitken, D.A., 1984, MNRAS, 209, 33p

- Roche, P.F. & Aitken, D.K. 1986, MNRAS, 221, 63
- Roche, P.F., Aitken, D.K., & Smith, C.H., 1991, MNRAS, 252, 282
- Rosen, H., & Novakov, T., 1978, Atmos. Environment, 12, 923
- Rouan, D., Omont, A., Lacombe, F., & Forveille, T., 1988, A&A, 189, L3
- Rowan-Robinson, M., 1980, ApJS, 44, 403
- Rowan-Robinson, M., 1982, MNRAS, 201, 281
- Rowan-Robinson, M., & Harris, S., 1983, MNRAS, 202, 767
- Sahai, R., 1990, ApJ, 362, 652
- Sahai, R., Wooten, A., Schwarz, H.E., Clegg, R.E.S., 1991, A&A, 251, 560
- Salpeter E.E., 1974, ApJ, 193, 585
- Scharmer, G.B. 1981, ApJ, 249, 720
- Schatz, G.C., & Elgersma, H., 1980, Chem Phys Lett, 73, 21
- Schonberg, K., & Hempe, K., 1986, A&A, 163, 151
- Schonberg, K., 1988, A&A, 195, 198
- Schonberner, D., 1983, ApJ, 272, 708
- Schonberner, D. 1989, From Miras to Planetary Nebulae, Ed. M.O. Mennessier & A. Omont (Gif-sur-Yvette:Editions Frontieres), p355
- Schutte, W., & Tielens, A.G.G.M., 1989, ApJ 343, 369
- Sedlmayr, E., 1989, Interstellar Dust, eds. L.J. Allamandola & A.G.G.M. Tielens, (Dordrecht:Kluwer), p467
- Simon, T., Morrison, D., & Cruikshank, D.P., 1972, ApJ, 177, L17
- Sivagnanam, P., Le Squeren, A.M., & Foy, F., 1988, A&A, 206, 285
- Sivagnanam, P., Le Squeren, A.M., Foy, F., & Tran Minh, F. 1989, A&A, 211, 341
- Skinner, C.J., & Whitmore, B., 1988, MNRAS, 231, 169
- Smith, E.V., Jacobs, K.C., 1973, Introductory Astronomy and Astrophysics, (Philadelphia:Saunders)
- Sopka, R.J., Olofsson, H., Johansson, L.E.B., Nguyen-Q-Rieu, & Zuckerman, B., 1989, A&A, 210, 78
- Stephens, J.R., & Russell, R.W., 1979, ApJ, 228, 780
- Strecker, D.W., & Ney, E.P., 1974, AJ, 79, 797
- Stricker, J., 1978, J Chem Phy, 68, 934
- Suh, K.W., Jones, T.J., & Bowen, G.H., 1990, ApJ, 358, 588

- te Lintel Hekkert, P., Versteeg-Hensel, H.A., Habing, H.J., & Wiertz, M., 1989, A&ASS, 78, 399
- Tielens, A.G.G.M., 1983, ApJ, 271, 702
- Tielens, A.G.G.M. 1989, From Miras to Planetary Nebulae, Ed. M.O.Menessier & A. Omont (Gif-sur-Yvette:Editions Frontieres), p186
- Tielens, A.G.G.M., & Allamandola, L.J., 1987, Interstellar Process, eds D.J. Hollenbach, H.A. Thomason Jr., (Dordrecht:Reidel), p397
- Thomas, J.A., Robinson, G., & Hyland, A.R., 1976, MARAS, 174, 711
- Trams, N.R., Waters, L.B.F.M., Lamers, H.J.G.L.M., Waelkens, C., Geballe, T.R., The, P.S., 1991, A&ASS, 87, 361
- Treffers, R, Cohen, M., 1974, ApJ, 188, 545
- Unno, W., & Kondo, M., 1976, Publ. Astron. Soc. Japan, 28, 374
- van de Hulst, H.C., 1981, Light Scattering by Small Particles, (New York:Dover)
- van der Veen, W.E.C.J., & Habing, H.J., 1988, A&A 194, 125
- van der Veen, W.E.C.J., Habing H.J., & Geballe, T.R. 1989, A&A, 226, 108
- van der Veen, W.E.C.J., & Rugers, M., 1989, A&A, 226, 183
- van Langevelde, H.J., van der Heiden, R., & van Schooneveld, C., 1990, A&A, 239, 193
- Wattenbach, R., Krugel, E., Roser, H.P., Nett, H., Schwaab, G., & Densing, R., 1988, A&A, 202, 133
- Werner, M.W., Beckwith, S., Gatley, I., Sellgren, K., Berriman, G., & Whiting, D.L., 1980, ApJ, 239, 540
- Whitmore, B.R. 1986, Ph.D Thesis, University of London
- Willem, F.J., de Jong, T., 1988, A&A, 196, 173
- Willson, L.A., Bowen, G.W., 1985, Relation Between Chromospheric-Coronal Heating and Mass Loss in Stars, eds, R. Stalio & J.B., Zirker, (Triest:Observatorio Astronomics di Trieste) p128
- Wilson, W.J., & Barrett A.H., 1968, Science, 161, 778
- Wilson, W.J., & Barrett A.H., 1972, A&A, 17, 385
- Wilson, W.J., Schwatz, P.R., Neugebauer, G., Harvey, P.M., & Becklin, E.E., 1972, ApJ, 177, 523
- Wood, P.R., 1979, ApJ, 227, 220
- Wood, P.R., 1981, Physical Processes in Red Giants, eds. I Iben Jr & A. Renzini,

(Dordrecht:Reidel) p135

Wood, P.R., 1986, Stellar Pulsation, eds A.N. Cox, W.M. Sparkes & S.G.

Starrfield (Berlin:Springer-Verlag) p250

Wood, P.R., 1989, From Miras to Planetary Nebulae, Ed. M.O.Menessier &

A. Omont (Gif-sur-Yvette:Editions Frontieres), p67

Wood, P.R., Cahn, J.H., 1977, ApJ, 211, 499

Wood, P.R., Faulkner, D.J., 1986, ApJ, 307, 659

Zappala, R.R., Becklin, E.E., Matthews, K., & Neugebauer, G., 1974, ApJ, 192, 109

Zuckerman, B. & Gatley, I. 1988, ApJ, 324, 501

\* Pegourie, B., Papoular, R., 1985, A&A, 142, 451

Pendleton, Y.J., 1987, Ph.D. thesis, Univ. Calif. Santa Cruz